Summary of Research for the Inertial Confinement Fusion Program at Los Alamos National Laboratory

Compiled by
David C. Cartwright
Principal ICF Program Manager

DISCLAIMER

MASTER

CONTENTS

Summary of Research

for the

Inertial Confinement Fusion Program

at

Los Alamos National Laboratory

compiled by
David C. Cartwright
Principal ICF Program Manager

ABSTRACT

The information presented in this report is a summary of the status of the Inertial Confinement Fusion (ICF) program at the Los Alamos National Laboratory as of February 1985. This report contains material on the existing high-power CO_2 laser driver (Antares), the program to determine the potential of KrF as an ICF driver, heavy-ion accelerators as drivers for ICF, target fabrication for ICF, and a summary of our understanding of laser-plasma interactions. A classified companion report contains material on our current understanding of capsule physics and lists the contributions to the Laboratory's weapons programs made by the ICF program. The information collected in these two volumes is meant to serve as a report on the status of some of the technological components of the Los Alamos ICF program rather than a detailed review of specific technical issues.

Inertial Confinement Fusion Overview

by David C. Cartwright

The accomplishment of energy gain through nuclear fusion in laboratory experiments will require the solution of a number of interesting, although very complex, scientific and technological problems. Both the Inertial Confinement Fusion (ICF) and Magnetic Fusion Energy (MFE) programs have been somewhat overly optimistic in their initial evaluations of the difficulties involved in controlling nuclear fusion. In both programs, most of the major problems were identified only after the construction and operation of a new and usually more powerful experimental facility. Researchers in both the ICF and MFE programs are now trying to build solid technical foundations for their programs in order to be able to predict results under different experimental conditions. Los Alamos completed construction of the Antares CO_2 laser facility in December 1983 and placed it on operational status for experiments in ICF. Antares, the world's largest operational laser, is the first in a series of new, higher intensity ICF drivers and is the successor to the smaller ($\leq$ 10-kJ) Helios eight-beam CO_2 laser facility at Los Alamos. The two others in the US are Nova, at Lawrence Livermore National Laboratory (LLNL), to be operational in the spring of 1985, and PBFA-II at Sandia National Laboratories (SNL), to begin operation in the fall of 1987. These three new facilities will permit experimentation with ICF targets under conditions of temperature and pressure that more closely simulate those required for an energy gain target.

The ICF mission statement for the Los Alamos National Laboratory is as follows:

The Los Alamos ICF program is one of the main efforts by the Department of Energy (DOE) to evaluate the scientific feasibility of inertially confined fusion, using intense lasers or particle beams to compress and heat small masses of deuterium-tritium fuel to thermonuclear burn conditions. The goals of the national program are:
- *to support nuclear weapons physics research, and*
- *to do research on the potential of inertial fusion for energy production.*

Key technical elements within the ICF program are:
- *the design and confirmation of performance of fuel-filled targets requiring minimum input energy, and*
- *the development of a laboratory driver suitable for driving such targets (at an acceptable cost).*

Whether addressing weapons applications or possible long-term potential as an energy source, there is no significant difference in the short-term program. In the longer term, important scientific and engineering problems would have to be addressed before ICF could be considered for commercial electrical power generation. Since the primary source of the funding is the DOE defense programs, the weapon physics goals will continue to receive emphasis throughout this decade.

Since Antares has been in operation for more than a year, and Helios was operational for 5 years before Antares, it is appropriate to review our present understanding of ICF physics based on CO_2 laser drivers. The purpose of this technical review is to present our level of knowledge of the coupling of CO_2 laser energy to the target, acquired by experiments with both the Helios and Antares laser facilities. In the subsequent chapters, the scientific and technological progress that has been made in the fields of plasma physics, capsule physics, materials fabrication, CO_2 and KrF laser systems, and heavy-ion fusion (in support of the ICF program at Los Alamos) will be reviewed. A review of the Los Alamos program to study the physics of laser fusion at short wavelength (that is 1/4 μm) will be presented in a future publication.

GENERAL REQUIREMENTS FOR ICF

Inertial confinement fusion attempts to mimic on a miniature scale the physics of a thermonuclear weapons device. A fuel of deuterium and tritium (DT) is heated rapidly to temperatures high enough to promote fusion reactions in the fuel, and at the same time, the fuel is compressed to densities large enough to facilitate reaction of a large fraction of the fuel before cooling by hydrodynamic expansion. However, the efficient use of the DT fuel in ICF is much more difficult than in a nuclear weapon.

The difficulty arises from the requirement to contain (in the laboratory) the energy released by the fusion reaction. This can be accomplished only if the yield is sufficiently low, which implies a small mass of fuel. For small fuel masses to support thermonuclear burn, in which the energy produced by fusion reaction is used to sustain the burn, the fuel must be condensed to high density. Specifically, to trap the energy of the α-particles produced in the DT fusion reaction, the areal density (ρR) must be equal to or greater than a certain constant C. That is, a fundamental scaling parameter for all ICF is the product of fuel density ρ and the radius R of the volume containing the fuel. It can be shown that if the product ρR is equal to a constant, then the density to which the fuel must be compressed increases as the reciprocal of the square root of the fuel mass, that is, $\rho \approx 1/\sqrt{M}$. Achieving the required compression without expending excessive energy from the driver is the basic requirement of ICF.

Figure 1 shows schematically the various steps required to convert the incident laser energy into hydrodynamic compression of the fuel. Information on steps (a) and (b) is being obtained using laboratory drivers such as Helios and Antares, but data concerning steps (c) and (d) will require new and more powerful drivers. Keep in mind that the objective is to achieve net energy gain from the fusion reaction. Thus, it is important to achieve as large an energy conversion efficiency as possible at each step in the sequence. Because we know that ICF will work at some large drive energy, it is important to determine energy conversion efficiencies and energy requirements for each individual step as the figure of merit for judging the potential for success for laboratory drivers such as CO_2. The remainder of this introduction summarizes the scientific processes governing each step shown in the linkage of laser energy to fuel compression in Fig. 1. What is treated as an assertion at this level is explained, and qualified, in the articles that follow.

CHARACTERISTICS OF CO_2-IRRADIATED TARGETS

When high-intensity laser radiation ($<10^{15}$ W/cm^2) strikes a solid surface, a plasma is formed. The infrared radiation (10.6 μm) produced by the CO_2 laser is absorbed by the plasma through a collective process known as resonant absorption. This process, which we have come to understand primarily through theoretical work, converts almost all of the absorbed laser energy into energetic electrons. The measured absorption for flat surfaces is about 40%, and refraction of the incident light in the plasma reduces the absorption to about 30% for curved surfaces. The energetic electrons produced during the resonant absorption process approach temperatures of 80 keV. This distribution of so-called "hot electrons" can exist superimposed on a second "cold" distribution because there are very few collisions in the low-density corona formed around the target. Experiments show that hot-electron temperature increases with laser intensity as $I^{0.4}$.

Because all of the energy absorbed from the laser beam initially resides in the hot electrons, it is mandatory to understand the subsequent transport of the electrons in order to predict how energy can be delivered to other portions of the target. Very large electric and magnetic fields develop, for conditions characteristic of CO_2-laser-driven targets, as a result of the large spatial gradients in temperature and density present in the plasma. The magnetic fields are confined to within a few hundred micrometers of the surface and may exceed a megagauss. Consequently, the magnetic forces dominate the motion of most electrons, and their transport is not described by mathematical solutions of the diffusion equations. The self-consistent theoretical treatment of plasma motion under the influence of an intense laser radiation field has been a major accomplishment of the theorists in this program.

For CO_2 laser intensities exceeding 2×10^{15} W/cm^2, the self-generated magnetic fields become large enough to prevent hot electrons from returning to their origins on the surface defined by the critical plasma density (10^{19} cm^{-3} for 10.6-μm radiation). As a consequence of this
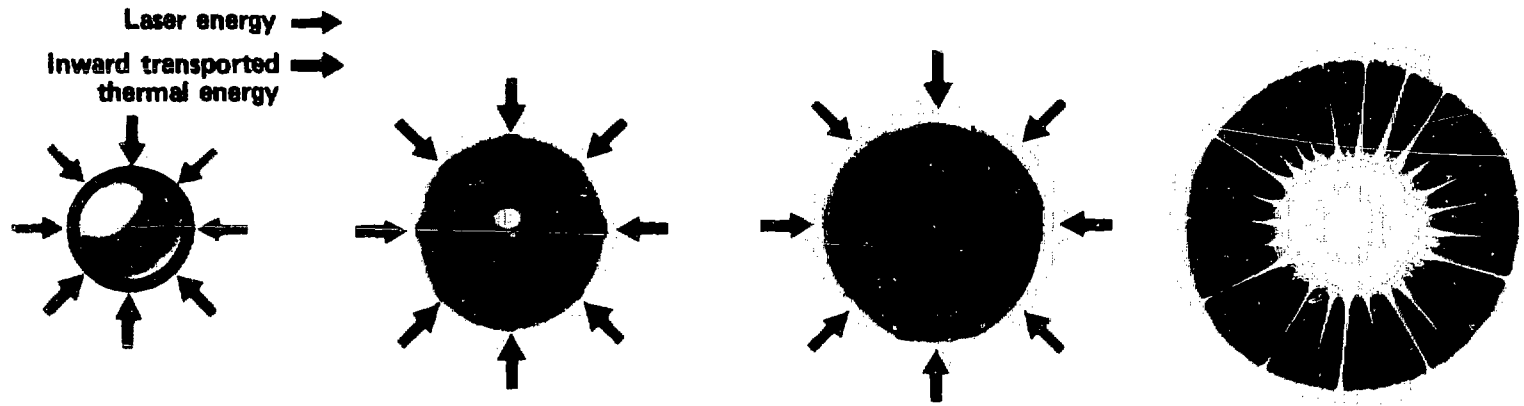
Atmosphere Formation

Laser or particle beams
rapidly heat the surface
of the fusion target
forming a surrounding
plasma envelope.

(a)

Compression

Fuel is compressed by
rocket-like blowoff of
the surface material.

(b)

Ignition

With the final driver pulse, the
full core reaches 1000 – 10,000 times
liquid density and ignites at
100,000,000°C.

(c)

Burn

Thermonuclear
burn spreads
rapidly through the
compressed fuel, yielding
many times the driver
input energy.

(d)

Fig. 1. Steps in the conversion of incident laser energy into hydrodynamic work compression on the fuel. Source is Ref. 1.

magnetically enforced charge separation, ions are accelerated away from the target surface. This ion "blow-off" is not efficient in driving an implosion of the fuel because the momentum per unit energy of the ions is low and represents an energy loss for targets. Elaborate target geometries have been designed that attempt to efficiently recover the energy carried by the fast ions.

For good hydrodynamic coupling of momentum to the fuel, the ablation of a large mass at the (low) velocity set by the thermal energy content of the ablator material is required. To minimize the energy needed to compress the fuel, it is necessary to minimize preheat to an energy level that places the fuel on an adiabat that does not greatly exceed $T \approx 5$ keV at the time of maximum compression. Further refinements are possible only if the central portion of the fuel is elevated to ignition temperatures by properly timed shock collisions. This central portion of the fuel can then trigger heating of the remainder of the fuel by local deposition of the α-particles released in the DT reaction.

In the Los Alamos program, we have attempted to capitalize on the great operational advantages of the CO_2 laser, the most efficient and inexpensive high-power laser available. To develop the next generation driver will require several hundred million dollars of investment. For this reason, all conceivable ways of using the absorbed energy in whatever form it might appear in the target (electrons, ions, x rays, and so forth) are being carefully and systematically explored. These efforts were reviewed by external panels of experts in 1982 and 1983. In the most recent review, the possible use of the large internal magnetic fields to provide insulation from preheat by hot electrons was suggested. Work in this regard has progressed to the development and computational testing of a novel target that combines advantages of both ICF and MFE by inclusion of magnetic fields for inhibition of electron thermal conduction. This target concept is now being tested using the Antares laser.

CONTRIBUTIONS BY ICF TO THE WEAPONS PROGRAMS

Almost since its inception, the ICF program has been viewed as a potentially significant contributor to the understanding of the physics of nuclear weapons design. Numerous studies over the years have attempted to define a role for ICF in weapons physics, identifying the potential for equation-of-state measurements, opacity measurements, thermonuclear burn studies once ignition was achievable, and large-scale x-ray vulnerability facilities once yields approaching 200 MJ were obtained.

The contributions from the ICF program to the weapons program are summarized below.

- One of the greatest contributions from ICF is its unique computer code capability.
- The national ICF program would be critical to the US defense program in the event of a comprehensive test ban treaty (CTBT) or a lowered threshold (LTBT) on nuclear testing. New drivers such as light ions (PBFA-II), lasers (for example, KrF), or HE-driven concepts could provide a means of exercising and maintaining design capability under a CTBT as well as a means of addressing the feasibility of fusion itself.
- Improvements in material fabrication developed within ICF program have been important ingredients in testing certain x-ray concepts for the Strategic Defense Initiatives (SDI) program.
- The Antares laser facility is a unique source of x-ray and microwave radiation and can be of direct use in studying the response of materials to this intense radiation. A future laboratory fusion facility could indeed study vulnerability, lethality, and weapons effects, particularly in the event of a CTBT.
- The physics of rare-gas halide lasers studied in the ICF program is highly beneficial to SDI considerations of laser weapons and their effects.

In addition to the early-identified results cited above, both the weapons and ICF programs have benefited from sharing and exchanging personnel. During its 12 years at Los Alamos, the ICF program has attracted many outstanding technical people to the Laboratory who might not otherwise have come and helped them develop in technical areas of *direct* interest to the weapons program. Now the Laboratory benefits from their contributions to other Laboratory activities.

THE FUTURE

Over 10 years of research have taught us a great deal about ICF on a laboratory scale, and it is certainly more difficult than originally envisioned. The inevitable inefficiencies in all the steps between providing incident energy and igniting a fuel have plagued the program. However, there still exists the certainty that ICF works well on some energy scale, and in our quest to provide unlimited energy by control of fusion, the workability of ICF should not be overlooked. We are still far from any practical use, but the promise warrants a sustained national effort. For at least the remainder of this decade,

we should fully utilize the potential of the research facilities and the technology base we have already established.

Should our attempts to devise a CO_2 laser target that will achieve high energy gain fail, technology development programs for both a new laser system (KrF) as well as an alternative to all lasers, a heavy ion-beam accelerator, are in progress at Los Alamos. The purpose of the KrF program at Los Alamos is to understand the science and technology required to develop an efficient, rep-ratable, low-cost, short-wavelength source of intense radiation that can be scaled to meet future ICF driver needs. In the case of the heavy-ion program, the purpose is to work with the other participants to identify and begin resolution of the key technical issues associated with a heavy-ion ICF driver. These programs are not so much intended to provide a large target-shooting capability as to establish the cost scaling of these particular systems for potential megajoule-level systems. The research activities on these two advanced ICF drivers are described in this review.

REFERENCE

1. H. G Ahlstrom, *Physics of Laser Fusion, Vol II, Diagnostics of Experiments on Laser Fusion Targets at LLNL*, Lawrence Livermore National Laboratory, January 1982, p 5.

High-Energy-Density Plasma Physics With Lasers

by David W. Forslund and Philip D. Goldstone

This section is a preliminary draft being prepared for publication in *Los Alamos Science*. It is meant primarily as an introduction to the complex plasma processes which occur in the process of laser fusion.

To successfully fulfill the promise of inertial fusion, an extremely wide variety of physical phenomena involved with the flow of matter and energy must be controlled with considerable precision. Experimental and theoretical studies of the deposition of laser light and transfer of that energy to particles have uncovered many new phenomena that have altered many simple models for use in fusion and that have greatly enhanced our understanding of extremely high-energy-density plasmas such as most probably exist in the atmospheres of white dwarfs or in galactic nuclei, albeit on a much shorter time and space scale. We must understand the physics of matter from 10^{-5}–10^3 g/cm^3 over distances of 10^{-5}–10^0 cm and times of 10^{-15}–10^{-8} s with particle energies ranging from 0.1 eV to 10^6 eV and magnetic fields ranging from none at all to 10^3 T. The physics involved is nearly collisionless plasma physics including the effects of spontaneously generated magnetic fields, high-density collisional physics, the atomic physics of weakly to highly ionized materials, and their effects on transport of photons of all energies as well as particles. Frequently the processes are far from equilibrium and require elaborate rate equations to reasonably accurately describe the effects.

The biggest problem for inertial fusion in general, and laser fusion in particular, has been the mechanism of deposition of laser light energy into the target and subsequent transport of that energy to the ablation surface. The very properties of lasers that allow them to produce extremely high power and intensity (which is necessary for fusion) can work against a desirable form of energy deposition. In particular, the wave nature of the light, the high coherence, and narrow bandwidth all contribute to peculiar collective effects in the deposition that reduce the efficiency of several of the above steps. In other words, these highly organized properties of the laser tend to drive the hot plasma in the target far from thermodynamic equilibrium with potentially serious consequences. Although these processes are not favorable for laser fusion, they enable one to achieve extremely high-enegy-density plasmas with very high specific energy per particle. In particular, laser fusion with CO_2 lasers at 10 μm is dominated by such effects and allows the physicist to view such exotica in all their complexity.

In this section, we discuss a number of these unusual collective processes as found in high-power CO_2 laser-target physics and briefly discuss some of the possible relationships with processes taking place in other physical systems far removed in scale from ICF research. The reader should note that shorter wavelength laser-plasma interactions tend to be more collisional, and the collective processes discussed here are generally less dominant.

The collective mechanisms we discuss initially result in the production of energetic electrons by the absorption of laser radiation in the target corona. The hot-electron energy then "cascades" into a number of energy flow channels (magnetic fields, acceleration of energetic ions, bremsstrahlung emission, heating of a dense "thermal" plasma, and microwave emission). Whereas much of our understanding of absorption processes has been theoretical because of the limited number of unambiguous experimental signatures of these processes at 10 μm, our understanding of energy flow through this hierarchy has largely been empirical, with theory providing explanation of our observations and a basis for predicting scaling of these phenomena.[1] In many cases, these theoretical explanations have provided new hypotheses to test experimentally as well as new insights into how the energy flow might be altered.

THEORETICAL TOOLS

We will begin by describing the methods we have used to study these processes and a little about how they have developed and improved over the years. The inertial fusion program has had a well-balanced program with considerable strength in both the theoretical and experimental areas. Because of the extreme complexity of the physics, it has been at the forefront in developing new theoretical tools as well as experimental techniques. The phenomena of interest change over time scales of picoseconds with the entire experiment occurring in about a nanosecond. Spatial resolution required to study the physics of targets measured in hundreds of micrometers to millimeters typically approaches 10 μm (the wavelength of the CO_2 light). Since much of the truly microscopic (submicrometer, subpicosecond) phenomena cannot be readily measured, but strongly influence the macroscopic behavior, computer simulation is relied on heavily to couple the microscopic phenomena to macroscopic observables. The WAVE code is a 2D particle simulation code that solves Maxwell's equations and the relativistic Newton's laws for the particles in the self-consistent three-component electric and magnetic fields. It typically advances 10^6 particles on a grid of 10^5 cells for 10^4 time steps to determine the processes that absorb the laser light and transport the energy from the low-density, hot-plasma regions to the denser regions. Only a portion of the physical problem can be modeled because one must limit the time step to a small fraction of the laser period and the grid size to the distance light travels in one time step. Consequently, the time that can be covered is only a few picoseconds and the distance is only about 10 wavelengths of light. Because of the limited time and space scale, the boundary conditions and initial conditions for fields and particles are unknown and must be estimated. Much of the skill in using the code involves guessing the right boundary and initial conditions that appear to be consistent with themselves, with hydrodynamic calculations, and with experiment.

An implicit form of the code, called VENUS,[2] has enabled one to greatly increase the time step and grid size (at the expense of some high-frequency phenomena) to consider realistic spatial scales, which allows the study of the central role of self-generated magnetic fields in electron transport and fast-ion emission. After their development by the ICF program, these new-generation codes rapidly spread to the magnetic fusion and space physics communities. Although quantum mechanical and atomic physics process are not included in these codes, they can accurately describe the fully developed strong turbulence that can occur in laser-plasma interactions, limited only by the computer resources. To better utilize the results of these codes, we test and evaluate various models to obtain scaling laws that can be reliably extrapolated into new regimes. For example, simplified models of the propagation and absorption of light in the plasmas have been verified as to their accuracy and range of validity with the WAVE code. In the last decade, the improvement in scale of problems accessible has increased by a couple of orders of magnitude because of improvements in computer hardware speed and in numerical algorithms (VENUS). This has greatly increased our understanding of the physical processes as discussed below.

EXPERIMENTAL TOOLS

In addition to the theoretical tools that have greatly aided our insight into the complex processes in these plasmas, a wide variety of experimental tools and techniques have provided the basic empirical information against which the theoretical models must be compared in an iterative process. Overall energy balance can be obtained by measuring the nonabsorbed light directly or by calorimetrically measuring all of the ion and x-radiation energy emitted from the target. Some hot electrons escape the target and can be detected with electron spectrometers; however, the bulk of the electron energy is observable primarily by measurement of the bremsstrahlung radiation from several kiloelectron volts to large fractions of a megaelectron volt, where possible with subnanosecond time resolution. Typically, electron temperatures of hundreds of kiloelectron volts are observed.[3] A variety of instruments can be used to determine the spectra of accelerated ions.

The heated target material emits soft x rays that are detected by multichannel soft x-ray spectrometers utilizing filtered vacuum x-ray (photo) diodes, along with ultrafast oscilloscopes developed in the nuclear weapons program, to provide time resolution of about 200 ps. Spatially restricting the area viewed by the soft x-ray diodes enables measurement of the brightness temperature as well as the color temperature of a specific part of the target surface. This is provided by multichannel x-ray collimators. The small targets used in the ICF program require that these collimators be made of precisely machined pinholes of approximately 150 μm diameter, aligned with respect to each other and the target to an accuracy of 25 μm using optical techniques.

Optical and x-ray emission can be spectrally resolved, or imaged using simple optical cameras or pinhole cameras, and either images or spectra can be time resolved to tens of picoseconds using image-converter streak cameras. The detailed atomic physics of the plasma corona, often far out of local thermodynamic equilibrium, can be examined using high-resolution x-ray and xuv spectrometers to observe the spectra from the corona. Details of the spectra such as line broadening and line shapes can be used together with detailed atomic physics models as a probe of the plasma conditions surrounding the ions of interest; this can be particularly useful in spectroscopically examining the conditions of the imploded fuel. The pinhole cameras, soft x-ray collimators, and x-ray spectrometers must be close to the target and must survive the intense x-ray and particle debris "blast" from each shot.

Imaging of the target plasma in x-rays characteristic of some transition of interest in the target or corona, for example a K-line resulting from a hot-electron-caused inner shell vacancy, enables the experimenter to track the flow of electron energy.

Detailed microfabrication technology is used to produce complex targets, with specific materials placed at strategic locations, so that their x-ray emission can be used as a "tracer" to determine the amount, or the time, of energy flow to these locations, as well as allowing detailed examination of plasma conditions from a well-defined region, without having to average over all densities and temperatures achieved in the plasma.

The availability of such a wide range of measurement technologies, together with the detailed ability to design experiments by microscopic modification of the targets, has allowed us to develop a detailed empirical base against which the theoretical picture of the processes involved can be compared.

COMPARISON WITH EXPERIMENT

. The insight gained from WAVE/VENUS simulations and verification of various models has led to the improvement in various physics packages in the 2D radiation flow/hydrodynamics code LASNEX and to a better choice of input conditions to the code. LASNEX then is used to model the hydrodynamics, electron transport, and radiation flow and possible thermonuclear burn in the target. Sometimes it can be used to evaluate models by observation of their effect on the macroscopic target

behavior. LASNEX has postprocessing packages such as TDG which allow it to generate directly outputs from various diagnostic instruments such as pinhole photographs, streak camera images, bremsstrahlung spectra, ion emission, and soft x-ray emission. Since the code also calculates the source spectra, it can be used to assist in the deconvolution of, for example, the electron temperature from the hard x-ray bremsstrahlung spectrum or the compressed-fuel properties from the x-ray pinhole images and x-ray spectra. By simultaneous modeling of a variety of phenomena on a given target shot, the use of the code greatly enhances one's confidence in understanding the target behavior. Frequently there has to be an iteration in LASNEX input conditions to match the experimental data. In other cases suggestions can be made to modify existing diagnostics or develop new ones to search for specific predicted signatures of physical phenomena. From this iteration process, new target concepts have been developed in an attempt to better utilize the energy flow.

LASER LIGHT TRANSPORT AND ABSORPTION

In large laser systems, the light must travel from the last large optical surface a long distance through a near-vacuum to the target. The intensity at the target is controlled to a large extent by the focal properties of the final optical element and is adjusted for direct-drive laser fusion to achieve nearly uniform illumination at the target. The initial illumination uniformity is not maintained, however, because as the target heats up, hot plasma is blown off. Because the index of refraction of a plasma depends on density as $n = 1 - \omega_p^2/\omega^2$, where $\omega_p^2 = 4\pi ne^2/m$ is the square of the local plasma frequency, ω is the laser frequency, and n is the electron density, the propagation of light in this plasma is altered from what it is in a vacuum. Linearly, the light may refract and not strike the target where it was originally. Nonlinearly, the light may break up into filaments because of localized heating of the plasma or the finite pressure of the light itself. This may cause local regions of light to be much more intense than others, which may degrade the symmetry of the implosion or increase the energetic electron generation.

A important first step in the overall energetics of laser fusion is the determination of how much of the incident light is absorbed in the target. Absorption is measured in variety of ways including measuring the scattered light

from the target and measuring the integrated ion blowoff kinetic energy from the target. Figure 1 shows the absorption on spheres of various sizes as a function of intensity as measured by ion calorimetry.[4] Typically, at the lower intensities shown at the left, the absorption is about 30%, whereas at high intensities it can exceed 60%.

What are the mechanisms of absorption and how can we identify which ones are actually operative in laser target experiments? Although inferences can be made from a variety of experimental data, most of the information on absorption processes have come from computer simulations and analytic theory, which have been iterated to reproduce the experimental data base. The simplest form of absorption of laser light results from collisions of electrons oscillating in the laser electric field with the background ions. This process, known as inverse brems-strahlung, works by randomly scattering the oscillating electrons off the ions. Thus, coherent oscillation energy is converted into random energy. By equating the dissipated light energy, $\nu E^2/8\pi$, to the heating rate,

ν_{ei} $nmv^2/2$, where $v = eE/m\omega$, we find that the bremsstrahlung absorption frequency is $\nu = \nu_{ei} n/n_c$, where n_c is the density at which $\omega_p = \omega$. The absorption length for light then is c/ν. Since the electron-ion collision frequency ν_{ei} varies as v^{-3}, inverse bremsstrahlung preferentially heats low-velocity electrons and thus keeps the plasma close to thermodynamic equilibrium. If L is the density scale height, then significant absorption occurs for $\omega L/c \approx 1$. If we balance the absorbed energy with the electron heat flux, we see that significant absorption only occurs for

$$I < 5 \times 10^{14}\, Z\, L(cm)/\lambda^4 ,$$

where Z is the ion charge state, L is the plasma scale length in cm and λ is the laser wavelength in micrometers. Thus, for L $\approx$ 1 mm and Z = 79, inverse bremsstrahlung is negligible for the CO_2 wavelength of 10 μm at intensities above 10^{12} W/cm. Therefore, some form of collective absorption that is somewhat less desirable than
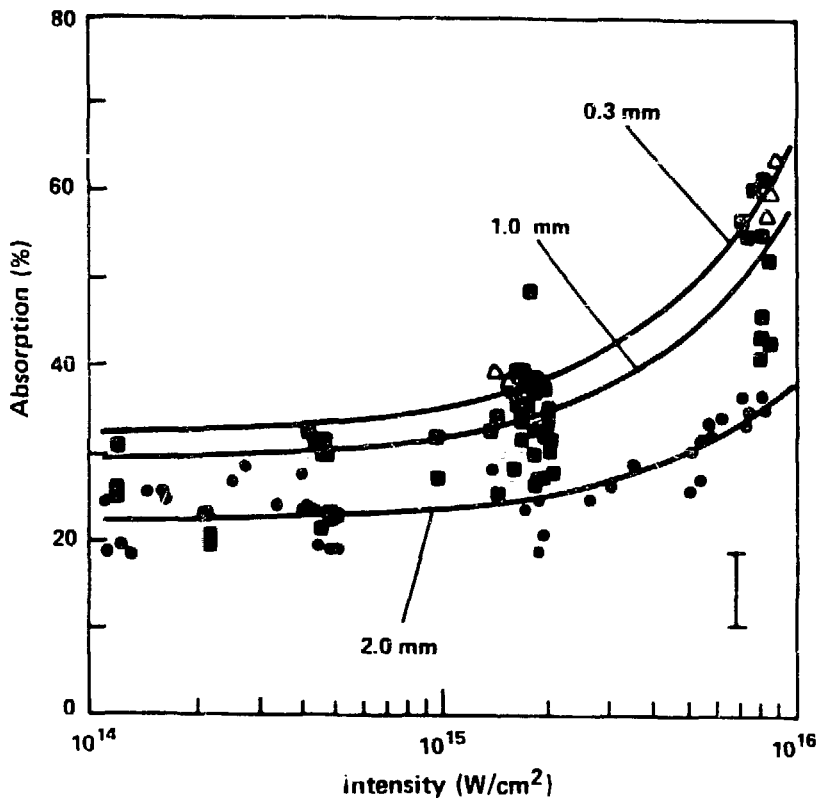

Fig. 1. Absorption as measured by ion calorimetry of the expanding plasma for spheres of varying size.

inverse bremsstrahlung must be relied on. At wavelengths less than 1 µm (for example, the 0.25-µm light of KrF lasers), inverse bremsstrahlung is very important and appears experimentally to dominate the absorption process, although some undesirable forms of collective absorption are still present to a modest extent.

An important quantity that affects the collective absorption processes is the pressure of the incident light wave, the so-called ponderomotive force, $F = \omega_p^2/\omega^2 \, \nabla \, |E|^2$. It is a low-frequency force proportional to the light intensity and the ratio of the plasma density to the critical density of the incident light. For example, at 10^{16} W/cm^2, the pressure of the light at its reflection point is about 5 Mbars! This large force is able to distort the flow of expanding plasma at low densities and is responsible for most of the instabilities induced by the incident radiation in the underdense plasma.

Because of this strong ponderomotive force, two basic mechanisms of collective absorption have been identified as important in all laser-plasma interactions and particularly important for CO_2 lasers.

The first is called resonant absorption,[5,6] in which the electric field of an obliquely incident laser beam can linearly couple to a longitudinal plasma wave in the low-density expanding plasma. For a wave with an incident angle θ, the electromagnetic wave is reflected from the region $n = n_c \cos^2\theta$ but may still tunnel to the resonant matching point as shown in Fig. 2. At the resonant point, the component of the electric vector along the density gradient induces time-dependent density fluctuations at the local plasma frequency. This acts as a source of plasma waves and extracts energy from the incident electromagnetic wave. The conversion efficiency depends sensitively on the incident angle and the scale length between these two points. For angles of incidence of the order of 20°, the scale length must be less than a wavelength of light to obtain an absorption of greater than 20%. In fact, the large ponderomotive pressure gradient of the reflecting light wave and the locally generated plasma wave produce a sharp density gradient in that region, which allows resonant absorption be an effective process. In Fig. 3, we show the sharp density gradient from a WAVE simulation[7] that extends to densities far above the critical density. An important experimental identification of resonant absorption at high laser intensities is from the large second harmonic emission of light produced. The nonlinear coupling of the density fluctuations of the plasma wave to the incident light produces the second harmonic through the current $j(2\omega) \approx v \, \delta \, n$. Its intensity is proportional to the incident light wave intensity and the plasma wave intensity. The scaling of the second harmonic emission is a strong function of incident laser intensity. At low intensity the 2ω emission is proportional to I^2. At high intensity, where
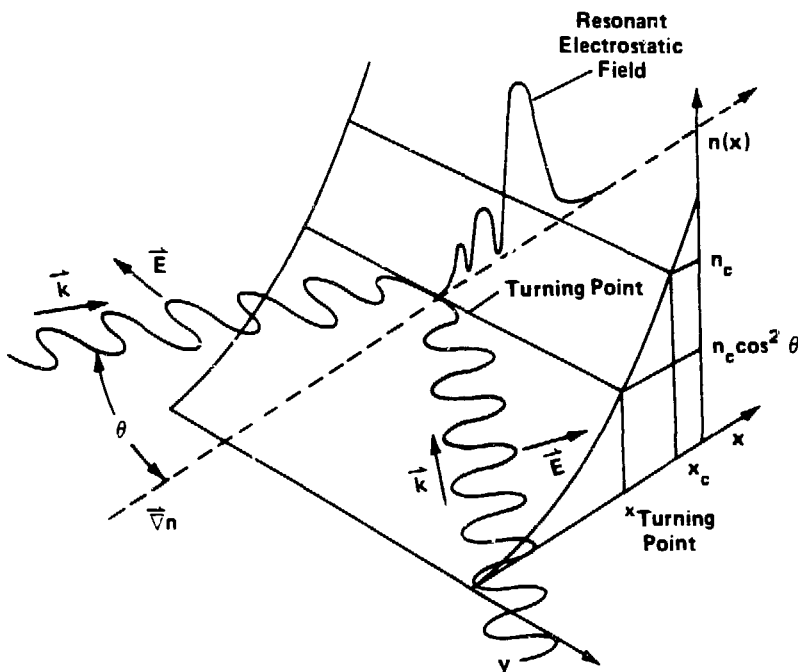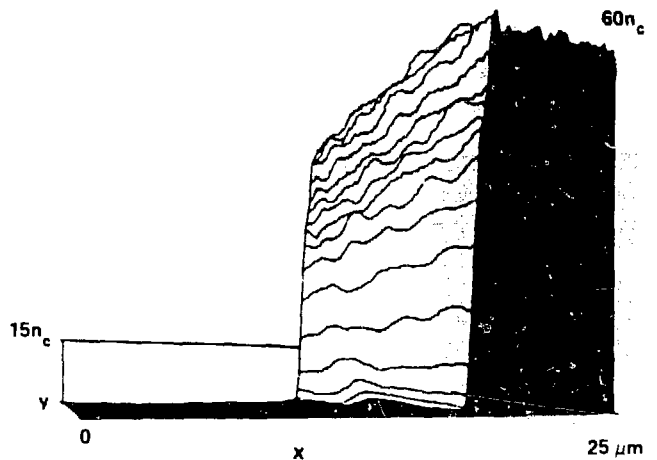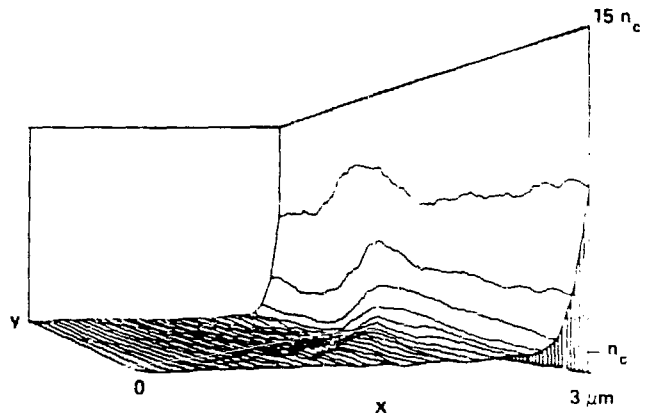

Fig. 2. The resonance absorption process

Fig. 3. Density gradients obtained from the WAVE code.

(a)

(b)

δn saturates because of nonlinearities, the 2ω emission is proportional to I.

WAVE BREAKING

Once the energy is placed into the plasma wave, it is quickly dissipated into the plasma by a number of mechanisms. Because of the extremely high intensity of the laser, the primary way in which it is absorbed is by a process known as wave breaking. In this process a few electrons can gain energies of hundreds of kiloelectron volts in less than one laser cycle (about 10^{-14} s) over distances of less than a micrometer as they are accelerated by the plasma wave. The energy they gain is proportional to the electric field of the plasma wave and its width. Since the width is narrower because of the steepened profile, the electron energy is reduced over the one that would occur in some gentle profile.[8] Although the acceleration process is quite coherent, it is observed in computer modeling to have a small random change from cycle to cycle, which injects stochasticity into the distribution, resulting in a near-Maxwellian hot-electron distribution.[9] Although nearly all of the electrons at the critical density can be heated by this process, only a small fraction of electrons above the critical-density surface is hot. Thus, we typically see a two-component electron plasma consisting of a large number of "cooler" electrons with a small number of energetic electrons over a broad energy spectrum that carry most of the heat. Because the equilibration time between the two components is quite long, this situation persists as long as the laser is at high power. An example of the distribution of electrons at high density is shown in Fig. 4. A major uncertainty in the
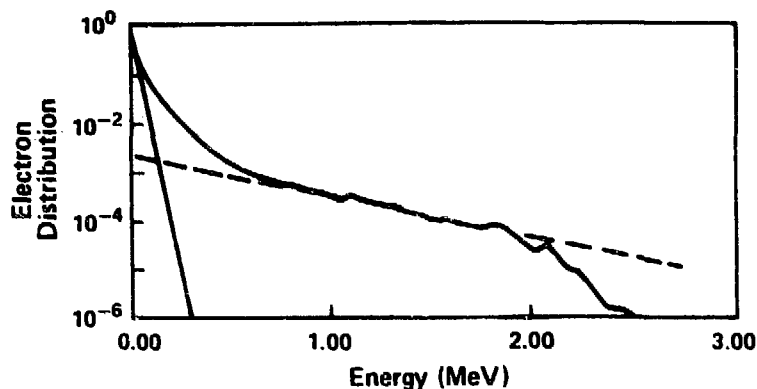
13

Fig. 4. The heated-electron distribution from a WAVE simulation.

simulations is what the cool background temperature is. Since it depends on the radiative cooling processes, the expansion of the solid material, ionization rates, and so forth, it cannot be determined self-consistently with the WAVE code but must be modeled with LASNEX. Nevertheless, this relatively simple theory has resulted in a reasonable match between theory and experiment[8] as to the magnitude of the hot-electron temperature and the nearly constant absorption of 20-30% that is observed from 10^{14}–10^{15} W/cm². The most spectacular confirmation of this process is the observation in experiment and simulations of high harmonics of the incident laser light.[7] In fact, experiments as illustrated in Fig. 5 have shown more than 35 harmonics of the incident light in the scattered-light spectrum, confirming the extreme nonlinearity of the interaction in the steepened density gradient. These high harmonics are a signature of the extremely anharmonic character of the acceleration seen by the electrons in the intense coherent resonant absorption plasma wave[10] as shown in Fig. 6. The plasma wave in the steep gradient sees a strongly spatially varying restoring force proportional to ω_p^2. The maximum harmonic content theoretically expected is up to the plasma frequency of the upper density shelf. The experiment then implies that the plasma wave is seeing densities up to 1000 times the critical density, or essentially solid density.

In recent years, however, experiments at higher intensity and more extensive calculations have indicated that this very steep gradient may not last for a long time.
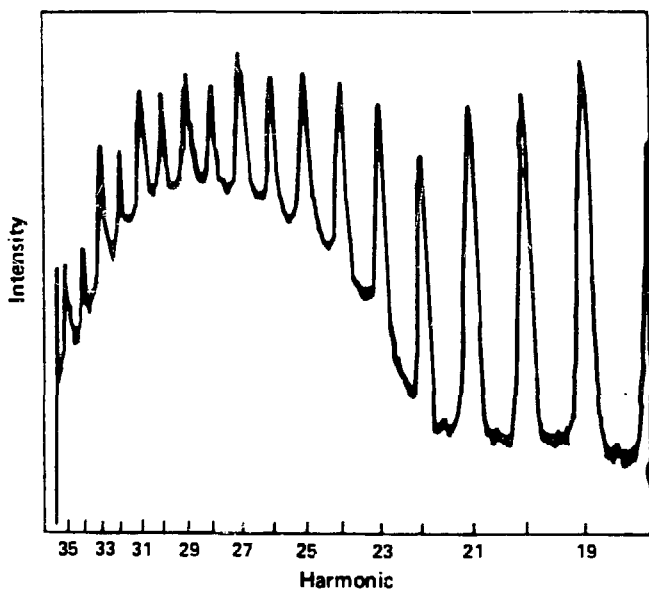

Fig. 5. Harmonics of the incident 10-μm light produced by nonlinear coupling mechanisms in the steep plasma gradient.
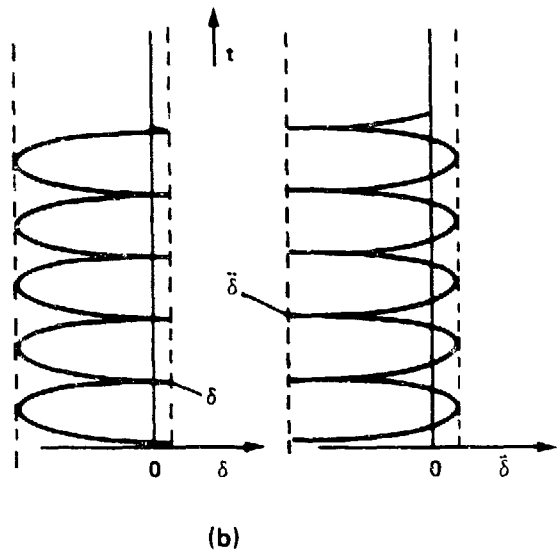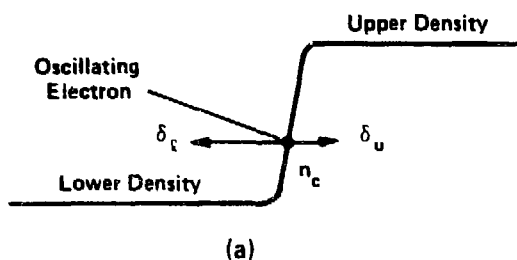
14

(a)

(b)

Fig. 6. The anharmonic restoring force on oscillating electrons near the density jump.

When the high harmonics are time resolved using ultrafast optical streak cameras, they are observed to last only during the rise time of the laser pulse, about 200 ps. This is in part due to the expansion of the plasma outward from solid density so that the plasma wave no longer sees the strong acceleration at those high densities. In addition, the nearly constant absorption coefficient observed at low intensity is observed to increase dramatically above about 10^{15} W/cm^2 as shown in Fig. 1. This suggests that an additional absorption process occurs at high intensity, which we attribute to a second mechanism discussed next.

PARAMETRIC INSTABILITIES

A second mechanism of collective absorption involves parametric instabilities, which are the nonlinear coupling of the light through the ponderomotive force to various plasma modes.[11,12] In these processes the ponderomotive force couples the harmonic oscillator equations for plasma waves with those for light waves at a different frequency from the laser. Typically, the conditions for instability are met most readily when the three natural frequencies, ω_1, ω_0, and ω, and the three wave vectors, k_1, k_0, and k satisfy conservation of energy and momentum:

$$\omega_1 = \omega_0 - \omega$$

and

$$k_1 = k_0 - k,$$

where the subscript 0 represents the pump laser, 1 represents the scattered (light) wave, and no subscript represents the plasma wave. The most important modes appear to involve coupling of light waves to electron plasma waves and ion sound waves. The coupling to electron plasma waves, known as stimulated Raman scattering, occurs at low densities, $\omega_p^2 < \omega^2/4$, and excites a broad spectrum of electron plasma waves that accelerate electrons to high energy over a long (typically
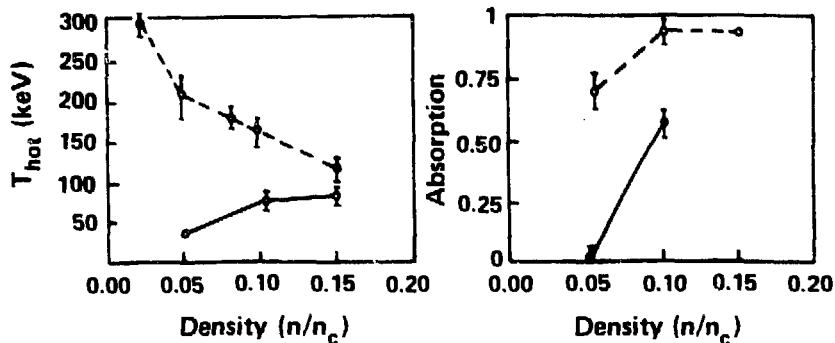
15

Fig. 7. Hot-electron temperatures and absorption in a long-scale-length plasma from WAVE. The solid curves correspond to a single pass of the laser light through the plasma. Dashed curves correspond to a reflection of the laser light at the plasma boundary and two passes through the plasma.

1-mm) distance. (The production of extremely energetic particles is being harnessed in the beat wave acceleration process. In this process, two lasers with a frequency difference equal to the plasma frequency are used to enhance the plasma wave amplitude over that generated by Raman scattering itself.) This acceleration over relatively large distances contrasts to the resonant absorption process described above. In addition, right at the quarter-critical density, the incident light can directly decay into two plasmons. The nonlinear state of these instabilities depends strongly on the density scale length and temperature of the underdense plasma. Unfortunately, plasma simulations are not able to self-consistently calculate the large-scale underdense plasma blowoff, and the experiments at 10 µm have been unable to measure it. Therefore, only representative calculations can be made in which one estimates the plasma initial conditions. These suggest that, as the plasma scale lengths approach a millimeter, this process may begin to dominate. The hot-electron temperature and absorption scaling from simulations are shown in Fig. 7. The hot-electron temperature is much higher at moderate intensities than it is from resonant absorption.

An additional coupling path of light to ion sound waves in underdense plasmas (known as stimulated Brillouin scattering)[13] results in less plasma heating because of the greater mass of the ions, although it has the potential of reducing the absorbed laser intensity. Calculations suggest that the ion waves become nonlinear so rapidly that the light is not scattered away but merely adds to the plasma heating rate. This heating rate, however, is lower than that from electron plasma waves. This process may be much more important at short laser wavelengths, where the ion sound waves do not become as nonlinear.

In addition to backscattering, there are also self-focusing and filamentation instabilities of the incident light.[14] Ponderomotive force-driven filamentation has a similar gain length to Brillouin scattering when the ions are very warm, $T_i = T_e$. At low intensities there is a thermal self-focusing instability resulting from bremsstrahlung heating that can reduce the density in a channel, refracting the light within the channel, which raises the intensity and further heats the plasma. This latter process may be particularly troublesome at short wavelengths. This instability can be viewed as arising from the strong anisotropy in the pressure of the incident light wave.

A number of parametric instabilities at the critical surface have been identified theoretically.[15] However, the steep density gradients induced by the ponderomotive force severely reduce these instabilities.

If fusion with CO_2 lasers is to work, one must stay at intensities and plasma conditions that do not allow parametric instabilities to develop and that rely on resonant absorption in a steepened density gradient to maintain the lowest hot-electron temperature. These conditions appear difficult to achieve at best. As mentioned earlier, some additional absorption process appears to be occurring above 10^{15} W/cm². Recent simulations at an intensity of 2.5×10^{15} W/cm² run for tens of picoseconds instead of only a few picoseconds[4] (made possible by the substantial increase in size of the Los Alamos computer facility) show a similar phenomenon. Figure 8 shows a contour plot of the density surface late in time. Note that the originally smooth, sharp density gradient has begun to break up and become rough. Associated with this roughness is a substantial increase in the absorption coefficient from about 25 to 60%. At the same time, the
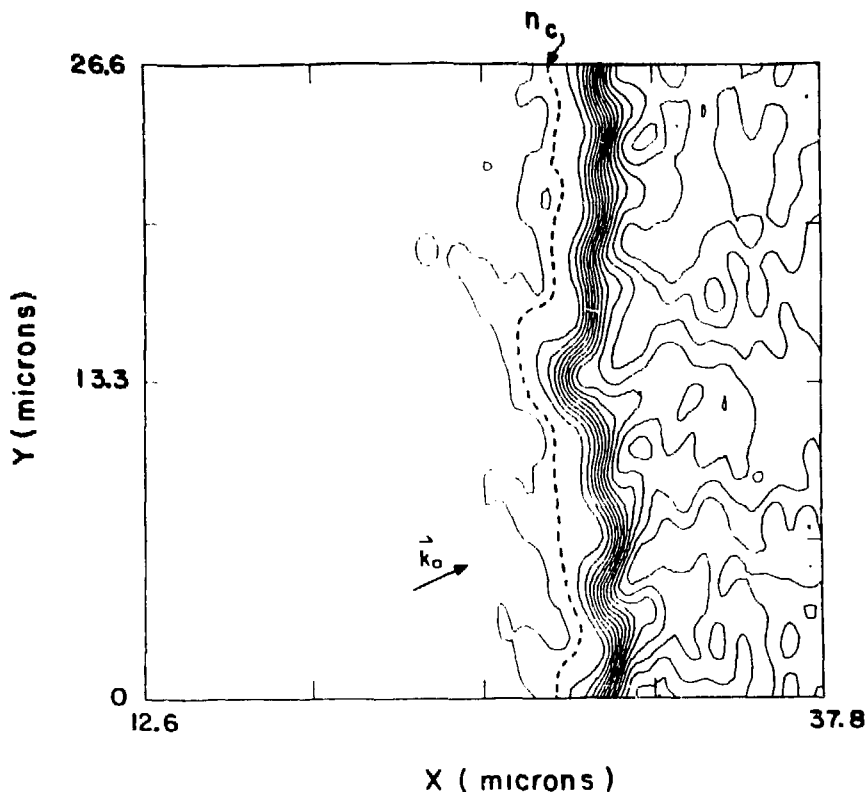
16

Fig. 8. Contour plot of the density late in time.

hot-electron temperature increases by a factor of 2 or 3 over that calculated for resonance absorption on the initially smooth surface. At 10^{16} W/cm^2, the surface is observed to become even more turbulent. Basically, the parametric instabilities at the critical density that were suppressed by the sharp gradient appear to become dominant at high intensity. This process may explain the increased hot-electron temperatures (hundreds of kilo-electron volts) observed on Helios at high intensities.[1,3]

We see then that the large amplitude of the laser radiation results in a highly nonequilibrium state of the plasma. It is so far from equilibrium that, for example, classical shock waves are altered. The region where resonant absorption occurs corresponds to a phase transition between a hot plasma in the presence of the laser light to a colder plasma without the laser light present. In this region rarefaction shocks[16-18] are generated, which have very different properties from conventional shock waves. Matter is put into an extremely unusual state that is probably only reproduced in exotic astrophysical situations. The fact that most of the absorbed laser energy is placed into a few energetic particles significantly reduces the implosion efficiency of fusion targets and makes the task very difficult.

FAST-ION GENERATION

Just as there are collective effects that control the absorption of laser light, collective plasma effects can also dominate the transport of electrons into targets. The hot-electron pressure in the corona can collectively accelerate the coronal ions to extremely high energies by collisionless processes. In the simplest model, a small number of electrons leave the target, but the nonzero impedance and inductance of the target support stalk allow electrostatic potentials of hundreds of kilovolts to develop at the target, confining the remainder. The confined electrons accelerate ions by working against the coronal plasma as they try to escape. Experimental measurement of the fast-ion energy shows that a substantial fraction of the absorbed laser light goes into fast ions.

17

particularly at high intensity (Fig. 9). For targets that are thick to hot electrons, so that an electron has only a single chance to bounce off the electrostatic sheath surrounding the target and work against the coronal ions, theoretical calculations (ignoring albedo effects) indicate that the fraction of energy in fast ions cannot exceed 5-10%, which is the fraction of electron energy lost in reflecting from the expanding plasma. Thus, we infer from these data that a mechanism exists to trap the electrons in the corona, allowing them to lose more of their energy to fast ions. This process is generically known as flux-limited transport. That is, there is some process that reduces the mean penetration velocity to less than it would be from a simple diffusion model. One process that can cause this phenomenon involves the generation of intense magnetic fields by the high-energy electrons themselves.

For a laser spot of finite size on a target surface or for not completely uniform illumination of a target, there is a temperature gradient along the surface over the laser spot, a strong density gradient along the surface over the laser spot, and a strong density gradient normal to the surface under the spot. These density and temperature gradients, which are perpendicular to each other, cause a magnetic field to be generated by the curl of the ambipolar electric field:

$$\partial\, B/\partial t = -\nabla \times E = \nabla n \times \nabla T/n \,.$$

The generation rate is extraordinarily high with a field of 1 MG reached in 1 ps with a density gradient of 10 μm, a spot size of 100 μm, and a temperature T of 50 keV. In the time it takes an electron to cross the laser spot, the field is strong enough to reduce the gyroradius of an electron to less than the density scale height. The electrons can no longer free-stream into the target but are confined by the magnetic field. In VENUS simulations[19] the electrons ExB drift along the target surface to great distances from the initial laser spot.[20] This reduces the transport inward under the laser spot and enhances the electron energy carried far from the laser spot. One of the consequences of the self-generated fields is that many of the ions are accelerated in an intense ion jet or plume normal to the target surface.
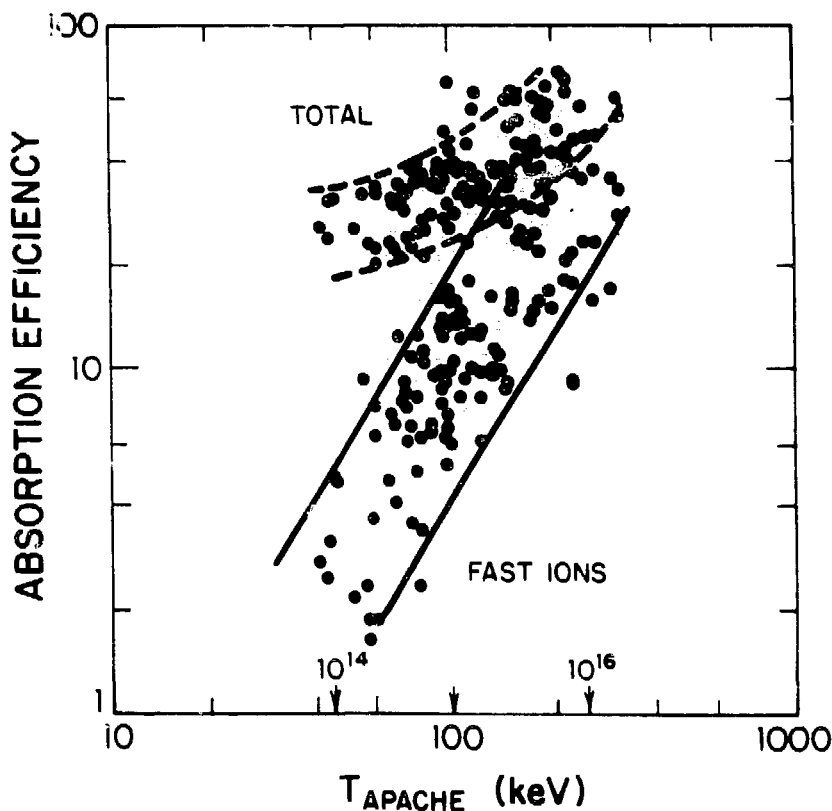

Fig. 9. Fast-ion production efficiency as a function of hot-electron temperature (from the APACHE hard x-ray spectrometer) and intensity.

Figure 10 shows the angular distribution of ions leaving a disk target as measured by calorimeters with three different thresholds provided by filtering. The plume has half-width at half maximum of about $10°$, in excellent agreement with particle simulations using VENUS. For targets smaller than about 1 mm, including small spheres, the effect is "washed out," and the ion angular distrubition becomes more isotropic. The effect is also washed out in thin targets, where electrons can travel from the laser spot by reflexing through the shell and disrupting the current flow that creates the magnetic fields. This acceleration process is quite equivalent to the one that occurs in intense ion diode experiments except that it is much higher intensity than any conventional diode. The accelerated ions could be used to drive a fusion target except that the collimation is not of sufficient quality to allow a large separation beween the diode and the ion target to prevent electron preheat. Experiments also suggest that ion emission may remain large at high intensity when the illumination is more uniform. At this point there is no conclusive theory that would reproduce

this effect. Measurements of the ion velocity distributions with magnetic analyzer spectrometers [so-called Thomson parabolas, which are ion spectrometers with parallel E and B fields and which produce velocity spectra $N(v)$ along parabolic tracks in the detector plane with different parabolas for each Z/A] indicate that much of the ion energy is carried by hydrocarbons independent of the target material. These hydrocarbons are surface contaminants on the target that are accelerated to the highest velocities in part because the lowest Z ions are accelerated most rapidly in the complex multispecies ion expansion. Although the ion spectrum from such a multispecies expansion is remarkably complex[21] and difficult to calculate theoretically, its gross properties are deceptively simple. As the ion mean energy is not far above that required to penetrate a 0.5-μm nickel filter, we can determine the ion "spectrum" by a set of transmission measurements in an array of differently filtered calorimeters. Figure 11 shows examples of such ion spectra for high- and low-intensity cases. Not only are these transmission curves well behaved, they can readily
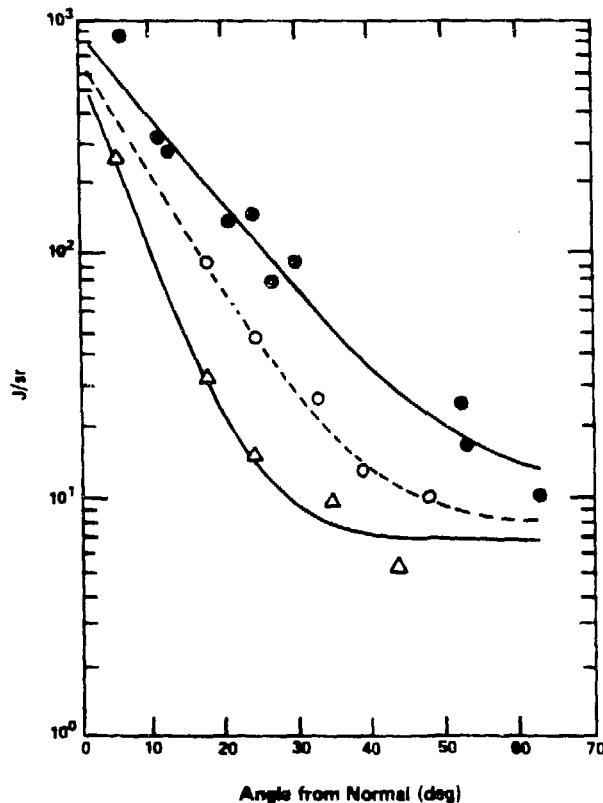

Fig. 10. Fast-ion angular distribution: • all ion energies, o $E \geqslant 100$ keV/amu, Δ $E \geqslant 500$ keV/amu.
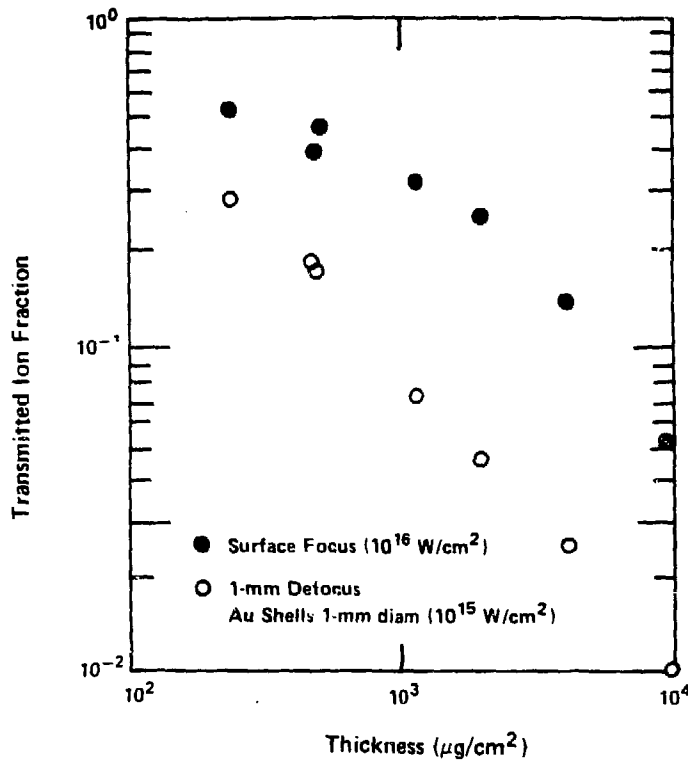
Fig. 11. Ion transmission spectra.

be fit to an isothermal expansion model taking the hot-electron temperature T directly from the bremsstrahlung measurements if we assume $Z/A \approx 1/2$. Transmission data as in Fig. 11 are useful in evaluating target design concepts. For example, the mass required to stop one half of the ion energy is an important parameter that can be used to determine whether this ion energy is exploitable in target design.

Whereas ion stopping powers are a weak function of Z, very heavy ions (such as tantalum and gold) have an appreciably shorter range than protons or carbon. Based on an analysis of the multispecies ion expansion, we conjectured that if low-Z surface contaminants could be removed, atoms of high-Z target material could be accelerated to similar velocities (the fastest proton in a typical expansion. measured with time-of-flight scintillator detectors. typically has a velocity of about 2×10^9 cm/s). In an experiment in which tantalum targets were heated with electron bombardment to white heat to drive off hydrocarbon, we observed energetic tantalum ions. The fastest ion observed corresponded to an energy of 500 MeV for tantalum, and Thomson spectrometer data

confirmed the absence of protons in the expansion while indicating that the tantalum ions were as much as 60 times ionized.

For targets with thickness less than the hot-electron range, electrons can pass through the target many times. reflecting off the expanding plasma sheath each time. This can greatly increase the absorbed energy placed into fast ions.

ASTROPHYSICAL IMPLICATIONS

Despite that fact that conditions produced in a target by a CO_2 laser are not favorable for producing fusion, they result in some of the highest energy density plasmas yet produced in the laboratory. For example, the hot-electron source produced by the laser is equivalent to a high-current, low-impedance electron beam source with a current in excess of 10^6 A and voltages of hundreds of kiloelectron volts. This results in a source impedance of about $0.001 \, \Omega$, much lower than can be produced by any conventional pulsed-power source. At the same time, this

intense "thermal" electron beam produces a reasonably collimated jet of space-charge-neutralized plasma traveling at speeds of 10^8–10^9 cm/s and maintaining its collimation over distances of at least 4 m. Although the distance scales and time scales are perhaps 25 orders of magnitude smaller, these jets are reminiscent of the galactic jets that have been so clearly identified from high-resolution radio wave photographs. This similarity extends even to the microwave emission of these objects, as we will discuss shortly. We argue here that the ability to measure not only the optical emission of these objects but also the ion motion directly makes study of these phenomena particularly attractive in the laboratory and highly complementary of the elegant astrophysical measurements. The intense magnetic fields that are intimately related to the generation of these ion jets are also known to be important in the accretion of matter in white dwarfs. Although we cannot, of course, study this accretion process directly, the detailed study of the mechanisms of acceleration and the verification of theoretical models could have a profound impact on astrophysical models.

An important means of knowing of the existence of galactic jets comes from their radio emissions. However, there remains considerable debate as to the processes that dominate in the production of microwaves from these extended objects. Similarly, in experiments done on Helios and Antares, we are able to observe these plasmas in the microwave region of the electromagnetic spectrum. Quite remarkably, these plasmas appear to be incredibly bright in the radio spectrum. In the range of 0.1-5 GHz, over a gigawatt of power is observed. Likewise, in measurements of emission in the 26- to 40-GHz band, nearly 1 GW has been observed. This is 0.01-0.1% of the incident laser light converted to microwaves. At the same time, the source is nearly a point source and has a pulse shape that nearly follows the laser pulse shape, with a rise time of 0.2 ns. The surprising efficiency of emission may be coupled to an enhanced level of plasma waves in the expanding corona, which couple efficiently to microwave emission. This is one of the important candidates for emission from galactic jets as well as from solar flares. A more detailed investigation of these processes in the laboratory could allow a significant discrimination between various theories of emission (such as synchrotron radiation or plasma wave emission) in astrophysical plasmas. Besides just measuring properties of the unique plasma produced by intense CO_2 laser light, the opportunity also exists for studying the propagation of the plasma plume through other ambient plasmas that could be imposed in the target chamber. This could shed light on the propagation of energetic ion jets through ionized plasmas. Do they maintain their physical integrity as they expand through the plasma? Is microwave emission altered as they strike another plasma? What is the emission in the submillimeter part of the spectrum? Theory suggests that it is much higher than at longer wavelengths. If one compares a normalized spectrum from a typical Antares target with that of the Crab nebula, for example, there is a striking similarity. Is this a coincidence or is there something in common between some of the emission processes? The uncovering of a wealth of exotic plasma behavior at extremely high laser intensity raises the possibility of new and important experiments that could not have been imagined a decade ago. The understanding of such processes already obtained from our theoretical and experimental efforts may provide insights valuable to our understanding of astrophysical processes.

REFERENCES

1. A. Hauer, et al. "Suprathermal Electron Generation, Transport, and Deposition in CO_2 Laser Irradiated Targets," in *Laser Interaction and Related Plasma Phenomena*, V. 6, p. 479 (Hora and Miley, eds., Plenum, 1984).

2. J. U. Brackbill and D. W. Forslund, *J. Comp. Phys.* 46, 271 (1982).

3. W. Priedhorsky, D. Lier, R. Day, and D. Gerke, *Phys. Rev. Lett.* 47, 1661 (1981).

4. D. R. Bach, D. E. Casperson, D. W. Forslund, S. J. Gitomer, P. D. Goldstone, A. Hauer, et al., *Phys. Rev. Lett.* 50, 2082 (1983).

5. D. W. Forslund, J. M. Kindel, K. Lee, E. L. Lindman, and R. L. Morse, *Phys. Rev. A* 11, 679 (1975).

6. D. W. Forslund, J. M. Kindel, K. Lee, and E. L. Lindman, *Phys. Rev. Lett.* 34, 193 (1975).

7. R. L. Carman, D. W. Forslund, and J. M. Kindel, *Phys. Rev Lett.* 46, 29 (1981).

8. D. W. Forslund, J. M. Kindel, and K. Lee, *Phys. Rev. Lett.* **39**, 284 (1977).

9. B. Bezzerides, S. J. Gitomer, and D. W. Forslund, *Phys. Rev. Lett.* **44**, 462 (1980).

10. B. Bezzerides, R. D. Jones, and D. W. Forslund, *Phys. Rev. Lett.* **49**, 202 (1982).

11. D. W. Forslund, J. M. Kindel, and E. L. Lindman, *Phys. Fluids* **18**, 1002 (1975).

12. D. W. Forslund, J. M. Kindel, and E. L. Lindman, *Phys. Fluids* **18**, 1017 (1975).

13. D. W. Forslund, J. M. Kindel, and E. L. Lindman, *Phys. Rev. Lett.* **30**, 739 (1973).

14. D. W. Forslund, et al., *Phys. Rev. Lett.* (1985).

15. D. W. Forslund, J. M. Kindel, Kenneth Lee, and E. L. Lindman. *Phys. Rev. Lett.* **34**, 193 (1975).

16. D. W. Forslund, J. M. Kindel, Kenneth Lee, and E. L. Lindman, *Phys. Rev. Lett.* **36**, 35 (1976).

17. K. Lee, D. W. Forslund, J. M. Kindel, and E. L. Lindman, *Phys. Fluids* **20**, 51 (1977).

18. B. Bezzerides, D. W. Forslund, and E. L. Lindman, *Phys. Fluids* **21**, 2179 (1978).

19. D. W. Forslund and J. U Brackbill, *Phys. Rev. Lett.* **48**, 1614 (1982).

20. M. A. Yates, D. B. VanHulsteyn, H. Rutkowski, G. A. Kyrala, J. Brackbill, et al., *Phys. Rev. Lett.* **49**, 1702 (1982).

21. F. Begay and D. W. Forslund. *Phys. Fluids* **25**, 1675 (1984).

22

The KrF Laser:
The Advance Toward Shorter Wavelengths

by Reed J. Jensen

I f energy is added to water in a swimming pool by using wavelengths comparable to the dimensions of the pool, water quickly peaks and sloshes over the edge. If, however, shorter wavelengths are used, the water, though rippling with motion, remains in the pool. There is an analogous problem when one uses laser energy to drive the implosion of a small fusion pellet. If longer wavelengths, say in the infrared, are used, then a portion of the energy "sloshes over" into undesirable modes (such as a few very hot electrons) that dissipate rather than drive the implosion. As our understanding of the physics of laser fusion has increased, awareness of the importance of fusion drivers with shorter wavelengths has likewise increased.

However, building an efficient, high-intensity laser that emits short-wavelength photons is a difficult balancing act for a number of reasons. The balancing becomes obvious when we look at the expression for laser gain. In a simple two-level laser, the gain coefficient (g) obeys the relationship

$$g \propto \lambda^2/t_{spont} \quad .$$

in which t_{spont} is the lifetime of the excited state against spontaneous emission and λ is the wavelength of the emitted photon. The gain itself is proportional to the factor e^g.

As we go to the high excitation levels needed for shorter wavelengths, the lifetimes of excited states tend, in general, to become short. This means the gain coefficient increases—an apparent advantage (although transition strengths can reverse this trend). But a short lifetime also means the excited atoms spontaneously emit their energy quickly. This latter fact is a disadvantage because the emitted photons stimulate further emissions, resulting in a

phenomenon called *amplified spontaneous emission* (ASE). In large-volume systems, such emission is parasitic, draining energy away too quickly and reducing system efficiency. In other words, it becomes difficult to store large amounts of energy in the lasing medium.

If this trend is resisted by the use of a system that emits short-wavelength photons from an excited state with a moderate lifetime, then the gain coefficient drops because of the factor λ^2. For example, a system with about the same upper-level lifetime as that of the CO_2 laser but emitting at a wavelength of 0.1 micrometer (μm) rather than 10 μm will have an inherent decrease in the gain coefficient of a factor of 10,000. This would make the gain, proportional to e^g, negligible. However, UV systems almost always have a much shorter lifetime that can result in a high gain.

There are exceptions to these trends that provide promising laser systems in the mid-ultraviolet, but in this region technical difficulties with optics and windows add to the difficulty of the balancing act. For example, common optical materials absorb strongly at these wavelengths. In essence, conventional optics will not suffice for wavelengths shorter than about $\frac{1}{4}$ μm, and truly novel techniques must be used.

THE KRYPTON FLUORIDE LASER

We are currently developing at Los Alamos the krypton fluoride (KrF) laser—a system that balances these facets to yield a highly efficient laser able to emit intense bursts of short-wavelength photons. For example, the KrF laser operates at $\frac{1}{4}$ μm, close to the short-wavelength limit for optics but, fortunately, just on the conventional-optics side. The excited-state lifetime of the

system is short—due both to spontaneous emission and to deactivation from collisions—making it impossible to store significant energy in the lasing medium. Counterbalancing this disadvantage is the laser's high gain, which yields a system able to amplify efficiently a rapid series of short pulses. As a result, considerable energy can be stored *outside* the laser during the beam's flight to the target. Such storage is accomplished by using a novel multiplexing scheme in which time-of-flight differences cause the series of pulses to meet simultaneously at the target. Thus we are developing a system that will be able to generate short, intense pulses of $\frac{1}{4}$-μm light highly desirable for the study of the physics of laser fusion at short wavelengths.

An Overview of the Laser

In early 1975 J. E. Velazco and D. W. Setzer at Kansas State University suggested using krypton and fluorine gas as a lasing medium,[1] and in June 1975 J. J. Ewing and C. A. Brau at AVCO Everett Research Laboratory reported the first laser oscillation for the highly efficient KrF system.[2] The potential energy curves shown in Fig. 1 illustrate the major reason for the high efficiency. The ground state is repulsive, and the "molecule" readily dissociates into neutral krypton and fluorine atoms. As a result, there is no accumulation of molecules in the lower laser level, and a significant population inversion can be achieved. The main laser transition occurs between the B $^2\Sigma_{\frac{1}{2}}$ excited state, made up of an attractive Kr^+F^- ion pair, and the X $^2\Sigma_{\frac{1}{2}}$ ground state. This transition can be pictured as the ion pair reverting back to the dissociating molecule by transferral of an electron from F^- to Kr^+ and emission of a photon with a wavelength of $\frac{1}{4}$ μm.

Gain. Measured gain coefficients for the KrF laser are in excess of 10 per cent per centimeter, so that a 1-meter amplifier would have a gain of e^{10}, or about 20,000, per pass through the amplifier. As pointed out above, such huge gains will not allow storage of large amounts of energy in the lasing medium as a population inversion; the excessive gains cause a loss of upper-level population by amplified spontaneous emission. By using the multiplexing scheme, however, we are able to extract the energy as a series of short pulses *while* the laser is being

pumped. This extraction suppresses the gain by reducing the gain coefficient according to the equation

$$g = \frac{g_0}{1 + \dfrac{I}{I_{sat}}} ,$$

where g_0 is the gain coefficient at low intensities (the small-signal gain), I is the laser intensity in the medium and I_{sat} is the so-called saturation intensity (an intensity based on photon energy, the stimulated emission cross section, and the upper-state lifetime of the lasing medium).

It is apparent that if energy is extracted from the amplifiers while the laser is running at an intensity three times I_{sat}, there will be a fourfold decrease in the actual gain coefficient. This reduction will bring the system gain down from about twenty thousand to a few hundred.
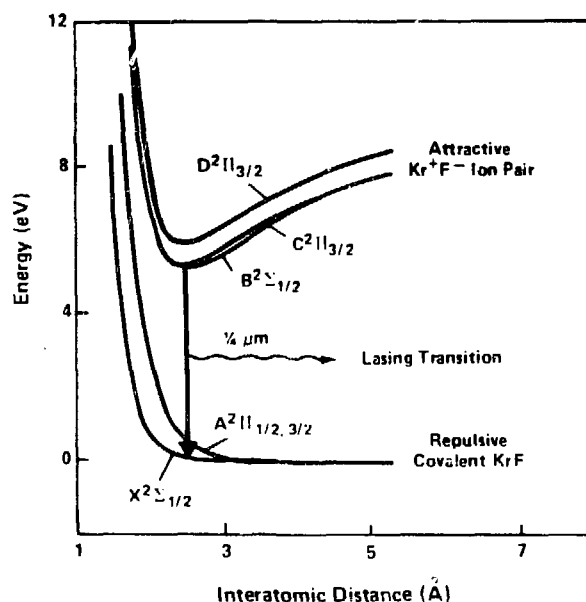
Fig. 1. The potential energy diagram for the KrF laser. The upper state of the lasing transition (B $^2\Sigma_{\frac{1}{2}}$) is one of the states for the Kr^+F^- ion pair. The lower state ($X^2\Sigma_{\frac{1}{2}}u$) is one of two covalent states that are repulsive and so dissociate, eliminating KrF molecules from the lower level and ensuring a large population inversion. [(Adapted from P. J. Hay and T. H. Dunning, Jr., *Journal of Chemical Physics* 66, 1306 (1977)].

Gas Kinetics

In a practical sense, the efficiency possible in the system is determined by how atoms are pumped into the upper laser level. Typically, the energy is added by ionizing a gaseous mixture that includes argon. The argon atoms play an active role by forming intermediate species, as shown in Fig. 2, a simplified flow chart for the gas kinetics of the Ar-Kr-F_2 system. Initially, all three types of atoms are ionized (here using an electron beam), but the path (1) that produces the largest population of KrF ion pairs (KrF*) in the upper laser level involves Ar_2^+. The second most important path (2) involves the ArF ion pair (ArF*). Once the KrF ion pair is reached, the desired exit channel is, of course, dissociation to Kr and F and emission of a photon.

The efficiency for conversion of pump energy to upper-state population could conceivably be increased by using more direct or lower energy channels to the KrF ion pair. In fact, immediate gains in efficiency can be realized by increasing the amount of krypton in the mixture, although this gas is more costly. Such an approach would emphasize the path (3) in which krypton is ionized directly—a more efficient route because of krypton's lower ionization energy.

Undesirable Absorption

Many of the species pictured in Fig. 2 absorb light of KrF frequency. What constraint does this place on the design of the KrF laser? Generally, for any absorbing
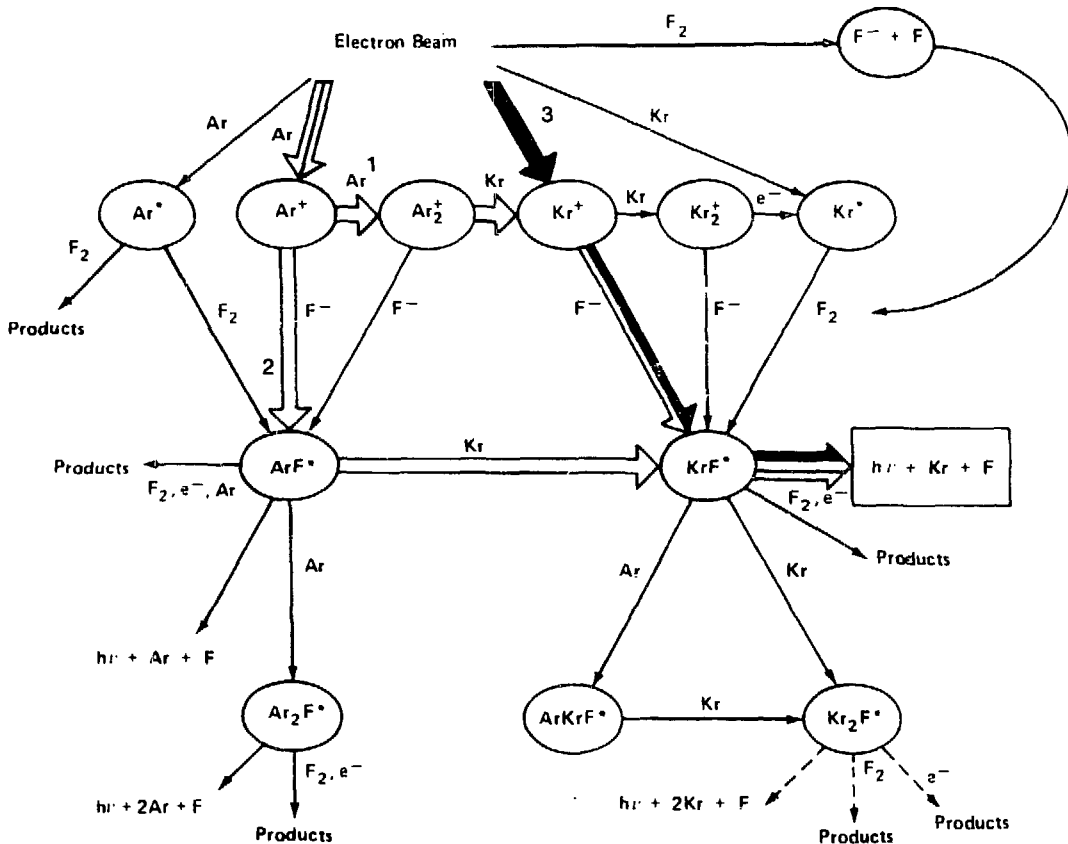
Fig. 2. Kinetic pathways for the KrF laser. Initially, all three atoms in the Ar-Kr-F_2 gas mix are ionized, but the most important path (1) to the KrF ion pair(KrF*)passes through Ar^+ and Ar_2^+ intermediates before a krypton atom is ionized. The Kr^+ ion then combines with a previously ionized fluorine atom. The second most important path (2) also starts with Ar^+ but then forms on ArF ion pair (ArF*) before exchanging with a krypton atom. Path (3) is energetically favorable because krypton ionizes easily, but the path only becomes important as the amount of krypton gas in the mix is increased.

species there is an intensity at which the absorption saturates—that is, the light overpowers the absorption process and starts to pass freely through the system. The uence for this condition is given by

$$\phi_{sat} = \frac{1}{\tau\sigma} \ ,$$

where τ is the relaxation time and σ is the absorption cross section for the absorbing species.

Unfortunately, some of the absorbing species in the KrF laser gas have low values of $\tau\sigma$ and do not saturate at fluences used for the design of this laser. The system, therefore, has a practical upper limit on the growth of fluence in the lasing medium. In other words, we have another balancing task; as intensity or fluence increases, the gain saturates but absorption by other species does not. It is believed that the limiting fluence for the KrF system is about 10 to 100 megawatts per square centimeter. Greater intensities can only be reached by using optical focusing and other techniques that are applied beyond the last amplifier.

Electron Beam

Ionization of the laser gas mix also has its difficulties. The gas contains fluorine, a halogen, which is an efficient electron scavenger. In fact, the formation of F^- by electron attachment plays a key role in the pumping scheme of Fig. 2. However, standard gas-discharge techniques used with many gas lasers generate electrons with energies of a few tenths of an electron volt (eV). Because attachment energies are also of this order, such a discharge has trouble sustaining itself if electron scavengers are present.

Further, in a standard ionization-stabilized discharge system, there is a tendency for the discharge to constrict into a few very hot arcs. This phenomenon leaves most of the gas unpumped, whereas the gas in the vicinity of the arcs is far overpumped and overheated. Even though a preionization device may help generate more homogeneous current flow, the discharge still tends to constrict into hot arcs because of the temperature dependence of the coefficient β in the electron replenishment equation,

$$e^- + M \rightarrow M^+ + \beta e^- \ .$$
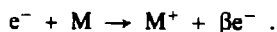
In other words, the number of secondary electrons generated when a primary electron collides with atoms in

the medium increases rapidly with temperature, and any area of enhanced conduction quickly forms an arc.

The solution to these problems, which would be especially severe at the higher intensities required in amplifiers, is to ionize the gas directly by pumping with an electron beam. In this case, the electrons enter the laser volume with energies of several hundred kiloelectron volts, and any difficulties with electron attachment are overpowered.

Likewise, an electron beam device avoids runaway arcs by injecting electrons directly into the gas through thin foil windows (Fig. 3). Electron homogeneity is established by field emission and propagation physics in the vacuum region around the cathode. The resulting even distribution of the primary electron current from the electron beam dominates all physics in the laser volume. Thus, the primary current in any particular volume of gas does not depend upon the conductivity of that gas.

Typically, electrons enter the laser volume at energies of 400 to 800 keV. In primary collisions gas ionization generates secondary electrons with an energy loss to the primary electron of about 30 eV per ionization. Thus each primary electron requires thousands of collisions to deposit its energy in the gas. Both primary and secondary electrons participate in the various pumping and attachment processes shown in Fig. 2.

With this pumping technique we find that for Ar-Kr-F_2 mixes about 24 per cent of the energy of the beam appears as population of the upper laser level. Once again, we see that the KrF laser has high intrinsic efficiency. The exact value of the efficiency depends, of course, on the conditions of the gas and the pumping circuit (for example, use of more krypton in the gas mixture should increase this value). So far, an overall efficiency from wall plug to laser beam of 4 per cent has been achieved. Such efficiency is still a little less than is achieved for the CO_2 laser, but by using improved gas mixtures and electrical delivery systems, we should achieve efficiencies greater than 10%.

High Repetition

Because KrF is a gas laser with relatively high efficiency, it can be pulsed at high repetition frequencies. To prepare for a subsequent pulse, the gas needs time for all intermediate fluorides to revert back to the elements and for electron beam-induced shock waves to damp out. This is achieved by exchanging the gas between pulses
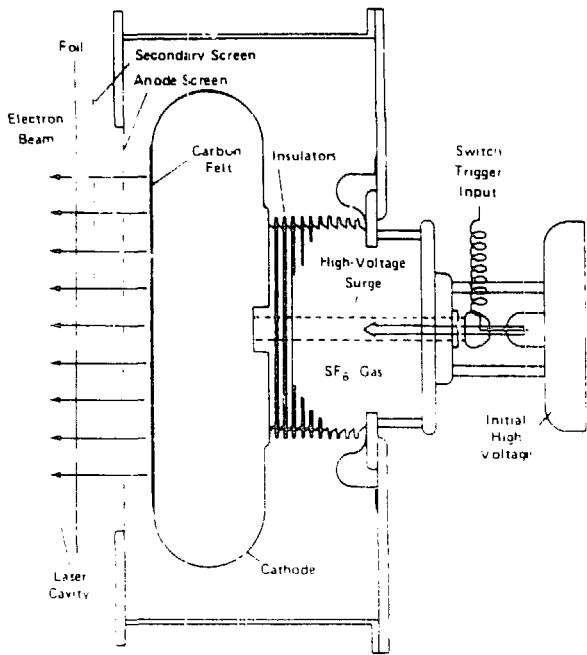
Fig. 3. A schematic of the diode for generating the electron beam. When the switch trigger is activated, high voltage surges from right to left on the cathode, where electrons are ejected toward the anode screen. These electrons also flow through a screen that eliminates stray secondary electrons and then through 2-mil titanium foil into the volume of the laser cavity. The electrons are emitted at energies of several hundred kiloelectron volts, and about 95 per cent are transmitted through the foil where they uniformly excite the laser gas. Critical to the design is the cylindrical high-voltage bushing (insulators and SF$_6$) that is between the switch and the cathode and which prevents undesirable arcing back toward the switch. To give an idea of the size of these electron-beam devices, the emitting surface of one of the cathodes in our recent large KrF amplifier (the Aurora system) measures 1 by 2 meters.

using modestly sized pumps. Also, spurious impurities, formed by fluorine attack on surrounding materials, are removed during the exchange with filters and "getters" (metals, such as sodium or calcium that react with the impurities). Using these techniques, KrF lasers have been operated at repetition frequencies greater than a kilohertz.

THE LOS ALAMOS PROGRAM

Los Alamos has been heavily involved in the development and use of KrF and other rare-gas-halide lasers since 1976. The work was done originally for the laser isotope separation program, and, in the first year, KrF lasers were used to generate macroscopic samples of photolytic UF$_5$ from UF$_6$. At that point we were developing high beam quality, multijoule gas-discharge (rather than electron-beam) lasers. In the late 1970s, Los Alamos pioneered gas cleanup schemes that paved the way to the long-lived rare-gas-halide lasers. These efforts culminated in a KrF laser that ran at 1 joule per pulse and 500 pulses per second. We also developed, jointly with Rocketdyne, another KrF laser that doubles this repetition rate.

At present we are constructing a prototype KrF laser system that uses electron-beam pumping in the amplifiers and that will demonstrate the production and extraction of laser energy and the optical techniques needed for a

KrF fusion laser. The system is called Aurora, and its various components—from the KrF oscillator through four stages of amplification—are shown schematically in Figs. 4 and 5. The gas-discharge oscillator will emit a single beam consisting of a 5-nanosecond, $\frac{1}{2}$-joule pulse. To achieve optical multiplexing, the original beam will be split into 96 beams before being sent through the various stages of amplification. The final amplifier, called the Large Aperture Module (LAM), will have a lasing volume that is 1 meter by 1 meter by 2 meters long and an output totaling about 15 kilojoules in the 96 beams.

Multiplexing

A prime motive for optical multiplexing is cost. It has been estimated that a cost minimum can be achieved for KrF laser fusion if there are from 50 to 100 beams, each less than 5 nanoseconds in duration, derived from a single electrical pulse. Rather than build 100 systems, we intend to use a single optically multiplexed system—a key concept to be demonstrated by the Aurora laser.

Multiplexing starts with the time and angle encoders (Fig. 5), which will take the original 5-nanosecond pulse and split it into 96 angularly separated beams. Each beam travels a different distance so that each is delayed
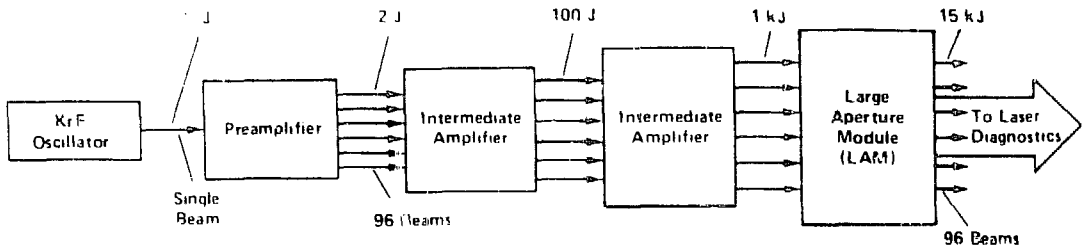
Fig. 4. The power amplifier chain for the aurora KrF laser system starts with a single ½-joule beam and ends with about 15 kilojoules divided among 96 beams.
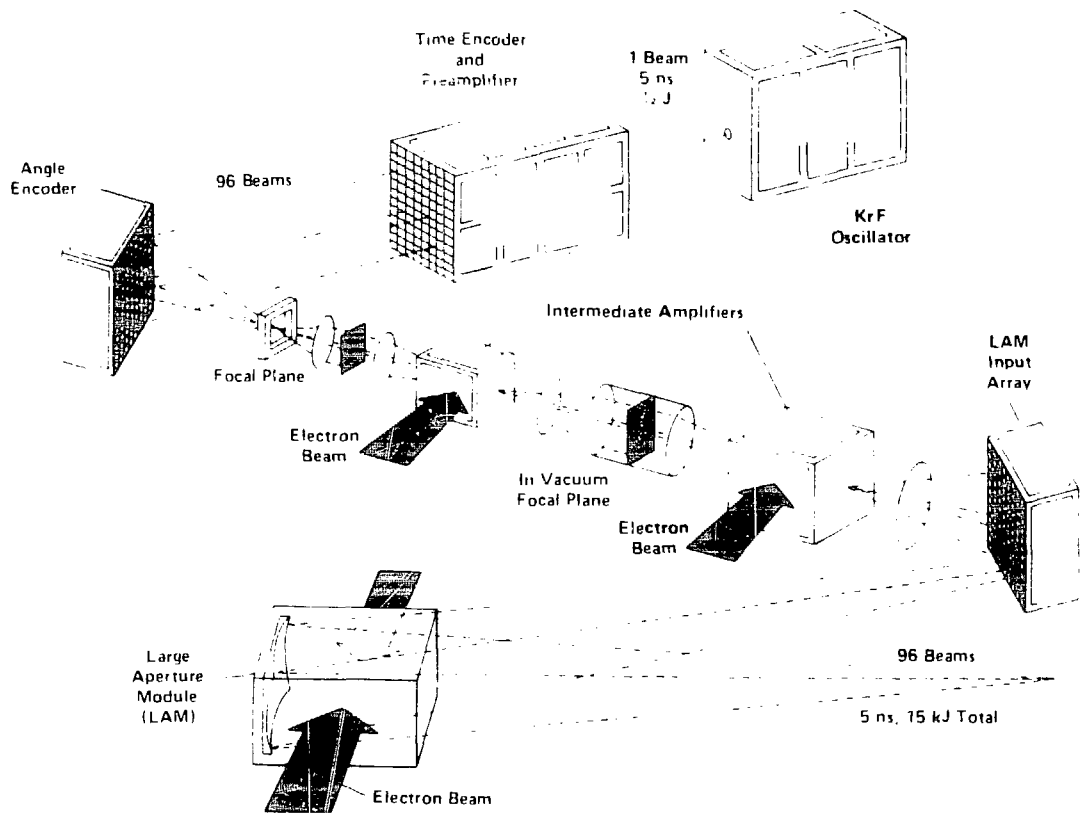
Fig 5. A conceptual layout for the Aurora laser system. The single beam with 5-nanosecond pulsewidth from the KrF oscillator is divided by the time encoder into a train of 96 temporally separated beams. This splitting is accomplished with aperture dividing, the use of partially reflective mirrors called beam splitters, and different path lengths for each beam. Preamplification also takes place in the same apparatus. The angle encoder aims each beam so that it will pass through the central region of both intermediate amplifiers. Final amplification to 15 kilojoules takes place in the large aperture module. The oscillator is driven by gas-discharge techniques, but the higher intensities in the amplifiers require pumping by electron beam. A demultiplexing arrangement is needed after the LAM if the 96 beams are to be brought to the target simultaneously (see Fig. 6).

28

differently; the resulting output consists of a train of 5-nanosecond pulses. Because the pulses are angularly separated, each passes through the amplifiers from a slightly different direction. The amplifiers are pumped for a relatively long time—about 600 nanoseconds—while the train of short pulses traverses their volume.

The same time-delay concept can be applied in reverse after the final amplification to cause all the beams to arrive at the target at once. A simplified version of this part of the system is shown in Fig. 6, illustrating how the time-of-flight for each beam would allow that all beams beams meet simultaneously at the target.

As noted earlier, the multiplexing technique allows us to take advantage of the high gain and high efficiency of the KrF gas laser to generate a short, high-energy pulse on target. The energy of the electron beam discharge is stored in the variously delayed flights of the 96 beams. Moreover, low-cost laser energy is provided by using one system in which the amplifiers run for a relatively long time rather than by using many short-pulse systems.

Figure 7 is a photograph of the final amplifier under construction. The large oval-shaped features are magnets

that provide a 3-kilogauss guide field to direct the electron beam straight into the laser chamber. The two large cylindrical tubes are water dielectric transmission lines that transmit the 1.3-megavolt electrical pulse to the cathode. One of those cathodes is pictured in Fig. 8 lying on a workbench with the carbon felt emitter surface upright. Figure 9 shows the amplifier being discharged to produce ultraviolet power.

The Aurora laser system will provide experience in nearly all of the issues involved in building a very large KrF laser fusion driver. We will gain experience not only in large KrF amplifier construction and operation but also in running a whole series of amplifiers with final flux close to the limiting flux for the system. A major issue in this, or any, large KrF laser system is damage to the windows and mirrors. We must develop coatings with good reflective or transmissive properties that also are resistant to fluorine attack and optical damage. At present, the size of apertures—and, therefore, the overall system cost—depends very sensitively on the threshold for optical damage. Work being performed at Los Alamos and by optical component suppliers is providing greatly improved damage performance.
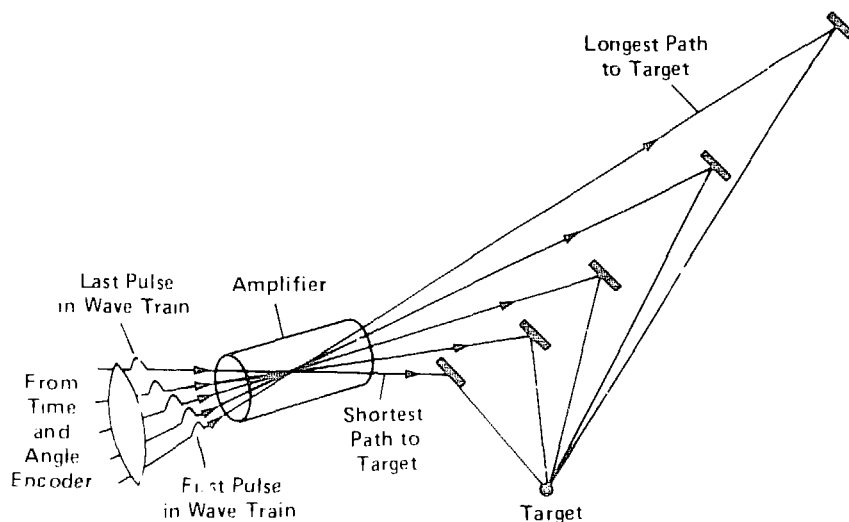
Fig. 6. A simplified optical angular multiplexing device. The five beams from the decoder represent a train of pulses that are separated in time. By adjusting path lengths so that the earliest pulse (crossing from bottom left to upper right) has the longest time-of-flight and the last pulse (crossing horizontally) has the smallest time-of-flight, the pulses can be brought together at the target simultaneously.
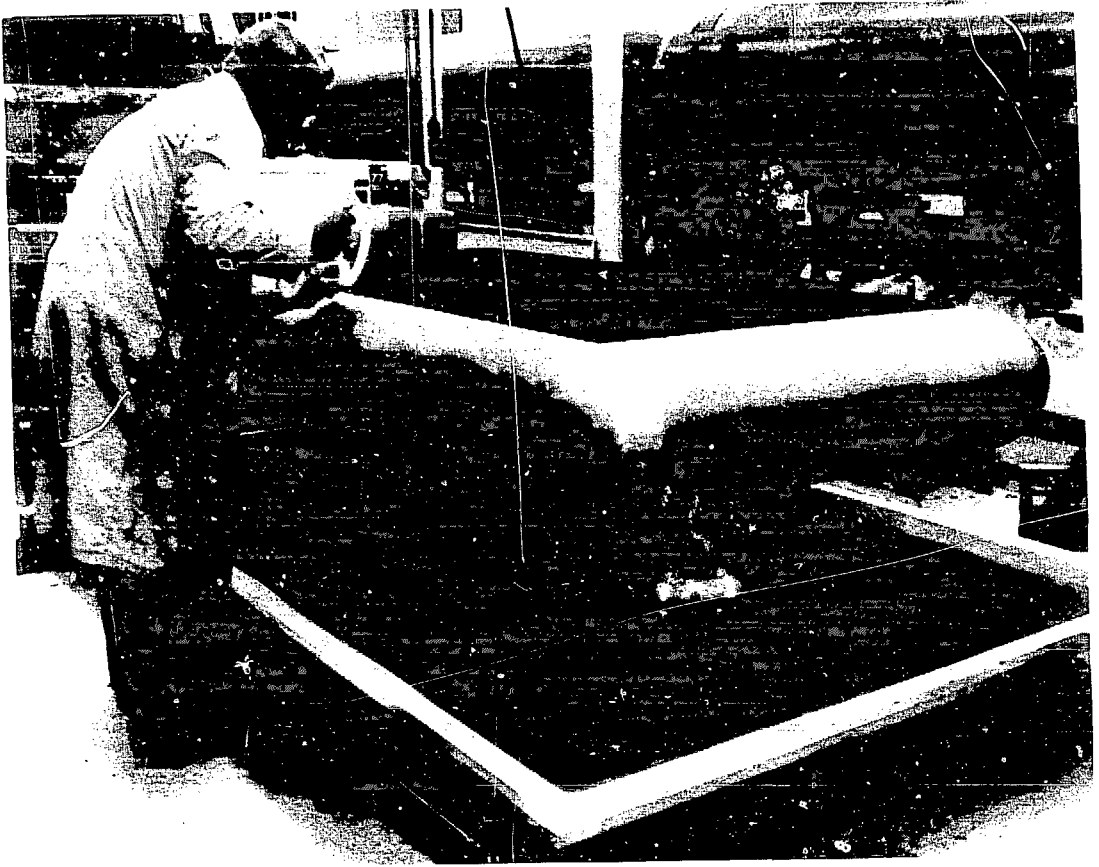
Fig. 7. The KrF laser system's final amplifier, the LAM, under construction.
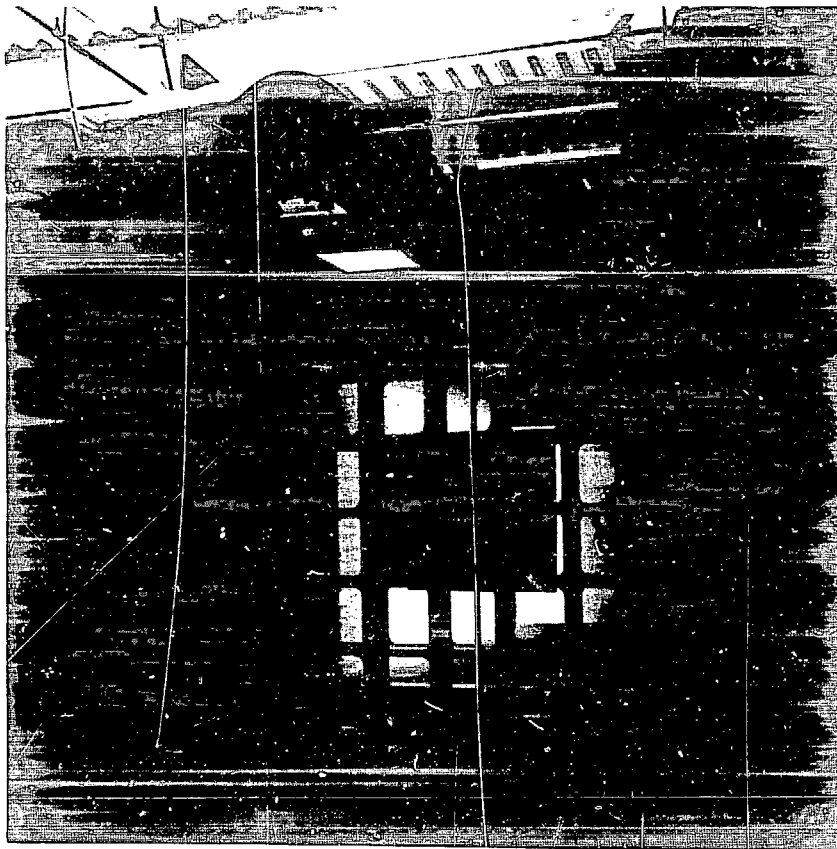
Fig. 8. One of the electron-beam cathodes for the LAM with the emitting surface upright.

Fig. 9. The LAM being discharged to generate ultraviolet power at a wavelength $\frac{1}{4}$ μm.

REFERENCES

1. J. E. Velazco and D. W. Setzer, "Bound-Free Emission Spectra of Diatomic Xenon Halides," *Journal of Chemical Physics* 62, 1990-19991 (1975).

2. J. J. Ewing and C. A. Brau, "Laser Action on the $^2\Sigma_{\frac{1}{2}} \rightarrow {}^2\Sigma_{\frac{1}{2}}$ Bands of KrF and XeCl," *Applied Physics Letters* 27, 350-352 (1975).

Diagnosis of Laser-Driven Implosions

by Allan Hauer

Since practical inertial fusion conditions can occur only in very highly compressed matter, a thorough understanding of dense imploded plasmas and their production is essential. In this section, a description is given of work that has been done on the diagnosis and modeling of dense plasmas and their creation by laser-driven implosion. Six characteristics of these dense plasmas are of particular interest:

1. Average (electron and ion) density and temperature in the compressed core.
2. Spatial variation of density and temperatures across the core.
3. Temporal variation of core conditions.
4. Velocity history of the implosion. (This parameter is highly coupled to the efficiency with which energy is imparted to the dense compressed plasma.)
5. The temporal history of neutron production and the total yield for DT-filled targets.
6. Integrity (or break up) of the imploding "pusher" shell and its effect on compressed core conditions.

LASER-DRIVEN IMPLOSION EXPERIMENTS AT LOS ALAMOS

Dense plasma implosion experiments at Los Alamos have been performed with CO_2 lasers as the drivers. Most of the diagnostic and modeling techniques that have been developed as part of these experiments are, however, of general applicability to all of ICF irrespective of the driver. Some aspects of this implosion/dense plasma work have actually benefited from the hot-electron ablation of characteristics of CO_2 laser drive.

The basic interactions involved in laser-driven implosions are illustrated in Fig. 1. With CO_2 lasers, most of the absorbed energy is initially channeled into a hot-electron distribution. The hot electrons are produced near the critical electron density region for CO_2 ($n_e \sim 10^{19}$ cm^{-3}), and the ablation occurs in denser regions deeper within the target. The distance between the critical and ablation surfaces is larger for longer laser wavelengths. Scattering of the hot electrons between the critical and ablation surfaces tends to symmetrize and smooth any initial nonuniformities in the laser illumination. The greater distance between the critical to ablation surfaces in CO_2 experiments tends to make symmetrization a more prominent effect than in experiments with shorter wavelength lasers.

DIAGNOSTICS FOR DENSE PLASMAS

Figure 2 illustrates a typical target used in high-compression laser-implosion experiments. Although many other target variations have been tested in the Los Alamos laser fusion program, this configuration can be used to illustrate many of the relevant aspects of implosion diagnostics.

Within the target is a glass shell filled with a variety of gases that is determined by the experiment of interest. DT is used as the fuel for thermonuclear yield, and spectroscopic diagnosis of plasma temperature and density is accomplished by seeding the DT fuel with a small amount of higher-Z material, such as neon or argon. Analysis of line emission from the higher Z material is one of the most direct diagnostics of compressed density.

The thick layer of plastic surrounding the glass shell reduces the preheat of the fuel due to suprathermal electrons and allows an ablative implosion of the shell. In earlier work of this type[1] only the thin glass shell was present, and long mean-free-path electrons tended to
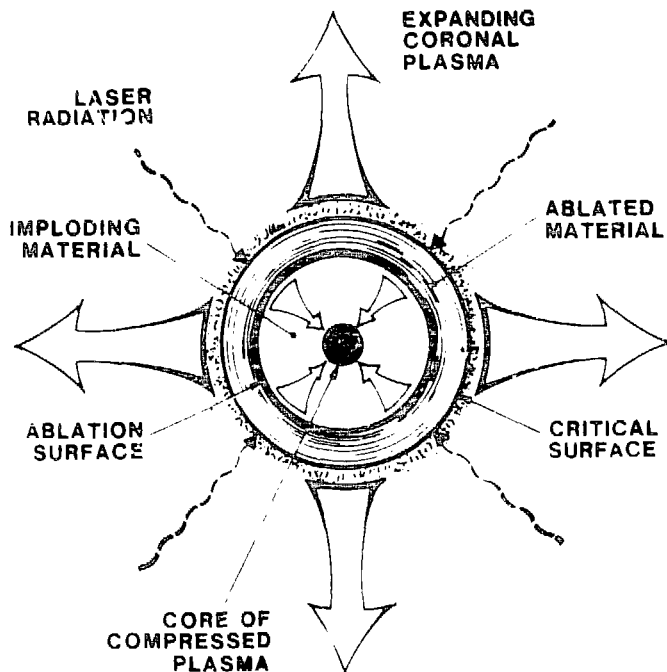
Fig. 1. Basic interactions involved in producing laser driven implosions.
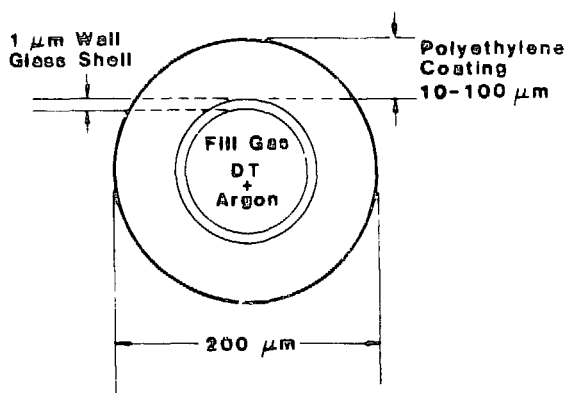
Fig. 2. Typical target used for CO_2 implosion experiments.

uniformly heat the entire shell and cause it to explode. The plastic outer coating slows the electrons and enables a slower ablative implosion that produces very dense plasmas of a few g cm³ density.[2]

In diagnosing much higher density implosions that will be possible in the near future, it might be desirable to construct the gas-containing shell completely out of low-Z material. It is anticipated that these implosions will reach very high pR's in the pusher, and the low opacity of

plastic shells might still allow for radiation diagnostics of the compression.

The diagnostics of these very dense plasmas fall into five major categories:

1. X ray spectroscopy
2. X-ray imaging
3. Time-resolved x ray detection
4. Nuclear product measurements
5. Particle (ion) detection

By using information from such a wide variety of measurement techniques, a comprehensive picture of the laser implosion can be formed.

X-Ray Spectroscopy

Spectroscopic analysis of emission from the higher Z material in the fill gas provides the most comprehensive information on plasma density and temperature. The general features of x-ray spectra from a laser-imploded plasma when argon was used as the high-Z diagnostic trace element are shown in Fig. 3. The three traces represent a progression (top to bottom) to higher densities. Qualitatively, we see that the lines become broader

Fig. 3. X-ray spectra observed from the implosion of various targets producing different final densities.

as the density rises. The top trace was obtained from an exploding pusher target irradiated with a 3.5-kJ (CO_2) laser energy and represents a compressed electron density of about $9 \ti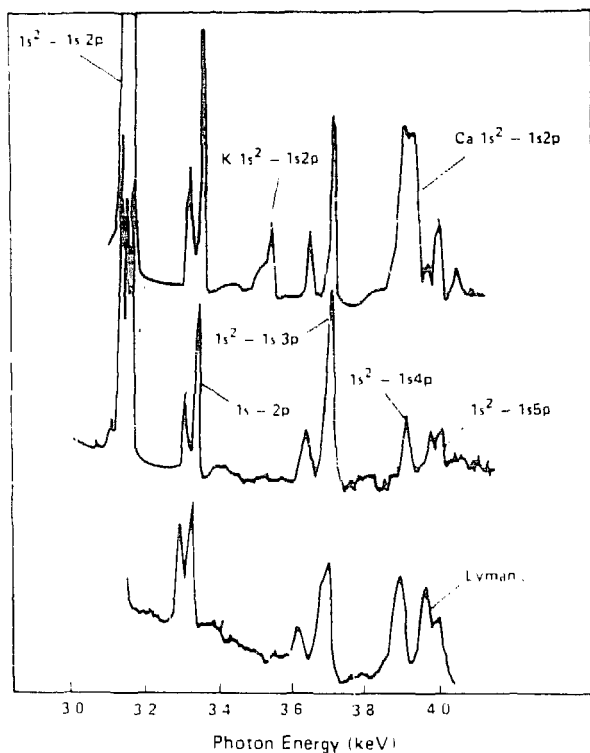mes 10^{22}$ cm^{-3}. The middle trace was obtained from a target with a coating of 25-μm $(CH_2)_x$ (and 4.5 kJ laser energy on target). The compressed electron density here is about 4×10^{23} cm^{-3}. The final trace was produced by a target with 50-μm $(CH_2)_x$ coating and about 5.8 kJ of laser energy. The compressed electron density is about 7×10^{23} cm^{-3}. In the experiment represented by the top trace of the figure, the laser heats the glass shell directly, and lines due to calcium and potassium (which are impurities in the glass) are excited. When a layer of about 25 um of plastic is added, these lines are suppressed.

Analysis of the profiles of these lines is one of the primary diagnostics of compressed density.* An important part of this analysis is a comparison with theoretical profiles, which are calculated as a function of density for

---

*See Ref. 3. In addition to the temperature dependence of line profiles, this reference also discusses other aspects of theoretical line profile calculations relevant to plasma density diagnostics.

helium-like and hydrogen-like emission. Some of the first helium-like profile calculations were performed as part of the Laboratory's implosion diagnostics program.[4] In Fig. 4, we show the results of detailed fitting of theoretical profiles to experimental points. Because the x-ray line spectra are time integrated, the value of compressed density obtained by this profile fitting represents an average value during the compressed phase.

Electron temperatures are measured by using both "line ratios" and "continuum slopes." The continuum slope method is the most straightforward, although it is sometimes complicated by hard x-ray background (due to the fast electrons). When special precautions are taken, temperature measurements of ± 50-eV accuracy are possible. Line ratio measurements are complicated by the very dense plasma conditions as the high density causes only a relatively small number of the members of a series to be present while causing the low-quantum-number transitions to be optically thick. This usually makes line ratios between ionization stages of a given species the best choice for determining the electron temperature. This, of course, introduces a dependence on electron density and the self-consistency between the density and the temperature must be carefully checked.

Time-integrated x-ray spectra (in this energy range) are measured using crystal-dispersing spectrographs. For example, the spectra in Fig. 3 were taken with a PET crystal whose (002) reflection planes have a 2D spacing of 8.74 Å.

Spatial resolution orthogonal to the dispersion (provided by a slit) allows accurate determination of the spatial distribution of emission. Careful characterizations have been made of the instrument profiles and response functions of such measurement systems as well as the effects of the spatial distribution of the radiating sources. Such information is carefully accounted for in comparing the measurements with theoretical modeling.
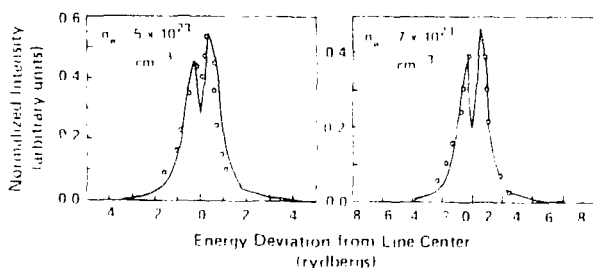

Fig. 4. Plasma density measurements are obtained from the fitting of theoretical line profiles to experimental points.

In the period around peak compression, most of the pusher is relatively cold (~300 eV) and dense. Continuum radiation from the core thus passes out through a relatively long path in material that is considerably colder than the fill gas, which produces absorption features in the spectrum. Analysis of these features can be used to determine the conditions in the pusher and can be important in overall characterization of the implosion. In Fig. 5, we show such an absorption spectrum produced by silicon ions in the glass.

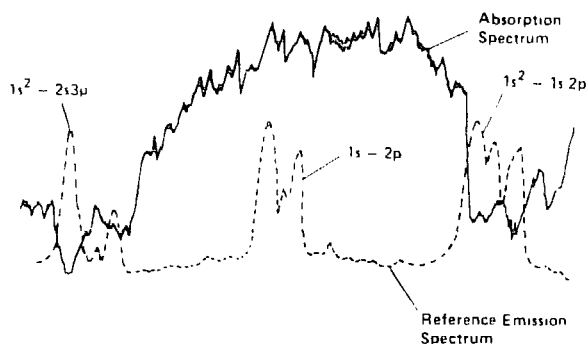Fig. 6. X-ray image of a laser-driven implosion.

Fig. 5. Silicon absorption spectrum.

In the section below, on the stability of laser driven implosions, we show how more detailed information can be obtained from absorption spectra.

X-Ray Imaging

The primary auxiliary method for the measurement of density is the determination of radiation source sizes by x-ray imaging. As mentioned above, the emission from the compressed core is usually spatially resolved by placing a slit perpendicular to the plane of incidence on the crystal. This produces one-dimensional spatial resolution orthogonal to the dispersion direction. Unfolding techniques[5] have been developed that allow determination of the source distribution. These techniques account for the integration along the line of sight and also take into account the finite size of the slit. By spatially resolving several optically thin lines, we can obtain a rough indication of the temperature variation within the compressed core. Knowing the average diameter of the compressed material and the initial fill pressure, we may determine a compressed density.

Broadband two-dimensional x-ray imaging of the compressed core can be performed with pinhole cameras or x-ray microscopes. In Fig. 6, we show an example of such an image. These images are primarily useful in diagnosing the two-dimensional symmetry of the implosion. Implosion symmetry by itself is an important implosion characteristic that will need to be studied in great detail the future.

By selective filtering of the images, gross indications of the temperature and density gradients in the compressed core can be obtained. These images do reveal one interesting characteristic of CO_2 laser-driven implosions That is, even with significant non-uniformity in the illumination, the hot-electron symmetrization effect tends to produce rather symmetric compressed cores.

Time-Resolved X-Ray Detection

Time resolution of broadband x-ray emission gives useful information on the velocity characteristics of the implosion. The subnanosecond time resolution required can be obtained with fast x-ray diodes or with an x-ray streak camera. In Fig. 7, we show an x-ray streak photo of an imploding target. In this particular case, the target was a thin (unfilled) gold shell irradiated with about 5 kJ of energy from the Helios CO_2 laser. The long pulse of soft radiation comes from the heating and ablation of the shell. The short burst of somewhat harder radiation comes from the implosion when the shell collapses to a compressed core.

Information such as this can be useful in characterizing the velocity time history of the implosion. Such information is particularly important as very high compressions are reached and stability questions become especially important.

X-RAY STREAK PHOTOS OF LASER IMPLOSION OF GOLD SHELL

Fig. 7. Streak measurement of the temporal profile of x-rays from a laser-driven implosion.

Nuclear Product Measurements

Yield from thermonuclear reactions is, of course, the end-product goal of ICF. When targets, such as that shown in Fig. 2, are filled with DT, significant thermonuclear neutron yield can be achieved. For example, on the Helios laser system with about 5 kJ on target, yields of near 10^9 neutrons per shot were achieved.
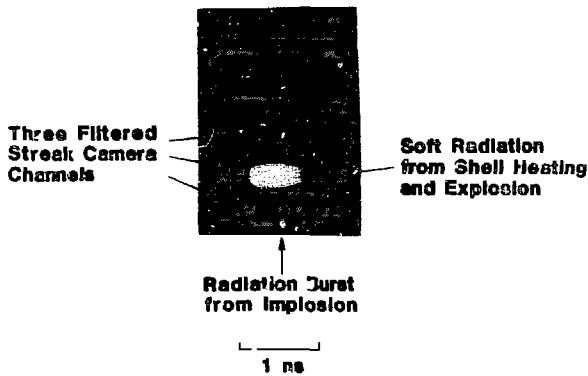
Neutron yield measurements can be used to provide an estimate of compressed density. The yield can be written

$$Y = n_{ion}^2 \langle \sigma v \rangle V \Delta t \quad , \tag{1}$$

where

n_{ion} = compressed ion density,
$\langle \sigma v \rangle$ = velocity-averaged cross
      section for DT reactions,
Δt = reaction or confinement time, and
V = reaction volume.

Unfortunately, in the temperature range in which we are presently operating, $\langle \sigma v \rangle$ varies roughly as T_{ion}^6. Inaccuracy in the measurement of T_{ion} thus (at present) makes the density determination only an order-of-magnitude estimation. It is, however, a very useful cross check to compare with more accurate density estimates from spectroscopy.

Time-resolved measurements of neutron production can provide important information on the characteristics of the implosion. For example, the timing of the peak of neutron production with respect to the rise of the laser can give an estimate of the implosion velocity. In Table I, we show measured laser rise-neutron delays as a function of plastic thickness for targets like that illustrated in Fig. 2. Total energy on target was about 5.5 kJ. These correspond to implosion velocities between 8×10^6 and 3×10^7 cm/s. The width of the time-resolved neutron signal can also be used to estimate the ion temperature of the compressed core.

TABLE I. Laser Rise-Neutron Delay vs Plastic Thickness

Plastic Thickness (μm)	Delay (nsec)
20	0.850
40	1.4
60	2.1

MODELING OF LASER-DRIVEN IMPLOSIONS

Numerical hydrodynamic codes are the primary methods used in analyzing these implosions. It is important to use these codes to simulate experimental diagnostic output. A strong interaction between theory and experiment can thus be established, which is of benefit to both.

Most implosion simulation work has been done with the Lagrangian hydrodynamic code LASNEX.[6] Non-LTE (local-thermodynamic-equilibrium) ionization dynamics and radiation transport are handled in real time (that is, in line with hydrodynamic variations) with an average ion model. Detailed radiation behavior, such as transport of an individual line profile, is handled in a post-processing mode. In other words, we assume that the detailed radiation behavior does not affect the overall dynamics of the problem. The output of temperature and density data is then used to calculate particular radiation information.

When we attempt very detailed comparisons between theory and experiment for laser plasmas, the question of non-LTE behavior arises. Because x-ray diagnostics are a

primary source of information on implosion dynamics, it is important to carefully model these radiation signatures.

The following simple considerations indicate the importance of non-LTE analysis in predicting radiation signatures. For a level to be in collision-dominated (CD) equilibrium with higher levels, we ignore pressure ionization effects and use the following criterion taken from Griem:[7]

$$N_e > 7 \times 10^{18} \frac{Z^6}{(n)^{L/2}} \left(\frac{kT_e}{Z^2 \, E_H} \right)^{1/2} cm^{-3} \quad , \qquad (2)$$

where N_e is the electron density (cm^{-3}), n is the principal quantum number, E_H is the ionization energy of hydrogen, and T_e is the electron temperature. For example, for n = 2, and Z = 18, $N_e > 4 \times 10^{24}$ cm^{-3}, while for n = 3, $N_e > 1.1 \times 10^{23}$ cm^{-3}. The state n = 2 is not in local thermodynamic equilibrium (LTE) with higher levels in past CO_2 laser implosion experiments (such as those utilizing targets like that shown in Fig. 1), while n = 3 is usually close. The helium- and hydrogen-like resonance lines often have a large optical depth, which brings n = 2 much closer to LTE than it would otherwise be (through absorption from the ground state). Clearly, to deal with questions such as the detailed transport of optically thick lines (for example, Lyman α and 1s^2-1s2p in Fig. 3), a detailed non-LTE radiation model must be utilized.

In order to calculate the radiation from these laser-driven implosions, an extensive collisional-radiative model has been constructed.* The time- and space-varying nature of the emitting region is included, although the final comparison is with a time-integrated spectrum. By calculating a large number of spectral features (line intensities, profiles, etc.), we can obtain a substantial confirmation of plasma conditions. The collisional-radiative model incorporates overall plasma conditions that are predicted by a one-dimensional version of LASNEX. Experimental measurements provide a substantial number of constraints on the choice of input conditions to these calculations. These measurements included (a) thermonuclear yield measurements, (b) ion temperature obtained from neutron temporal broadening, (c) implosion times from time-resolved neutron signals.

----

*In collaboration with the Plasma Radiation Group at the Naval Research Laboratory.

(d) hot-electron temperature measurements, and (e) absorbed energy measurements. The calculational procedure is thus composed of two steps. LASNEX calculation of the overall plasma conditions (where experimental measurements affect the choice of LASNEX initial conditions) constitutes the first step. In the second step, detailed radiation characteristics are calculated with the collisional-radiative (CR) model (using LASNEX-calculated input conditions). A flow diagram illustrating the calculational procedure is given in Fig. 8.

An example of the results of such modeling is given in Fig. 9 for a target quite similar to that shown in Fig. 2 that was irradiated with about 4 kJ on the Helios laser system. The final compressed electron density was about 3.5×10^{23} cm^{-3}. The neutron yield was about 2×10^8.

Detailed comparisons between theoretical modeling and experimental measurements for a variety of diagnostics such as imaging, spectroscopy, and nuclear measurements can provide a comprehensive picture of laser-driven implosions.[8] In future experiments, it will be vital to continue this pattern of detailed comparison and feedback between theory and experiment.

STABILITY OF LASER-DRIVEN IMPLOSIONS

One of the most crucial issues for the ultimate success of ICF is the stability and uniformity of the imploding pusher shell. The uniformity could be disrupted by classical hydrodynamic instabilities (such as Rayleigh-Taylor) that occur at the interface between different density materials. Disruption of the symmetry could also be caused by other effects such as nonuniformities in the ablation drive.

Several preliminary experiments have been performed to develop diagnostics of shell stability. The experiments can be divided into two general categories: acceleration and deceleration phase experiments that study break up and instability early in the implosion and near stagnation, respectively.

Acceleration Phase Stability

The acceleration phase work has been done with cylindrical-shell targets that have been imploded with relatively uniform eight-beam CO_2 laser illumination. Typically, about 5 kJ was incident on target. Cylindrical
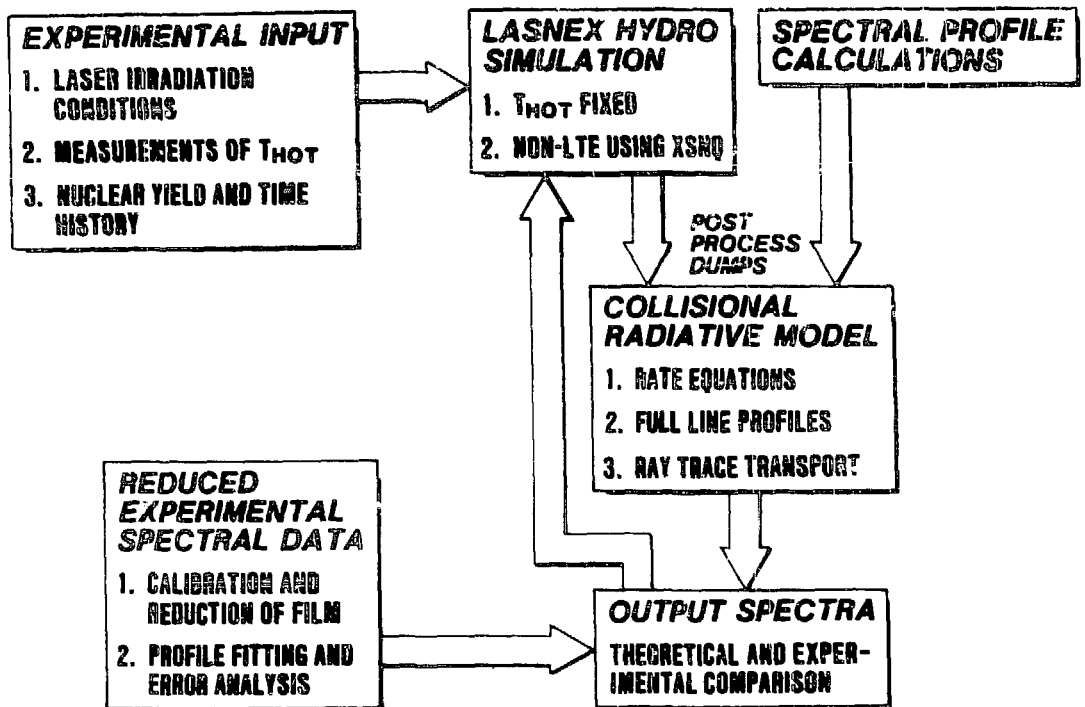
Fig. 8. Flow diagram of the calculational procedure used in simulating x-ray signatures of laser implosions.

configurations offer many advantages in stability experiments. The open geometry facilitates diagnosis while testing the effects of implosion convergence. The cylindrical geometry is also convenient for comparison with some types of theoretical modeling.

In the present work, the targets were cylindrical shells of copper and aluminum with and without plastic coating. The basic target configuration is illustrated in Fig. 10. The targets were about 200 μm in diameter with walls about 2 μm thick. The uncoated shells behaved much like explosive pushers, whereas the plastic-coated targets behaved similarly to the quasi-ablative targets used in the implosion experiments described earlier.[2] The eight beams were independently targeted (and defocused) around the cylindrical surface of the targets.

In addition to the simple shells, some of the targets had initially imposed perturbations, as shown in Fig. 11, which were arranged to maintain a constant wall thickness. The period of the perturbations was about 25 μm with an amplitude of 0.5 μm. The axial perturbations (Fig. 11a) are compatible with the cylindrical symmetry in LASNEX, which permitted the results from LASNEX calculations to be used for some preliminary scoping of the types of growth expected.

The implosions were diagnosed primarily with x imaging of self-emission. Several pinhole cameras arranged to provide imaging along, and perpendicula the cylindrical axis. In Fig. 12, we show a compar between the implosions of coated and uncoated c drical shells (viewing along the cylindrical axis), n from images that were filtered for about 1.5-keV ra tion. The comparison here is very similar to the explo versus semiablative studies done in the high-density s of spherical implosion experiments. Also shown in 12 is an image taken with a view perpendicular to axis, which confirms that it is possible to obtai relatively uniform implosion all along the cylindrical (that is, the views in Fig. 12a and 12b are not end effe

We now turn to the targets that contained prearrar perturbations. Targets that contained perturbations always coated with plastic so that perturbed ver unperturbed comparisons are only made for the s ablative case. In Fig. 13, we show a comparison of on pinhole camera views for unperturbed and pertur cases. In all cases where perturbations were present, compressed core is significantly larger (weaker c pression) and is surrounded by a halo of radia material that, in many cases, contains a periodicity.
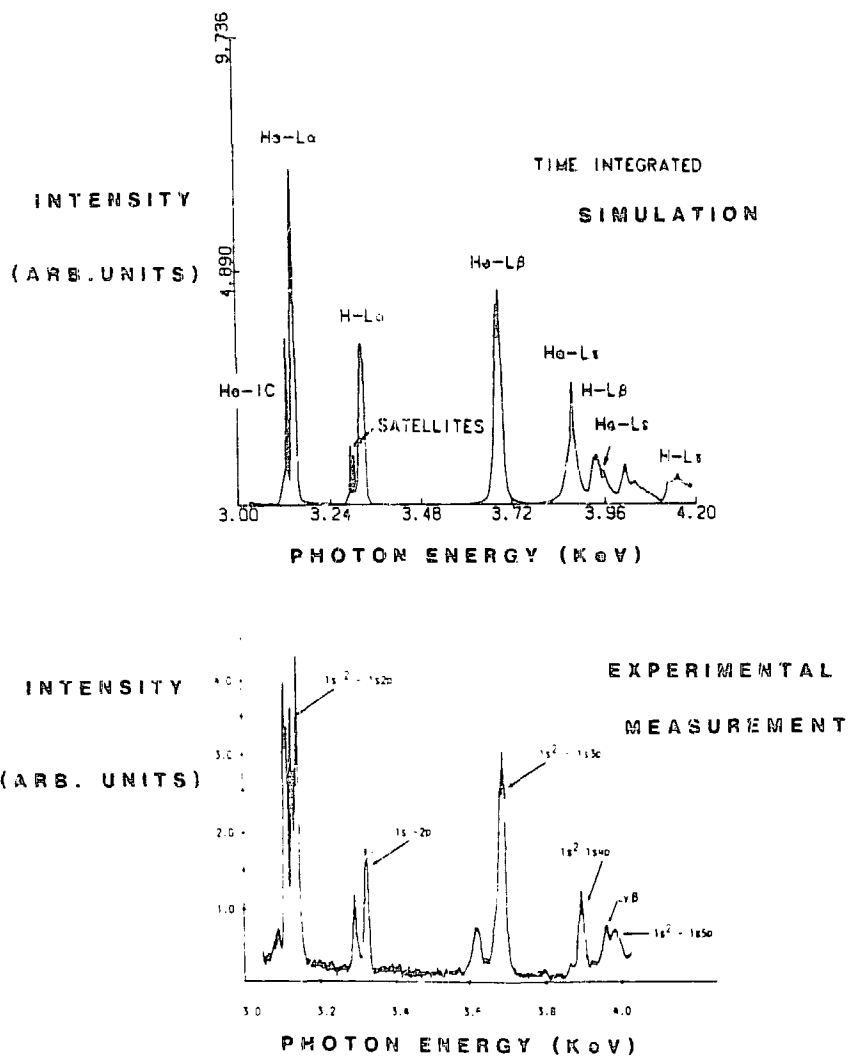
Fig. 9. Comparison between theory and experimental of time-integrated x-ray spectrum.

**Cylindrical Metal Shell
(Typically 2 μm Thick)**

~700 μm

~200 μm
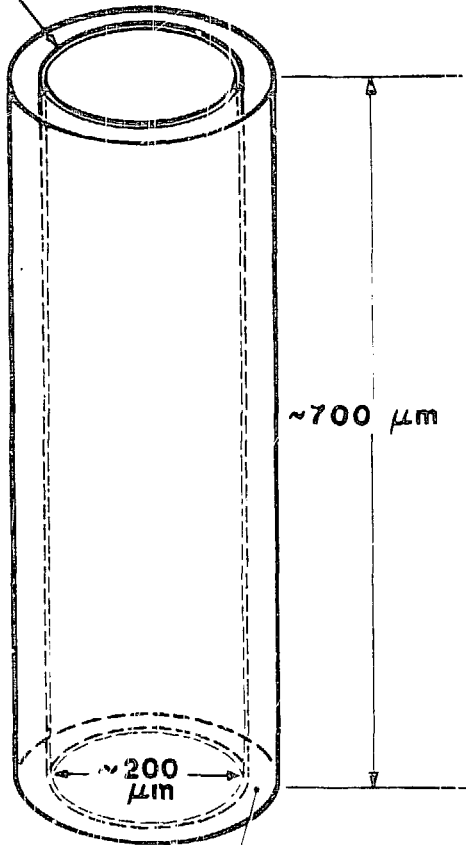
**Plastic Coating
(40 μm Thick)**

Fig. 10. Basic target configuration used in cylindrical stability experiments.

**Axial
Perturbations
in Cylinder Wall**
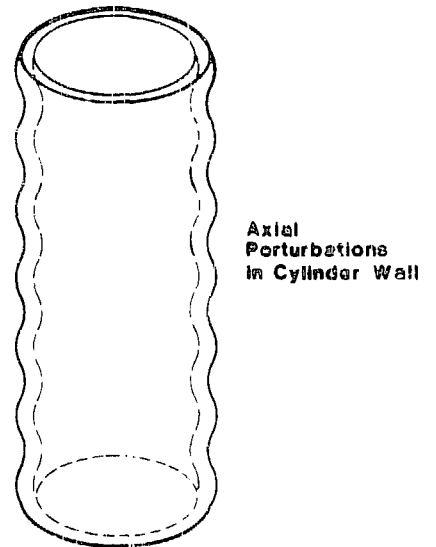
Fig. 11. Perturbations imposed on the cylindrical targets.

**Azimuthal
Perturbations
in Cylinder Wall**

2 μm

25 μm
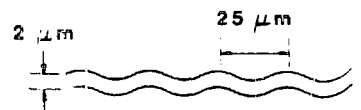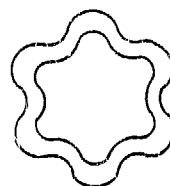
**Structure of Perturbations
(Maintains Constant
Thickness)**

X-RAY IMAGE OF ABLATIVE vs EXPLOSIVE IMPLOSION OF CYLINDRICAL SHELLS

Thin Shell (Explosive)
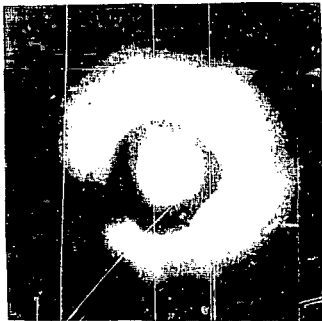
Plastic Coated Shell (Ablative)

View Along Axis

(a)
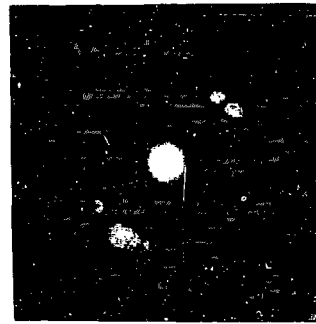
View Along Axis

(b)

View Perpendicular to Axis

(c)

Fig. 12. X ray images of the implosion of coated and uncoated cylindrical shells.

X-RAY IMAGES OF ABLATIVE CYLINDRICAL IMPLOSIONS WITH AND WITHOUT IMPOSED PERTURBATIONS
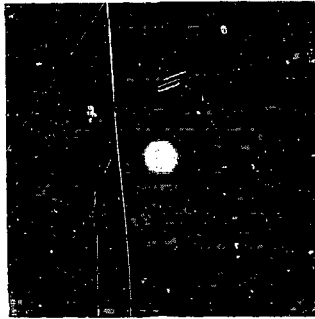
Without Perturbations   **With Perturbations**
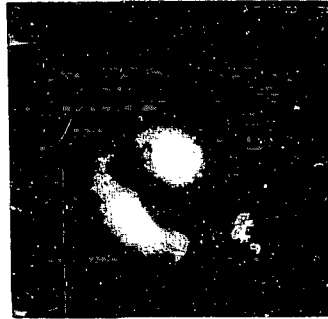
Fig. 13. X-ray images of the implosion of coated and uncoated cylindrical shells.

print in Fig. 13 does not adequately show this periodicity. The nature of this structure is being analyzed further.

The basic conclusions from these preliminary experiments are as follows:

- Strong, uniform cylindrical implosions can be produced. The CO_2 laser is actually an advantage here, giving added symmetrization.
- Evidence of shell breakup was observed in the case of initially perturbed cylindrical targets.
- Cylindrical configuration experiments offer a number of advantages in stability/shell breakup experiments.

Compression Phase Stability

The compression phase stability studies were performed on targets that are quite similar to that shown in Fig. 2.

This series of experiments was designed to be a first test of diagnostic techniques appropriate for studying the breakup of imploding shells. Figure 14 shows the basic target configuration used in these tests. Glass shells (about 350 µm in diameter) were filled with about 12 atm of DT. In some of the targets, the DT was seeded with about 0.1-0.2 atm of argon. Some of the shells were then
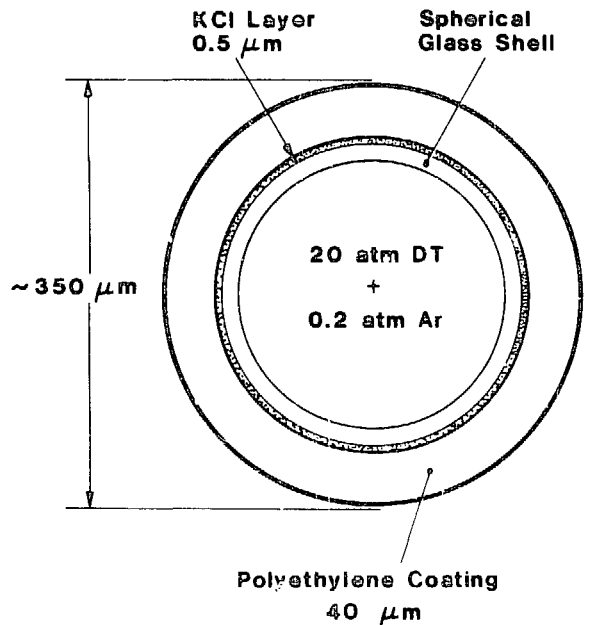
Fig. 14. Target configuration used in spherical shell break up experiments.

coated with about 0.5 μm of potassium chloride. Other targets contained no potassium chloride coating but were fabricated from glass shells with a high content of calcium and potassium. Finally, the targets were coated with about 40 μm of plastic, which made them similar to the targets used in the high-density series described earlier.

When such targets are laser imploded, there are typically large temperature gradients in the compressed cores. These gradients can be utilized in the diagnosis of shell stability.

Spectroscopic observation of potassium and chlorine radiation served as the signature of shell breakup. These species could only radiate if they penetrated into the central high-temperature regions of the compressed core. If the potassium chloride remains in the outer portions of the shell, previous experimental measurements and theoretical calculations show that it would be at a temperature of about 250 eV. This is too low a temperature for efficient excitation of hydrogen- or helium-like potassium and chlorine lines. The argon lines are used to accurately characterize the compressed core conditions. With careful spectral analysis, this information will allow a determination of the amount of shell material mixed into the core.

The targets were chosen to be slightly larger than those in the high-density series, and this produced a weaker compression. Because in this series we were primarily interested in development of the measurement technique, we wanted a larger compressed core that could be more easily diagnosed (for example, easier x-ray imaging).

The eight beams of the laser were focused 300 μm beyond center, giving a T_{hot} (determined from x rays) of about 100 keV. In Fig. 15, we show a typical spectrum

obtained in these experiments. The argon lines show an implosion of modest density ($n_e \sim 2\text{-}3 \times 10^{23}$ cm^{-3}) with a temperature of about 600 eV. This temperature would be more than adequate to strongly excite chlorine lines. The most striking feature of the spectrum in Fig. 15 is, however, the strong chlorine and potassium absorption features. These features indicate that most of the potassium chloride has remained in the cold outer regions of the shell; in other words, there is little evidence of shell breakup. The spectra remained very similar to that in Fig. 15 throughout this experiment. In Table II, we summarize the parameter variation present in this series of experiments. Over the range of parameters in Table II, no evidence of breakup was observed.

Some evidence of breakup was observed in the following case:

- The target had no potassium chloride coating but had a high concentration of potassium in the glass shell itself.
- There was significant laser beam imbalance.

In Fig. 16 we show an example of this case, and a definite potassium emission feature is noted. There is also some evidence of weak absorption features to the left of the potassium line. Potassium would thus have been seen in both absorption and emission, which indicates partial shell breakup. This is the type of information that we hope to quantify in future experiments.

The initial aspect ratio (pusher thickness/diameter) in these experiments was relatively low (~4). In future experiments we should strive to increase this. This may require replacing the plastic layer with a thin metal layer (to increase the aspect ratio). This, in turn, may favor the use of backlighting to diagnose the compressed core.
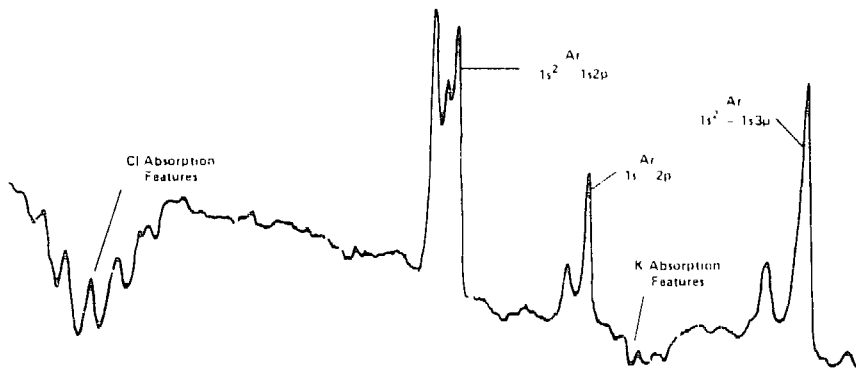
Fig. 15. Typical x ray spectrum obtained from the implosion of a target similar to that in Fig. 14.

TABLE II

Inner (glass) shell wall (t)	$0.8\,\mu m < t < 1.8\,\mu m$
No. laser beams (b)	$6 < b < 8$
DT gas fill pressure P (atm)	$8 < P < 15$

The Use of Backlighting and Absorption Spectroscopy

In the diagnosis of very dense implosions, the temperatures may sometimes be inadequate for self-emission to be a useful diagnostic. In such cases it may be possible to use an external source of radiation (such as another laser-irradiated target) to backlight the imploding target). In a more sophisticated sense, it may also be possible to use an external source of radiation to perform absorption spectroscopy and obtain more detailed information than could be obtained with a simple shadowgraph. This possibility is in fact already demonstrated by the spectrum shown in Fig. 15.

The absorption spectra represent "self-backlighting," with radiation from the core passing out through the cold absorbing layers. The information is, however, the same as would be obtained if the probing radiation were from a completely external source. As an example of the type of information that can be obtained from spectra such as that in Fig. 15, we consider a simple analysis to obtain the average ρR of the potassium chloride layer.

For one of the absorption features (which corresponds to a particular ionization state) we can write:

$$\int K_{\nu}d\nu = \frac{\pi e^2}{mc}\,Nf \quad , \tag{3}$$

where

K = absorption coefficient,
N = number of ions in the ground state, and
f = average oscillator strength for the transitions involved.

We note that

$$I = I_0\,e^{-KR} \quad , \tag{4}$$
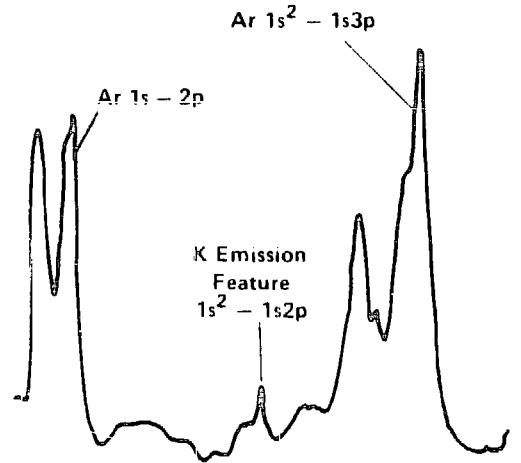
Fig. 16. X-ray spectrum showing potassium emission feature.

where R is the path length through the absorbing medium.

Combining Eqs. (3) and (4), we can write approximately

$$\int \ln\left[\frac{I_0(\nu)}{I(\nu)}\right] d\nu \cong \frac{\pi e^2}{mc}f\,[\rho R] \quad . \tag{5}$$

Using Eq. (5) for the spectrum in Fig. 15, we obtain an average value of ρR of about 10^{-4} g/cm^2. This is consistent with values predicted by hydro simulation.

In the near future, absorption and backlighting techniques should provide a wealth of implosion diagnostic information.

SUMMARY

Techniques have been developed for measuring many characteristics of the very dense plasmas produced in laser-driven implosions. Measurements have been compared with theoretical modeling to provide an accurate picture of these implosions.

Methods are currently under development for addressing the crucial question of implosion stability, one issue that is central to all of inertial confinement fusion. Preliminary tests of some aspects of these ideas have been successful.

In the future the density of these implosions will increase and alterations and extensions of the diagnostic methods discussed here will be required. One of these extensions will involve the use of an auxiliary laser plasma x-ray source to backlight and probe the compressed plasma.

REFERENCES

1. B. Yaakobi, D. Steel, E. Thorsos, A. Hauer, and B. Perry, *Phys. Rev. Lett.* **39**, 1526 (1978).

2. A. Hauer, K. Mitchell, D. Van Hulsteyn, T. Tan, E. Linnebur, M. Mueller, P. Kepple, and H. Griem, *Phys. Rev. Lett.* **45**, 1495 (1980).

3. A. Hauer, in *Spectral Line Profiles* (de Gruyter, Berlin, 1981).

4. P. C. Kepple and K. G. Whitney, U. S. Naval Research Laboratory Report No. 4565 (unpublished) performed under contract to Los Alamos National Laboratory.

5. M. M. Mueller, *Bull. Am. Phys. Soc.* **24**, 1053 (1979), and Los Alamos Scientific Laboratory document LA-UR-78-2698 (1978).

6. G. Zimmerman and W. Kruer, *Comments Plasma Phys. Controlled Fusion* **2**, 85 (1975).
   W. A. Lokke and W. H. Grasberger, Lawrence Livermore National Laboratory report UCRL 52276 (unpublished).

7. H. R. Griem, *Plasma Spectroscopy* (McGraw-Hill, New York, 1964) (available from University Microfilms).

8. A. Hauer, K. Mitchell, D. Van Hulsteyn, and E. S. Linnebur, "Comprehensive Analysis of High Density CO_2 Laser Driven Implosions Experiments," Los Alamos National Laboratory memorandum P-4-4/29/80/-189, 1980; A. Hauer, K. Whitney, P. Kepple, and J. Davis, *Phys. Rev. A* **28**, 963 (1983).

High-Power CO_2 Systems

by C. R. Mansfield and W. H. Reichelt

The concept of using short-pulse, high-energy lasers to drive fusion reactions dates back to the early 1960's, but fusion experiments became possible only after the development of large, powerful glass and gas laser systems proved feasible in the late 1960's and early 1970's. A generic laser system (Fig. 1) for fusion experiments consists of five basic blocks: (1) a short-pulse generator with amplifiers in which the short pulse of 0.5-10 ns and appropriate spectral characteristics is created; (2) the main power amplifier, which amplifies the pulse energy to design points during its transit; (3) the target chamber, which provides the necessary experimental vacuum environment where the optical energy is brought to focus on the target; (4) the optical train; and (5) the control systems that connect the short-pulse generator, power amplifier, pulsed power, target systems, and the optical train into an integrated unit.

The main thrust of fusion laser development at Los Alamos National Laboratory has, until recently, been directed toward CO_2 laser systems. Carbon dioxide lasers are usually operated at a wavelength of about 10.6 μm, although many other lasing wavelengths are possible. The earliest work at Los Alamos concentrated on the production of 1-ns pulses and the amplification of those pulses. The largest uncertainties in the early program centered around the design of large, energetic amplifiers. Two general types of amplifiers arose out of the early work. The difference in the type depends on the means of development of a stable electrical discharge. The first type of amplifier operates with a self-sustained electric discharge. The second type is one in which the electrical discharge is maintained by means of an external source of electrons (electron gun). In the second type, the high-energy electrons injected into the gas produce a stable
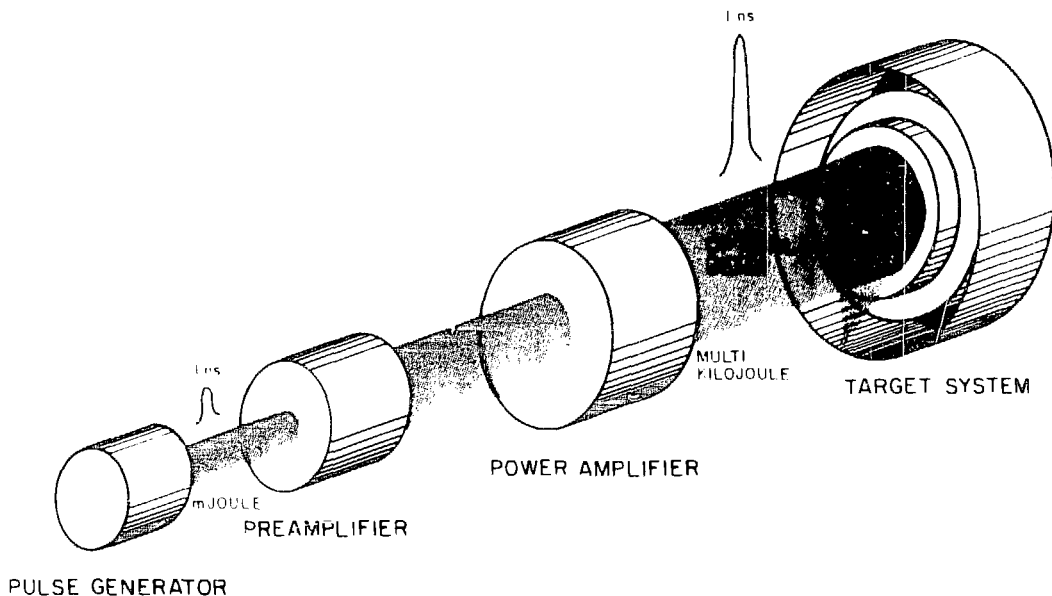
Fig. 1. The major components of a high-energy laser system. The fifth major component, the control system, is not shown.

low-impedance region of ionization into which energy can be deposited from a second electrical energy source.

The electron-beam (e-beam)-controlled discharge laser, a technological breakthrough, was invented independently at Los Alamos and at the AVCO Everett Research Laboratory. It was scalable to large apertures and was the most efficient system known. We recognized from experiments and analyses that to scale to large amplifiers, the e-beam-controlled devices were required; hence, our development effort was directed primarily toward electron-beam-sustained devices. Since the self-sustained discharge lasers were efficient and relatively easy to build and maintain, commercial applications soon became apparent and such lasers quickly became commercially available. The need for amplifiers in the Antares class of energy output (10-20 kJ) has not found commercial application, so this type of laser continues to be specially built for a particular use.

The hardware development effort was augmented by an intensive analytical effort that led to a general understanding of the physical processes occurring in CO_2 laser discharges. This analytical effort has carried on through the years and has provided the foundation for each successive laser system designed and built at Los Alamos. The 15-yr Los Alamos effort has recently culminated in the completion of the Antares laser system, currently the world's largest operational laser system.

The elements of the electron-beam-sustained amplifier are shown in Fig. 2. Electrons are generated in the gun section either by thermionic emission from hot filaments or by field emission from refractory metal blades. Electrons are accelerated by high electric potentials (200-500 kV) and pass through vacuum-tight foil windows into the gas lasing volume; the primary electrons create secondary electrons in the CO_2 gas mixture. When the high electric field from the main power source is applied to the preionized gas region, the secondary electrons are accelerated and undergo inelastic collisions with the gas molecules. Through these collisions the gas molecules are raised to excited vibrational states (Fig. 3). As the pulse passes through the discharge region, it stimulates the emission of photons from the excited molecule. The molecular transition energy is transferred to the pulse, amplifying its energy. The amplification of the discharge medium is characterized by the quantity e^{gL}, where g is the net gain per unit length and L represents the length of the gain region. In general, gL values are about 6-8 in typical laser amplifiers.

The importance of the preionization of the laser gas is emphasized by the fact that the electric field strength in the discharge region required to create good secondary electron excitation results in voltage differences of about 500 kV in regions of reasonable size. Without the preionization of the gas, catastrophic high-voltage arcs would form.
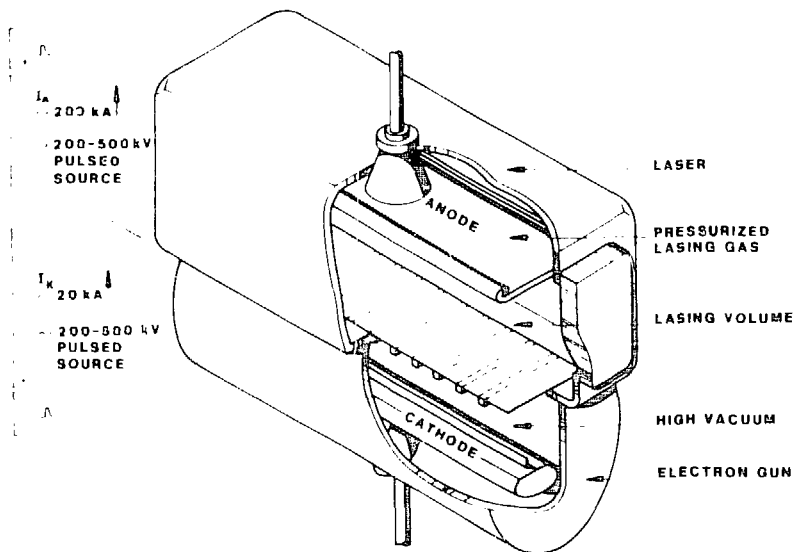
Fig. 2. Elements of an electron-beam-sustained gas discharge laser. The beam of electrons from the electron gun ionizes the laser gas. Energy can then be uniformly deposited in the gas by the main gas discharge.

(a) ELECTRICAL EXCITATION

(b) LASING
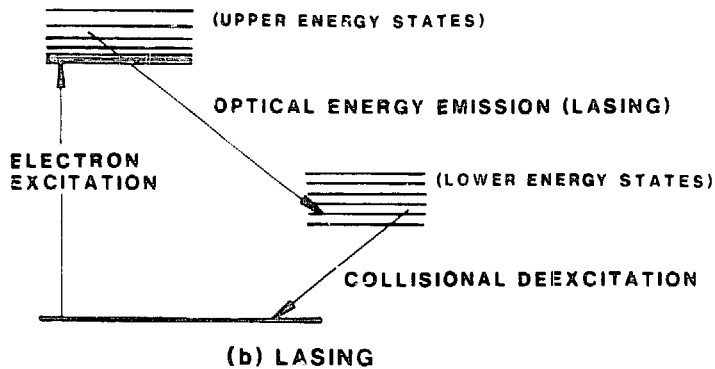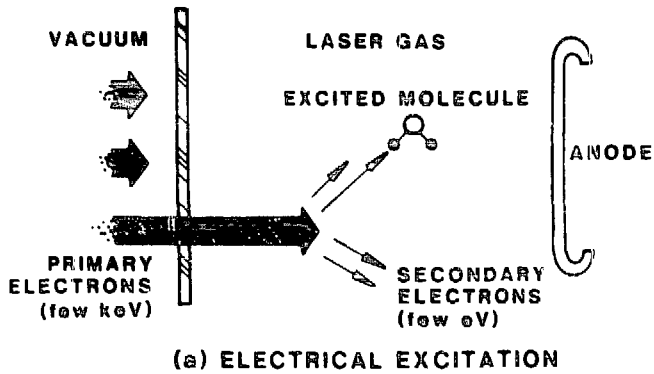
Fig. 3. Dynamics of the laser process: (a) deposition of electrical energy in the laser gas by secondary electron collisions with gas molelcules; (b) extraction of the optical energy from the excited gas molelcules.

ANTARES AMPLIFIER DESIGN

The design of the Antares power amplifiers is the result of evolution through the earlier designs and completed systems. The first system fabricated was similar to the one shown in Figs. 2 and 4a.

In this configuration, one electron gun served one amplifier The final single-power amplifier had an optical aperture of 25 cm. In the interest of design economy and to reduce the number of pulsed-power systems required to drive the electron guns, the next generation system used one gun to serve two amplifiers as shown in Fig. 4b. The Gemini (2-beam) and Helios (8-beam) laser systems successfully used this design of dual optical beam modules. The optical aperture of these systems was scaled up to 35-cm diameter. Figure 4c indicates a patented but not fabricated design in which one gun served four amplifiers. The ultimate logical extension of thought then led us to use one gun to serve an annular laser amplifier as shown in Fig. 4d. This indeed represents schematically the

Antares power amplifier configuration; it is a 12-sector annular design with a 46-cm optical aperture. The evolution of the design of power amplifiers at AVCO Everett Research Laboratory followed a similar path and resulted in the design of an annular system.

The original design goal of the Antares laser was to reach scientific breakeven with laser fusion. To this end Antares was designed as a six-amplifier system with an output of 100 kJ in a 1-ns pulse. By 1980, sufficient questions had arisen from the experience with Helios and the advancement of computer models to give doubt as to whether this goal could be reached. These questions centered on the efficiency of the coupling of the 10-μm laser light with the target. As a result the goal of Antares was changed to one of evaluation of CO_2 as a laser fusion driver by extrapolation of the Helios data to higher energy. With the new goal in mind, the Antares system was redesigned as a two-amplifier system that would be capable of delivering 40 kJ to a target in a 1-ns pulse.

(a) SINGLE SYSTEM

(b) DUAL SYSTEM (HELIOS)

(c) QUAD SYSTEM

(d) 12 BEAM (ANTARES)
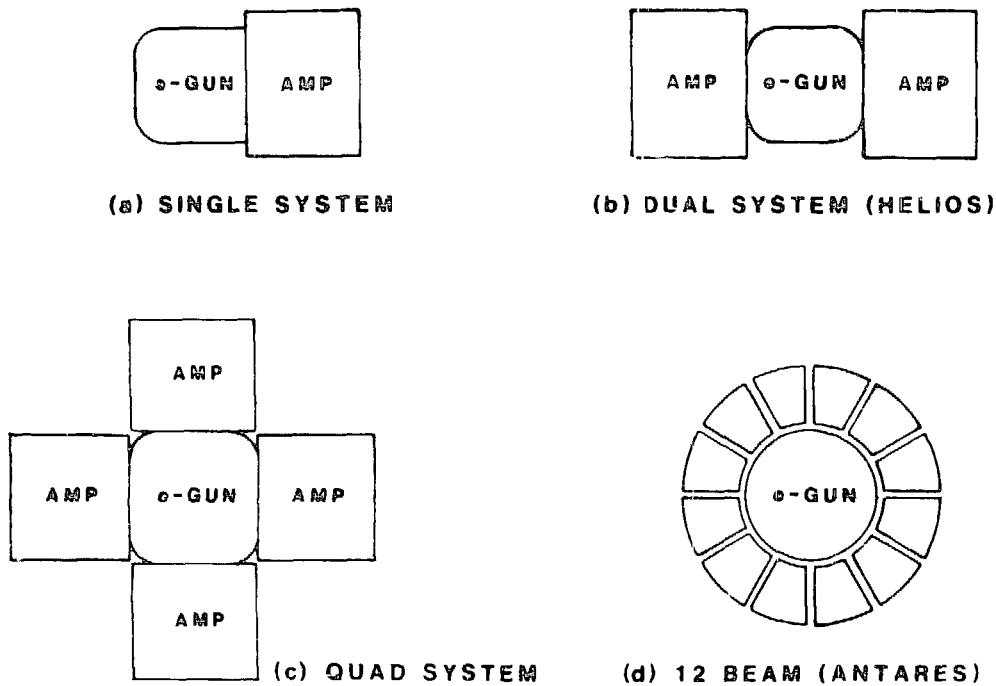
Fig. 4. Evolution of the design of high-energy gas discharge lasers. The sharing of one electron gun by several discharge regions creates a considerable savings in complexity and cost.

The analytical efforts resulted in computer modeling codes that were refined as the early hardware systems came on line and as data from experimental operations became available. These refined codes provided the basis for the engineering design of the Antares laser system. These codes enabled us to predict the engineering parameters for any system configurations and included (1) selection of CO_2 gas mixtures; (2) specification of discharge sizes, pressures, gas voltages, and currents; and (3) prediction of electric and magnetic effects on the discharge and gun current trajectories.

As shown in Fig. 4d, the general design of the Antares power amplifiers consisted of 12 discharge regions spaced in an annulus around a central electron gun. This design was further refined to have four discharge regions spaced uniformly along the length of the amplifier. The final result was a system with 48 discharge regions of 33-cm thickness, a 35.7-cm trapezoidal half-width, and a 75-cm length. This annular design represented a compact packaging concept and was a radical departure from the configurations of previous laser systems.

Before the Antares design, the lasing mixes consisted of CO_2, N_2, and He. One reason helium was used was that it permits the desired electron energies to occur at lower electric fields in the discharge, thereby reducing the chance of high-voltage potential arcing. In a system as large as Antares, helium recovery is both necessary and expensive. Calculations indicated that higher energy could be stored in He-free mixtures, which would result in higher energy extraction. The use of He-free gas mixtures would result in a more efficient laser amplifier. However, high-pressure, He-free electric discharges required higher voltages (~ 500 kV) than had been used previously. It was not known if high-voltage cables and terminations were practical under these operating conditions. Substantial magnetic effects were predicted on the discharge uniformity. Parasitic oscillations both linear and circumferential in the high-gain amplifiers were of major concern and not amenable to sufficiently reliable calculations.

SYSTEM PROTOTYPES

The technical uncertainties prompted the construction of a prototype amplifier that could reasonably duplicate power amplifier sizes and problems. The prototype design was full scale in diameter. The gain region was longer (150 cm vs 75 cm) than the length of each of the four gain

51

subsections in the amplifier design. The longer gain length provided a rigid test of magnetic field effects in that they were more severe than those in the actual amplifier designs. Only 3 of the 12 prototype discharge channels were electron-beam-sustained discharge channels. In the other nine channels, the discharge was simulated by the use of conductors.

The prototype amplifier answered many of the uncertainties in the Antares design:

- A new design of an efficient electron gun was demonstrated. This electron gun incorporated a self-biasing grid for current regulation.
- High-voltage, Helium-free operation proved to be successful.
- A prototype inductance-capacitance energy storage network worked well.
- Cables and cable terminations designed for 500-kV operation performed as expected.
- Satisfactory gain distribution across the discharge as well as gain shaping in the individual channels was demonstrated.
- Parasitic oscillation thresholds were demonstrated to be manageable.

The prototype program demonstrated that adequate performance could be expected from the Antares power amplifiers. The major physics and engineering uncertainties in the design were resolved and the program could proceed on schedule.

There were other prototype programs in progress at the same time as the power amplifier prototype. These prototypes included beam diagnostics and beam alignment. The beam alignment prototype was a major undertaking in itself. This prototype consisted of a layout of a single sector of the optical train including computer control of all of the necessary elements. The later prototyping proceeded in parallel with the fabrication of the power amplifier. Careful planning of the experimental programs was required to bring these later prototyping efforts to the hardware stage in time to fit into the construction schedule.

In the prototype program, we developed antireflecting surfaces, which were optically black at $\lambda = 10 \ \mu m$, that proved effective in parasitic suppression. These were based on LiF, an excellent absorber of 10-μm radiation. Antireflecting surfaces were made by LiF plasma spraying or by the application of LiF-loaded paint. The prototype itself yielded data that were used to further refine the computer codes necessary to improve the Laboratory's modeling capability.

FINAL ANTARES CONFIGURATION

The present Antares laser system (Figs. 5 and 6) is combined result of earlier experience with the th previous laser systems and the extensive prototype t ing.

In the Antares system, the front end must delive 100-J, 1-ns pulse, to each of the main power amplif with the proper combination of energy, CO_2 line cont contrast ratio, and pulse shape. The front end is oscillator-preamplifier chain as indicated in Fig. 1. 1 short-pulse generators (Fig. 7) are currently in plac the Antares system: one from the Gemini laser syst which represents reliable, "old" technology, and a sec that is just becoming operational t d represents state the-art development. The new short-pulse generator permit long-pulse (to 10-ns) shaping currently require inertial confinement fusion experiments. This oscill system is shown in Fig. 8. It consists of three indepe ent, single-line cw oscillators that are grating tunec operate on a specific wavelength. The amplitude pulse length of each independent oscillator output p can be selected. The independent pulses are combi and amplified in the first preamplifier stage. An elec optic switch (a Pockel cell) is used to switch out the f combined pulse length. The switch provides the propriate energy contrast ratio.

The pulse is divided into two by a beam splitter, beam for each main power amplifier, before the f stages of preamplification. The final preamplifier stag called the driver amplifier. This amplifier (Fig. 9 patterned after the Helios amplifiers (Fig. 4b) with exception that the driver amplifier electron guns are g controlled devices. The driver amplifier electron g produce two beams of 250-kV electrons with a curr density of 50 mA/cm². The amplifiers operate with a mix of N_2:CO_2 at a pressure of 1200 torr. The po source for the discharge is a Marx generator. wh develops a voltage pulse with a peak voltage of 300 The optical train in the driver amplifiers is configured three-pass, on-axis, Cassegranian system. The 1-J in to the driver amplifiers is amplified to 100 J and sen the power amplifiers as an annular beam with an ou diameter of 15 cm and an inner diameter of 9 cm.

The power amplifiers must accept the 100-J out from the driver amplifier and raise the pulse energy to 15- to 20-kJ design level at its exit. The final des configuration is shown in Fig. 5.
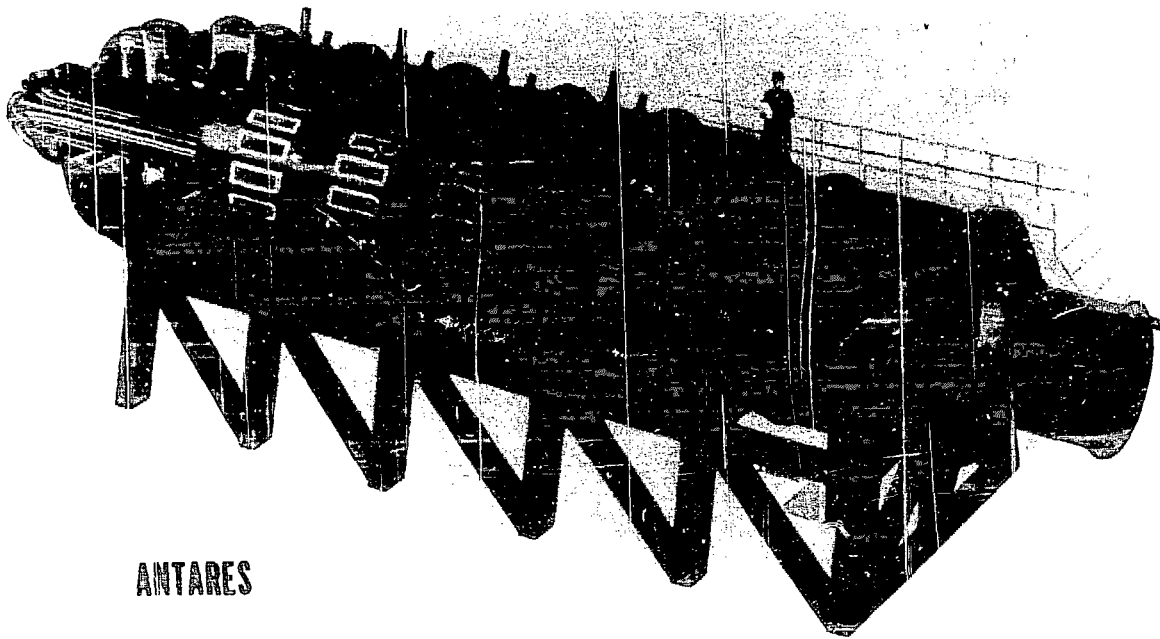
ANTARES

POWER AMPLIFIER

The general configuration of the power amplifiers is of 12 active sectors in an annular array around a central electron gun. The dimensions of the amplifier are in turn controlled by the necessity of keeping the laser energy fluences below the damage threshold for optical materials. In the case of mirrors, absorbed energy from the beam can cause surface melting if the incident energy flux is too high. The high electric fields associated with the short, powerful light pulses cause dielectric breakdown in transmissive elements when the light flux is above damage threshold. The best transmitter of 10-μm radiation is NaCl. The only windows in the system are needed to form the boundary between the target vacuum and ambient air and between the target vacuum and the lasing gas. The state of the art in fabrication of NaCl along with the damage threshold and the required output in turn determine, respectively, the total output area, the size of the individual sectors, and ultimately, the number of sectors. For polycrystalline NaCl, an 18-in. diameter is the state of the art. Allowing for optical mounting, 1000 cm^2 is available in each sector then available with 12 sectors for beam passage. A reasonable average

energy flux is 1.7 J/cm^2. Each of the 12 sectors can deliver 1700 J or a total of 20.4 kJ for a power amplifier. The copper-surfaced mirrors are designed for fluxes of 4 J/cm^2.

POWER AMPLIFIER ELECTRICAL PARAMETERS

The size of the optical windows determines the size of the individual discharge regions. To keep within those limits and provide a reasonable discharge region from the standpoint of the electrical requirements, the discharge regions were designed with a nearly trapezoidal cross section as is shown in Fig. 10. From the data obtained during work with the prototype amplifier and the results of the computer modeling, the laser mix was chosen as 4:1 N_2:CO_2. At a pressure of 1800 torr and with four gain regions of 75-cm length, lasing conditions with sufficient energy storage is reached with a specific electric field of 10 V/cm·torr and a current density of 7 A/cm^2. These requirements in turn demand that the anode voltages be nearly 550 kV and the discharge impedance be around 2.5 ohms.

53
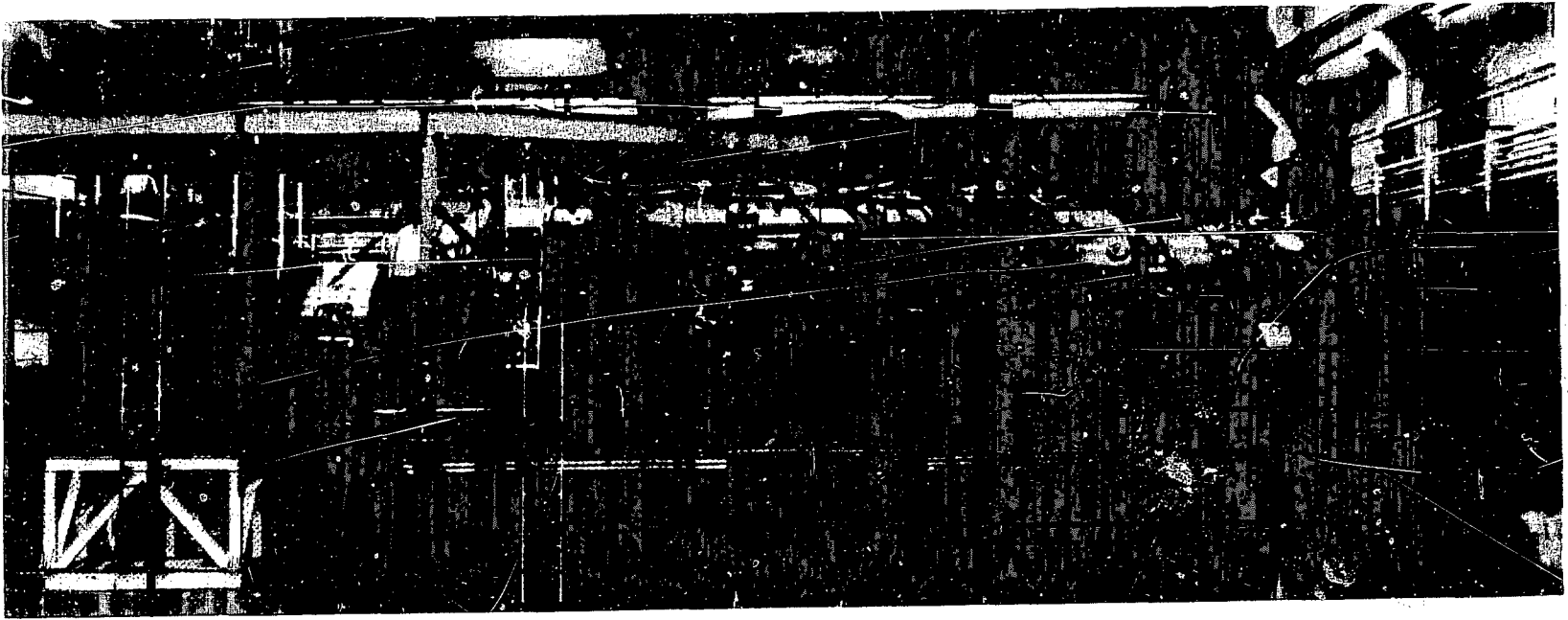
Fig. 6. This photograph shows many of the details of an Antares power amplifier. The structure in the middle is the power amplifier and the input/output optic module. The main power feed lines can be seen to enter the power amplifier in four regions. The electron gun Marx, the structure on the left, is the power supply for the electron gun.
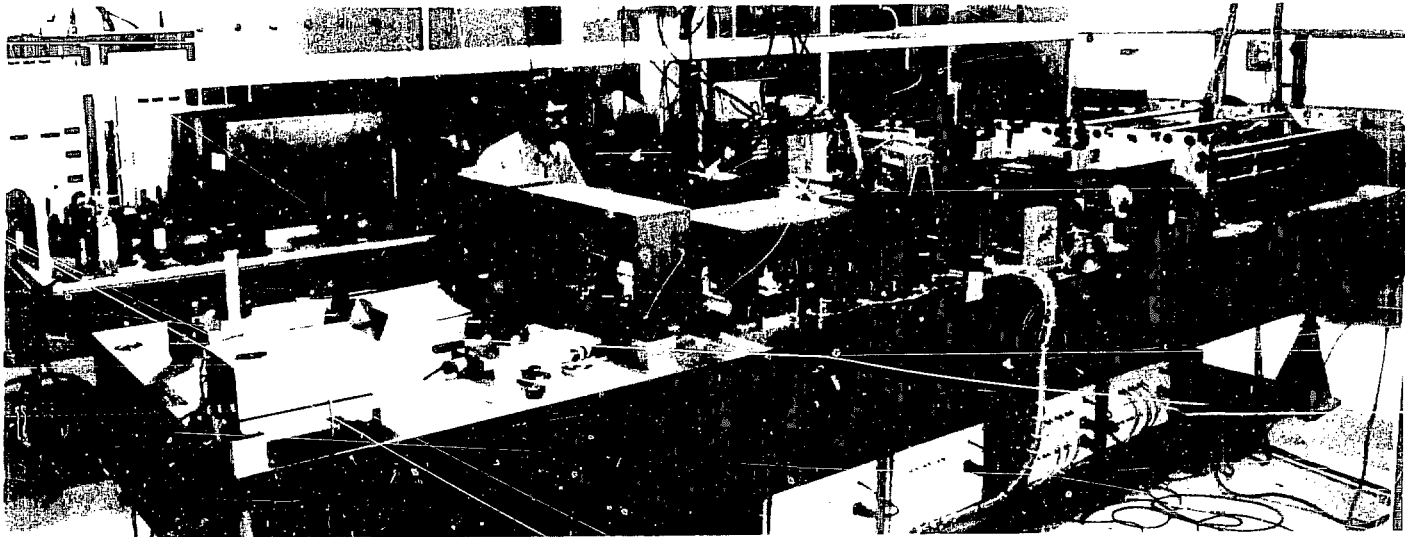
Fig. 7. The multiline oscillator (foreground) and the Gemini oscillator (background) are located in the oscillator room of the Antares front end
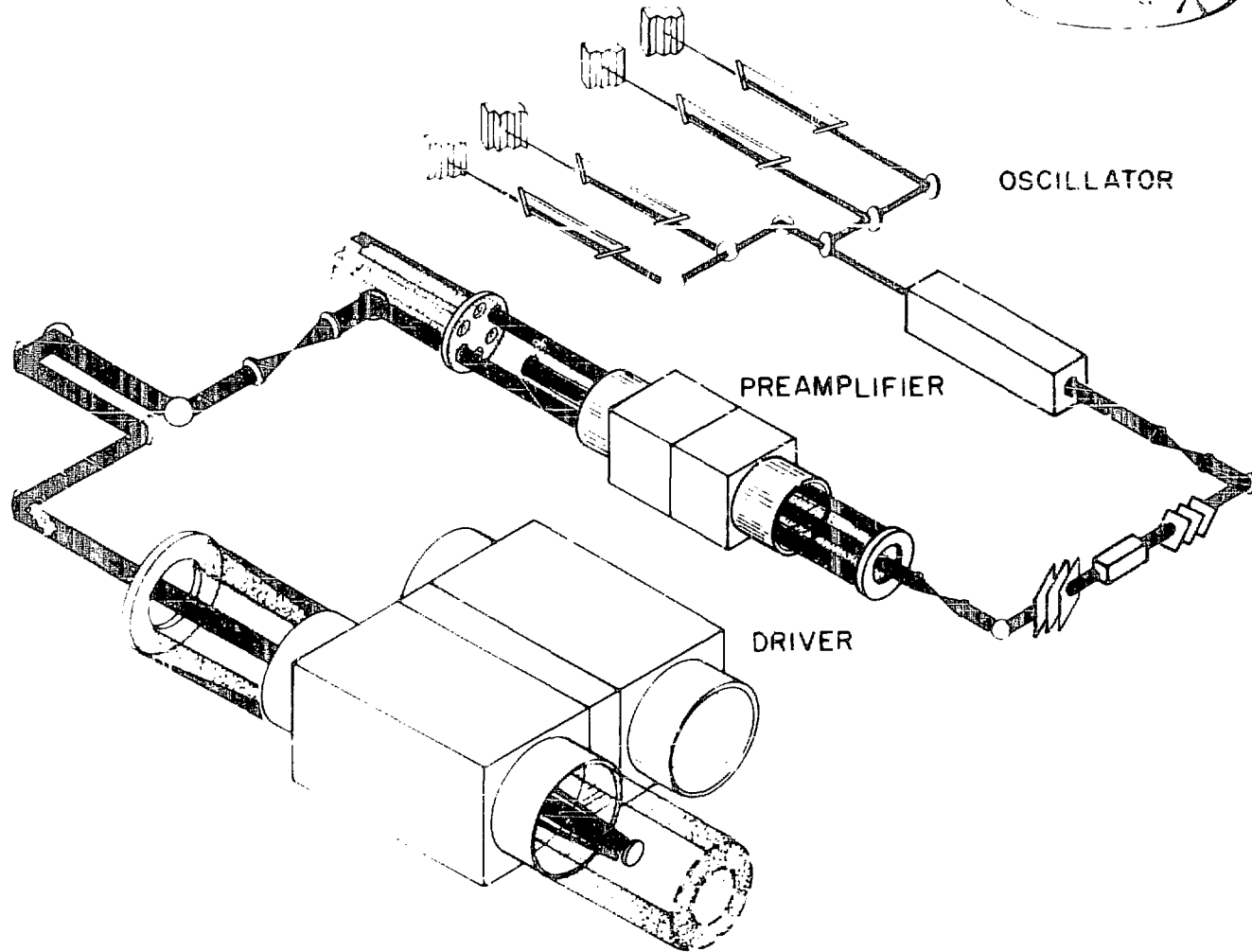
Fig. 8. Optical schematic of the Antares front end. The pulses that are amplified by the power amplifiers are formed in the front end. A short pulse is generated in the oscillator and then amplified to be a 100-J. 1-ns pulse after two stages of amplification.
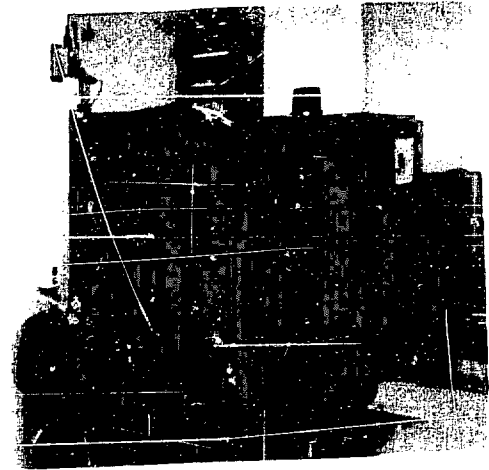
Fig. 9. The driver amplifier is located in the amplifier room of the Antares front end. The two optical paths follow the black tubes that extend out of the amplifier. Part of the beam forming optics are located on the table at the left.
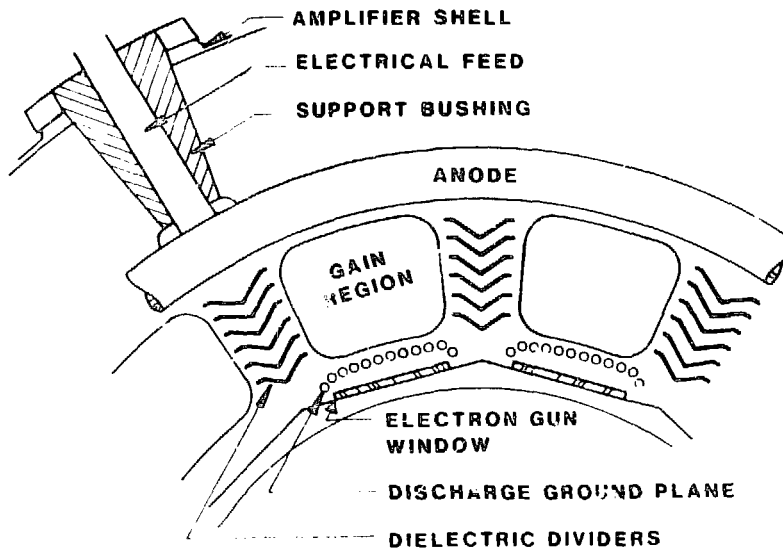
Fig. 10. Cross section of a portion of the gain region in the Antares power amplifier. Twelve independent gain regions are electrically and optically separated by dielectric (nonconductive) dividers. Each group of 12 regions is electrically driven from one anode. Six electrical feed lines supply each anode.

The time constant of the relaxation of the upper CO_2 laser level of 4.5 μs makes short pump times more efficient. A laser pumping time to peak gain of 3 μs was selected as a compromise between desirable high pumping efficiency (short pulse), low current density (long pulse), and large circuit inductance (long pulse). Lower current densities produce lower magnetic fields and, thereby, less undesirable electron beam deflection. Large circuit inductances are easier and less costly to achieve. The characteristics of the Marx generators, which power the gas discharges and the electron gun, are shown in Table 1. The design gain of the laser is 2.7 m^{-1}; hence, the amplifiers were designed to achieve a single-pass gain of 8.0. The physical size of the Antares power amplifiers

and their relationship in the laser hall can be seen in Fig. 11.

POWER AMPLIFIER OPTICAL SYSTEM

The optical layout of the Antares system is shown in Fig. 12. This figure gives the relationship between the various segments of the optical system. The power amplifier optical system is designed as a two-pass, off-axis Cassegranian system. A single sector of the power amplifier optical train is shown in Fig. 13. The input 100-J, annular beam is subdivided into 12 segments by a machined polygonal copper mirror. The input segments

TABLE I. Key Parameters of the Energy Storage System[a]

	V_o(kV)	V_L(kV)	I(kA)	Q(C)	L(μH)	C(μF)
Power Amplifier	1000/12000	450/550	150/200	~1.0	~2.4	0.420
Electron Gun Marx	525/600	475/550	20/25	~0.1	~3.5	0.375

[a] V_o = Open circuit voltage;   Q = Charge transfer;
  V_L = Peak load voltage;   L = Marx inductance;
  I   = Peak load current   C = Marx capacitance.
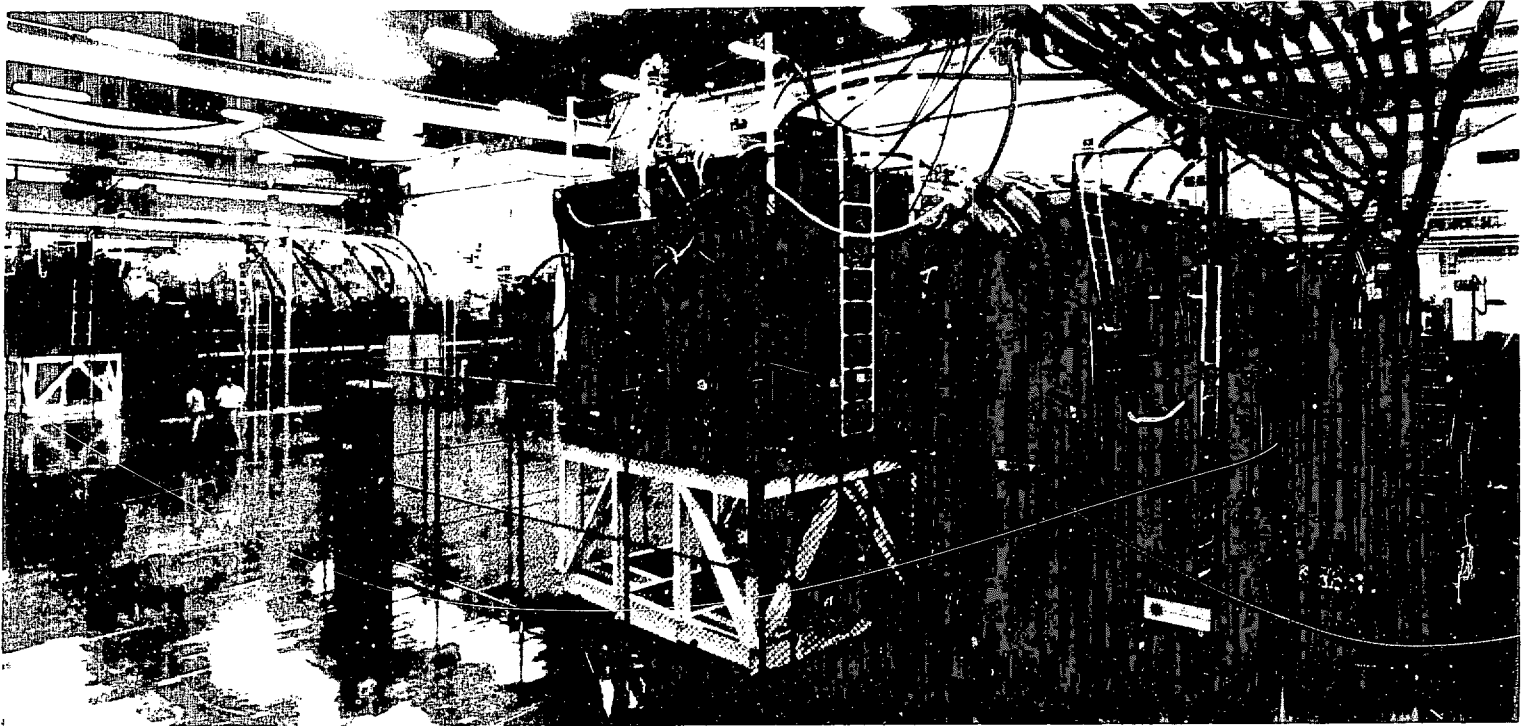
Fig. 11. The Antares Laser Hall. The room containing the two power amplifiers is nearly th size of a football field.
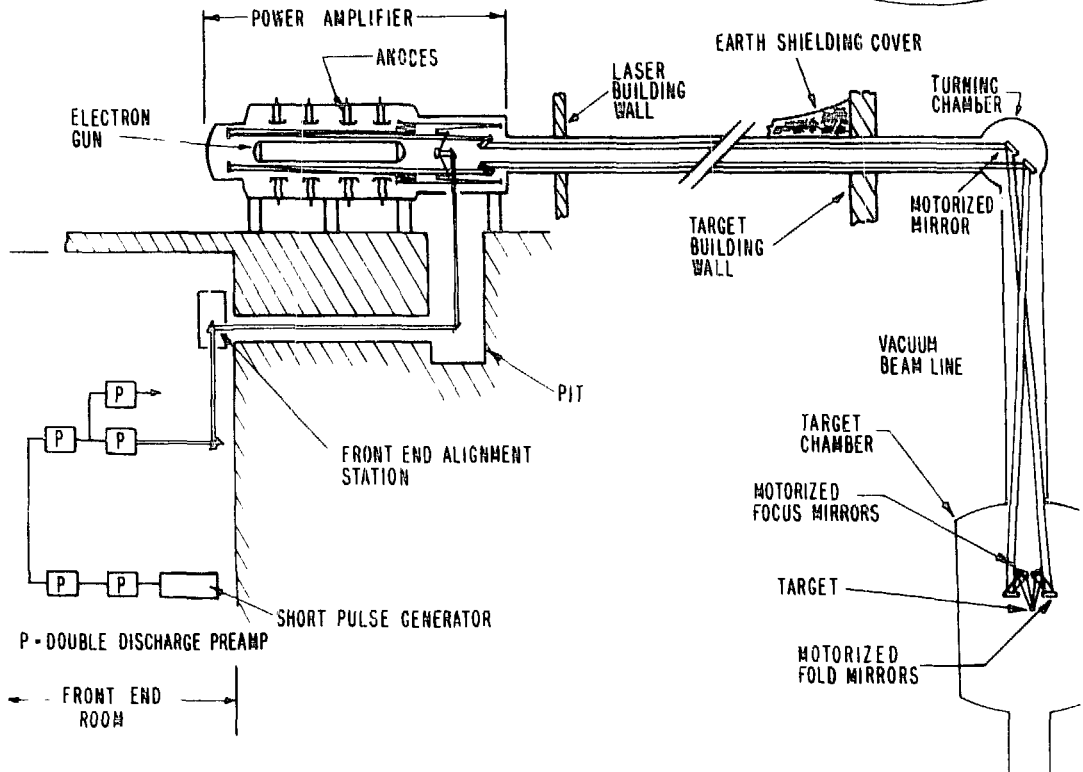
Fig. 12. The Antares optical system is laid out in four major segments. These segments are the front end, the front end alignment station, the power amplifier, and the target system.

have an area of about 10 cm². Each of the 12 sector beams is brought to a focus in a spatial filter fabricated from LiF. The plasma generated at the focus lasts for several microseconds and serves as an optical shutter to prevent the return of back-running beams to the front end where with further amplification they could do major damage. The pulse is then introduced into the power amplifier as a divergent beam. After its first pass through the four gain regions, it is reflected and collimated by a concave mirror for a second pass through the discharge region. The 5-J input energy insures that as the pulse makes its second pass through the discharge, virtually all of the available energy stored in the amplifiers is extracted. As the 12 beams exit the power amplifier, they are compressed into an annulus of 1-m² area and an outer diameter of nearly 1.5 m.

PARASITIC OSCILLATION SUPPRESSION

In a high-gain cavity, as exists in the Antares system the suppression of parasitic oscillations is of critica importance. Nonreflecting, optically black surfaces (a 10 μm) are required. During the early stages of testing, a of the exposed surfaces within 5 cm of the beams wer coated with a paint loaded with LiF. Even though th paint had a very low reflectivity, oscillations were er countered when the amplifier was pumped at a single pass gain greater than about 2.7. A great number c possible parasitic modes were identified, some of whic were characteristic to the Antares mechanical desigr One of these was a ring laser mode in which a ray fror the amplifier collimating mirror could strike an off-axi surface after passing through the four gain region:

ANTARES POWER AMPLIFIER OPTICAL SCHEMATIC

1	VACUUM INPUT WINDOW
2	TURNING MIRROR
3	POLYHEDRON MIRROR
4	TURNING MIRROR
5	TROMBONE MIRRORS
6	FOCUS MIRROR
7	SPATIAL FILTER
8	INPUT WINDOW
9-12	RELAY MIRRORS
13	ABSORBER WINDOW
14	BACK REFLECTOR
15	OUTPUT WINDOW
16-17	PERISCOPE MIRRORS
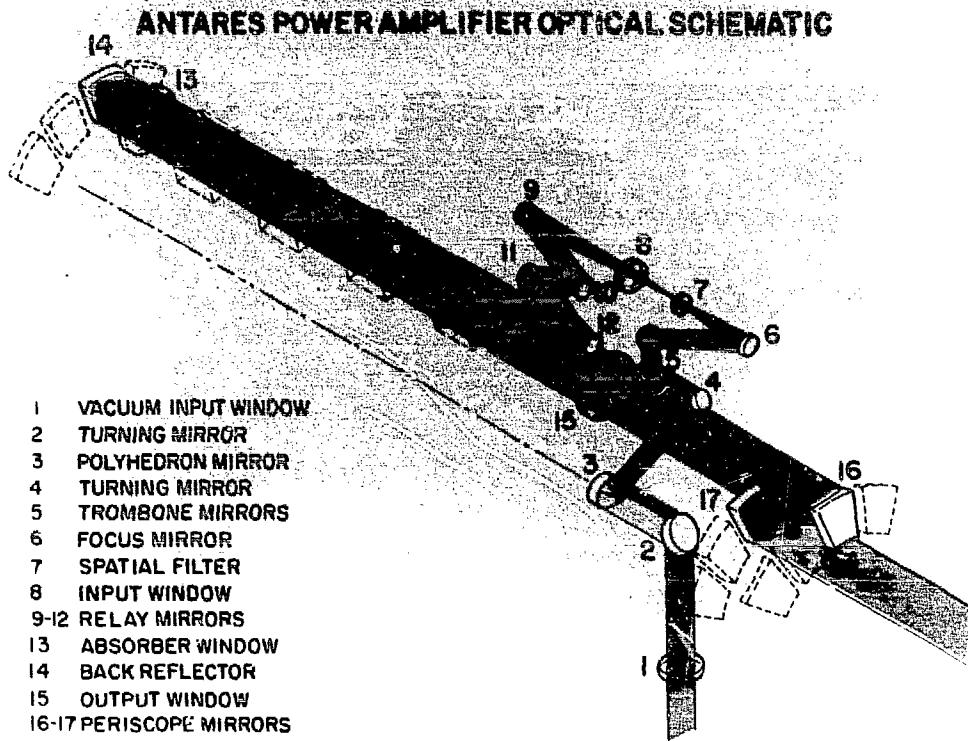
Fig. 13. One sector of the power amplifier optical train. The cross-sectional area of the optical beam increases in proportion to the energy so that the energy density remains below the damage threshold for optical materials.

undergo a Fresnel reflection off the output window, and return to the collimating mirror through the four gain regions. It was necessary to design a set of baffles coated with plasma-sprayed LiF. After installation of these baffles, the stability threshold of the entire system rose to a net gain of 6.0. The addition of saturable absorber to raise the stability limit to a net gain of 8.0 provides a very small loss in net amplifier output. As a result of the use of plasma-sprayed LiF baffles, the Antares laser is one of the, if not the most, stable high-power lasers ever built.

TARGET SYSTEM

The target system contains both the target vacuum system and the target optical system.

Target Vacuum System

The beams from both of the power amplifiers travel through a vacuum from the output of the power amplifier to the target. The system (Fig. 14) is made of stainless steel, enclosing a volume of about 1000 m³, which can be maintained at a pressure of 2×10^{-5} torr. The pumping time to reach this pressure, about 8 h, is limited by the possibility of damaging target diagnostic equipment. The power amplifiers are connected to the target chamber by 1.5-m-diam beam tubes. The target chamber is an 8-m-diam cylinder closed on both ends with spherical caps to produce a 7-m-long volume. The vacuum is maintained with cryogenic pumps. Two pumps are mounted on the target chamber and two pumps are mounted on each of the beam tubes. Targets are inserted into the target

Fig. 14. The target vacuum system includes the beam tubes and the target chamber. Only one of the beam tubes leading from the power amplifiers is visible in this photograph. The target vacuum system encloses a volume of about 1000 m³.

chamber through an air lock and transported on an inclined track to their central position. Final positioning of a target is performed by the use of two large reference telescopes with a resolution of 10 μm.

Target Optical System

The 12 beams are compressed into an annulus with a 1.5-m major diameter as they enter the target vacuum system. The individual beams are set to be slightly convergent as they leave the power amplifier. The beams would be brought to a focus at a point about 800 ft from the power amplifier if there were no further focusing. At the turn chambers, the beams are grouped into three clusters of four beams by directing them toward the fold mirrors in the target chamber. The positioning of the fold mirrors in the target chamber can be seen in Fig. 15. The three sets of fold mirrors direct the beams outward toward the 24 focusing mirrors. The focusing mirrors are diamond-machined, off-axis parabolas that operate at an f-number of 6.3. The net result is that a target is illuminated on six sides by six beam clusters of four beams each.

A pointing accuracy of 25 μm is required at the target position for each of the 24 beams. At the request of an experimenter, the beams may be independently directed to any point within a 1-cm volume. The focal spot size is diffraction limited by the polyhedron mirror to 200 μm.

ALIGNMENT SYSTEM

Seismic and thermally induced movement generated by the impulse loading in the gas required an alignment system to bring the 24 beams to the proper pointing and centering on the optical beam paths. The optical alignment system was chosen after experimental consideration of several approaches. The present "see-through" system was fully prototyped with actual hardware and computer controls before the decision was made to implement it. The alignment system is designed to automatically align 168 optical elements.

Alignment of the optical system is carried out in two stages. First, the system is aligned with visible light. Second, the fold and focus mirrors are adjusted with a cw CO_2 laser.

The visible alignment system relies on a video tracking system to identify light sources. The error signal from the tracker that characterizes the difference between the measured and the expected positions of the light sources is fed into a computer-controlled feedback loop that generates the signals to control the stepper motors on the appropriate mirrors. A typical feedback loop is shown in Fig. 16. The light sources are fiber-optic elements, which in some cases are imbedded in mirrors and in other cases are placed into position by movable arms. Secondary alignment is achieved by projecting a CO_2 laser beam through the entire optical train and sensing its position at the target. This correction eliminates dispersion errors between visible and CO_2 wavelengths that arise chiefly from the wedged exit salt windows. The system has demonstrated alignment accuracies at the target of about 40 μm.

BEAM DIAGNOSTICS

The large apertures and high energy densities of the optical pulse required that new approaches be taken in diagnosing the quality of the Antares optical beams. New calorimetric techniques were developed to meet these needs. The energy transmitted at several points in the system is measured to provide an indication of the operation of the system on each shot. The following data are measured on each shot:

- total energy exiting the front end in each beam line,
- total energy entering the input salt window of the power amplifier,
- total energy entering each sector of the power amplifier,
- total energy entering the target system on each beam line, and
- wave shape of the total pulse entering the target system from each beam line.

Since the measurements of amplifier energy must be made on a noninterference basis, a means had to be devised to sample a fraction of the beam energy. The measurement of the output of the power amplifiers presented a particular problem in that the space required to sample all of the sectors would have been prohibitive. To overcome this difficulty, the decision was made to sample the integrated output of the entire amplifier. This was accomplished by designing the output salt windows with a wedge angle between the surfaces and arranging the positions of the windows so that the second Fresnel reflection from each window produced a beam that was directed toward the center of the beam tube. The configuration is shown in Fig. 17. By proper choice of the wedge angle of the windows, the 12 sector beams were
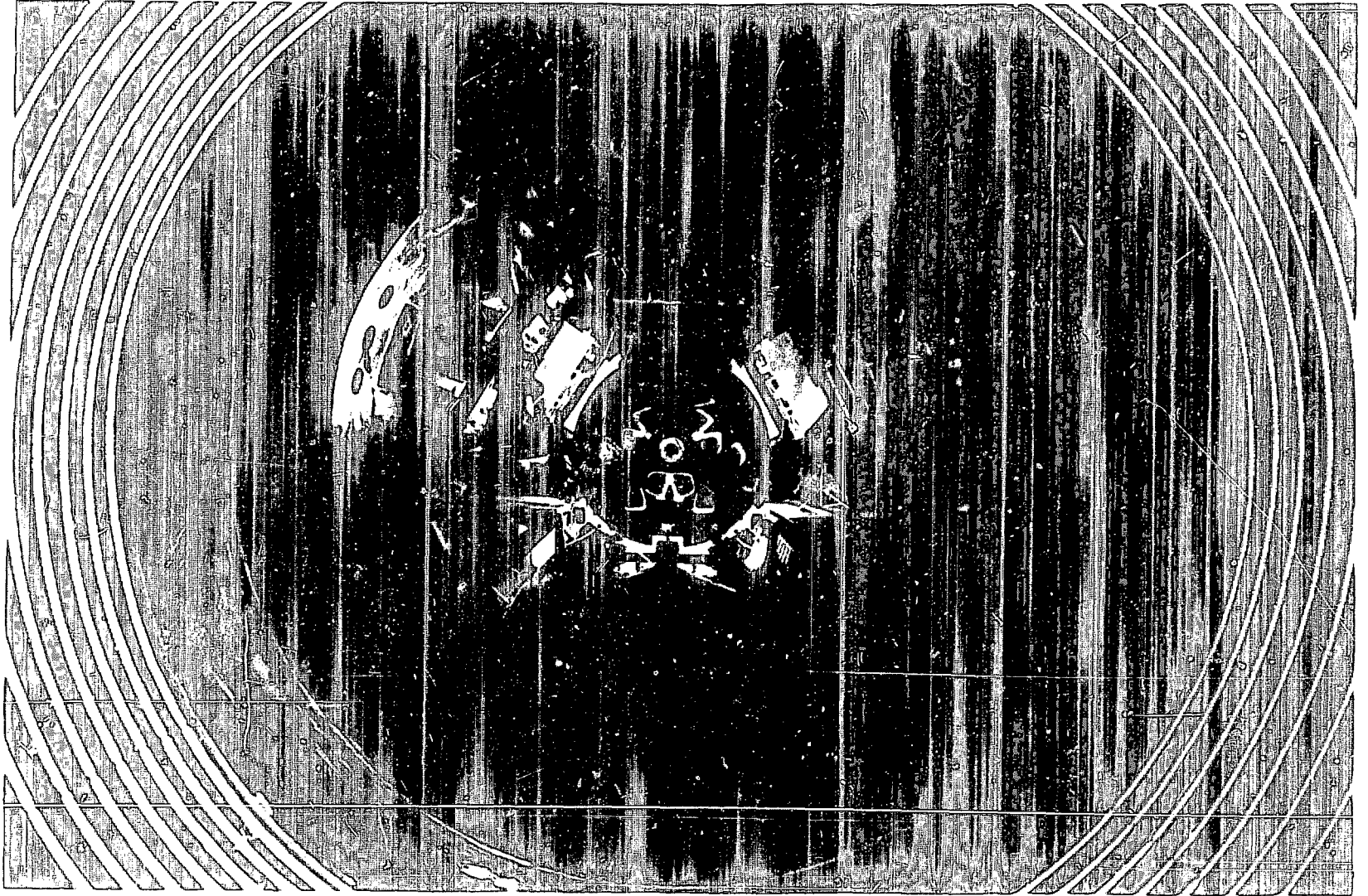
Fig. 15. This is a view of the target chamber as seen from the turn chamber. The grouping of the beams into three groups of four beams can be seen in the antiparasatic baffle at the center of the photograph. The targets are mounted within the structure at the center of the scene.
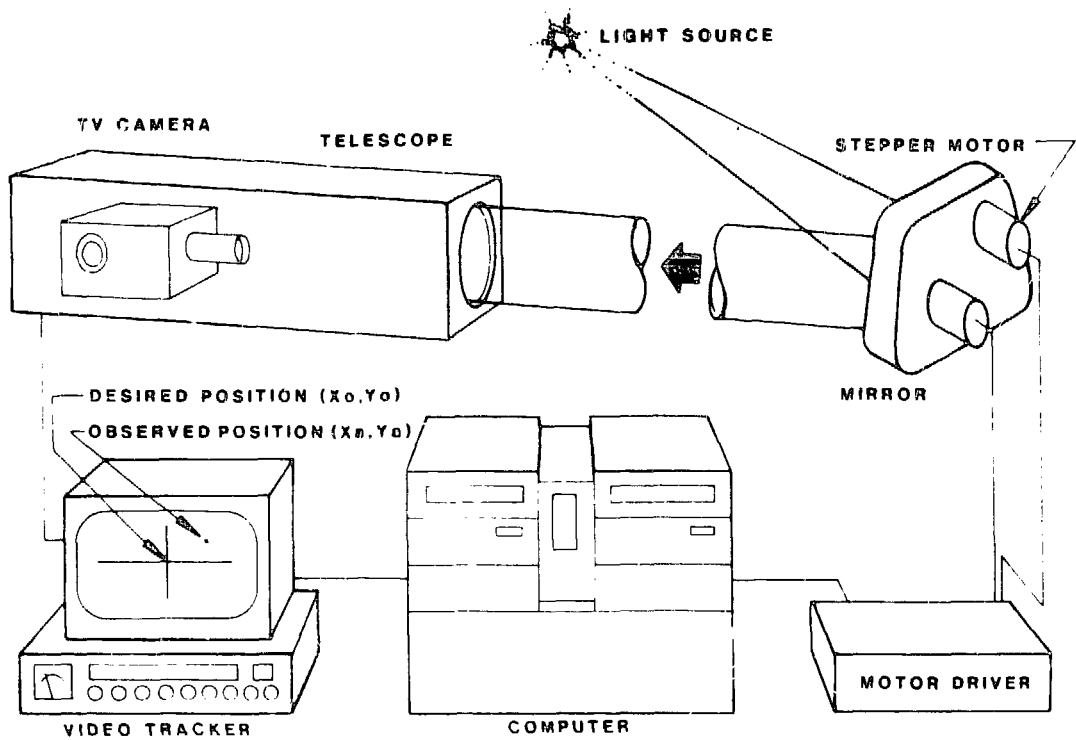
Fig. 16. Alignment of the optical train is carried out in several stages by a computer-controlled feedback loop. Visible light sources at critical locations are centered in the field of view of a TV camera by feeding the alignment error to a computer that in turn drives the stepper motors on a mirror in the correct direction to minimize the alignment error.
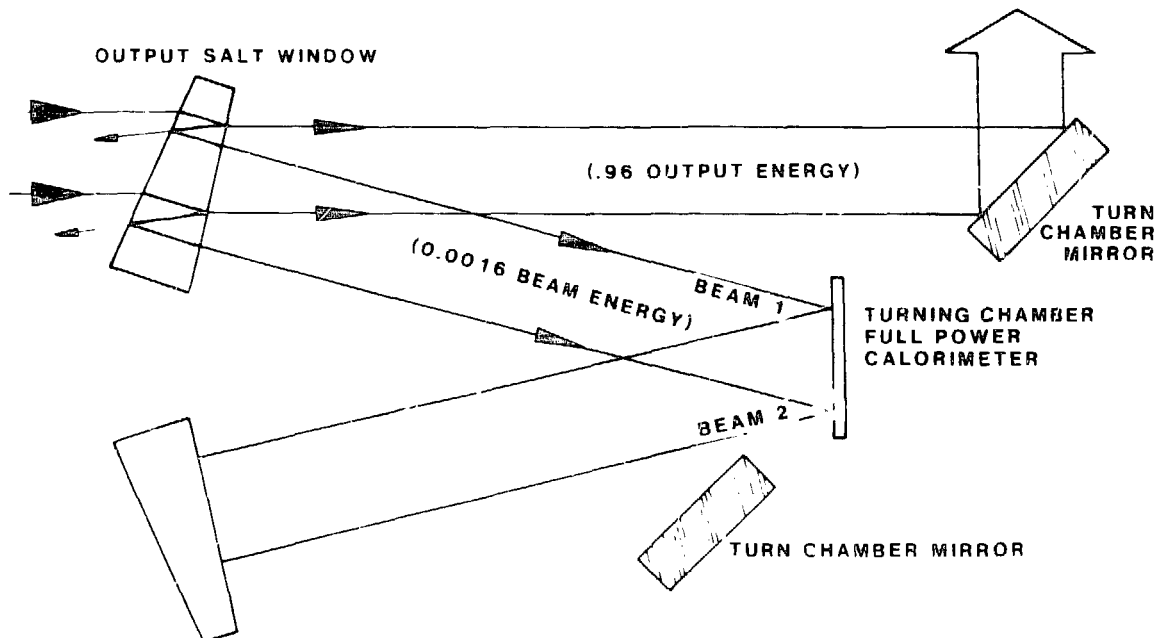
Fig. 17. The full output energy of the Antares power amplifiers is measured by sampling the Fresnel losses that occur at the output salt windows. About 4% of the incident light is reflected at each window surface. The output salt windows are fabricated and mounted so that the doubly reflected beams from all 12 sectors overlap on a calorimeter located at the turn chamber.

made to intersect at a point near the turn chambers. Since only about 4% of the incident beam energy is reflected at each surface, the energy in each sector beam was attenuated by a factor of about 0.0016 when it arrived at the turn chamber. This attenuation kept the total energy (12 sectors) arriving at each calorimeter below the damage threshold of the material used for the calorimeter.

A new type of calorimeter was developed to measure the wide aperture beams found in Antares. These calorimeters use a Kapton/copper laminate as the absorber material. Kapton is an excellent absorber at 10.6 μm and has a relatively high laser damage threshold. The temperature rise of the copper backing is directly related to the energy incident on the calorimeter to the degree that the calorimeters may be treated as a tertiary standard. Calorimeters of this design were inserted into each sector of the alignment system to characterize the output of the alignment system and to calibrate the operating calorimeters located at the turn chambers.

SYSTEM CONTROL AND DIAGNOSTICS

During the initial design of Antares, it was recognized that manual operation of the system would be extremely difficult because of the size and complexity of the system. We considered the experience of the preceding laser systems in the control requirements for Antares. The decision was made to tie all of the functions—charge and fire, alignment, diagnostics, and so forth—into a common integrated control network. Because of the complexity of the system, the decision was also reached to have no hard-wired logic within the system but to base all of the system operation on software. The control system is based on a network (Fig. 18) of distributed computers. The integrated control computer, a PDP 11/60, controls the timing and firing of the system. Data archival is carried out by a PDP 11/70. Operation of each of the main pulsed-power systems and of the optical alignment and beam diagnostics are carried out by three PDP 11/60 minicomputers. The minicomputers download software and operating parameters to LSI-11 microcomputers located throughout the system. Communication between the LSI-11 microcomputers is handled by the minicomputers.

The data are digitized and transmitted over fiber-optic cables throughout the computer network (a total of 40 km of fibers). All operation data are archived and are on screens and available for future use. There are no traditional control panels. The interface between the oper-

ator and the machine is established by means of touch-sensitive display screens. The displays are created and can be changed through software programming.

SYSTEM STATUS

All of the subsystems in Antares were essentially complete in October 1983. At that time energy had been delivered from both amplifiers into the target vacuum system at the 15-kJ-level. The quality of the beams produced by the power amplifiers can be judged by the burn pattern (Fig. 19) that was obtained at the turn chamber of beamline-2. When diffraction at the edges of the beams is taken into account, it can be seen that the output energy density is very uniform. The spatial coherence of the output can be judged by the Fresnel bright spot occurring in the shadow of the mirror that injects the beam into the power amplifier (the notch in the outer edge of each individual burn pattern). By the end of December 1983, targets had been shot with all 24 beams. The present record energy delivered to target is 27.5 kJ in a 1-ns pulse.

In the 12 months following the commencement of the target-shooting program, the operation of the Antares system has continued to improve. The system passed through a period of 6-8 months that can be classed as adolescence, during which problems with the system were found and corrected and the confidence in the system was gained. The Antares laser has now become an adult, operational system. The present system capabilities are broad. The overall range of the capabilities of the system include the following:

- Delivery of 30-35 kJ to target in a 1-ns pulse
- Variable pulse length from 1-10 ns
- Independent alignment of the individual beams to 24 positions within a 1-cm^3 volume
- Alignment precision to 40 μm
- Variable delay of pulse arrival at target
  ±1.5 ns within one power amplifier
  ±100 ns between power amplifiers

The times to align the system are dependent on the alignment precision required by the experimenter. If the required tolerance is greater than 200 μm, then the system has been shot at 25-minute intervals. When the best possible alignment has been required, then two 24-beam shots and/or three 12-beam shots have been recorded in a single day. The key machine parameters are listed in Table 2, where a comparison is made between the design parameters and the achieved operating results.
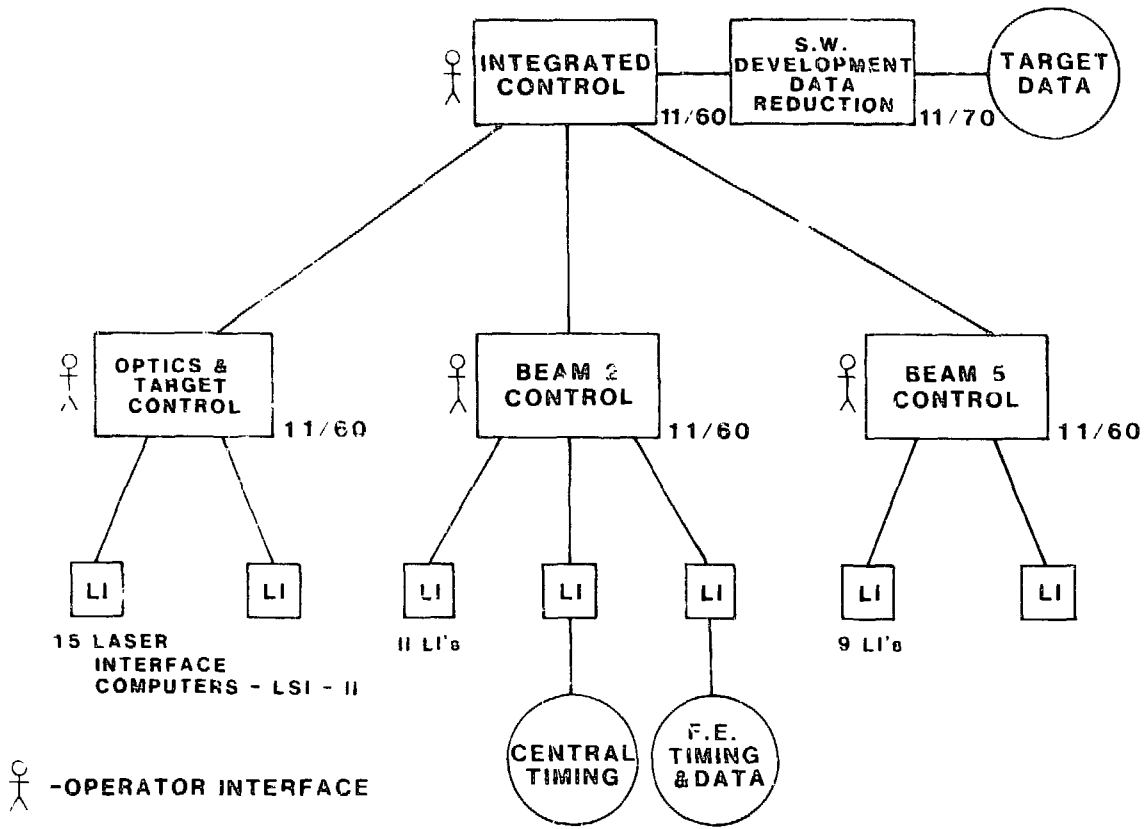
Fig. 18. In the Antares Integrated Control Network, over 40 computers are linked together to control the entire laser system.
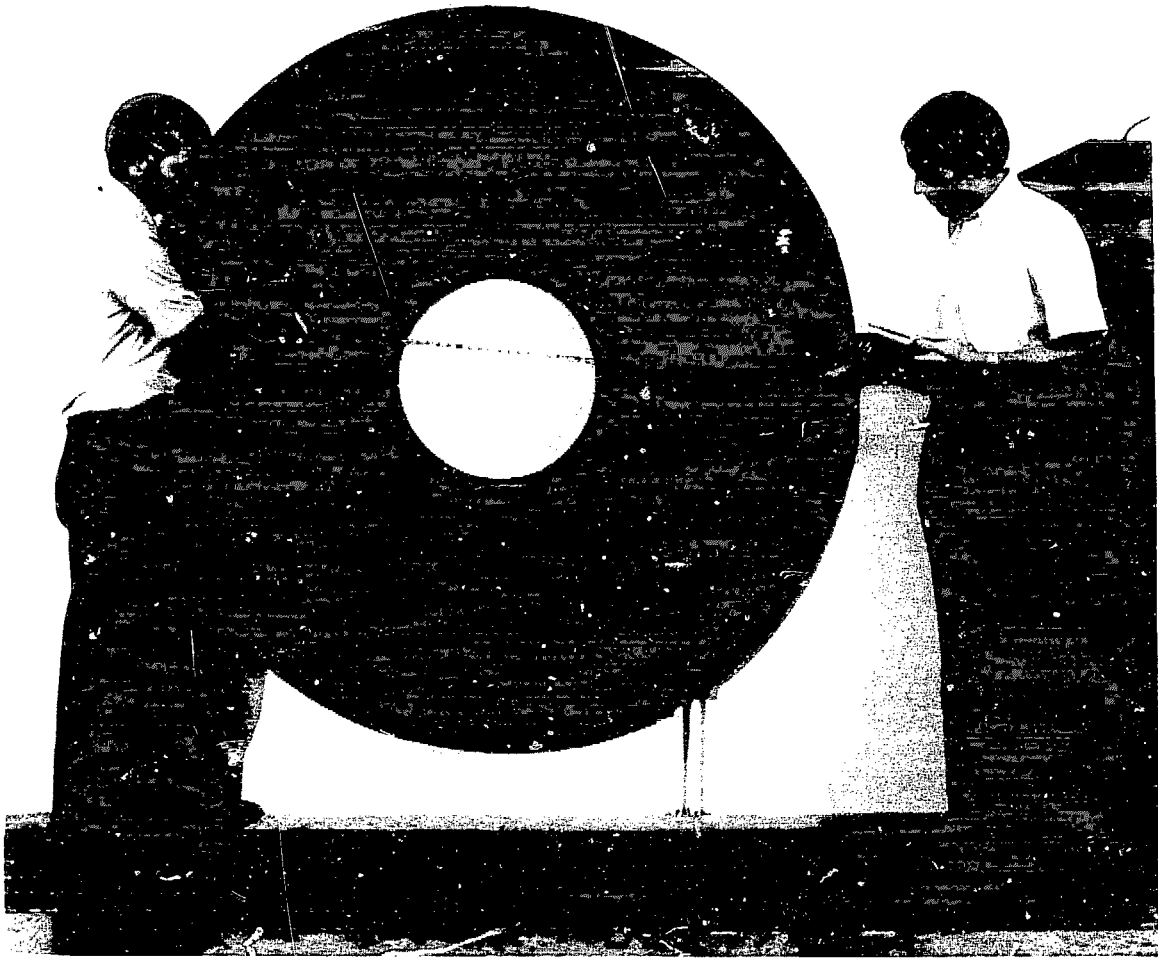
Fig. 19. The laser output from one power amplifier was recorded by burning this pattern into a sheet of photographic paper. The total energy required to produce this burn pattern was about 8 kJ and was delivered in a single 1-ns pulse. The uniformity of the laser output can be judged from the uniformity of the burn pattern.

TABLE II. Key Machine Parameters

Parameter	Design	Operational
e-Gun voltage	525 kV	510 kV
e-Gun current	25 kA	20 kA
e-Gun current density	50 mA/cm^2	40 mA/cm^2
Anode voltage	550 kV	475 kV
Anode current	220 kA	190 kA
Discharge current density	7.0 A/cm^2	6.0 A/cm^2
Average electric field	18.0 kV/cm	15.5 kV/cm
Pressure	1800 torr	1700 torr
E/p	10.0 V/cm·torr	9.1 V/cm·torr
Average gain length	8	7.5
Average output fluence	1.7 J/cm^2	1.3 J/cm^2
Energy	20 kJ	15 kJ

A vigorous target-shooting program is now under way. A fueled target such as the one shown in Fig. 20 has been shot in order to demonstrate the production of neutrons and to verify the operation of the various target diagnostic systems. Figure 21 is an open-shutter photograph of a shot where about 20 kJ of energy was directed onto a target.

During the testing of the Antares subsystems and their integration, most design goals have been attained. Not enough experience has been obtained to verify advertised or mean times between failures of the equipment. Some redesign was necessary, particularly to attain the voltage hold-off of the electron gun and to eliminate gain-limiting parasitic oscillations in the power amplifier. Based on limited gain and energy measurements in the driver and power amplifiers, we now believe that Antares will attain its final goal, delivery of 35- to 40-TW pulses to inertial fusion targets.

Fig. 20. A 200-μm-diam glass microballoon like the ones that would be filled with a mixture of deuterium and tritium for an energy extraction experiment. This particular microballoon (unfilled) was shot with only one beamlet and only about 1 J from the front end to demonstrate the size of a beamlet focused on the target. The hole drilled by that shot can be seen on the right side of the microballoon.
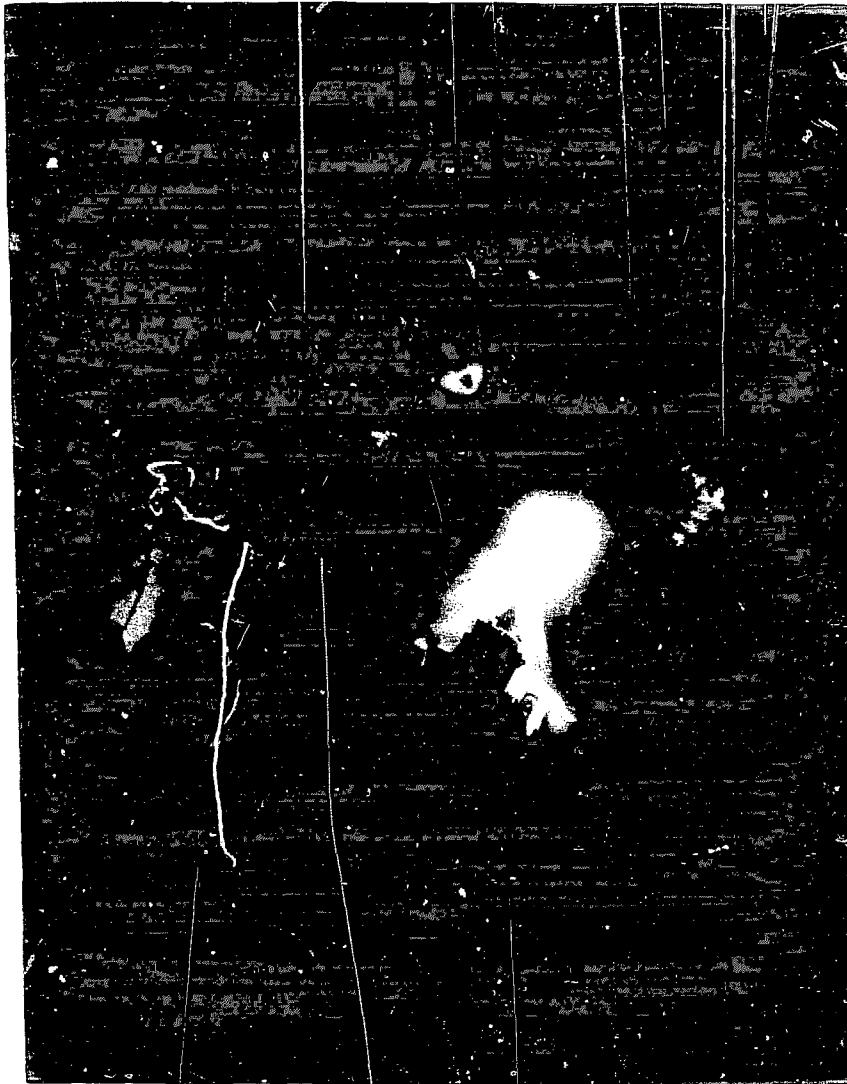
Fig. 21. Flash of light from a target shot with about 20 kJ of energy from Antares. The target insertion mechanism (on the left) covered with a plasma sheath. The plasma sheath results from the interaction of the plasma and light from the target with the surface of the target insertion mechanism. The object at the upper right is an x-ray pinhole camera. The circular pattern on the lower right is the specular reflection off of the tool marks on the mounting plate located below the target.

Target Fabrication for Inertial Confinement Fusion Research

by Richard Mah, David V. Duchane, and
Ainslie T. Young

INTRODUCTION

Fusion targets, whe re; for the laser program or the particle beam program, are not difficult to picture because they are simply a series of concentric spherical shells. Yet realization of this simple design poses extraordinary difficulties. The targets are small, less than a millimeter in diameter overall. Each shell must possess specific properties ranging from strength at low densities to high atomic number and density for improved compression. The tolerances are exacting—10 times more so than those common in the aerospace industry. No wonder we sometimes feel that the target designers are asking us to fabricate the impossible from some imaginary material! Every effort must be expended to meet the designers' demands, however, for their theories and computer codes can be verified only by experiments with real targets.

We have had considerable success in target fabrication, developing new technologies, new materials, and new tools. We will outline some of these developments and then briefly indicate the value of our efforts to other areas of technology.

FUSION TARGETS

Figure 1 shows the components of a typical fusion target. An overall view of much of our programmatic research and development can be gained by considering the fabrication of each component, beginning with the innermost.

Tamper

The spherical shell known as the tamper transmits implosive force to the deuterium-tritium fuel, thereby compressing it to the density at which fusion occurs. Like all the other shells, the tamper must be extremely spherical, uniform in thickness, and smooth. (These requirements follow from the goals of symmetric implosion and clean burn.) Impermeability to the gaseous fuel, strength, and resistance to embrittlement by the fuel are primary considerations in selecting a tamper material. Commonly used materials include glass and metals ranging from beryllium to gold. We focus here on metal tampers since glass tampers are available simply by selection from commercially available hollow glass spheres.

We fabricate metal tampers by electroforming, which involves electrochemical deposition, electroplating, or autocatalysis of the desired metal on a sacrificial spherical substrate. Electroplating, which is applicable to conducting substrates of metal or metallized glass, is a well-developed technique made unusual in this application by the exacting tolerances on thickness uniformity, by the requirements on both physical and mechanical properties, and by the necessarily small size of the substrates. Figure 2 shows an apparatus we have developed for electroplating spherical substrates smaller than 500 μm in diameter. Constant, random motion of the spheres between two cathodes assures that all surfaces are uniformly plated.

Conducting substrates larger than 500 μm in diameter are electroplated in a track-plating apparatus. Uniform plating is achieved in this apparatus by the random rolling of the spherical substrates, each within a restricted area, over the surface of a flat cathode (the track). An advantage of track plating is that the plated material is mechanically worked during plating (by contact of the spheres with the track) and thus has superior mechanical strength and fine grain structure.
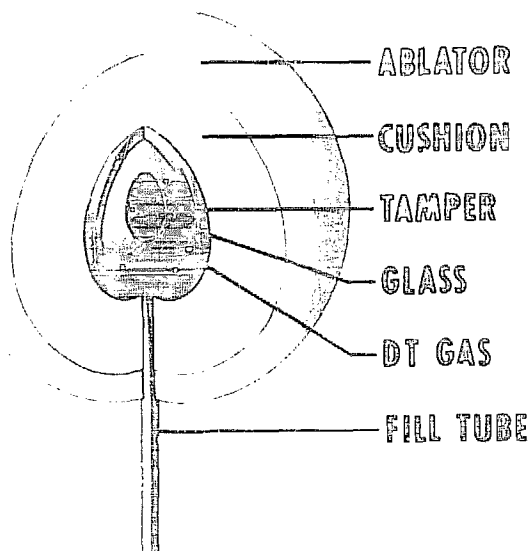
Fig. 1. Schematic of a typical fusion target. Each component plays a specific role in conversion of energy from the driver to the implosive energy necessary for fusion of the fuel.

Tampers can be deposited on nonconducting substrates by autocatalysis, or "electroless" plating. In this process the substrate catalyzes reduction of the metal from a metastable solution. Although finding a substrate material with appropriate catalytic action is difficult, the process produces tampers of very uniform thickness and with very smooth surfaces (Fig. 3). Electroless plating of substrates smaller than 500 µm in diameter is performed in an apparatus in which the spheres are kept in constant, random motion in a reaction chamber by alternating the flow direction of the metastable solution.[1,2]

Some recent target designs call for tampers of metals, such as beryllium and aluminum, that cannot be deposited from aqueous solution. We are, therefore, investigating electrodeposition from organic solvents and possibly molten salts. The major obstacle in this research is the hazardous nature of such deposition media. In the meantime, other processes called physical vapor deposition (PVD) and chemical vapor deposition (CVD) are used to provide tampers from a number of materials not currently obtainable by electrochemical processes.

The term PVD includes electron-beam evaporation, sputtering, and ion plating. To achieve uniform deposition on spherical targets with these line-of-sight processes, we have designed double-axis rotators that orient all areas of the sphere equally (on the average)

toward the vapor source.[3] We are also investigating the possibility of levitating smaller targets during coating by use of a vibrating "bouncer pan" or with a molecular beam (Fig. 4).[4] Nevertheless, the PVD process is hampered by its low deposition rate (<0.001 in./h) and the limitation of being able to process only 1-12 targets at a time.

In the CVD process, a gaseous compound of the material for the target (WF_6, for example) undergoes chemical reduction or thermal decomposition on the surface of the target substrate. The desired metals are deposited on small targets in a bed of substrates fluidized by the reactive gas. This produces a fluidized bed, a churning mass of particles that is formed by directing a flow of gas upward through a volume of particles of appropriate size and density. The continuous, random motion of the fluidized substrates ensures that all surfaces are exposed (on average) to the same temperature and gas flux, and very uniform coatings are deposited even on substrates with complex geometry. In addition, the collisions among the substrates provide a peening action that helps to break up growth patterns in the deposit that would normally produce large, columnar grains. As a result, the coating usually consists of fine, equiaxed grains and is thus strong and smooth.[5]

73
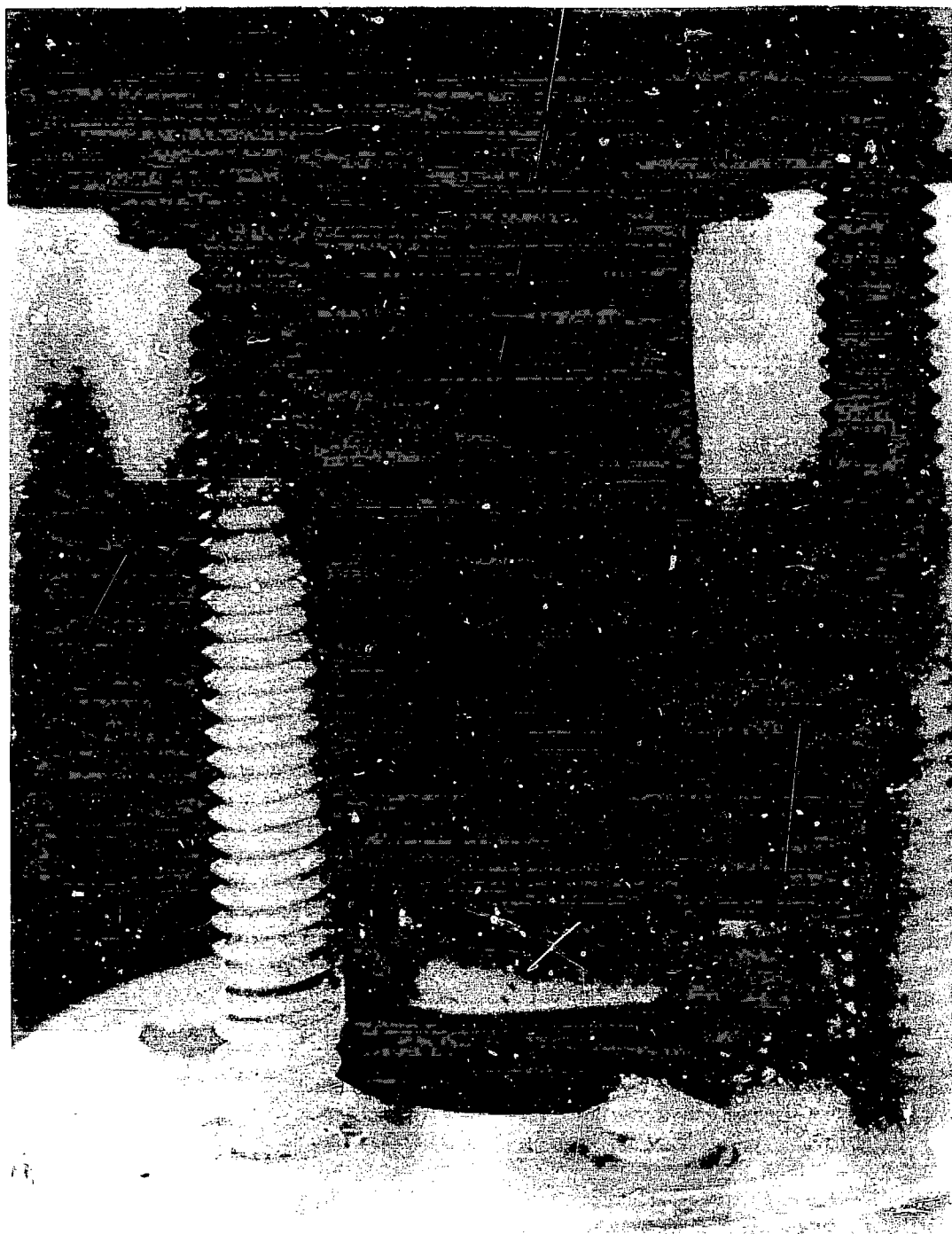
Fig. 2. An apparatus for electroplating small (less than ~500 μm in diameter) conducting spheres. The spheres are forced against one and then the other of two cathodes of fine-mesh screen by alternating the flow direction of the electroplating solution. The constant, random motion of the spheres assures uniform deposition of the plated material. The large polyethylene balls prevent agglomeration of the small spheres.

Photomicrographs of 14-µm-thick nickel tampers
ed by autocatalysis (electroless plating) on a
al glass substrate. The intact sphere (a) and the
ed sphere (b) show, respectively, the great smooth-
ed the thickness uniformity that can be obtained
is electrochemical process.

Fig. 4. Magnifying video display for monitoring physical
vapor deposition on spherical substrates levitated by flow of
gas through an array of fine capillary tubes. Shown on the
screen (along with its shadow) is a levitated hollow glass
sphere, which is 300 µm in diameter.

75
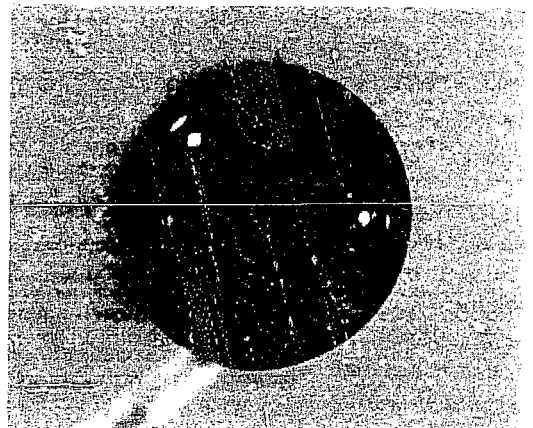
Cushion

The cushion provides a stand-off distance between the tamper and the ablator. This cushion, ideally a "structural void," originally consisted of full-density low-Z polymeric materials, but more recently has been made of rigid plastic foam. When the cushion layer consisted of a full-density polymer, two techniques were used. The first technique involved micro- and ultraprecision machining to produce hemishells that were later assembled around the tampers. This technique will be described in more detail in connection with fabrication of ablators. The second technique (described here) involved two methods for direct deposition of a polymer from the gas phase: the low-pressure plasma (LPP) process and the vapor-phase pyrolysis (VPP) process.

In the LPP process, a radiofrequency voltage between two electrodes produces a low-pressure plasma of the monomeric material, which then polymerizes on the tamper surface. Small tampers (less than 500 μm in diameter) are levitated above vibrating shaped electrodes during the coating process. Pulsing in the monomeric vapor and maintainance of the electrode temperature below ~10°C forms very smooth layers with thicknesses between 1 and ~60 μm from such monomers as p-xylylene and cycloacetetraene (Fig. 5).[6]

In the VPP process, p-xylylene is pyrolytically degraded to the reactive diradical species, which then polymerizes over the surface of the object to be coated. We have adapted this well-known process to deposit uniformly thick, smooth layers on stalk-mounted or levitated tampers. The uniformity in thickness of a 600-μm-thick cushion layer prepared by the VPP process varies by less than 3%, and its smoothness is marred only by a few micrometer-sized "bumps." Greater surface smoothness of thinner layers can easily be obtained by increasing the turbulence of the reactive gas. We have, for example, prepared defect-free coatings up to 70 μm thick with surface irregularities of less than 0.1 μm from peak to valley.[6]

Both the surface smoothness and thickness uniformity of these deposited cushion layers can be greatly enhanced by lapping techniques originally developed for metals and since refined for polymers. These techniques will be discussed below in connection with the fabrication of ablators.

More recently, better hydrodynamic performance has been achieved by using plastic foams. These must have very low density (0.05 g/cm^3 or less) and small cell size (less than 5.0 μm in diameter). They must be free of impurities and amenable to fabrication to precise tolerances. Such foams were unknown before their development at Los Alamos.

We make foams of this type by cooling a homogeneous polymer solution in such a manner as to induce an inverse phase separation (that is, of solvent from solution) at the temperature at which the polymer and solvent become immiscible (the spinodal point). The polymer forms a foam matrix, and the solvent forms discrete, uniform droplets in this matrix. Removal of the solvent droplets from the matrix generally results in a porous, open-cell plastic foam in which the voids are replicas of the solvent droplets. The foam is rigid when made with polymers that are inherently inflexible. The density of the foam is determined by the concentration of the polymer solution.

We have prepared small-cell, low-density, rigid foams from such polymers as polystyrene, poly(4-methyl-1-penetene), tradenamed TPX, and substituted celluloses and starches. Hemishells of these foams can be made by inducing the inverse phase separation in an appropriate mold. In some cases, micromachining can be used to improve the dimensional properties of the foam material. Foams made from TPX have a very uniform structure, but the low compression strength of such foams (about 10 lb/in.^{2}) makes them difficult to machine to exact tolerances by normal techniques. To eliminate this difficulty, we have developed a polymer-solvent system in which the solvent droplets are solid at room temperature. The solid solvent reinforces the delicate cell walls and thus protects them from damage during machining. The solvent is then extracted with alcohol.[7]

Ablator

The energy of the radiation from the driver is deposited in the shell known as the ablator (see Fig. 1). The absorbed energy causes material to be ejected outward from the ablator, producing a "rocket" effect that transfers inward momentum to the tamper, which results in compression of the fuel. Ablators are fabricated from various materials primarily by machining.

The small sizes and close dimensional tolerances typical of fusion targets dictate that ablators be machined with ultraprecision tools. With such tools and single-crystal diamond tool bits we can, for example, produce surfaces with a peak-to-valley roughness of 0.05 μm.

An important aspect of precision turning is the constancy of rotational speed and accurate rotational motion
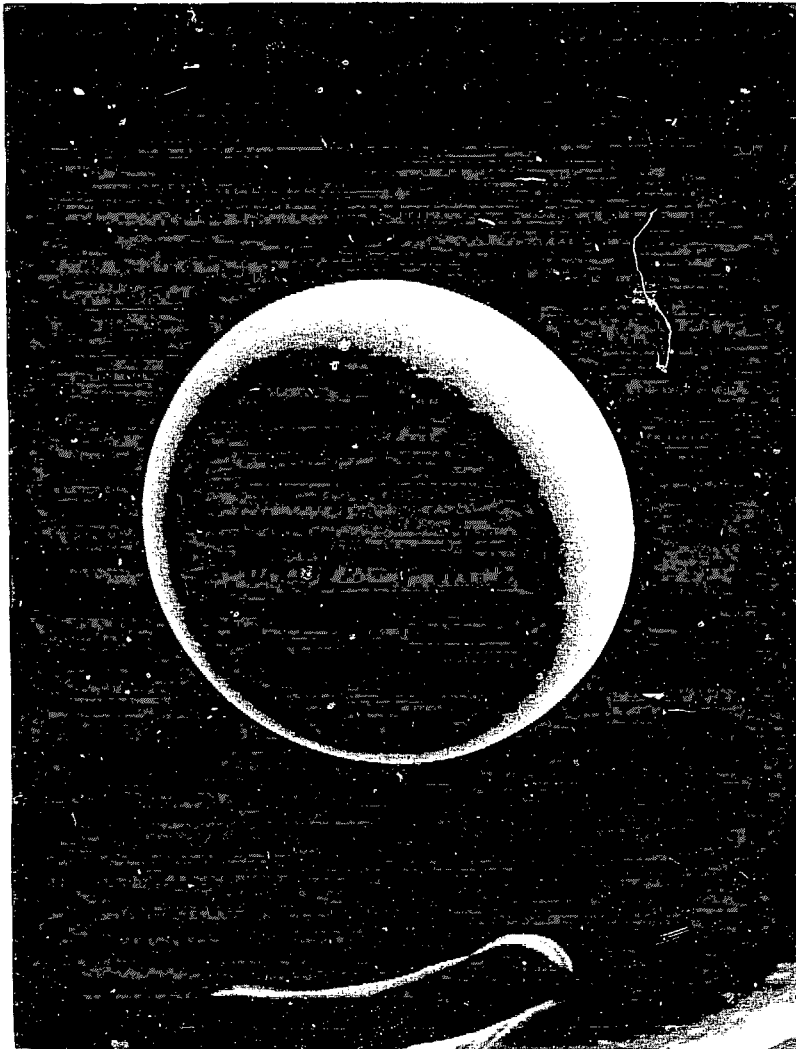
Fig. 5. Scanning electron micrograph of a 300-μm-diam hollow glass sphere laser fusion target coated by the low-pressure plasma process with a 5-μm-thick layer of parylene. Note the surface smoothness of the coating.

provided by air-bearing spindles. We have available two small lathes with air-bearing spindles and vibration-isolating magnetically coupled drive motors. We also have a larger ultraprecision lathe (Fig. 6), built to Los Alamos specifications by Pneumo Precision, Inc., that combines the features of air-bearing spindles and slideways with those of computer control. This lathe is used for metal optics and other high-precision fabrication at Los Alamos. To increase our machining capability we are now preparing specifications for another lathe with a programmable rotary axis and the same accuracy as that of the Pneumo lathe.

Although the surface finishes produced by ultra-precision turning are excellent, they can be further improved (except on many face-centered-cubic materials) by lapping, or polishing with fine abrasive particles. By using submicrometer-sized grit and air balancing to check the progress of the lapping, we can obtain surfaces that are smoothed to about 0.003 μm peak to valley. These are the smoothest surfaces attainable with a mechanical technique. Shapes other than spheres or hemispheres can be lapped with special equipment.[8]

Fig. 6. Ultraprecision lathe built to Los Alamos specifications by Pneumo Precision, Inc. The position feedback system of this machine, which is based on laser interferometry, has a resolution of 0.025 μm. Its low-friction air-hearing slideways allow precise contouring, and any surface of revolution can be generated by simp'. programming. The slideways are mounted on a massive granite block, which in turn is supported on three air-bag vibration isolators. With this lathe we use single-crystal diamond tool bits for machining most plastics and some nonferrous metals. We use cubic boron nitride and conventional carbide tool bits for machining materials (such as beryllium) that are incompatible with diamond tool bits.

OTHER APPLICATIONS

It is not surprising that our efforts on the multifaceted task of target fabrication have led to materials and technologies of interest and benefit to other research and development programs. We mention briefly a few of these other applications to indicate the variety of problems in which materials science plays a fundamental role.

⊚ The polymeric foams developed for the cushion layer may benefit biomedical research. Porosity is considered essential in synthetic veins and arteries to provide anchoring points for biological species that inhibit the natural tendency of the body to build up a thick layer of scar tissue around foreign objects. The synthetic vascular prostheses currently in use, primarily woven Dacron and Teflon structures, have pores that vary widely in size. In contrast, the cells of the foam produced by the inverse phase separation process are remarkably uniform and can be made in the range of 25 μm in diameter, the size believed to be most desirable for biological uses.[9]

⊚ A process called chemical infusion, which was developed for smoothing polymeric surfaces, may also benefit biomedical research. Experiments on laboratory animals have indicated that silicone rubber veins infused by this process with stearate ions may be rejected less often than are untreated artificial veins.[10]

⊚ Miniature coaxial cables fabricated in support of inertial confinement fusion experiments may simplify surgical removal of brain tumors. High-frequency electrical signals transmitted through such a

cable, which is less than 0.1 mm in diameter, may enable the destruction of cancerous cells without damage to surrounding tissue.[11,12]

● Laser welding, the method used to braze fill tubes onto tampers, may greatly simplify fabrication of radioactive components. Components of plutonium, for example, must be welded in a glove box, and with conventional techniques this condition necessitates contamination of expensive welding equipment. In contrast, a laser welding beam could be directed onto the component through special glove-box windows and could even be transported throughout a facility along optical fibers.

● Tools like those developed for uniformly coating target components by physical vapor deposition are now routinely used for coating rare-earth radiochemical tracers on experimental nuclear weapon components.

● High-strength single-crystal whiskers, which were fabricated and studied for possible use as support structures in laser fusion targets, are now the key component in the Los Alamos structural ceramics program. These whiskers of silicon carbide or silicon nitride have tensile strengths approaching 4 000 000 psi. Composites of such whiskers and ceramic materials have very high tensile strengths and high resistance to fracture.

Clearly, target fabrication and the associated research and development encompass many diverse endeavors. Formerly, these were pursued at several scattered Laboratory sites. But since the fall of 1983, most of our activities have been gathered in a single, specially designed building, the Target Fabrication Facility. This facility includes clean rooms for target assembly, a laboratory in which the targets are filled with the deuterium-tritium fuel, a machine shop, and laboratories for electroplating and physical and chemical vapor deposition, for developing and producing polymer foams, for laser welding and solid-state bonding, and for characterizing the various target components. Beyond the obvious advantages of space and equipment, the facility allows greater ease of communication among those involved in materials science, fabrication technology, and materials characterization.

REFERENCES

1. A. Mayer and W. Doty, "Advances in Plating Discrete Hollow Glass Microshells," Technical Digest Conference on Inertial Fusion, Optical Soc. of America, San Diego, California, 1980, p. 96.

2. A. Mayer and D. S. Catlett, "Plating Discrete Microparticles for Laser Fusion Targets," Plating and Surface Finishing, March 1978, p. 42-46.

3. G. A. Reeves, "Physical Vapor Deposition onto Small Spheres," Technical Digest Conference on Inertial Fusion, Optical Soc. of America, San Diego, California, 1980, p. 60.

4. S. F. Meyer, "Metallic Coating of Microspheres," J. Vac. Sci. Tech. 18 (3), 1198-1204 (1981).

5. D. W. Carroll and W. J. McCreary, "Fabrication of Thin-Wall, Freestanding Inertial Confinement Fusion Targets by Chemical Vapor Deposition," J. Vac. Sci. Tech. 20 (4), 1087-1090 (1982).

6. R. Liepins, M. Campbell, J. S. Clements, J. Hammond, and R. J. Fries, "Plastic Coating of Microsphere Substrates," J. Vac. Sci. Tech. 18 (3), 1218-1226 (1981).

7. A. T. Young, D. K. Moreno, and R. G. Marsters, "Preparation of Multishell ICF Target Plastic Foam Cushion Materials by Thermally Induced Phase Inversion Process," J. Vac. Sci. Tech. 20 (4), 1094-1097 (1982).

8. R. L. Rhorer, "Update on Precision Machining at Los Alamos," Proc. Soc. Photo-Optical Instrum. Eng., San Diego, California, Vol. 433, 1983, p. 107-111.

9. J. C. Stanley, W. E. Burkel, S. M. Lindenauer, R. H. Bartlett, and J. G. Turcotte, Eds., Biologic and Synthetic Vascular Prostheses (Grune and Stratton, New York, 1982).

10. D. V. Duchane, "Polymeric Mandrels — Supersmooth Surface by an Infusion Process," J. Vac. Sci. Tech. 18 (3), 1183-1186 (1981).

11. W. L. Bongianni, "Fabrication and Performance of Strip-Centered Microminiature Coaxial Cable," IEEE Proceedings, Vol. 22 (September 1984).

12. M. Kachmer, Ed., "Brain Tumors Succumb to New Microwave Probes," Microwave and RF, November 1983, p. 30-46.

Heavy-Ion Fusion

by Roger O. Bangerter

I t is widely believed that many proposed fusion devices would produce energy if they could be made large enough. Stars and thermonuclear weapons are two demonstrated examples that support this belief. In particular, because thermonuclear explosives are inertially confined, the scientific feasibility of inertial confinement fusion (ICF) has already been demonstrated at large scale. Sufficiently large magnetic fusion devices will almost certainly also produce net energy.

Large devices, however, might not make good environmental, engineering, or economic sense. Thus, for commercial applications of fusion, the important question is not whether fusion can produce energy—but rather,

Can a fusion energy system be built that makes good environmental, engineering, and economic sense?

Fusion scientists have always implicitly recognized that this question is the important one, but in recent years the question has been stated explicitly with increasing frequency and urgency.

For example, Lawrence Lidsky of MIT has been extremely critical of some proposed fusion devices because, in his opinion, they do not make good engineering sense. His article,[1] widely quoted in the media, has further focused attention on the importance of engineering and economics in fusion energy production.

ION BEAMS

Interest is increasing in what we call heavy-ion fusion because it is an approach that appears to offer significant advantages for a real fusion power—a plant that would make good environmental, engineering, and economic sense.

The idea of igniting inertial-fusion targets with intense ion beams is not new. Researchers realized in about 1975 that more than 50 years of engineering development had culminated in long-lived, efficient accelerators that could reliably produce ion pulses at high repetition rates (1 hertz and higher). Furthermore, the beams from these machines are now focused over large distances onto small targets. An example of such a machine is the LAMPF accelerator at Los Alamos (Fig. 1). Experiments now reenforce the theory that interaction between the ion beam and the target is devoid of many of the problems (such as low absorption and hot electrons) that have plagued laser fusion.

From an engineering standpoint, such accelerators appeared suitable to drive an inertial fusion power plant. Accelerators were not considered seriously earlier because all existing accelerators were low-power devices by inertial fusion standards. However, by 1976 many researchers concluded that the power problem was not fundamental.[2] In fact, it appeared that several types of accelerators, including radio-frequency linear accelerators (rf linacs), synchrotrons, induction linacs, and pulsed-power diodes might provide adequate power (greater than 10^{14} watts in short bursts of about 10 nanoseconds). The efficiency and pulse repetition rate of synchrotrons are low compared with the linac systems. Therefore, research on synchrotrons for ICF has nearly stopped, but research programs are active in the other three technologies in the United States and abroad.

Although pulsed-power diodes are included among the accelerators that might provide adequate power, we must recognize that diodes lack the demonstrated lifetime and pulse repetition rates of rf linacs and induction linacs. There are other important distinctions between ion diodes and the other accelerators. Diodes are limited in voltage. At present, ion diodes operate at less than 10 megavolts (MV). The highest voltages contemplated are several times that. If we assume 10 MV is typical, we must accelerate 10 megamperes (MA) of current to achieve the required 10^{14} watts. By contrast, both rf linacs and induction linacs are multistage devices. There is no difficulty, in principle, in accelerating ions to arbitrarily high energies. There are, however, two practical difficulties: cost and ion range. Cost is discussed later; ion range, which is discussed now, is an important consideration that bears directly on the type of accelerator that can be used for inertial fusion.
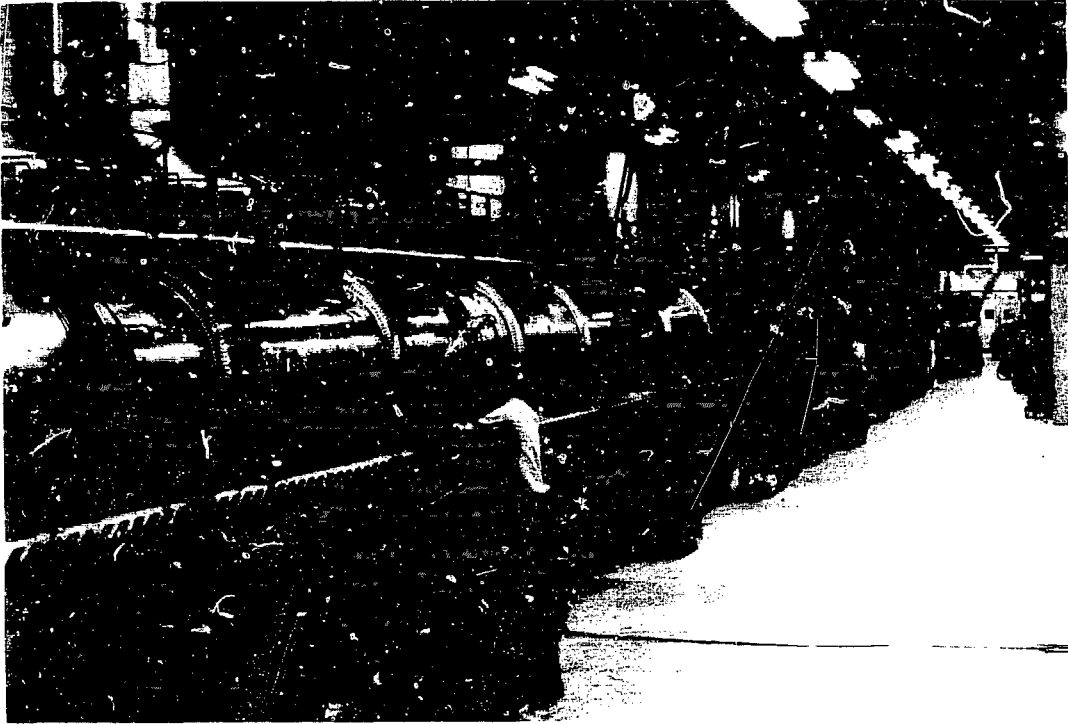
Fig. 1. LAMPF, the Clinton P. Anderson Meson Physics Facility at Los Alamos, a one-half-mile-long linear accelerator that produces a beam of protons with a maximum energy of 800-million electron volts and an average beam current of 1 milliampere.

Range

To provide adequate pressure to implode a target, specific energy deposition in the outer layers of the target must exceed about 20 megajoules per gram (MJ/g). For a spherical target, the specific energy deposition is given by $E/4\pi r^3$, where E is beam energy (in MJ), r is the target radius (in cm), and R is the ion range (in g/cm^2). For typical values of E (several MJ) and r (several mm), R cannot exceed several times 0.1 g/cm^2 and still satisfy the 20 MJ/g criterion. In fact, ion ranges less than 0.1 g/cm^2 are preferable as such ranges increase the specific energy deposition for a given target radius. High specific energy is expected to improve target performance.

Ion range as a function of ion kinetic energy is shown for several different elements in Fig. 2. If we take 0.1 g/cm^2 as the desirable ion range, protons or other light ions are acceptable with kinetic energies in electron volts (eV) up to about 0.01 gigaelectron volts (GeV); however, heavy ions, such as lead ions, allow kinetic energies up to about 10 GeV. Diodes, with 10 MV that can accelerate protons to kinetic energies of 0.01 GeV, are thus suitable
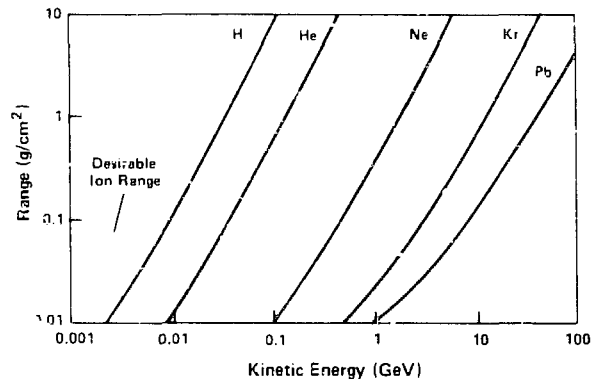
Fig. 2. Ion range as a function of kinetic energy for a variety of ions. Heavy ions allow the use of multistage accelerators with high-energy beams but, at the same time, keep the range of the ions in the desired region, at or below 0.1 g/cm^2.

81

for light ions; multistage accelerators, for heavy ions. (In common usage "light-ion fusion" is nearly synonymous with "ion-diode fusion," and "heavy-ion fusion" is nearly synonymous with "multistage-accelerator fusion.") At 10 GeV the current required to achieve 10^{14} watts of singly charged heavy ions is only 10 kA rather than the 10 MA required for diodes. This difference of three orders of magnitude in current requirement is one of the distinctions between light-ion fusion and heavy-ion fusion.

Perhaps a more fundamental difficulty with diode devices is that all of the beam energy is delivered at a single accelerating gap. This results in highly stressed components, and it is not surprising that these diodes have not demonstrated adequate lifetime or pulse repetition rates. Some suggested diode-fusion devices employ multiple accelerators to obtain the required beam power. This relieves, but does not eliminate, the problem of highly stressed components. In the remainder of this discussion, we consider only multistage accelerators for which, fortunately, 10 GeV is a reasonable voltage.

There is also a major difference in the requirements for the two types of multistage accelerators; with rf linacs, storage rings (sometimes called accumulators) are necessary to achieve the required 10 kA, whereas induction linacs should not require storage rings. In fact, the design current for the advanced test accelerator (ATA) electron induction linac now coming on-line at the Lawrence Livermore National Laboratory is 10 kA, and about 7.5 kA has already been achieved.

The U.S. program focuses on induction accelerator research, whereas the Europeans and Japanese are studying rf linacs for heavy-ion fusion. Although much of what we discuss here applies to both types of multistage accelerators, we will emphasize the induction linac, which, in its simplest form, can be thought of as a series of transformers with the beam as the secondary. The current to the primaries is provided by capacitors and switching devices (Fig. 3). Each transformer is energized only while the beam passes through it.

We now return to the question of cost.

CONSIDERATIONS FOR POWER PRODUCTION

To understand why accelerators are attractive for fusion, it is necessary to examine the requirements that must be satisfied by any commercial power plant. We consider three general issues relevant to nearly all power plant technologies: environmental acceptability, total plant capacity (usually roughly proportional to plant cost C), and the cost of electricity r_e.

Although all methods of energy production have some environmental impact, fusion should be acceptable. Fusion plants can, in principle, be several orders of magnitude better than fission reactors in limiting undesirable production of long-lived radioactive isotopes.[1]

As mentioned earlier, the size of a fusion device is important. Power companies prefer plants of small cost
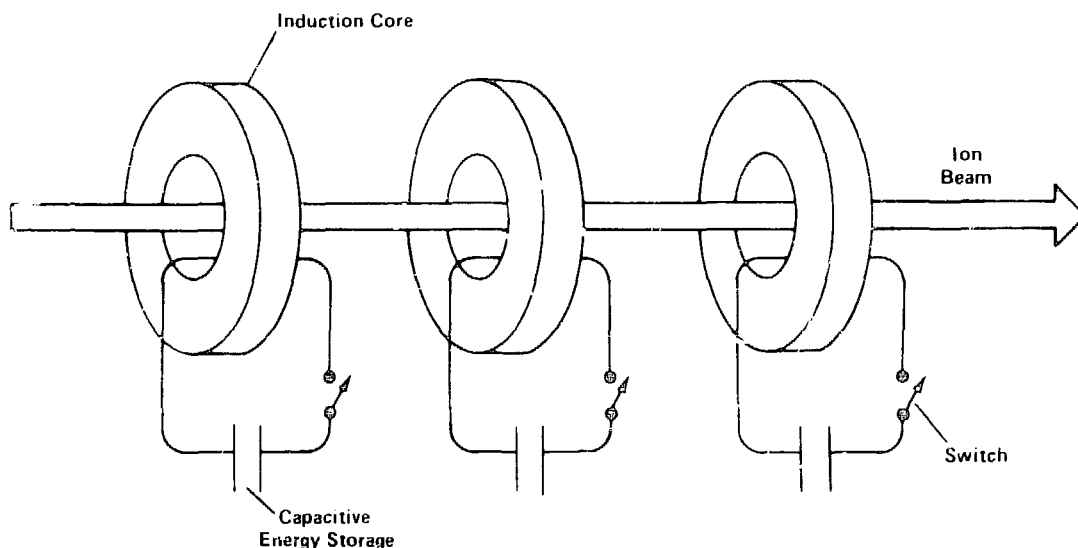
Fig. 3. The induction linac as a series of transformers with the beam acting as the secondary.

and capacity. There are several reasons for this preference. Large power plants, costing perhaps several billion dollars, can severely strain the capital assets of even large utility industries. Moreover, large plants, which offer little flexibility in terms of siting and market size, are slow to construct (a major problem for the nuclear industry) and produce large perturbations on the power grid when they go off-line. Perhaps more importantly, high cost can be a severe impediment to the introduction of any new energy technology.

The third consideration, cost of electricity, can be illustrated conveniently with total plant cost in two-dimensional space, as shown in Fig. 4. Consider a reference point located at C equal to 2.5×10^9 dollars and r_e equal to 50 mills per kilowatt hour. If either a plant or electricity can be made more economically, it is beneficial; therefore, the areas labeled "better" and "worse" are clearly better or worse, respectively, than the reference point. The situation is not as clear in the areas labeled with question marks. For example, a utility might choose to incur higher plant capital costs to reduce the price of electricity.

We now examine the features of a power plant that would enable us to move in the "better" direction, and one ICF feature is particularly attractive. The driver and reaction chamber are relatively independent components, and the fusion energy release occurs in a volume of space smaller than the volume of a pea. The energy yield of each target can be varied by large factors; the plant capacity can be varied by even larger factors by adjusting both the yield and the pulse repetition rate. Thus, in principle, there is much flexibility in the design of ICF plants, and small plants are possible. For this feature of ICF to be useful, the driver and reactor chamber must be inexpensive so that the cost of electricity can be low.

The size and cost of a reaction chamber are related directly to target yield so that smaller yield means smaller
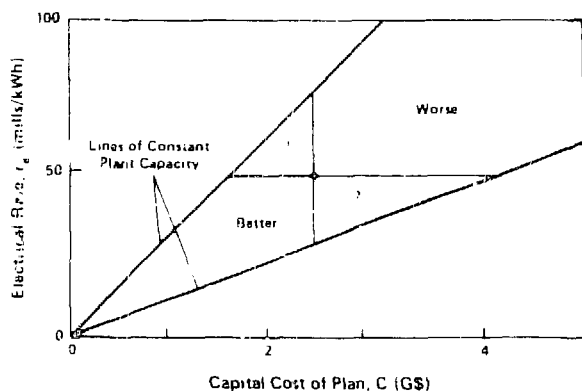
cost. Also, both target yield and driver cost decrease with driver energy. Thus it should be economically advantageous to reduce driver energy and, at the same time, increase the driver repetition rate to obtain the desired thermonuclear power output. There are, however, limits to this strategy. One is the maximum repetition rate at which the driver can operate. Another involves the product of driver efficiency η, target energy gain G, and the efficiency ϵ of the reactor and turbines. A simplified power flow diagram of an ICF power plant is shown with these parameters in Fig. 5. Clearly $\eta G \epsilon$ must exceed unity to produce any net power. Because ϵ is typically about one-third, ηG is required to be greater than three.

To have enough net power to be economical, it is commonly assumed that ηG must exceed about 10. In reality, the lower limit for ηG depends on the cost of drivers, reaction chambers, turbines, generators, and so forth. The simple criterion of $\eta G \leq 10$ is adequate here.

Target gain calculated as a function of driver energy[3] is shown in Fig. 6. These curves are based on single-shell targets, and the range shown is appropriate for both heavy-ion accelerators and short-wavelength lasers. More complex multiple-shell targets give somewhat higher calculated gain, but the physics uncertainties are larger and fabrication is apt to be more difficult. Figure 6 shows that attempts to lower driver cost by decreasing driver energy also decreases target gain G; the requirement for ηG can then be met only if the driver has high efficiency η.

Quantitatively, we expect that η should be about 0.25 for heavy-ion accelerators. We could then satisfy our ηG criterion with target gains as low as 40. By contrast, a KrF laser is unlikely to have an η that exceeds 0.05,[*] which would require a target gain in excess of 200. Using the top curve in that figure, we see that a gain of 40 can be achieved with an input energy of 2 MJ so that the yield would be about 80 MJ. On the other hand, to achieve a

Fig. 4. Cost considerations for an electric generating plant. Because the cost of electricity is approximately proportional to electric output divided by capital cost, sloping lines (two of which are shown) correspond to constant electric output. The point represents a typical fusion power plant design. Heavy-ion fusion is attractive because it has many attributes that might allow power plants to operate in the region labeled "better."
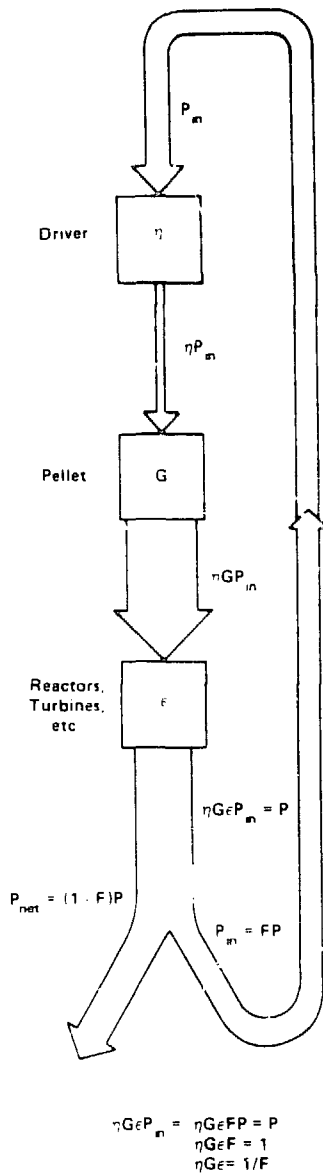
Fig. 5. A simplified power flow diagram for an ICF plant. Of the power P coming from the turbines, a fraction F is recirculated (P_{in}), and a fraction (1-F) becomes the useful power generated by the plant (P_{net}). The equations show the relationship between F and the product of driver efficiency η, target energy gain G, and the efficiency ϵ of the reactor and turbines.

gain of 200 requires more than 20 MJ of input energy, and the corresponding yield would be greater than 4000 MJ. Thus, the size and cost of a reaction chamber is expected to depend strongly on driver efficiency. Because KrF lasers are one of the most attractive laser candidates
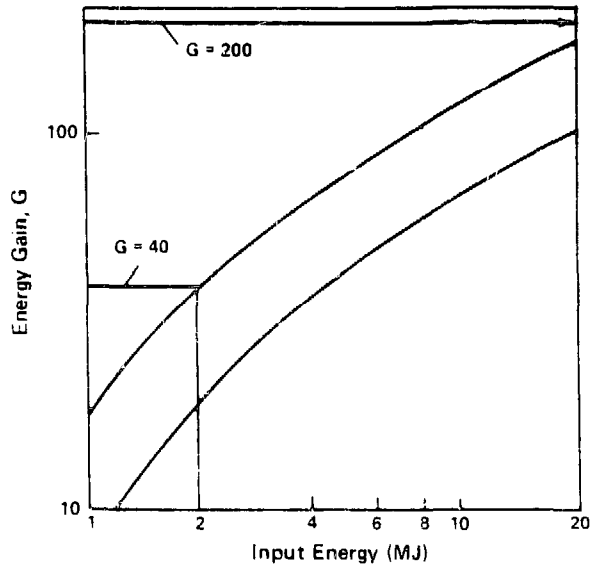
Fig. 6. Calculated target gain as a function of driver energy for single shell targets. The range shown is appropriate for both heavy-ion accelerators and short-wavelength lasers. However, the high efficiency of the heavy-ion accelerators should allow these devices to operate a a gain of around 40 rather than at the gain of 200 expected for lasers thereby lowering the size and cost of the reaction chamber.

for ICF, it is evident that high efficiency is a very important advantage of accelerators over lasers. Designing single-shell targets with gains higher than those shown in Fig. 6 might be possible. Indeed, some current estimates of target gain exceed those shown; however, even the gains illustrated in the figure have not been demonstrated. Accelerator fusion has a larger safety factor than does laser fusion. based on these considerations.

Driver Requirements

Other driver features that enable one to move in the "better" direction are reliability and durability. Low reliability increases the cost of electricity because i reduces the output of a given capital investment. Good durability is important because high repair and replacement costs increase the cost of electricity. The drive features necessary for economically exploiting the favorable flexibility of ICF are

1. low cost,
2. high repetition rate,
3. high efficiency.
4. reliability, and
5. durability.

These five features lead us to the consideration of accelerators as inertial fusion drivers. Features 2 through 5 have either been demonstrated at existing accelerators or appear to be reasonable extrapolations of existing technology.

The cost of accelerators, the first item on the list, has been, and remains, an issue. It might be possible to build a 3-MJ accelerator for about five hundred million dollars. Although this compares favorably with proposed laser system , pursuing cost reductions is still very important.

There are additional requirements that must be satisfied. Some of these, such as favorable implosion dynamics, are nearly driver-independent and are discussed elsewhere in this review. However, three driver-dependent requirements are discussed here:

1. high peak power,
2. an ability to focus the beam, and
3. acceptable physics for the beam-target interaction.

Peak beam power greater than 10^{14} watts is required, as noted earlier, and this has *not* been demonstrated at existing accelerators. The second requirement, the ability to focus the beam, is related to high power. Target gain decreases with increasing focal-spot radius—at least for focal radii greater than 1 or 2 mm. Adequate focusing *has* been demonstrated at existing accelerators but never at the power levels required for ICF. These two requirements are discussed in the next section.

The interaction between beam and target must behave properly, in that the beam must be absorbed but must not penetrate too deeply into the target. Moreover, the beam must not produce secondary particles or photons that preheat the fuel and prevent efficient compression. The beam-target interaction has been a critical issue for laser fusion, and some laser-light wavelengths are almost certainly unacceptable for ICF applications. Discussion of the interaction physics follows the next section.

HIGH POWER AND BEAM FOCUSING

High power and beam focusing are related because, although single ions can be aimed with very high precision, the mutual interaction of a large number of charged particles (space-charge forces, for example) complicates matters. This mutual interaction is also a problem for acceleration. During acceleration the beam must be held together both transversely and longitudinally by applied focusing fields. Transverse focusing is usually provided by electrostatic or magnetic lenses. Long-

itudinal focusing is provided by time-varying accelerating fields. If beam power or current is increased, the repulsive space-charge forces of the beam ultimately overpower the applied focusing fields. In some cases the interaction of the beam with the accelerator structure can produce instabilities that limit the beam power to values far lower than the limit set by the lens strength.

Phase-Space Density

Liouville's theorem also sets important limits on power and focusing. As it is usually applied to accelerators, this theorem states that the six-dimensional phase space density of ions at the end of the accelerator cannot exceed the phase-space density at the ion source. (Beam-cooling mechanisms that violate this condition do not seem applicable to heavy-ion fusion.)

The target radius limits the two transverse spatial dimensions of the focused beam. For a given energy, the peak power requirement limits the longitudinal extent of the beam. Because of effects such as third-order aberrations, what can be realized with focusing lenses puts an upper limit on the angular divergence of the beam approaching the target. Because angular divergence is roughly proportional to transverse beam momentum, this translates to corresponding upper limits on transverse beam momentum. "Chromatic" aberrations of the lens system (the fact that ions of different momenta have different focal lengths) place an upper limit on the spread of longitudinal momenta in the beam. Thus, the target plus the final lens system place an upper limit on the six-dimensional phase-space volume of the beam emerging from the accelerator. This corresponds to a *lower* limit on the phase-space *density* of the beam because the number of ions is fixed by target considerations. Fortunately, the phase-space density available from practical ion sources is orders of magnitude larger than the lower limit so that the Liouville constraint can, in principle, be satisfied. However, in all real accelerators there is some growth in occupied phase volume.

For many applications it is useful to consider six-dimensional phase space to be a product of three two-dimensional phase spaces. The volume or area of each subspace is referred to as emittance: the growth of occupied phase volume, as emittance growth.

One important question for heavy-ion fusion is whether the phase volume constraint can still be satisfied in the presence of realistic emittance growth. There are several potential sources of emittance growth. For rf

linacs, a large number of turns are used in the storage rings to obtain the required current amplification. In this process of multiturn injection, some unoccupied phase space is unavoidably mixed with occupied phase space resulting in substantial emittance growth—probably a factor of 2 or more in each transverse dimension. This source of emittance growth does not exist for induction linacs.

Other potential sources of emittance growth in both rf and induction linacs include nonlinear space-charge forces, imperfections in the accelerator, and instabilities that involve interactions between the beam and the accelerating structure or interactions between the beam and any residual gas in the reaction chamber from the previous explosion. Many of these effects have been studied analytically and numerically with encouraging results, but perhaps the most encouraging comes from a series of experiments in progress at Lawrence Berkeley Laboratory.[4] In these experiments it has been possible to transport a highly space-charge-dominated beam through a transport channel containing more than eighty electrostatic lenses without observable emittance growth.

Experimental Results

As all real beams have nonzero emittance, the particles in a beam will, in general, not move exactly along the axis of a transport channel. If a single ion is injected off-axis (in position or angle), it oscillates about the axis with a frequency (or wavelength) determined by its charge, mass, and momentum and by the strength of the lenses (restoring force). We call such oscillations betatron oscillations. If a large number of particles are injected into a channel, their mutual repulsion works against the restoring force of the lenses, and the wavelength and amplitude of the betatron oscillations increase relative to the single-particle values.

It is convenient to compare the relative importance of the lens-focusing forces and the space-charge forces by comparing the parameters that appear in the equation for the betatron frequency ω:

$$\omega^2 = \omega_o^2 - 1/2\omega_b \qquad . \qquad (1)$$

Here ω_o is the betatron frequency in the absence of space charge, and ω_{bp} is the so-called beam plasma frequency given by

$$\omega_{bp} = \sqrt{4\pi nq^2/m} \quad , \qquad (2)$$

where q and m are, respectively, the ion charge and m and n is the ion density of the beam. As ion density space charge increases, the plasma frequency increas reducing the betatron frequency. It would not be surpı ing if beam instabilities occur when ω_{bp} becomes co parable to ω_o. Indeed, analytic theories, based on ide ized particle distribution functions, show that this is case.

Another way of characterizing the strength of focus is in terms of "phase advance." Most commonly, lenses in an accelerator are quadrupole. These len have the property of focusing in one transverse direct and defocusing in the orthogonal transverse direction. alternating the orientation of the lenses so that in ea plane every other lens is focusing or defocusing, a called alternating gradient channel is obtained. It is v known in optics that when a focusing lens is preceded followed by a defocusing lens of equal strength the effect is focusing. Thus an alternating gradient chan focuses in both transverse dimensions. Each pair quadrupole lenses (including the contiguous lens spaci is referred to as a cell. The change in phase of betatron oscillations as the beam passes through one is called the phase advance per cell σ, which is denoted in the absence of space charge.

In general, small values for σ/σ_o are desirable beca they correspond to high current. Unfortunately, analy theory predicts the onset of unstable regions as this ra is lowered.

We now compare the results of analytic theory w the experiments performed at the Lawrence Berke Laboratory. Figure 7 is a plot of ω_{bp}^2 as a function σ/σ_o for various values of σ_o. The parameter ω_{bp}^2 is u because, for a fixed ion charge, mass, and velocity, t quantity is proportional to the ion density n and thus proportional to the current density of the beam. Note t σ/σ_o decreases from one to zero, that is, the pha advance per cell changes from the case of no spa charge ($\sigma = \sigma_o$) toward the case of higher beam curre (lower σ/σ_o ratios). (The experiments were perforn with cesium ions at about 160 keV. The cell length v 30.48 cm so that $\sigma_o = 90°$ corresponds to $\omega_o^2 \approx 3 \times 1$ /sec².)

In Fig. 7 the regions of instability predicted by analy theory are the dotted parts of the curves. Experimen results are the rectangular areas, with stable regic shown in black and unstable regions shown in whi Remarkably, the beams are more stable than predict allowing lower values of σ/σ_o than we thought possil
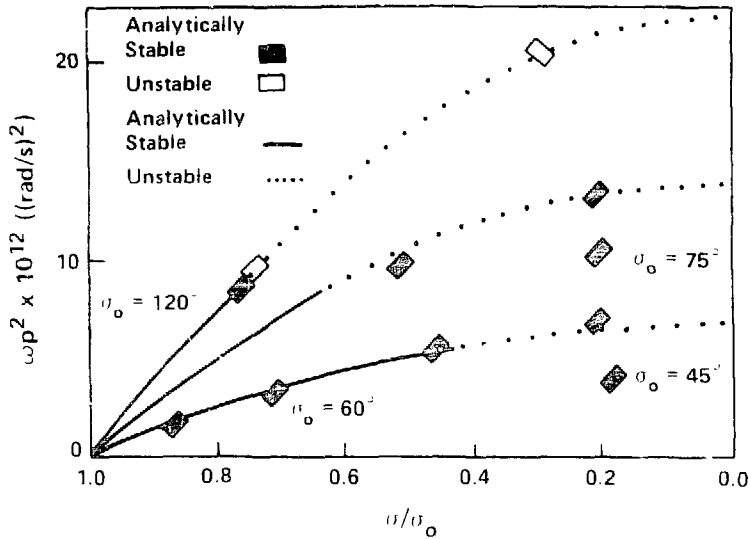
Fig. 7. Beam stability. When we compare the results of analytic theory (curves) and the Lawrence Berkeley Laboratory experiments (boxes), we see that the beams are more stable than predicted (note the experimentally stable regions on the two lower curves). The parameter ω_{bo} is the plasma frequency, and ω_{bo}^2 is proportional to the beam current density. The parameter σ measures the change in phase advance per cell of the betatron oscillations; σ_o is the phase advance in the absence of any space charge (figure adapted from Ref. 4).

several years ago. Fortunately. the experiments are consistent with recent numerical simulations that use more realistic distribution functions than does the analytic theory.

The new results are encouraging because they imply that for a given emittance. the beam current can be increased by a factor of a few over the value assumed several years ago. In particular. for a given total beam energy. higher current allows a reduction in the volume of magnetic material required for the induction cores. thereby lowering the cost. Alternatively, the new results allow a decrease in phase-space volume for a given amount of magnetic material.

Even with these new. higher limits on transportable power, other techniques must be developed to ensure the generation of high-quality, well-focused beams carrying the 10^{14} watts required for ICF. One of these techniques uses multiple beams; a second. "pressure windows."

Multiple Beams

For the required 10^{14} watts, it seems best. at present. to accelerate each beam in its own focusing-lens system but to use common induction cores. Thus each core shown in Fig. 2 would have multiple beams going through it. The experiments at Lawrence Berkeley were performed with a single beam. Moreover, there was no attempt at longitudinal focusing or acceleration. Los Alamos and Lawrence Berkeley are now constructing an experiment, designated the multiple-beam experiment. to test these features. About three years will be required to complete the experiment.

Pressure Windows

Calculations show that space-charge forces are not strong enough to prevent beam focusing; however, instabilities may occur when the beam propagates through residual material in the reaction chamber. As the beam passes through the gas. a plasma is produced that might generate some of the well-known beam-plasma instabilities. Most conceptual studies of heavy-ion-fusion reactors avoid this issue by designing reactors with low enough residual pressure (less than 10^{-3} to 10^{-4} torr) that insufficient plasma is formed to generate instabilities.[5,6] This conservative approach may not be necessary. It has been suggested that "pressure windows" may exist where

87

focusing is possible in the presence of gas.[7] For example, between about 10^{-3} and 10^{-1} torr, we expect the so-called two-stream instability to be a serious problem. However, between about 10^{-1} and 1 torr, the two-stream instability should be collisionally suppressed, and propagation may be possible. Between about 1 and 10 torr, enough plasma is produced to charge neutralize the beam. In this case, the magnetic fields of the beam may cause it to self-pinch into a stable "pencil beam" that can be propagated to the target. Pressures above 10 torr are inadmissible because of multiple scattering.

In summary, present results on both high power and beam focusing (that is, on the transport of ions to the target) are encouraging. A multiple-beam experiment is being built to test and refine these results. But what happens once the beam reaches the target?

BEAM-TARGET INTERACTIONS

The stopping of charged particles in matter has been studied for about 70 years. The simplest theories that just calculate the energy transferred by binary Coulomb collisions from the beam ions to the electrons in the stopping medium explain the principal features of the beam-target interaction. Although agreement between theory and experiment is excellent at low intensities, it has not yet been possible to test the theories with fusion-intensity beams. However, as binary Coulomb collisions must occur, even with intense beams, the range of ions in a fusion-intensity beam is unlikely to be substantially larger than calculated. Thus the range of ions is not a major issue in the assessment of heavy-ion fusion, although more accurate range information will ultimately be required to optimize specific target designs. A more urgent issue is whether the beam-target interaction will generate particles or photons that excessively preheat the target fuel.

Typical high-gain targets with deuterium-tritium fuel can tolerate about 10^5 J/g of preheat energy in the fuel. For fusion, a target requires about 10^9 joules of beam energy per gram of fuel. The mass of the fuel is usually 10 per cent of the total mass of the target. Thus, if the preheat is deposited uniformly throughout the target, preheat energy less than about 0.1 per cent of the total beam energy is acceptable. In the following discussion, we pessimistically assume that all energy deposition in the fuel occurs early enough to contribute to preheat.

Secondary particles or photons capable of penetrating deeper than the ion beam might be produced through the electromagnetic interaction as "knock-on" electrons and ions, electrons from plasma instabilities, bremsstrahlung and x rays. Likewise, the nuclear interaction might generate such products as charged nuclear debris gamma rays, and neutrons. We will examine these possibilities separately.

Knock-On Electrons and Ions

These are secondary charged particles generated in elastic collisions between ions in the beam and electron or nuclei in the target. We can calculate the maximum kinetic energy that an electron could get from an ion in a head-on, nonrelativistic collision. Then, using standard range-energy tables, we can show that the maximum electron range is always less than the range of the ion that produced it. Thus knock-on electrons cannot generate preheat.

What about ions? When we examine the effect of the field of an ion in the beam and compare the transfer of kinetic energy from such an ion to either electrons or ion in the plasma, we find that, because of the difference in mass, the energy loss to ions is about 10^{-4} times lower than it is for electrons. Thus, nearly all the beam energy is transferred to electrons, but, as we saw above, their range is too short to cause a preheat problem. On the other hand, although knock-on ions will penetrate further, the maximum energy that they could get from the beam is an order of magnitude lower than 0.1 per cent of beam energy deemed acceptable for preheat. Thus, knock-on ions should not cause a problem.

Electrons from Plasma Instabilities

Some work has been done in this area but more is needed. Generally, calculations show that if instabilities do exist, they do not accelerate many electrons to velocities substantially greater than the beam velocity. The electron velocity must exceed several times the beam velocity before the electron range exceeds the ion-beam range. Therefore, few electrons from plasma instabilities could penetrate into the fuel.

Bremsstrahlung

This radiation would be generated primarily from knock-on electrons. The fraction of electron energy

radiated as bremsstrahlung depends on the energy of the electrons and the atomic number of the target material. For typical electron energies and target materials, the bremsstrahlung is smaller than 0.1 per cent of the electron energy. Thus, bremsstrahlung is not a problem.

X Rays

When the incident ion excites bound electrons, x rays can be produced. By considering the x-ray absorption opacities of typical materials in a target and making the outrageously pessimistic assumption that all the beam energy is converted into x rays, we can calculate an upper limit on the energy absorbed per unit mass. For a typical target, the beam deposits about 10^7 J/cm^2. Because thermal x rays are copiously produced at energies of 1 keV or less and are usually accounted for in the target design, only x rays in the 10- to 100-keV range need be considered for preheat. At these energies, the absorption opacity of the fuel is about 0.01 cm^2/g so that only 10^5 J/g would be absorbed in the fuel if *all* the beam energy went into such x rays. Therefore this source of preheat is unimportant.

Charged Nuclear Debris

Cross sections for nuclear reactions are never much larger than simple geometrical cross sections, which give mean free paths of 10 to 100 g/cm^2. Because the ranges of typical ions are 0.01 to 0.1 g/cm^2—a factor of 100 lower, only 1 per cent of the particles is involved in nuclear reactions that might generate charged nuclear debris. Detailed calculations show that preheat from this source is acceptable.

Gamma Rays

As in the case of energetic x rays, the absorption opacity is so small for gamma rays (about 0.1 cm^2/g at a typical energy of 1 MeV) that fuel preheat would not be a problem even if all the energy of the interacting nuclei were converted to gamma rays.

Neutrons

The mean free path of neutrons in deuterium-tritium fuel is several grams per square centimeter, which cor-

responds to an effective absorption opacity of several tenths. Thus a calculation identical to that for gamma rays again gives acceptable preheat.

The tentative conclusion is that the interactions are compatible with the requirements of ICF.[8] Nevertheless, it seems prudent to test this conclusion before building a full-scale fusion accelerator.

Los Alamos and Lawrence Berkeley Laboratory plan to build a test accelerator capable of providing a definitive test of the beam-target interaction.[9,10] This test accelerator and its associated experimental program are designated the high-temperature experiment. The completion of the accelerator is currently planned for 1989 or 1990.

The high-temperature experiment will not test just the beam-target interaction. It will also provide a facility for studying beam focusing. The high-temperature experiment, which will develop and test accelerator technology at a level beyond the multiple-beam experiment, will still not be large enough to produce significant fusion energy. It will provide engineering and cost data that are essential to a sound evaluation of the promise of heavy-ion fusion.

Present theory and experiments indicate that heavy-ion accelerators are well suited to inertial fusion power production. Although lasers and light-ion diodes can provide essential physics information in the near future, it is the author's opinion that heavy-ion accelerators offer the best prospects for commercial energy production.

The multiple-beam and high-temperature experiments will go a long way toward determining if this opinion is correct.

REFERENCES

1. Lawrence M. Lidsky, "The Trouble with Fusion," *Technology Review* 86, 32-44 (October 1983).

2. "ERDA Summer Study of Heavy Ions for Inertial Fusion," R. O. Bangerter, W. B. Herrmannsfeldt, D. L. Judd, and L. Smith, Eds., Lawrence Berkeley Laboratory report LBL-5543 (December 1976).

3. R. O. Bangerter, J. W.-K. Mark, and A. R. Thiessen, "Heavy Ion Inertial Fusion: Initial Survey of Target Gain Versus Ion-Beam Parameters," *Physics Letters* 88A, 225 (1982).

4. W. Chupp, A. Faltens, E. C. Hartwig, D. Keefe, C. H. Kim, C. Pike, S. S. Rosenblum, M. Tiefenback,

D. Vanecek, and A. I. Warwick, "A High Current Heavy Ion Beam Transport Experiment at LBL," Lawrence Berkeley Laboratory report LBL-17256 (January 1984).

5. "HIBALL—A Conceptual Heavy Ion Beam Driven Fusion Reactor Study," Vols. 1 and 2, University of Wisconsin report UWFDM-450; Kernforschungszentrum Karlsruhe report Kfk-3202 (December 1981).

6. "Heavy Ion Fusion Reactor, HIBLIC I," Nagoya University, Nagoya 464, Japan, Institute of Plasma Physics report IPPJ-663 (January 1984).

7. C. L. Olson, "Final Transport in Gas and Plasma," in *Proceedings of the Heavy Ion Fusion Workshop*, Lawrence Berkeley Laboratory report LBL-10301;

Stanford Linear Accelerator Center report SLAC-PUB-2575 (September 1980), p. 403.

8. R. O. Bangerter, "Ion Beam Interactions with ICF Targets," in *Laser Interaction and Related Plasma Phenomena, Vol. VI*, H. Hora and G. H. Miley, Eds. (Plenum Publishing Corporation, New York, 1984) pp. 1013-1027.

9. R. O. Bangerter, "Accelerator Inertial Fusion—A National Plan for the Development of Heavy-Ion Accelerators for Fusion Power," Los Alamos National Laboratory document LA-UR-81-3730, December 1981.

10. R. O. Bangerter, "Heavy-Ion Fusion Accelerator Research Program Plan for FY84-FY89," Los Alamos National Laboratory document LA-UR-83-1717, May 1983.

ABSTRACTS OF ICF SUPPORTED
RESEARCH PUBLICATIONS SINCE 1982

EXPERIMENTAL PLASMA PHYSICS AND ATOMIC PHYSICS

THEORETICAL PLASMA PHYSICS

SPACE PHYSICS

DRIVER TECHNOLOGY AND FACILITIES

MATERIALS TECHNOLOGY

ICF SYSTEM STUDIES

PATENTS

REPRINTS IN
EXPERIMENTAL
PLASMA PHYSICS
AND
ATOMIC PHYSICS
SINCE
1982

PLASMA ARMATURE RAILGUN STUDIES[a]

J.V. Parker, W.M. Parsons, C.E. Cummings, W.E. Fox
Los Alamos National Laboratory
Los Alamos, NM 87545

It has been nearly a decade since the first plasma armature railgun experiments at ANU. Despite extensive development work during the intervening years the plasma armature railgun has not demonstrated the high velocity performance which was generally anticipated. In fact, only a handful of experiments have exceeded the 5.9 km/s velocity achieved at ANU and the highest reported velocity is only 11 km/s.

During the past year a detailed investigation of plasma armature railgun performance has been carried out as part of the HYVAX program at Los Alamos. The principal results of this investigation are:

1. Ablation of material from the walls by the plasma armature is the most important limitation on railgun performance.

2. Ablation sets an upper limit to the velocity which can be achieved for a given rail geometry and operating current, independent of projectile mass, given by

$$v_{max} = L' 1/2a \ v_a$$

where v_a is the arc voltage and a a proportionally constant relating arc input power to mass ablation rate.

3. The current distribution in the plasma armature varies rapidly with time and position so that quasi-static models of the plasma armature have limited utility.

- Near the maximum velocity the arc current distribution can become very complex, exhibiting effects such as: separation from the projectile, multiple current peaks, and rapid deceleration.

The results summarized above are supported by a large body of experimental data taken on the HYVAX-1 railgun. HYVAX-1 is a single stage, 11 mm. diameter bore device with an active length of 2.75 meters. The power supply comprises three independent capacitor bank modules which can be sequenced to provide a controlled current waveform. Typical operating conditions are: projectile mass of 1.0 to 1.5 grams, injection velocity of 800 to 1800 m/s, peak current of 00 to 300 kA, and final velocity of 2 to 4 km/s.

Diagnostics include the usual voltage, current and magnetic probe measurements. Significant improvements in our understanding of arc behavior have resulted from using magnetic probes which sense the rail current. Recording the integrated output of these probes provides a measure of the current flowing in the rails at 6 to 9 positions along the barrel, thus providing both temporal and spatial information about the plasma current distribution.

Ongoing experiments are addressing the affect of ore materials on ablation phenomena with the goal of improved high velocity performance.

Pittsburgh Hilton

June 3-5, 1985

Subject category and number:

Electromagnetic Launchers

22.

☐ Prefer oral session

☐ Prefer poster session

☒ No preference

Submitted by

signature
Jerald V. Parker
same name typewriter
Los Alamos National Laboratory
company
Group F-7, MS-E525
address
Los Alamos, New Mexico 87545
city state zip
(505) 667-3119
telephone

Important

Evidence for Collisional Damping in High-Energy Raman-Scattering Experiments at 0.26 µm

R. E. Turner, Kent Estabrook, R. L. Kauffman, D. R. Bach,[a] R. P. Drake, D. W. Phillion,
B. F. Lasinski, E. M. Campbell, W. L. Kruer, and E. A. Williams

Lawrence Livermore National Laboratory, University of California, Livermore, California 94550

(Received 28 August 1984)

Experiments using 1.5 kJ of 0.26-µm wavelength light to irradiate thin "burn-through" targets show less stimulated Raman scattering (SRS) than similar experiments at 0.53 µm. The SRS from high-Z (Au) targets is 3 orders of magnitude less than SRS from low-Z (CH) targets irradiated at similar intensities. These results are the first direct observation of collisional damping of the Raman instability in high-Z targets as predicted by theory and simulations.

Raman scattering[1-5] (SRS) in laser-produced plasmas can generate high-energy electrons, which can degrade laser-fusion target gain. In nearly all previous laser-plasma experiments, SRS has been limited by steep density gradients, which restrict the phase-matching regions to relatively small lengths. However, the reactor-size targets envisioned for future laser-fusion experiments will produce much longer density-gradient lengths. Here we report the observation of an important alternative limiting mechanism, electron-ion collisions, which can inhibit SRS.

In these experiments, uv laser light irradiates thin films causing them to expand rapidly. By the peak of the 1-nsec laser pulse, the electron density is near resonance ($n_c/4$) for the Raman[5] and $2\omega_{pe}$[6] instabilities. Other instabilities that can produce hot electrons occur near critical density $[n_c = 10^{21}[(1.06 \ \mu m)/\lambda_0]^2 \ e^{-}/\text{cm}^3]$ and are thus mostly excluded from these observations. With plastic (CH) targets, the fraction of the incident energy scattered as Raman light is 5 times smaller for irradiations with a laser wavelength (λ_0) of 0.26 µm than for 0.53 µm. With Au targets, the decrease is more than 4 orders of magnitude. We use theory and simulations to show that the suppression of SRS with increasing laser frequency or target Z is due to collisional damping of SRS.

These experiments used one arm of the 74-cm-aperture Novette laser. An array of potassium dihydrogen phosphate crystals quadrupled the frequency of the 1.05-µm laser light to produce up to 1.5 kJ of light at 0.26-µm wavelength in a near Gaussian pulse of 0.9–1.2 nsec full width at half maximum (FWHM).[3] A mask at the center of the lens and the chromatic aberration of the $f/4$ focusing lens caused the uv light to focus in a region free from residual 1.05-µm and 0.53-µm light.[7] The experimental intensities quoted here are the average laser power divided by the illuminated area as determined from x-ray micrographs (x-ray energy of ~1–1.5 keV). We define the beam diameter, D, as the FWHM of the x-ray intensity. Although the laser beam is known to be nonuniform,[9] and qualitatively less uniform than the beam at 0.53

µm, localized regions of higher intensities should enhance, not reduce, the growth of Raman scattering.

The targets were 6-µm-thick CH or 0.4-µm-thick Au foils, supported on large washers. The thicknesses were chosen, by LASNEX calculations, so that the maximum electron density on-axis would be slightly less than $n_c/4$ by the peak of the laser pulse. The parabolic density scale lengths[1] are calculated to be (500–1000)λ_0 in both the axial and radial directions for both CH and Au. The targets were irradiated at normal incidence, with the focus in front of the target. The focal-spot diameters were 300 to 350 µm, resulting in average target-plane intensities of $(1-2) \times 10^{15}$ W/cm^2.

A streak camera and optical system, mounted orthogonal to the laser beam, provided time-resolved one-dimensional spatial images along the direction of the laser axis.[10] This instrument looked at the 313-nm bremsstrahlung emission from both the front and the back expanding plasmas. When the plasma is optically thin (low-Z green experiments), this emission is proportional to the line-averaged product of the density squared and the square root of the temperature. The simulation line integrals are in good agreement. A time-resolved optical spectrometer measured the Raman light scattered at 135° to the laser beam. Calibrated photodiodes, filtered to look only at SRS from below $n_c/4$ (0.35 µm < λ_0 < 0.5 µm), measured the absolute level of Raman-scattered light at various angles (between 105° and 169° from the laser). Spectroscopy verified that all Raman light emissions were within this range of wavelengths.

The results are summarized in Fig. 1. The error bars enclose all the data obtained during the experiments. We estimate the absolute accuracy to be within a factor of 2; the principal source of error arises from the finite number (10) of photodiodes and the resulting uncertainty in the true angular distribution of the scattered light. The data analysis is identical to that discussed by Drake et al.[11] Most of the SRS energy was within 45° of direct backscatter, although no measurements were made back through the $f/4$ lens.

Figure 1 also shows the data from previous 0.53-µm

189

Measurement and Analysis of Near-Classical Thermal Transport in One-Micron Laser-Irradiated Spherical Plasmas

A. Hauer, W. C. Mead, and O. Willi

Los Alamos National Laboratory, Los Alamos, New Mexico 87545

and

J. D. Kilkenny, D. K. Bradley, and S. D. Tabatabaei

Imperial College, London, United Kingdom

and

C. Hooker

Rutherford Appleton Laboratory, Chilton, Didcot, United Kingdom

(Received 10 August 1984)

Solid spherical layered targets have been uniformly illuminated at irradiances of 10^{14} to 10^{15} W/cm^2. Extensive diagnostics including time-resolved x-ray emission and optical probing were used to determine the plasma ablation rate and the plasma blowoff conditions. Comparisons with hydrodynamic simulations show that the thermal conduction is well characterized by a flux limit $f_e = 0.08 \pm 0.02$, with a steep temperature gradient. The steepness of the heat front was confirmed with time-resolved spectroscopy.

Knowledge of energy transport from the region of the laser-light absorption to denser portions of laser-produced plasmas is crucial to an understanding of the laser-induced ablation process.[1-3] Extensive recent computer simulation work[3] has led to the expectation that "classical" transport in spherical laser-heated plasmas can generally be approximated by flux-limited diffusion with a flux limiter in the range of $f_e = 0.06$–0.2. Early work, largely involving flat targets, indicated strong to moderate inhibition of the heat flux relative to classical predictions.[4] Some of the more recent work involving spherical targets has indicated transport levels closer to classical,[5] with evidence of a penetrating foot in one case.[6] Other work indicates some flux inhibition even in spherical geometry.[7]

In the present experiment we have used a comprehensive set of diagnostics to characterize the plasma conditions and thermal transport in a spherically symmetric plasma. We have made time-resolved spectroscopic measurements (using both low- and moderate-Z radiating ions) of the penetration of the heat front in spherical plasmas. In addition, we have used optical probing to measure simultaneously the density profile of, and the magnetic field in, the underdense plasma. Comparisons with hydrodynamic modeling show that (a) all observables are consistent with a high flux limit and (b) the heat front shows no observable foot.

The targets used in this study consisted of solid glass spheres (~ 160 μm diameter), containing Si and Ca (among other constituents), coated with three layers: (1) CH (0.5 to 2.5 μm thick), (2) Al (0.1 μm), and (3) CH (0.5 to 2.5 μm). The solid glass ball prevented implosion of the target (and subsequent inward movement of the critical surface).

The targets were uniformly illuminated with the six-beam, 1.06-μm, laser facility at the Rutherford Appleton Laboratory.[8] The six beams were focused by $f/1$ lenses with optical axes along the faces of a cube. Incident irradiance levels were in the range $(1.5$–$15) \times 10^{14}$ W/cm^2. The laser pulse had an approximately Gaussian temporal profile with 0.83-ns full width at half maximum (FWHM).

The radial intensity profiles of the beams were measured. Small-scale structure results in about 30% rms variation in intensity. The overlap of the six beams and beam-to-beam energy variation resulted in about 50% (peak-to-valley) large-scale variation in incident irradiance across the surface of the sphere.[9]

The primary diagnostic of thermal transport was time-resolved x-ray line spectroscopy. X-ray line emission was observed first from the thin aluminum layer (sensing temperatures of 200–350 eV) and later from the silicon (~ 250–400 eV) and calcium (~ 500–700 eV) in the glass ball.[10]

X-ray emission from the target was dispersed (with a thallium acid phthalate crystal) onto the slit of a streak camera covering 1.7 to 2.4 eV. The spectral and temporal resolutions were about 500 ($\lambda/\Delta\lambda$) and 50 ps, respectively. A seventh laser beam with very short duration (~ 100 ps) was used

2563

SUPRATHERMAL ELECTRON GENERATION TRANSPORT AND DEPOSITION IN

CO_2 LASER IRRADIATED TARGETS

Allan Hauer, R. Goldman, R. Kristal, M. A. Yates,
M. Mueller, F. Begay, D. van Hulsteyn, K. Mitchell,
J. Kephart, H. Oona, E. Stover, J. Brackbill, and
D. Forslund

Los Alamos National Laboratory
University of California
Los Alamos, NM

ABSTRACT

    In CO_2 laser interaction with matter most of the absorbed
energy is initially channeled into a hot electron distribution.
In many cases, resonance absorption is thought to be the
dominant mechanism producing this distribution.   Stimulated
scattering may also play an important role.

    In the coronal region of the laser plasma, hot electrons
suffer losses that fall into two basic categories. First, hot
electron energy is used in the sheath to accelerate fast ions.
In some cases this can be a very efficient process.   This is an
important interaction, since some ICF concepts use energetic
ions as the drive mechanism. The other coronal loss mechanism
is the loss of energy to cold electrons through the drawing of a
return current. Some aspects of the absorption and coronal loss
processes will be illustrated by experiments on laser irradiated
shells.

    Experiments on both axial and lateral energy transport and
deposition in spherical targets are described. A variety of
diagnostics have been used to measure hot electron transport and
deposition including bremsstrahlung and inner shell radiation
and soft x-ray temperature measurements.   Self-generated
electric and magnetic fields play an important role in the
transport and deposition of the hot electrons. In some cases
distinct patterns of surface deposition consistent with magnetic
field configurations have been observed.

479

Determination of laser intensity and hot-electron temperature from fastest ion velocity measurement on laser-produced plasma

T. H. Tan, G. H. McCall, and A. H. Williams

University of California, Los Alamos National Laboratory, Los Alamos, New Mexico 87545

Measurements of the velocity of the fastest ion emitted by a CO_2-laser-produced plasma were made, and it was found that the relationship between velocity and laser flux was given by $V_i = 5.7 \times 10^6 \phi_i^{1/6}$ for single-beam illumination. Comparison with computer simulation, ion velocity spectrum, and x-ray data indicate that the hot-electron temperature is given by $T_x = 7.5 \times 10^{-18} V_i^2$. Measurements of emission from multiple-beam experiments and from experiments at 1.06 μm wavelength are also described. Some simple models are used for discussion and correlation of the data.

I. INTRODUCTION

When a high-intensity laser beam interacts with matter, electrons play a primary role in absorption of light and in energy transport. The hot-electron distribution which results from the interaction depends on the laser pulse shape, power, focusing conditions, and wavelength, and therefore the measurement of hot-electron temperature provides important information about the interaction dynamics or the laser focusing and pulse quality. Determination of hot-electron temperature by measuring the slope of the high-energy x-ray continuum spectrum[1] has been a generally accepted technique for low-laser-intensity interaction. At high intensity, however, the presence of substantial background noise and the instrumental limitation in energy discrimination can affect the accuracy of actual x-ray energy spectrum determination. In addition, the copious emission of fast ions from the laser-produced plasma com[...]ates the correlation of the x-ray spectrum with the actual source hot-electron distribution. On the other hand, because of the collective behavior of plasma, the motion of the hot electrons can generate an extremely high electrostatic potential which results in the emission of ultrafast ions.[1-4] Therefore, we can expect the fast-ion expansion to correlate closely with the hot-electron distribution.[1] Thus, the study of fast ions provides another means to probe quantitatively the hot electrons generated in the plasma. In this paper, we shall demonstrate experimen-tally that the fastest-ion velocity does, in fact, uniquely correlate with single-beam laser flux on target, and that by an empirical fit and an analytical model, the temperature T_x that characterizes the hot-electron energy distribution can also be inferred. Relevant x-ray measurements, wavelength scaling, and the effects of multibeam illumination on hot-electron distribution determination have been examined and will be included in the discussion.

II. FASTEST ION VELOCITY MEASUREMENT AND LASER INTENSITY ON TARGET

Figure 1 shows an oscilloscope trace of a typical fast-ion signal from a CO_2-laser-produced plasma measured with a scintillator–photomultiplier detector[5] which can detect a single ion. Many such detectors have been fielded, and their distances from the target range from 1.5 to 3 m. The writing speed of the oscilloscope is set between 10 to 100 nsec per division. The first pulse is produced by x rays generated in the plasma and is useful as a zero-time fiducial. The fast-rising ion signal is characteristic of a plasma produced by a fast-rising laser pulse, and the rise time can be used as a laser diagnostic. If the main laser pulse is preceded by a low-intensity precursor, such as from a prepulse or prelase, the ion signal rise time is significantly longer than for the case shown in Fig. 1, probably because of a change in plasma scale length. The sharp rise also shows that there is a maximum ion velocity.

Figure 2 shows the distribution of the fastest-ion velocity V as a function of laser intensity for flat and spherical targets illuminated by a single beam at 10.6 μm wavelength using three laser systems at the Los Alamos National Laboratory: SBS, a single-beam prototype; Gemini, a two-beam prototype, and Helios.[5] Each system overlapped in intensity and pulse length with the next-higher energy system. Energy on target ranged from 0.5 to 1000 J, and pulse lengths (FWHM) ranged from 0.6 to 1.6 nsec. Focal spot diameters ranged from 70 to 130 μm. The data, shown in Fig. 2, were controlled samples where the beam spot diameter which encircled 80% of incident laser energy was measured at the

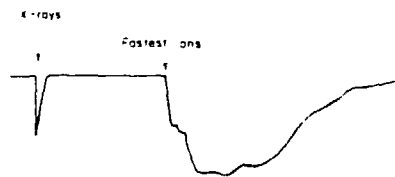FIG. 1. Oscilloscope trace of a typical fast-ion signal from a CO_2-laser-produced plasma. The first pulse was produced by plasma generated x rays which served as a zero-time fiducial.

97

Return-Current Heating and Implosion of Cylindrical CO_2-Laser-Driven Targets

A. Hauer and R. J. Mason

Los Alamos National Laboratory, University of California, Los Alamos, New Mexico 87545

(Received 1 April 1983)

The Helios laser system has been used to deliver 2.3 kJ to the capped end of 0.75-mm-long, 130-μm-diam hollow rods of 5-μm wall thickness. Soft-x-ray pinhole pictures demonstrate the cylindrical implosion of these targets. The measured 130-eV core temperatures from the filtered pictures and the 7×10^6-cm/s collapse velocity from optical streak photographs are consistent with heating by a 0.8×10^6-A return current, representing the recycling of 15% of the hot-electron emission.

At intensities which exceed 10^{15} W/cm^2 most of the energy absorbed from CO_2 lasers goes directly into a relatively small number of highly energetic (>200 keV) suprathermal electrons.[1] This energy must be transferred to a much larger number of localized thermal electrons to accomplish laser fusion. Since direct classical coupling of the suprathermals to the background plasma has proven inefficient, we have initiated an effort to use the self-generated fields in specialized targets to improve the energy transfer. Charge imbalance develops as suprathermals leave a laser spot. The resultant E fields can draw a return current, if an appropriate path is provided. Benjamin et al.[2] have demonstrated the existence of these currents, and their ability to heat a target support stalk. This Letter reports the first experimental results from targets designed to use the return currents to heat and implode a thin-walled hollow cylinder—to produce a micro Z pinch.

A schematic of the "augmented return current" (ARC) targets used in the experiments is given in Fig. 1. Four tightly focused CO_2-laser beams from the Los Alamos Helios laser system impinge on the capped end of a long hollow, low-Z cylinder, coated with a thin layer of metal (gold or aluminum). The cylinder is mounted at the center of a large high-Z disk. Suprathermals generated at the focus will drift toward the disk in the plasma surrounding the cylinder. A thermal return current is drawn back along its walls. Resistivity of the walls results in Joule heating of the thermals. The B field from the resultant current loop can implode and further heat the cylinder.

Experiments were performed on targets with a variety of diameters and lengths. The smallest cylinders were matched to the minimal laser spot diameter. Their length was set at roughly 5 diameters to maximize the aspect ratio for cur-

rent-related effects, under the constraint of minimum mass—for maximum temperature gain from energy deposition. The minimum wall thickness was set by limits on structural integrity. The metal layer was added to provide a brighter signature in x-ray pinhole pictures. The earlier experiments[2] recorded currents from electrons escaping to the walls of the target chamber. The ARC targets were designed to augment this current through the axial alignment of the cylinder and beams, with a cylinder much thicker than the earlier 10-μm stalks, and with the addition of the collector disk for possible suprathermal entrainment. The presence of thermoelectric, $\nabla n \times \nabla T$ B fields has been recognized for some time.[3-5] The cylindrical return currents and any pinch effect should serve to enhance these fields. Suprathermal drift down the cylinder[7] is consistent with a B field, directed as in Fig. 1, and with an outwardly directed E field for containment of the electron cloud. The axial E-field component, drawing the return current against resistivity, introduces a "tilt" in the $E \times B$ drift, which should aid capture of the suprathermals by the cylinder wall. Alternatively, the B field around the cylinder should help to shield its interior from suprathermal preheat.[5] The return-current effects discussed here will be reduced to the extent that deposited energy is lost to fast-ion blowoff. However, cylindrical geometry may serve to reduce fast-ion losses, as compared to those from foils,[6] since the area
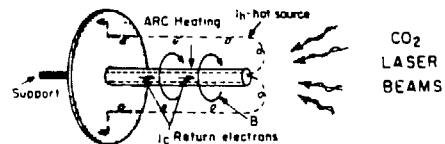

FIG. 1. Sketch of the ARC target design.

459

Detailed observation and analysis of radiation from high-density laser-imploded targets

Allan Hauer

Los Alamos National Laboratory, University of California, Los Alamos, New Mexico 87545

K. G. Whitney, P. C. Kepple, and J. Davis

U.S. Naval Research Laboratory, Washington, D.C. 20375

High-energy CO_2-laser radiation has been used to implode gas-filled spherical targets to very high densities ($10^{23} < n_e < 10^{24}$ cm^{-3}) and temperatures (~ 800 eV). The imploded gas was composed primarily of DT with a small amount of argon seed. The detailed observation of radiation from the argon was a primary diagnostic of the imploded-plasma conditions. An extensive analysis of the emitted argon spectrum provides a rich source of information on plasma parameters. In most cases one could not assume local—thermodynamic-equilibrium conditions. A very detailed collisional-radiative model was constructed in order to analyze the spectrum. In view of the complexity of the calculations that had to be performed and the care needed in data acquisition and processing, the agreement between theory and experiment was very good.

I. INTRODUCTION

Laser-driven implosions have produced high-temperature compressed plasmas with densities comparable to or greater than ordinary solids (a few g/cm^3).[1-3] A whole new regime of very high-density, high-temperature plasma conditions has thus been opened for laboratory investigation.

The production of very high-density compressed plasmas is central to the inertial-confinement fusion concept. Analysis of the radiation from these dense plasmas is an important source of information on their conditions. This analysis may, however, involve relatively complicated modeling techniques. In this paper we describe techniques that have proved useful in the modeling of radiation from compressed plasmas with a density of a few gm/cm^3. The experiment analyzed here has been reported previously.[2]

In Fig. 1, we show a typical target used in high-compression laser-implosion experiments. The targets are

FIG. 1. Target used to produce high-density laser-driven implosions.

imploded by irradiating them with high-intensity CO_2-laser light from the Los Alamos National Laboratory Helios laser facility. Laser energy on target ranged from 3–6 kJ and the half width of the pulse was 600–800 ps.

Within the target is a glass shell filled with a variety of gases; DT is used as the fuel for thermonuclear burn. Spectroscopic diagnosis of plasma temperature and density is accomplished by seeding the DT fuel with a small amount of higher Z material, such as neon or argon. Analysis of line emission from the higher Z material is one of the most direct diagnostics of compressed density.

The thick layer of plastic surrounding the glass shell reduces the preheat of the fuel due to suprathermal (~ 100 keV) electrons and allows an ablative implosion of the shell. In earlier work of this type[4] only the thin glass shell was present. Long-mean-free-path electrons tended to uniformly heat and thus explode this shell. In the present work a slower less explosive implosion[2] has produced considerably higher densities of the order of 20 times the liquid density.

In Fig. 2, we show the general features of argon emission from highly compressed plasmas. The top trace was taken with an exploding pusher target irradiated by about 3.5-kJ laser energy on target and represented a compressed electron density of about 9×10^{22} cm^{-3}. The middle trace was obtained from a target with a coating of 25-μm $CH_2)_x$ (and 4.5-kJ laser energy on target). The compressed electron density here is about 4×10^{23} cm^{-3}. The final trace was produced by a target with 50-μm $CH_2)_x$ coating and about 5.8 kJ of laser energy. The compressed electron density is about 7×10^{23} cm^{-3}. In the experiment represented by the top trace of Fig. 2 the laser heats the glass shell directly; lines due to calcium and potassium, which are impurities in the glass, are excited. When a layer of about 25 μm of plastic is added these lines are suppressed.

The densities in these experiments[2] were measured primarily by fitting time integrated x-ray spectral profiles to theoretical calculations. The theoretical calculations were made for specific densities and did not attempt to take
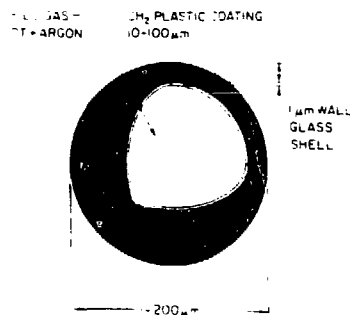
Intensity-Dependent Absorption in 10.6-μm Laser-Illuminated Spheres

D. R. Bach, D. E. Casperson, D. W. Forslund, S. J. Gitomer, P. D. Goldstone, A. Hauer,
J. F. Kephart, J. M. Kindel, R. Kristal, G. A. Kyrala, K. B. Mitchell,
D. B. van Hulsteyn, and A. H. Williams

University of California, Los Alamos National Laboratory, Los Alamos, New Mexico 87545

An intensity dependence of the absorption of 10-μm laser light on CO_2-laser–fusion targets has been observed. Absorption on gold spheres increases from 25%–30% at 10^{14} W/cm² to 30%–40% at 10^{16} W/cm², with most of the variation occurring above 10^{15} W/cm². Concurrently, hot-electron temperature scales as $T_{hot} \propto I^{0.43}$ over the entire range. The absorption variation is interpreted as enhanced resonant absorption. It is suggested that as intensity is increased, the critical surface in the irradiated region becomes increasingly unstable, thereby permitting greater surface distortion and more favorable coupling conditions for resonant absorption.

PACS numbers: 52.25.Ps, 52.35.Ra, 52.50.Jm

The absorption of laser energy is an important factor in the overall performance of a laser-fusion capsule. At the 10.6-μm wavelength produced by CO_2 lasers, spherical-target absorption was previously shown to be in the range 20%–30% for intensities ≤ 10^{15} W/cm² and below.[1,2] We report here the observation of an increase in absorption to as high as 60% when intensity is increased to 10^{16} W/cm².

The experiments reported here were done on the Los Alamos National Laboratory eight-beam Helios CO_2 laser facility,[3] at energies up to 5 kJ. The targets were gold spheres mounted on slender glass stalks. The diameters were 0.3, 1, and 2 mm, with wall thickness between 0.3 and 31 μm. Absorption was measured with an array

FIG. 1. Absorption vs intensity for gold spheres: triangles, 0.3 mm diam (9 shots); squares, 1.0 mm diam (62 shots); dots, 2.0 mm diam (43 shots). Error bar is average for all shots and includes the standard deviation of the various calorimeters. The curves are least-squares linear fits to the data.

of fourteen calorimeters[4] deployed around the target chamber, each sensitive to particle flux as well as to x-ray photons; scattered 10-μm light is specifically rejected.

Figure 1 shows the absorption as a function of intensity. The latter is varied primarily by defocusing and occasionally by total-energy variation. Individual beam intensity at best focus is computed with a 100-μm spot diameter containing 75% of the energy, and a pulse width of 0.75 ns (full width at half maximum). For all eight beams, an energy-weighted average is used to determine laser intensity. Defocused intensity is obtained from simple geometric considerations with an $f/2.4$ beam expansion from the waist.

The data show a very clear doubling in absorption for 0.3- and 1-mm-diam spheres as intensity is increased from 10^{15} to 10^{16} W/cm². The effect is not as dramatic with the 2-mm spheres, absorption increasing from 25% to only ~35% at 10^{16} W/cm². The variation with target diameter may be an instrumental effect. Measurements of the ion angular distribution on flat targets show the presence of an ion plume in the direction of the target normal. In the present experiments the normal is nominally toward the laser focusing mirrors. The ions involved are not collected by the calorimeter system and may represent an increasingly significant amount of undetected absorbed energy as the target radius increases. However, we cannot rule out the possibility that the diameter variation is real, a point which we will return to later.

Additional supporting evidence for the intensity variation has been obtained from scattered-light measurements under single-beam illumination on 1-mm-diam targets. The $f/2.4$ focusing optics

Use of Laue-geometry x-ray diffraction in the spectroscopy of laser plasmas

Allan Hauer

Los Alamos National Laboratory, University of California, Los Alamos, New Mexico 87545

Laue x-ray crystal diffraction geometry offers a number of advantages for the spectroscopic diagnosis of laser plasmas. Applications of this diffraction configuration, such as absorption spectroscopy, time-resolved spectroscopy, and x-ray polarization measurements are described.

Crystal x-ray spectroscopy has become a common and useful diagnostic of laser-produced plasmas.[1] Most of this work has utilized what is termed Bragg-diffraction geometry, in which the x-ray-diffracting planes are approximately parallel to the entrance surface. Laue geometry utilizes diffraction from planes that are approximately perpendicular to the entrance surface.[2] The most important aspect of this geometry is that it produces quasi-focusing, as shown in Fig. 1(a). All wavelengths from a point source are diffracted to lie (approximately) along the same line perpendicular to the axis that passes through the source point and is parallel to the diffracting planes.[3]

The focusing is not completely stigmatic for either perfect or mosaic crystals. As is shown in Fig. 1(b), the width of the diffracted beam is governed by the thickness of the crystal.[4] The width of the diffracted beams, and thus the approximate focusing resolution, is

$$W = \frac{t \sin(2\theta_B)}{\cos\theta_B}, \qquad (1)$$

where t is the crystal's thickness and θ_B is the Bragg angle. Given this limitation on the spatial resolution, the quasi-focusing characteristic is still quite useful in spectrograph design. Kinematic diffraction theory[5] shows that the maximum diffracted intensity in the Laue geometry occurs when the crystal's thickness is $1/\mu_0$, where μ_0 is the linear absorption coefficient. A rough expression for the resolution could thus be written as

$$W = \frac{\sin(2\theta)}{\mu_0 \cos\theta_B}. \qquad (2)$$

A high-energy spectrograph utilizing this geometry has already been operated.[6] In this paper several other ideas are described for applications of Laue-geometry diffraction to laser plasma spectroscopy.

One application of Laue diffraction is in absorption spectroscopy. The dense compressed core of laser-imploded plasmas may sometimes be too cool to produce usable self-emission (e.g., for diagnosis of compressed density). One method of diagnosing such plasmas would be to use an external source of radiation and employ absorption spectroscopy. This, however,

poses some problems for instrumentation. One wants to probe a region of small spatial extent. Crystal diffraction, however, requires an angular spread (given by Bragg's law) in order to produce dispersion. In Fig. 2, we show two Laue diffraction configurations that are applicable to absorption spectroscopy. If the source is small, the configuration of Fig. 2(a) is appropriate. In Fig. 2(a) diffraction from the second crystal is used to protect the film from being blackened by direct radiation from the main target. This configuration requires the rather precise alignment that is characteristic of double-crystal spectroscopy.[2] A small source may be more appropriate for strong high-energy continuum generation, since high laser flux will lead to higher plasma temperatures. If a more distributed source of x rays is employed, the configuration in Fig. 2(b) is appropriate. The quasi-focusing geometry will efficiently shield against background radiation (such as hard x rays generated by the primary target itself).

We consider a typical example of the application of the configuration in Fig. 2(b). For a moderately dense compressed core, probing with radiation in the region of 10 keV might be appropriate. Consider a band from 10 to 12 keV. For a Ge crystal (220 planes and $2d = 4.0$ Å), the Bragg angle would vary from 18 to 15 deg. In practice, the probe source cannot be located closer than
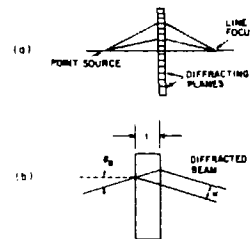
Fig. 1. (a) Quasi-focusing produced by Laue-geometry diffraction; out of the plane of this figure the beam is diverging. The line focus is normal to the plane of the figure. (b) Illustration of the effect of crystal thickness on focusing.

Experimental Evidence for Self-Generated Magnetic Fields and Remote Energy Deposition in Laser-Irradiated Targets

M. A. Yates, D. B. van Hulsteyn, H. Rutkowski, G. Kyrala, and J. U. Brackbill

Los Alamos National Laboratory, Los Alamos, New Mexico 87545

In a series of experiments using two-, four-, and eight-beam 10.6-μm-laser irradiation of a variety of target geometries, a significant amount of energy was found to be deposited in regions remote from the focal spots. The deposition patterns can be predicted with a self-generated magnetic field model.

Lateral transport of energy away from laser focal spots can play an important role in redistributing energy deposition in laser-fusion targets. Work has been reported investigating the qualitative[1] and quantitative[2] nature of this transport. Recently, using a plasma simulation, Forslund and Brackbill[3] have identified convective transport of electrons in self-generated magnetic fields as an important mechanism for surface transport in laser-irradiated foils. In one simulation with a laser intensity of 5×10^{13} W/cm^2 in a 60-μm spot and a hot-electron temperature of 20 keV, peak fields of the order of 1 MG were calculated. The calculation has not been performed at higher intensities comparable to those used in experiment ($\sim 10^{16}$ W/cm^2) because the code does not handle the relativistic effects of the high-energy electrons generated at these intensities. In general, the ratio of electron to magnetic field pressure is of order 1 in a magnetized sheath whose thickness is large compared with the electron gyroradius. This Letter presents experimental evidence for the nonuniformity of energy deposition predicted by the magnetic field model in a variety of target geometries progressing from flats to cylinders to spheres.

From the simulations, a simple qualitative model has been developed. Briefly, the model describes lateral energy transport by electrons in magnetic fields generated at the periphery of the *laser spot by lateral temperature gradients* in the corona. These gradients are maintained by electrons confined and drifting in the magnetic field, resulting in the convective transport of energy from the beam spot to the edge of the magnetized region. The interaction of the magnetic field and electrons produces a thermal magnetic wave[4] which propagates across the surface until disrupted by fringing fields at the target edge or by destructive interference with the wave propagating from an adjacent beam.

A result of this description is that the higher-energy electrons which transport energy away from the laser spot are magnetically insulated from the target surface. However, where thermal magnetic waves from adjacent beams interfere, as depicted in Fig. 1(a), there is a magnetic field null. At that point the electrons deposit their energy into the target. We have performed an experiment with two beams on a flat target which dramatically shows this effect, as seen in Fig. 1(b). In addition, we have taken data in more complex geometries which also show patterns of deposition consistent with transport dominated by self-generated fields.

All experiments were performed at the Helios laser facility[5] of the Los Alamos National Laboratory. This is a carbon-dioxide system with a
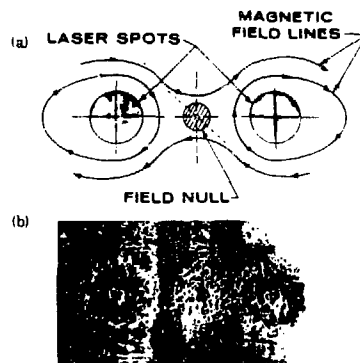
FIG. 1. Energy deposition region between two laser beams as (a) predicted by simulations using convective electron transport in self-generated magnetic fields and (b) recorded experimentally with an x-ray pinhole camera from two beams spaced 1 mm apart on a flat gold target.

Acceleration of multi-species ions in CO₂ laser-produced plasmas: Experiments and theory

Fred Begay and David W. Forslund

University of California, Los Alamos National Laboratory, Los Alamos, New Mexico 87545

Experimental and theoretical results on the properties of CO₂ laser-induced carbon and polyethylene (CH₂) plasmas at laser intensities of ~ 10¹⁵ W/cm² are presented. The Thomson parabola technique is used to measure the ion velocity distribution in the underdense expanding plasma which is collisionless and isothermal. A model which treats the problem of the collisionless expansion of an isothermal electrostatic multi-cold-ion quasineutral plasma will be used to interpret the experimental results. Experiments and theory show that the effect of hydrogen in the CH₂ target induces a cutoff in the carbon ion velocity distribution. Theory suggests that acceleration field attenuation effects modify the behavior of these plasmas. Data suggest that the space–time evolution of the ion velocity distribution is completed before an ionization-recombination equilibrium is reached. Experimental results from the underdense region are used to estimate plasma parameters near the critical surface, which show that the presence of hydrogen in the target apparently greatly reduces the thermal temperature near the critical surface, probably due to enhanced lateral energy transport.

I. INTRODUCTION

In laser–matter interaction experiments, a basic understanding of the dynamics of the expanding plasma in the low-density coronal region is essential to describe the effects of interaction processes, such as laser absorption and scattering, on the implosion efficiency. The inertial confinement process must proceed with high implosion efficiency to achieve successful thermonuclear fusion yields. The diversion of absorbed laser energy from the implosion process to the production of energetic ions and electrons and other losses must be minimized.

Much attention has been devoted to the question of expanding collisionless ion flows in laser-induced plasmas.[1,2] In these studies the properties of single-ion flows were investigated. The expansion into vacuum of a collisionless plasma with two ion species was first treated by Gurevich *et al.*[3]

In this paper we propose a model which treats the expansion into a vacuum of a collisionless electrostatic plasma with an arbitrary number of ion species. If the initial conditions are properly chosen, the density and velocity flow solutions in our model are in agreement with the density and velocity flow solutions reported in Ref. 3. The model will be tested with experimental data from laser-induced carbon and polyethylene plasmas. In particular, we wish to examine the effect of hydrogen impurities on carbon plasmas. We have found that this work is the first to investigate both experimentally and theoretically the effect of hydrogen impurities on carbon plasmas.

Results from many investigations[4] on typical density and temperature profiles of the laser ablation process are summarized in Fig. 1, where four regions have been defined as a function of different states of matter.

(1) The undisturbed solid (I) bounded by the shock front (s),

(2) the shock compressed region (II) bounded by the ablative surface (a),

(3) the overdense heat conduction zone (III) bounded by the critical density layer (c) and

(4) the underdense expanding plasma (IV).

This paper will primarily report on the experimental and theoretical results in region IV, where the underdense expanding plasma is collision-less and isothermal. We attempt to determine the electron temperature in the low-density corona, how that varies with target material, and what are the implications for energy transport.

Many CO₂ laser-matter experiments[5] have been performed at Los Alamos to investigate the effect of target impurities and surface contamination on the behavior of laser-induced plasmas.

Experimentally, we observe that the pure carbon plasma expands isothermally, and that the C⁺⁶ ions do acquire asymptotic kinetic energies of approximately 9 MeV. The C⁺⁵ and C⁺⁶ ions appear to self-consistently attenuate the
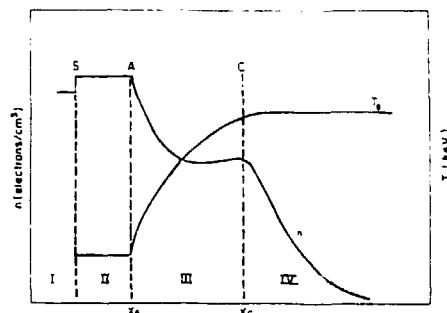
FIG. 1 Typical density–temperature profiles versus distance of the laser ablation process

Surface plasma absorption in an integrating sphere at high optical flux levels

Richard Kristal

University of California, Los Alamos National Laboratory, P.O. Box 1663, Los Alamos, New Mexico 87545.
Received 2 March 1982.

Integrating spheres have been used in the past to make 4π scattered light measurements on laser irradiated targets.[1,2] From these measurements absorption of laser light by targets has been inferred. In investigating the extension of this technique to higher-energy laser fusion measurements, a strong nonlinearity was observed in the sphere response. It takes the form of a saturation of the energy output signal as the input energy is increased. The problem was traced to optical breakdown of the walls of the sphere with significant absorption occurring in the plasma generated on the walls.
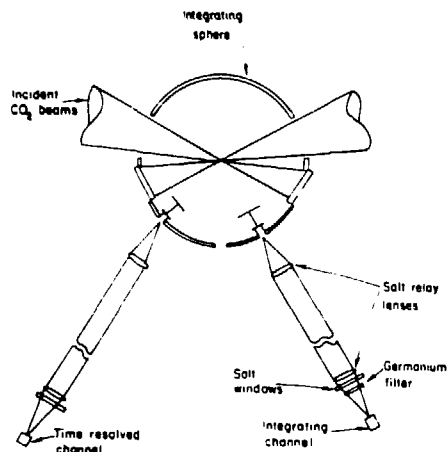
Fig. 1. Integrating sphere experimental configuration

A diagram of the experimental setup is shown in Fig. 1. The sphere is 30-cm diam with a diffuse gold-coated interior surface. Two laser beams enter the sphere through $f/2.4$ entrance holes. The laser source was the Los Alamos Gemini two-beam CO_2 laser facility with a capability of up to ~500
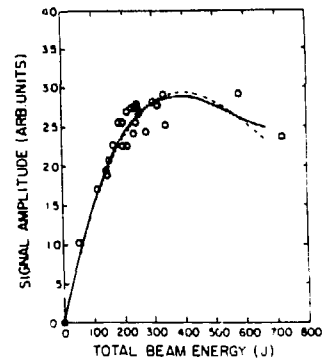
Fig. 2. Energy monitor (integrating channel) response vs total beam energy. Solid curve is least-squares third-degree polynomial fit. Dashed curve is computed from time-resolved data normalized to the polynomial fit at 300 J.

J/beam in a 1-nsec pulse at $\lambda = 10.6\ \mu$m. Two detectors were used on the sphere, one integrating and one time-resolved. Both were pyroelectric but of different material and design. The detectors were coupled by salt optics to baffled access holes in the sphere. The sphere and optics were mounted inside the evacuated target chamber (10^{-6}–10^{-5} Torr) in which experiments were performed; the optical detectors were mounted outside the vacuum chamber.

To use the sphere for target reflectivity measurements it is calibrated *in situ* by firing the beams directly into the empty sphere. The beams then impinge on solid copper diffuser plates. In this mode and in ideal conditions the signal ob-

104

SURVEY OF ATOMIC PHYSICS ISSUES IN EXPERIMENTAL
INERTIAL CONFINEMENT FUSION RESEARCH.*

Allan Hauer

University of California
Los Alamos National Laboratory

E. J. T. Burns
Sandia National Laboratory

Atomic processes impact many of the interactions important to
inertial confinement fusion. For example, ionization of bound
electrons represent one of the primary stopping mechanisms for
both ions and electrons. Atomic processes are also important in
predicting the behavior of the very dense plasmas which are central
to the success of inertial fusion. Atomic spectroscopy is an
important diagnostic of ICF plasmas.

INTRODUCTION

Inertial confinement fusion (ICF) requires the production of high temperature,
high density plasma. Laser driven implosions have, for example, been able to
produce plasma densities of the same magnitude as ordinary solids (a few
g/cm^3) with temperatures of the order of a kilovolt. Atomic processes play
an important role in the generation of such plasma conditions. In addition,
atomic spectroscopy has become an important diagnostic of ICF plasma conditions.

Atomic processes are also very important in the physics of ICF drivers. Design
of ion sources and accelerators, beam propagation, more efficient and variable
wavelength lasers, are crucial problems in the ICF field. Space does not,
however, permit dealing with this very important component of the ICF field.

In Fig. 1, we illustrate the general nature of the interactions involved in
particle and laser driven compression.
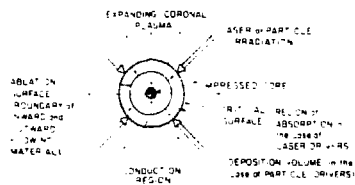
Figure 1.
Schematic of Laser/Particle
Target Interaction

In the case of laser heating, energy is absorbed at an electron density near
the critical value for the laser involved (10^{19} cm^{-3} for CO_2, 10^{21}
cm^{-3} Nd:glass). Atomic processes can be quite important in the ionization
and recombination dynamics in the absorption region.

REPRINTS IN
THEORETICAL PLASMA PHYSICS
SINCE
1982

Two-Dimensional Simulations of Single-Frequency and Beat-Wave Laser-Plasma Heating

D. W. Forslund and J. M. Kindel

Los Alamos National Laboratory, Los Alamos, New Mexico 87545

and

W. B. Mori, C. Joshi, and J. M. Dawson

University of California, Los Angeles, California 90024
(Received 9 October 1984)

Finite-beam, two-dimensional particle simulations of single- and double-frequency laser-plasma heating are presented. In the single-frequency case, Raman backscatter and side scatter initially heat the plasma. Even in the absence of strong forward Raman scattering, strong subsequent electron heating is observed. When two collinear laser beams with $\Delta\omega = \omega_p$ are used, a coherent plasma wave heats the electrons to many megaelectronvolts. In the latter case, ion dynamics eventually disrupts the heating process.

Recently there has been a great deal of interest in underdense plasma heating by intense laser beams.[1] In order to understand the various processes occurring in such a plasma, we have carried out two-dimensional (2D) mobile ion particle simulations using finite laser beams incident onto a large-scale highly underdense plasma. Previous 1D simulations have indicated that Raman backscattering (RBS) and forward scattering (RFS) can play an important role in heating the electrons to high energies in such plasmas. An important question is whether the heating process is altered by 2D effects. Some of the 2D phenomena are Raman side scattering (RSS), self-generated magnetic fields, Weibel instabilities, whole beam self-focusing, and filamentation. In this Letter we show that these competing effects do indeed occur. Furthermore, at very high laser intensities electrons can be strongly heated even in the absence of coherent forward Raman scattering.

In order to understand the energies of electrons produced in wave-particle interactions, 2D simulations of beat heating of the plasma by two collinear lasers with frequency difference equal to the plasma frequency have been carried out. In this case a very coherent, large-amplitude plasma wave is set up at wave number $k_p = k_0 - k_1$. The time to saturation and the saturation amplitude of the plasma wave electric field is in reasonable agreement with Rosenbluth and Liu's[2] theory. This coherent plasma wave heats the electrons to many megaelectronvolts and produces maximum electron energies predicted by single-particle theory.[3]

The simulations were carried out using the particle code WAVE on a Cartesian grid in the x-y plane. The plasma is $60c/\omega_p$ long in both x and y. The laser beam has a $\cos^2 y$ transverse profile with zero amplitude at $10c/\omega_p$ and $50c/\omega_p$ in y. Other parameters are $T_i/T_e = 1$, $m_i/m_e = 1836$, and $(2kT/mc^2)^{1/2} \sim 0.1$. Simulations were carried out with different laser and

plasma parameters to cover the parameter regime of interest in both laser fusion and the plasma beat-wave accelerator.[3] As representative of these simulations, we discuss two particular cases in this paper.

First, a single-frequency laser beam with an rms intensity $v_0/c = 0.8$ and a rise time τ of $800/\omega_p$ is injected from the left-hand boundary in the x direction into a plasma with $\omega_0/\omega_p = 5$. Here $V_0/c = eE_z/mc\omega_0$ is the quiver velocity in the laser field E_z and ω_0/ω_p is the ratio of the laser frequency to the plasma frequency. Raman backscatter/stimulated Compton scatter (SCS) is first to appear with a broad frequency spectrum peaked at frequency $\omega_0 - \omega_p$ at time $300/\omega_p$. The RBS/SCS plasma wave with $v_\phi/v_{th} \sim 1.5$ does trap and heat a few electrons to a maximum energy of ~ 100 keV. An interesting feature revealed by the 2D simulations, as shown in the contour plot of Fig. 1(a) even at this early stage, is the generation of a magnetic field in such an underdense plasma. At this early time, $300 \times \omega_p^{-1}$, the magnetic field is typically $\omega_c/\omega_p \sim 0.1$ (~ 200 kG for CO_2 parameters) and has a pattern characteristic of hot-electron filamentation due to the Weibel instability,[4] as shown in the slice plot of Fig. 1(b). On the other hand, later in time when direct laser heating dominates, the magnetic field can reach $\omega_c/\omega_p \sim 0.6$ and it is indicative of a current pattern produced by a single beam of energetic electrons moving down the axis and a relatively colder return current of electrons on the outside of the directed electron beam.

The most striking difference between the 1D and 2D simulations, however, is the occurrence of RSS in the latter. RBS evolves very quickly into RSS as the plasma begins to heat up and damping for the short-wavelength plasmons increases. Initially, RSS occurs in the backward hemisphere over a broad range of angles but at later times occurs predominantly in the forward hemisphere. In Fig. 1(c) the contour plot of the

LA-UR 84-1357

Plasma Heating at Collisionless Shocks Due to the Kinetic Cross-Field Streaming Instability

D. WINSKE,[1] MOTOHIKO TANAKA,[2] C. S. WU,[3] AND K. B. QUEST[1]

Heating at collisionless shocks due to the kinetic cross-field streaming instability, which is the finite beta (ratio of plasma to magnetic pressure) extension of the modified two stream instability, is studied. Heating rates are derived from quasi-linear theory and compared with results from particle simulations to show that electron heating relative to ion heating and heating parallel to the magnetic field relative to perpendicular heating for both the electrons and ions increase with beta. The simulations suggest that electron dynamics determine the saturation level of the instability, which is manifested by the formation of a flattop electron distribution parallel to the magnetic field. As a result, both the saturation levels of the fluctuations and the heating rates decrease sharply with beta. Applications of these results to plasma heating in simulations of shocks and the earth's bow shock are described.

1. INTRODUCTION

It has been well established for many years that the heating of plasma at collisionless shocks results from the interaction with waves generated by microinstabilities, through many experimental investigations both in the laboratory and in space of the heating of the plasma and associated wave spectra and theoretical studies of the instabilities and their consequences. Summaries of this work over the past two decades can be found in the reviews by Biskamp [1973], Boyd [1977], Davidson and Krall [1977], Greenstadt and Fredericks [1979], and the collection of invited talks at the 1984 Chapman Conference on Collisionless Shocks.

The types of waves and the characteristics of the heating which result depend on the sources of the free energy that drive the instabilities, which in turn depend on the nature of the shock. For example, at quasi-perpendicular supercritical shocks the principal dissipation mechanism is the reflection and subsequent thermalization of some of the incident ions. Such reflected ions lead to the observed foot or pedestal structure in the magnetic field, bimodal ion distributions, strong ion heating, and long-distance scale over which such heating occurs [Montgomery et al., 1970; Greenstadt et al., 1980]. The reflection process has been clearly observed recently at the bow shock [Paschmann et al., 1982; Sckopke et al., 1983] and in simulations [Leroy et al., 1981, 1982; Forslund et al., 1984]. Electron heating for these shocks is usually less intense and occurs over a much shorter distance, typically the length of the magnetic transition starting at the front edge of the foot [Bame et al., 1979]. At quasi-parallel shocks, however, the presence of large-amplitude waves extending over a long distance obscures the shock transition and the nature of the heating process [Greenstadt et al., 1977].

For quasi-perpendicular shocks when ion reflection is not dominant, the principal source of the instabilities which heat the electrons and ions is the cross-field current [e.g., Biskamp, 1973; Lemons and Gary, 1978; Wu, 1982]. This cross-field current implies a relative electron-ion drift, which gives rise to various instabilities. While in some of the laboratory experiments clear identification of the particular instabilities which provide the dissipation can be made [e.g., Boyd, 1977; Fahrbach et al., 1981], this has not been true of spacecraft observations of collisionless shocks. Such shock encounters usually exhibit a very broad spectrum of electrostatic and electromagnetic noise [e.g., Rodriguez and Gurnett, 1975; Gurnett et al., 1979; Greenstadt et al., 1980]. The identification of the individual wave modes is difficult, hampered by the fact that only Doppler shifted frequencies are measured and the wave vectors are not resolved. The heating at such shocks in space is primarily in the ions [Thomsen et al., this issue], while for shocks in the laboratory the principal heating often occurs in the electrons [e.g., Boyd, 1977], although strong ion heating is sometimes observed [e.g., Davidson and Freidberg, 1976].

The principal instabilities which are thought to occur at shocks are the ion acoustic and "lower hybrid" modes. The ion acoustic instability is a short wavelength (approximate electron Debye length), high frequency (approximate ion plasma frequency) electrostatic mode which has been studied extensively (see reviews by Biskamp [1973], Galeev [1976], Boyd [1977], and Papadopoulos [1977]). It gives rise to a large resistivity and heats the electrons in the bulk of the distribution and the ions in the tail of the distribution, as has been verified by computer simulation [Dum et al., 1974]. Evidence for the existence of ion acoustic modes at shocks derives from the observed electrostatic noise and the fact that the width of many shocks is consistent with the threshold condition for the ion acoustic instability [Morse and Greenstadt, 1976; Russell et al., 1982]. The threshold condition has also been used to distinguish between resistive and diffusive laminar shocks [Mellott and Greenstadt, 1984]. The principal difficulty with the ion acoustic instability is that this threshold value, which must be exceeded in order to excite the instability, is rather large ($v_d/c_e > T_i/T_e$, where v_d is the relative electron drift speed, v_e is the electron thermal speed, and T_e (T_i) is the electron (ion) temperature).

In many laboratory experiments as well as usually at the bow shock, conditions for the excitation of the ion acoustic instability are not satisfied. In such cases the principal heating and resistivity is thought to come from the lower hybrid modes. The term lower hybrid is used here to describe various related instabilities: the modified two-stream instability [McBride et al., 1972], which is an electrostatic fluidlike mode, the kinetic cross-field streaming instability [Wu et al., 1983], which is its extension to finite beta (ratio of plasma to magnetic pressure), and the lower hybrid drift instability [Krall and Liewer, 1971], which includes relative drifts due to gradi-

[1] Los Alamos National Laboratory, New Mexico.
[2] Institute for Fusion Studies, Hiroshima University, Japan.
[3] Institute for Physical Science and Technology, University of Maryland, College Park.

108

Measurement and Analysis of Near-Classical Thermal Transport in One-Micron Laser-Irradiated Spherical Plasmas

A. Hauer, W. C. Mead, and O. Willi

Los Alamos National Laboratory, Los Alamos, New Mexico 87545

and

J. D. Kilkenny, D. K. Bradley, and S. D. Tabatabaei

Imperial College, London, United Kingdom

and

C. Hooker

Rutherford Appleton Laboratory, Chilton, Didcot, United Kingdom

(Received 10 August 1984)

Solid spherical layered targets have been uniformly illuminated at irradiances of 10^{14} to 10^{15} W/cm². Extensive diagnostics including time-resolved x-ray emission and optical probing were used to determine the plasma ablation rate and the plasma blowoff conditions. Comparisons with hydrodynamic simulations show that the thermal conduction is well characterized by a flux limit $f_e = 0.08 \pm 0.02$, with a steep temperature gradient. The steepness of the heat front was confirmed with time-resolved spectroscopy.

Knowledge of energy transport from the region of the laser-light absorption to denser portions of laser-produced plasmas is crucial to an understanding of the laser-induced ablation process.[1-3] Extensive recent computer simulation work[3] has led to the expectation that "classical" transport in spherical laser-heated plasmas can generally be approximated by flux-limited diffusion with a flux limiter in the range of $f_e \approx 0.06-0.2$. Early work, largely involving flat targets, indicated strong to moderate inhibition of the heat flux relative to classical predictions.[4] Some of the more recent work involving spherical targets has indicated transport levels closer to classical,[5] with evidence of a penetrating foot in one case.[6] Other work indicates some flux inhibition even in spherical geometry.[7]

In the present experiment we have used a comprehensive set of diagnostics to characterize the plasma conditions and thermal transport in a spherically symmetric plasma. We have made time-resolved spectroscopic measurements (using both low- and moderate-Z radiating ions) of the penetration of the heat front in spherical plasmas. In addition, we have used optical probing to measure simultaneously the density profile of, and the magnetic field in, the underdense plasma. Comparisons with hydrodynamic modeling show that (a) all observables are consistent with a high flux limit and (b) the heat front shows no observable foot.

The targets used in this study consisted of solid glass spheres (~ 160 μm diameter), containing Si and Ca (among other constituents), coated with

three layers: (1) CH (0.5 to 2.5 μm thick), (2) Al (0.1 μm), and (3) CH (0.5 to 2.5 μm). The solid glass ball prevented implosion of the target (and subsequent inward movement of the critical surface).

The targets were uniformly illuminated with the six-beam, 1.06-μm, laser facility at the Rutherford Appleton Laboratory.[8] The six beams were focused by $f/1$ lenses with optical axes along the faces of a cube. Incident irradiance levels were in the range $(1.5-15) \times 10^{14}$ W/cm². The laser pulse had an approximately Gaussian temporal profile with 0.83-ns full width at half maximum (FWHM).

The radial intensity profiles of the beams were measured. Small-scale structure results in about 30% rms variation in intensity. The overlap of the six beams and beam-to-beam energy variation resulted in about 50% (peak-to-valley) large-scale variation in incident irradiance across the surface of the sphere.[9]

The primary diagnostic of thermal transport was time-resolved x-ray line spectroscopy. X-ray line emission was observed first from the thin aluminum layer (sensing temperatures of 200-350 eV) and later from the silicon ($\sim 250-400$ eV) and calcium ($\sim 500-700$ eV) in the glass ball.[10]

X-ray emission from the target was dispersed (with a thallium acid phthalate crystal) onto the slit of a streak camera covering 1.7 to 2.4 eV. The spectral and temporal resolutions were about 500 ($\lambda/\Delta\lambda$) and 50 ps, respectively. A seventh laser beam with very short duration (~ 100 Γ was used

2563

Nonlinear evolution of the lower-hybrid drift instability

J. U. Brackbill, D. W. Forslund, K. B. Quest, and D. Winske

Los Alamos National Laboratory, Los Alamos, New Mexico 87545

The results of simulations of the lower-hybrid drift instability in a neutral sheet configuration are described. The simulations use an implicit formulation to relax the usual time step limitations and thus extend previous explicit calculations to weaker gradients, larger mass ratios, and long times compared with the linear growth time. The numerical results give the scaling of the saturation level, heating rates, resistivity, and cross-field diffusion and a demonstration by comparison with a fluid electron model that dissipation in the lower-hybrid drift instability is caused by electron kinetic effects.

I. INTRODUCTION

The lower-hybrid drift instability remains one of the most widely studied microinstabilities, with many applications to both laboratory and space plasmas. Laboratory devices in which the instability has been predicted by theory to occur, inferred to be present from experimental data or actually observed, include: theta pinches,[1-5] field-reversed configurations,[6-9] reversed field z pinches,[10,11] tormac,[12] tandem mirrors,[13] and bumpy tori.[14] Regions in space where the instability is thought to exist include both the ionosphere[15-18] and the magnetosphere (bow shock,[19] magnetopause,[20] and magnetotail[21,22]). While all of these applications have received some attention, the two configurations most commonly studied in recent years with regard to the instability involve a neutral sheet geometry: field-reversed configurations (FRC's, i.e., reversed field theta pinches) and the Earth's magnetotail. In the first case the lower-hybrid drift instability is thought to be responsible for the anomalous particle loss across the separatrix,[6,7] which eventually leads to the destruction of the configuration, and the anomalous flux loss in the region of the field null.[8] The lower-hybrid drift instability has also been invoked as the cause of the enhanced resistivity needed for reconnection in the magnetotail,[21,22] although the mechanism by which the instability penetrates to the high-beta region at the field null is still unresolved.

The lower-hybrid drift instability is a likely source of turbulence in many of these configurations because it is rather easy to excite. It is driven by density and temperature gradients (which can be very weak), relatively insensitive to the temperature ratio, and completely suppressed only at very high (~ 1) beta.[23] Generally, most of the theoretical work has involved local, linear analysis, including various effects (finite beta,[23-27] shear,[11,28] curvature,[29,30] etc.) as needed for specific applications. Nonlocal analyses have also been carried out, but because of the complexity of the calculations, over much more limited parameter ranges.[31] These calculations have enhanced the credibility of local theory as well as addressed important issues, such as the penetration of the linear eigenmodes to the field null in the reversed field geometry, which is beyond the scope of local theory. Nonlinear theory has also been actively pursued.[32-37] Efforts have been primarily aimed at investigating the saturation mechanism(s) for the instability (as will be reviewed later). Besides its intrinsic interest, the saturation level of the fluctuations is needed when evaluating appropriate quasilinear expressions for the resistivity and heating rates.[38,39]

Numerical simulation has also played an important role in verifying linear theory, eliciting saturation mechanisms, and in emphasizing the nonlinear consequences (heating, resistivity, diffusion) of the instability. A number of such calculations have been done in two dimensions[40-42] or with pseudo-two-dimensional techniques,[43] both in simple sheath geometries and in reversed field configurations.[44,45] The latter calculations are especially interesting because a characteristically different mode develops at the field null, presumably as a nonlocal, nonlinear consequence of the lower-hybrid drift instability excited outside of this region. Generally, however, the simulations have been limited by the size of present day computers to examining either the evolution of the instability only through the linear growth and saturation stages or to the use of somewhat artificial parameters (e.g., mass ratios $m_i/m_e \sim 100$ instead of 1836) to compress time and distance scales. The present study is motivated in part by the development of an implicit particle code VENUS.[46] The implicit formulation relaxes the well-known restrictions on time step and cell size, allowing the extension of previous calculations to either larger mass ratios, weaker gradients, and larger system sizes (allowing more modes to interact) or to long times compared with the linear growth time. The long time behavior is especially important because the instability is usually observed in this state where its slow, nonlinear evolution causes diffusion and heating in laboratory experiments that are crucial when considering the scaling to reactor size devices. Similarly, in space plasmas an understanding of the steady-state microscopic diffusion and heating processes that occur at the bow shock and magnetopause is needed to determine the overall energy balance in the magnetosphere.

The major portion of this paper is divided into three parts, early time, saturation, and late time, corresponding to the natural phases of evolution of the instability. In Sec. II (early time) the geometry is described, a brief summary of the simulation method is given, and properties of the linear modes obtained from simulation are compared with linear theory. The saturation phase is described in Sec. III. Various saturation mechanisms are reviewed and results of the simulation are used to show that the scaling of the simulation agrees with several of the theories. The saturation mechanism is further clarified by studying the mode structure in

110

Solution of Elliptic Equations
Using Fast Poisson Solvers

PAUL A. BERNHARDT AND J. U. BRACKBILL

Los Alamos National Laboratory
Los Alamos, New Mexico 87545

Certain nonseparable elliptic equations may be transformed into a sequence of Poisson equations. The solutions of these equations are efficiently found using fast Poisson solvers. The method is illustrated by solving for the internal electric potential in convecting plasma clouds.

1. INTRODUCTION

In a recent review article by Detyna [4], it is stated that there are "no rapid elliptic solvers (RES) capable of solving a general nonseparable elliptic partial differential equation (EPDE) in 2 or 3 dimensions." There exist, however, RES which may be applied to general separable EPDEs. It is the purpose of this paper to show that linear self adjoint EPDEs have a series solution or have an iterative solution such that each term in the solution is described by a separable EPDE. RES in the form of fast Poisson solvers provide these terms. The solution procedure, which is an extension of the method described in Brackbill and Forslund [1], is illustrated with an example of the internal electric potential associated with nonlinear plasma transport.

2. DERIVATION OF THE RECURSIVE SERIES

Consider the self adjoint, nonseparable generalization of Poisson's equation in two dimensions

$$\frac{\partial}{\partial x}\left[A(x,y)\frac{\partial}{\partial x}\phi_0(x,y)\right] + \frac{\partial}{\partial y}\left[B(x,y)\frac{\partial}{\partial y}\phi_0(x,y)\right] = S_0(x,y), \qquad (1)$$

where $\phi_0(x,y)$ is the unknown function. A and B are nonzero functions with the same sign. Depending on boundary condition (Dirichlet, Neumann, periodic, or mixed) $S_0(x,y)$ may have to satisfy certain compatibility conditions.

Equation (1), in general, cannot be solved directly with rapid elliptic solvers. The solution of (1) is based on (1) splitting the derivatives into curl free and gradient free parts and (2) using the identities $\nabla \times \nabla \psi = 0$ and $\nabla \cdot \nabla \times \phi = 0$ to isolate terms

In two dimensions, we define the functions ρ_0, ϕ_1, and ψ_0 by

$$A\frac{\partial\phi_0}{\partial x} = \frac{\partial\psi_0}{\partial y} + \frac{\partial\phi_1}{\partial x} \qquad (2a)$$

$$B\frac{\partial\phi_0}{\partial y} = -\frac{\partial\psi_0}{\partial x} + \frac{\partial\phi_1}{\partial y} \qquad (2b)$$

Substitution of (2a) and (2b) into (1) yields Poisson's equation,

$$\frac{\partial^2\phi_0}{\partial x^2} + \frac{\partial^2\phi_0}{\partial y^2} = S_0(x,y) \qquad (3)$$

The equation for ϕ_1 is found by equating expressions for $\partial^2\phi_0/\partial x\partial y$ obtained from (2a) and (2b).

$$\frac{\partial^2\phi_0}{\partial x\partial y} = \frac{\partial}{\partial y}\left(\frac{1}{A}\frac{\partial\psi_0}{\partial y}\right) + \frac{\partial}{\partial y}\left(\frac{1}{A}\frac{\partial\phi_1}{\partial x}\right) = -\frac{\partial}{\partial x}\left(\frac{1}{B}\frac{\partial\psi_0}{\partial x}\right) + \frac{\partial}{\partial x}\left(\frac{1}{B}\frac{\partial\phi_1}{\partial y}\right) \qquad (4)$$

Equation (4) is rewritten as

$$\frac{\partial}{\partial x}\left(A^*\frac{\partial\phi_1}{\partial x}\right) + \frac{\partial}{\partial y}\left(B^*\frac{\partial\phi_1}{\partial y}\right) = S_1(x,y), \qquad (5)$$

where $A^* = 1/B$, $B^* = 1/A$, and

$$S_1(x,y) = \frac{\partial}{\partial x}\left(A^*\frac{\partial\psi_0}{\partial y}\right) - \frac{\partial}{\partial y}\left(B^*\frac{\partial\psi_0}{\partial x}\right)$$

Equation (5) is of the same form as Eq. (1). A substitution similar to Eqs. (2a) and (2b), i.e.,

$$A^*\frac{\partial\phi_1}{\partial x} = \frac{\partial\psi_1}{\partial y} + \frac{\partial\phi_2}{\partial x} \qquad (6a)$$

$$B^*\frac{\partial\phi_1}{\partial y} = -\frac{\partial\psi_1}{\partial x} + \frac{\partial\phi_2}{\partial y} \qquad (6b)$$

yields another Poisson's equation for ψ_1,

$$\frac{\partial^2\psi_1}{\partial x^2} + \frac{\partial^2\psi_1}{\partial y^2} = S_1(x,y), \qquad (7)$$

and another generalized Poisson's equation for ϕ_2,

$$\frac{\partial}{\partial x}\left(A\frac{\partial\phi_2}{\partial x}\right) + \frac{\partial}{\partial y}\left(B\frac{\partial\phi_2}{\partial y}\right) = S_2(x,y). \qquad (8)$$

Ultrahigh gradient particle acceleration by intense laser-driven plasma density waves

C. Joshi*, W. B. Mori*, T. Katsouleas*, J. M. Dawson*, J. M. Kindel† & D. W. Forslund†

* University of California, Los Angeles, California 90024, USA
† Los Alamos National Laboratory, Los Alamos, New Mexico 87545, USA

Space-charge waves driven by resonantly beating two laser beams in a high-density plasma can produce ultrahigh electric fields that propagate with velocities close to c. By phase-locking particles in such a wave, particles may be accelerated to very high energies within a very short distance.

DURING the past four decades, we have witnessed an increase of six orders of magnitude in the output energy of high-energy accelerators, while the cost per MeV has been reduced by a factor of 16 per decade. But can this progress continue? Current accelerators, such as the Stanford linac, have accelerating fields of 200 keV cm⁻¹. However, for particle energies beyond 10 TeV, one had to invent schemes that can produce fields of at least 10 MeV cm⁻¹. In any particle accelerator scheme, the basic requirement for obtaining particles with ultrahigh energies is an intense longitudinal electric field that interacts with particles for a long time. Since highly relativistic particles move nearly at the speed of light c, the energy gained by the particles, $\int E \cdot dl$, is maximum if the field is made to propagate with the particles. Extremely large electric fields propagating with phase velocities close to c can be produced by space charge waves in a plasma (ionized gas). The maximum electric field that can be produced by such a wave is approximately $\sqrt{n_e}$ V cm⁻¹, where n_e is the plasma electron density per cm³. Thus for plasma densities in the range 10^{16}–10^{20} electrons cm⁻³, the longitudinal electric fields E_L, can be as large as 10^8–10^{10} V cm⁻¹. We now show that such high-gradient, high-phase velocity plasma density waves can be driven by intense laser beams. If particles could be phase-locked in such waves, this scheme has the potential for accelerating particles to ultrahigh energies in very short distances.

Theory

If an intense laser beam is propagated in a plasma, then in certain conditions, the transverse electric field of the laser (which may reach values of 10^9–10^{10} V cm⁻¹) can be very effectively transformed into a longitudinal electric field of a plasma density wave. In the laser accelerator scheme known as the 'Plasma beat wave accelerator' proposed by Tajima and Dawson[1,7], such a plasma wave can be driven by beating two colinear laser beams, with frequencies and wavenumbers (ω_0, k_0) and (ω_1, k_1), in a plasma resonantly, such that the frequency and the wavenumber of the plasma wave are

$$\omega_{epw} = \omega_0 - \omega_1$$
$$k_{epw} = k_0 - k_1 \qquad (1)$$

To achieve the ultrahigh accelerating gradients, high-density plasmas ($10^{16} < n_e < 10^{20}$ cm⁻³) must be used. Also, because the laser of frequency ω_0 cannot penetrate a plasma whose density exceeds the critical density n_c, corresponding to the plasma frequency $\omega_p = \omega_0$, plasmas with densities less than the quarter critical density must be used. Physically, the plasma wave consists of regions of space charge, which propagate with a phase velocity v_{ph} that is equal to the group velocity of the beat wave $v_g = c(1 - \omega_p^2/\omega_0^2)^{1/2}$. These arise because the spatial intensity gradient of the beat wave envelope, which is in the direction of propagation, exerts a periodic force (ponderomotive force) on the plasma at wavenumber k_{epw}. The plasma wave is thus an electrostatic wave with E_{epw} parallel to k_{epw}.

When two parallel propagating laser beams beat in a plasma

resonantly, the plasma density fluctuations grow rapidly. Using fluid equations it can be shown that for $v_0/c \ll 1$, the plasma wave electric field, which is proportional to the perturbed density, initially grows in time with a growth rate

$$\delta = \left(\frac{1}{4} \frac{v_0(0)}{c} \frac{v_0(1)}{c} \omega_p \right) \text{s}^{-1} \qquad (2)$$

where $[v_0(0,1)]/c = eE_{(0,1)}/m\omega_{(0,1)}c$ is the normalized oscillatory velocity of an electron in the laser field. Wavebreaking is approached when the perturbed density becomes as large as the initial density; however, to reach this limit the plasma wave must remain in phase with the beat wave. As the plasma wave grows, the relativistic effect on the frequency mismatch becomes important[2] and the plasma wave saturates at a lower amplitude given by

$$\varepsilon = \frac{eE_{epw}}{m\omega_{epw}c} = \left(\frac{16}{3} \frac{v_0(0)}{c} \frac{v_0(1)}{c} \right)^{1/3} \qquad (3)$$

Once the saturation amplitude is reached, the plasma wave amplitude actually begins to decrease, if this process alone acts to sustain the plasma wave[3].

As the plasma wave is an electrostatic wave, we can use Poisson's equation, $E_{epw} = 4\pi e n_e/k_{epw}$, to estimate the maximum electric field that we might expect if we assume that the perturbed electron density is equal to the initial density (the so-called cold
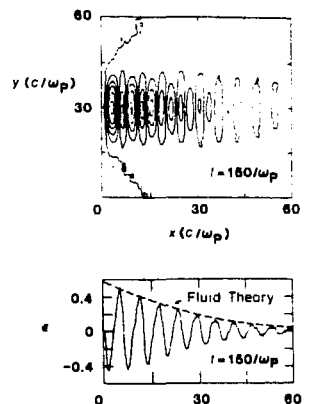

Fig. 1 Potential contours of the space-charge density wave driven by the two laser beams at time $150/\omega_p$ (*a*) section through the centre of the longitudinal electric field of the plasma wave (*b*). The dotted line in *b* shows a comparison of the rate of plasma wave build-up as predicted by the fluid theory with that obtained in these two-dimensional simulations.

Laser-induced profile modification: Effect of electron response

C. H. Aldrich, R. D. Jones, and K. Lee

Applied Theoretical Physics Division, University of California, Los Alamos National Laboratory, Los Alamos, New Mexico 87545

Physical processes which occur at the critical surface such as resonance absorption and scattering of the incident laser light are very sensitive to the exact form of the laser induced density profile. The presence of "overdense bumps" in density profiles has been seen experimentally and calculated theoretically using a simple isothermal model. These structures are important, in that they could, in an experimental situation, reflect a significant amount of light before it reaches the critical surface and considerably affect the physics occuring within a laser pellet target. A generalization of a previous calculation by using an arbitrary equation of state (density response of the electrons to the electrostatic potential ϕ) of the form $\rho = \rho(\phi)$ is obtained. In particular, two models for the electronic response (one including the effects of the presence of trapped electrons within the overdense shock structures) calculating the resulting effect on the produced density profiles are investigated. Qualitatively, it is found that the presence of overdense structures and their one-dimensional stability within an underdense plasma is unaffected by the more general electronic response. Conditions for the existence of these structures are discussed and a detailed comparison with full particle in cell (PIC) code simulations is made, emphasizing the trapped electron model where excellent agreement is obtained.

I. INTRODUCTION

The absorption and scattering of laser light at the critical surface of laser-driven fusion targets is an extremely important factor in the eventual success of laser fusion. These processes are very dependent on the exact form of the induced density profiles. Other processes such as energy transport into the plasma, harmonic generation,[1] magnetically induced surface transport, etc., depend sensitively on the amount of profile steepening at the critical surface. The possible presence of locally overdense structures in the underdense shelf could drastically affect the amount of energy arriving at the critical surface and thus coupled to the plasma. Density modification has been observed experimentally,[2-6] and there have been numerous simulations and calculations of it.[7-17] The fact that the laser steepens the density profile was first pointed out by Forslund et al.[7] The structure of the profile has been calculated by Lee et al.[8] in the limit of zero absorption and by Stellingwerf et al.[18] when light is absorbed at the critical surface by the plasma. Virmont et al.[14] and Mulser et al.[15] considered the effects of spherical geometry. Mulser et al.[16] examined the case of supersonic to supersonic transitions, but Powers et al.[15] demonstrated that these transitions were unstable. The only stable transitions were subsonic to supersonic transitions considered earlier. Max and McKee[13] noted that the laser pressure or the pressure from the heated electrons could drive a shock wave into the target. Sanmartín and Montañez[10] noted that the exact form and strength of the shock were very dependent on the time dependence of the heating. Mayer et al.[17] and Max et al.[12] considered the effect of phenomenologically altered heat flow on the density profile. And recently, Jones et al.[19] and Forslund et al.[20] have considered the effects of self-generated magnetic fields on the density profile.

    .   We wish to present in this paper a simple analytic model for the formation of density profiles induced by an incident laser beam and to investigate the effect of the electron response on the profile steepening and the existence of "overdense bumps" or compression-rarefaction shocks. In an earlier paper[9] we discussed three possible types of density structures for a laser normally incident on an expanding slab of plasma. These structures are pictured diagramatically in Fig. 1. Here the laser is incident from the right with the plasma expanding from the left. The first structure (a) consists of a rarefaction wave connecting the upstream density to a plateau-like area ending in a rarefaction shock at the critical surface. The second structure (b) is a combination of a rarefaction shock at the critical surface and a compression shock downstream. This combination we have denoted as a compression-rarefaction shock. The last structure (c) is basically a piston where all the particles are turned around by the impinging laser beam reflecting them back upstream. This
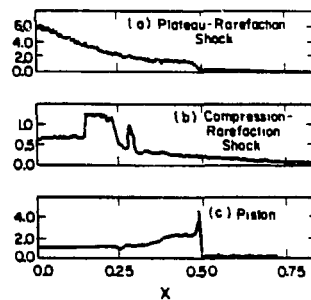

FIG. 1. Three possible density profiles (a) rarefaction plateau, (b) compression-rarefaction shock, and (c) piston.

113

Collisionless Dissipation in Quasi-Perpendicular Shocks

D. W. Forslund, K. B. Quest, J. U. Brackbill, and K. Lee

Los Alamos National Laboratory

Microscopic dissipation processes in quasi-perpendicular shocks are studied by two-dimensional plasma simulations in which electrons and ions are treated as particles moving in self-consistent electric and magnetic fields. Cross-field currents induce substantial turbulence at the shock front reducing the reflected ion fraction, increasing the bulk ion temperature behind the shock, doubling the average magnetic ramp thickness, and enhancing the upstream field aligned electron heat flow. The short scale length magnetic fluctuations observed in the bow shock are probably associated with this turbulence.

INTRODUCTION

Understanding of the dissipation of energy in collisionless magnetic shocks has been sought for many years. Satellite observations of the earth's bow shock illuminate the structure of collisionless shocks including ion reflection [*Montgomery et al.*, 1970; *Paschmann et al.*, 1982], magnetic field overshoot [*Heppner et al.*, 1967; *Livesey et al.*, 1982], thickness of the transition layer [*Russell and Greenstadt*, 1979], electron and ion heating rates [*Bame et al.*, 1979], and high-frequency fields [*Greenstadt et al.*, 1980; *Rodriguez and Gurnett*, 1975, 1976] in the shock layer itself. Compared with these observations, one-dimensional particle simulations [*Biskamp and Welter*, 1972; *Auer et al.*, 1971] typically overestimate the number of reflected ions because cross-field resistivity is absent. One-dimensional hybrid simulations [*Leroy et al.*, 1981, 1982] that treat the resistive heating phenomenolcgically describe the thickness of the foot region and the overshoot region. However, the mechanism for electron heating is unknown and the proper ramp thickness is not obtained in such models. Here, some preliminary results are presented from two-dimensional plasma simulations of quasi-perpendicular shocks that resolve the ion and electron time and space scales. The new results not only reproduce or extend most of the one-dimensional simulation results reported earlier, but also allow one to identify important new electron and ion dissipation processes in the earth's bow shock and to observe upstream field aligned electron heat flow.

SIMULATION RESULTS

The bow shock is modeled in two dimensions by a newly developed implicit particle-in-cell simulation technique [*Brackbill and Forslund*, 1982]. Very high frequency, ω_{pe}, oscillations are eliminated without removing electron inertial and kinetic effects. In the simulation code VENUS [*Brackbill and Forslund*, 1982], two spatial coordinates and three velocities are treated for each species in the self-consistent, three-component electric and magnetic fields. Numerical dissipation in the code is smaller than the dissipation in the shock due to self-consistent collisionless collective effects.

A magnetic piston is used to drive the shock. The piston, a tangential discontinuity which pushes the plasma towards

the left, is generated at the right boundary by a transverse electric field E_y (Figure 1). By analogy with the earth's dayside magnetopause, the piston is a magnetic barrier through which the magnetic field intensity increases and the number density drops to zero. In the frame moving with the piston, a super Alfvénic plasma hits the barrier, launching compressional waves which propagate upstream and steepen to form a shock. The angle between upstream B and $\hat{n}$ is 78° and allows for some motion of the electrons along the field lines into and out of the shock.

The simulation parameters chosen are for a $\beta_e = 2$ plasma with $\beta_i = 2$ or 0.2 and an Alfvén mach number of the shock of 4.5. The units of length in our figures are upstream c/ω_i (typically of order 100 km). velocity is shown in units of the upstream Alfvén speed, and time is given in terms of the inverse ion gyrofrequency, Ω_i^{-1}. For economy, we have chosen $m_i/m_e = 100$ and $\omega_{pe}/\Omega_e = 20$.

The direction of the ambient field relative to the simulation plane can strongly affect the types of instabilities allowed in the code. This can be used to advantage in studying shocks. For example, in a perpendicular shock propagating in the x direction through an ambient magnetic field in the y direction, the diamagnetic currents are in the z direction and thus out of the plane of simulation. Thus cross field current instabilities are not allowed, but pitch angle scattering instabilities are. However, by rotating the ambient field out of the plane, the currents move into the plane allowing cross-field instabilities to occur. We make use of this difference to illustrate the transition from essentially zero cross-field resistivity to the finite level self-consistently produced by cross-field current instabilities.

In Figure 2 we show phase space plots with B in the simulation $(x - y)$ plane $(B_z = 0)$ and $T_i/T_e = 10$. In this plane cross-field current driven instabilities cannot be excited, so we anticipate a quasi-laminar shock structure with substantial ion reflection. The three components of velocity of ions and electrons are plotted versus the coordinate x at $\Omega_i t = 4.5$ to show the ion reflection and heating of ions and electrons behind the shock.

At the time chosen the shock position is approximately $x = 12c/\omega_i$, and is separated from the piston by a distance of $6-7c/\omega_i$. As will be seen, the separation distance corresponds to several ramp thicknesses, so the processes operating within the ramp may be examined separately from those near the piston. Additionally, the shock separation from the left wall is large enough so that boundary effects may be neglected.

Collisionless Dissipation in Quasi-Perpendicular Shocks

D. W. Forslund, K. B. Quest, J. U. Brackbill, and K. Lee

Los Alamos National Laboratory

Microscopic dissipation processes in quasi-perpendicular shocks are studied by two-dimensional plasma simulations in which electrons and ions are treated as particles moving in self-consistent electric and magnetic fields. Cross-field currents induce substantial turbulence at the shock front reducing the reflected ion fraction, increasing the bulk ion temperature behind the shock, doubling the average magnetic ramp thickness, and enhancing the upstream field aligned electron heat flow. The short scale length magnetic fluctuations observed in the bow shock are probably associated with this turbulence.

INTRODUCTION

Understanding of the dissipation of energy in collisionless magnetic shocks has been sought for many years. Satellite observations of the earth's bow shock illuminate the structure of collisionless shocks including ion reflection [*Montgomery et al.*, 1970; *Paschmann et al.*, 1982], magnetic field overshoot [*Heppner et al.*, 1967; *Livesey et al.*, 1982], thickness of the transition layer [*Russell and Greenstadt*, 1979], electron and ion heating rates [*Bame et al.*, 1979], and high-frequency fields [*Greenstadt et al.*, 1980; *Rodriguez and Gurnett*, 1975, 1976] in the shock layer itself. Compared with these observations, one-dimensional particle simulations [*Biskamp and Welter*, 1972; *Auer et al.*, 1971] typically overestimate the number of reflected ions because cross-field resistivity is absent. One-dimensional hybrid simulations [*Leroy et al.*, 1981, 1982] that treat the resistive heating phenomenologically describe the thickness of the foot region and the overshoot region. However, the mechanism for electron heating is unknown and the proper ramp thickness is not obtained in such models. Here, some preliminary results are presented from two-dimensional plasma simulations of quasi-perpendicular shocks that resolve the ion and electron time and space scales. The new results not only reproduce or extend most of the one-dimensional simulation results reported earlier, but also allow one to identify important new electron and ion dissipation processes in the earth's bow shock and to observe upstream field aligned electron heat flow.

SIMULATION RESULTS

The bow shock is modeled in two dimensions by a newly developed implicit particle-in-cell simulation technique [*Brackbill and Forslund*, 1982]. Very high frequency ω_{pe} oscillations are eliminated without removing electron inertial and kinetic effects. In the simulation code VENUS [*Brackbill and Forslund*, 1982], two spatial coordinates and three velocities are treated for each species in the self-consistent, three-component electric and magnetic fields. Numerical dissipation in the code is smaller than the dissipation in the shock due to self-consistent collisionless collective effects.

A magnetic piston is used to drive the shock. The piston, a tangential discontinuity which pushes the plasma towards

the left, is generated at the right boundary by a transverse electric field E, (Figure 1). By analogy with the earth's dayside magnetopause, the piston is a magnetic barrier through which the magnetic field intensity increases and the number density drops to zero. In the frame moving with the piston, a super Alfvénic plasma hits the barrier, launching compressional waves which propagate upstream and steepen to form a shock. The angle between upstream B and is 78.7 and allows for motion of the electrons along the field lines into and out of the shock.

The simulation parameters chosen are for a $\beta = 2$ plasma with $\beta_e = 2$ or 0.2 and an Alfvén mach number of the shock of 4.5. The units of length in our figures are upstream c/ω_{pi}, typically of order 100 km; velocity is shown in units of the upstream Alfvén speed, and time is given in terms of the inverse ion gyrofrequency, Ω^{-1}. For economy, we have chosen $m_i/m_e = 100$ and $\omega_{pe}/\Omega_e = 20$.

The direction of the ambient field relative to the simulation plane can strongly affect the types of instabilities allowed in the code. This can be used to advantage in studying shocks. For example, in a perpendicular shock propagating in the x direction through an ambient magnetic field in the z direction, the diamagnetic currents are in the z direction and thus out of the plane of simulation. Thus cross field current instabilities are not allowed, but pitch angle scattering instabilities are. However, by rotating the ambient field out of the plane, the currents move into the plane allowing cross-field instabilities to occur. We make use of this difference to illustrate the transition from essentially zero cross-field resistivity to the finite level self-consistently produced by cross-field current instabilities.

In Figure 2 we show phase space plots with B in the simulation $(x-y)$ plane $(B_z = 0)$ and $T_i/T_e = 10$. In this plane cross-field current driven instabilities cannot be excited, so we anticipate a quasi-laminar shock structure with substantial ion reflection. The three components of velocity of ions and electrons are plotted versus the coordinate x at $\Omega t = 4.5$ to show the ion reflection and heating of ions and electrons behind the shock.

At the time chosen the shock position is approximately $x = 12c/\omega_{pi}$ and is separated from the piston by a distance of $6-7c/\omega_{pi}$. As will be seen, the separation distance corresponds to several ramp thicknesses, so the processes operating within the ramp may be examined separately from those near the piston. Additionally, the shock separation from the left wall is large enough so that boundary effects may be neglected.

Magnetic Surface Waves in Plasmas

Roger D. Jones

Applied Theoretical Physics Division, Los Alamos National Laboratory, University of California,
Los Alamos, New Mexico 87545

The existence of a new type of surface wave in plasmas is demonstrated. These waves are intimately connected with the self-generation of magnetic fields in the laser-plasma interaction. The waves resemble waveguide modes in that a number of discrete modes can exist. The modes are localized to within a collisionless skin depth of the surface and, in the collisionless fluid limit, there is no restriction on the distance the waves can propagate.

Spontaneously generated magnetic fields in laser-produced plasmas have been observed for many years.[1-3] These observations, along with their obvious impact on the inertial-confinement fusion program, have been the motivation for the many papers that have appeared on the subject in the last decade.[4-8] Transport of energy along surfaces,[7,8] anomalously fast plasma blowoff,[8] and insulation of the laser-heated electrons from the target interior[7,8] (known in the laser fusion community as flux limitation) have all been attributed to properties of self-generated magnetic fields. All these phenomena require sharp discontinuities in plasma properties (e.g., density, temperature, and atomic charge) for their existence. Therefore, the understanding of the normal surface modes in a plasma is crucial to the understanding of these phenomena. In this Letter, I demonstrate the existence of an entirely new set of plasma surface modes. It will be shown that (1) the self-generated magnetic field plays an essential role in the propagation of these waves; (2) a number of discrete modes exist, as in a waveguide; (3) in the collisionless fluid limit, there is no restriction on the distance the waves can propagate; (4) the waves are localized around the surface on scale lengths of the order of a collisionless skin depth; and (5) the phase and group velocities are very dependent on the density and temperature profiles at the surface. While this work has been motivated by programmatic aspects of the inertial-confinement fusion program, it is felt that the results are quite general and applicable to any plasma that contains sharp density and/or temperature gradients.

We choose a density profile similar to the one illustrated in Fig. 1(a). In regions A and C we require the density gradient scale lengths to be large compared with the scale length of the density jump in region B. We will permit the den-

sity to vary in the x direction only. The ions are assumed to be cold and fixed. Quasi charge neutrality is also assumed. Collisions have been neglected. The temperature profile is permitted to be arbitrary and no heat flux is permitted. We choose the magnetic field to lie in the z direction and to vary only as a function of x, y, and time. We will look for waves localized in x around region B and propagating in the y direction. The equations for the electron hydrodynamics are

$$\nabla \cdot n\vec{v} = 0, \tag{1}$$

$$\frac{\partial}{\partial t}(\vec{\psi} - \vec{\Omega}) - \nabla \times \vec{v} \times (\vec{\psi} - \vec{\Omega}) = -\nabla \times \frac{1}{mn}\nabla p, \tag{2}$$
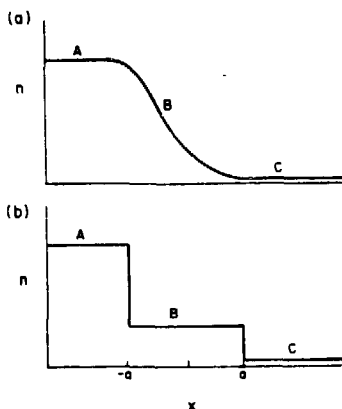
FIG. 1. (a) Density profile. The surface, region B, separates region A from region C. (b) Density profile for analytic solution. In region B the profile is nearly flat.

    1269

Implicit Moment PIC-Hybrid Simulation
of Collisional Plasmas*

RODNEY J. MASON

Los Alamos National Laboratory, Los Alamos, New Mexico 87545

A self consistent scheme was developed to model electron transport in evolving plasmas of arbitrary classical collisionality. The electrons and ions are treated as either multiple Eulerian fluids or collisional particles in cell. Particle suprathermal electrons scatter off ions, and drag against fluid background thermal electrons. The background electrons undergo ion friction thermal coupling, and bremsstrahlung. The components accelerate in electric fields obtained by the Implicit Moment Method, which permits $\Delta t \gg \omega_p^{-1}$ and $\Delta x \gg \lambda_D$,—allowing the treatment of problems 10^2–10^3 times more complex than those accessible with older explicit methods. The fluid description for the background plasma components permits the modeling of transport in systems spanning more than a 10^3 fold change in density, and encompassing contiguous collisional and collisionless regions. Results are presented from application of the scheme to the modeling of CO_2 laser generated suprathermal electron transport in expanding thin foils, and in multi foil target configurations.

1. INTRODUCTION

At laser wavelengths exceeding 0.5 μm a significant fraction of the light absorbed by laser fusion targets is deposited in suprathermal electrons. These are marginally collisional and distribute the absorbed energy throughout the target. As they move, they set up self consistent electric fields which draw return currents in the background, generally strongly collisional, thermal electrons. These fields also set the ions into motion, changing the target geometry, in which the suprathermals must transport. A detailed model of this complex coupled phenomenology is required if we are to develop the intuition and understanding needed to engineer the use of suprathermals in the design of targets for high compression. Here, our efforts toward the development of such a model were confined to a one dimensional treatment. However, our choice of approach has been guided by the ease with which it might be generalized to higher dimensions.

484

Space-time evolution of the beam-plasma instability

Michael E. Jones, Don S. Lemons, and Michael A. Mostrom

Advanced Concepts and Plasma Applications Group,
Los Alamos National Laboratory, Los Alamos, New Mexico 87545

Particle-in-cell simulations of the beam-plasma instability confirm that the behavior of the interaction can be described as a wave packet that continually grows in both space and time. A consequence is that the energy deposition length of the instability becomes shorter in time, offering increased potential for this interaction to be used as an inertial fusion driver.

The beam-plasma, or two-stream instability, is one of the oldest and most familiar microinstabilities in plasma physics. Recently, there has been renewed interest[1] in this instability in connection with an inertial fusion driver. In the Anomalous Intense Driver (AID) concept[2] intense relativistic electron beams, produced by pulsed power machines, would heat a 10^{17} to 10^{20} cm^{-3} density plasma, surrounding an inertial fusion pellet, to multikilovolt electron temperatures. Efficient transfer of energy from the beam to the plasma would be accomplished via the beam-plasma instability. Subsequently, the hot, high-density plasma would provide efficient coupling of the energy to the pellet. By not impinging the beams directly on the pellet, one would avoid the problems of fuel preheating while retaining the advantage of high energy in relativistic electron beams.

Crucial to the success of this concept is the ability of the beam-plasma instability to deposit the beam energy in a sufficiently short distance. Short energy deposition distances provide the high-energy densities needed for inertial fusion. The energy deposition length in turn depends on whether the beam-plasma instability is convective (time-independent spatial growth) or absolute (growing temporally at fixed position).

Careful and detailed experiments on the beam-plasma instability have shown that a time-independent spatial growth of the instability is obtained.[1-6] For this reason the instability is generally believed to be convective. Criteria for when an instability is convective or absolute has been given by Briggs.[7] However, he noted that for the simple case of the cold-fluid one-dimensional, electrostatic dispersion relation for the beam-plasma system, his "pinch-point" analysis fails to give a definitive answer about the nature of the instability.

The dispersion relation for this case is well known:

$$1 - \omega_p^2/\omega^2 - \omega_b^2/(\omega - kv_b)^2 = 0, \tag{1}$$

where ω is the Laplace transform (in time, t) variable, k is the Fourier transform (in space, z) variable, v_b is the beam velocity, and ω_p is the electron plasma frequency. To generalize this dispersion relation to relativistic beams, one simply replaces the square of the beam-plasma frequency ω_b^2 by ω_b^2/γ^3, where γ is the Lorentz factor of the beam. Such dispersion relations are obtained by taking the Laplace-Fourier transforms of a set of equations describing the system. They are often analyzed by assuming k to be real and known and solving for complex ω. The resulting solutions describe the temporal growth of spatially periodic disturbances. Conversely, one may solve for real ω and complex k to obtain spatially growing solutions. However, the actual response of the system must be obtained by inverting the Laplace-Fourier transforms, taking into account the sources of the disturbances. The inverse transforms for the system with the dispersion relation given by Eq. (1) for weak beams can be approximated using the saddle point method.[8,9] A delta function source at $t = 0$ and $z = 0$ is assumed, thus obtaining the Green's function response of the system. The result is

$$E \sim \begin{cases} \exp(i\omega_p \tau)\exp\left[(3\sqrt{3}/4)(\omega_b z/v_b)^{2/3}(\omega_p \tau)^{1/3}\right], \\ \quad v_b t > z > 0, \\ 0, \quad z < 0, \quad z > v_b t, \end{cases} \tag{2}$$

where E is the electric field and $\tau \equiv t - z/v_b$.

The response given in Eq. (2) can be called "absolute" since E grows in time for a fixed position z. However, for fixed t there is also growth in space, reminiscent of a convective instability. In fact, Eq. (2) describes a wave packet that moves in space and grows as it moves. It is easy to show that the peak of the wave packet moves at a velocity $2/3 v_b$, which is the group velocity of the most unstable wave obtained from the usual dispersion relation analysis for real k and complex ω. Furthermore, in a reference frame moving with this velocity, the electric field grows at a maximum growth rate obtained from the dispersion relation analysis.

Although the wave-packet analysis is for an extremely simple model of the beam-plasma system, inclusion of other physical effects, such as finite plasma and beam temperature, does not alter qualitatively the wave-packet behavior.[10] To further investigate this behavior and its relevance to inertial fusion drivers, several particle-in-cell simulations have been performed. Most previous simulations of the beam-plasma instability have used periodic boundary conditions. This forces k to be real and the linear growth rate for this case is observed. However, the space-time behavior described by Eq. (2) cannot be observed unless aperiodic boundaries are used, as is the case for the simulations presented here. Figure 1 illustrates the growing wave-packet behavior observed in one of the simulations. The computer code used here is CCUBE, a 2½-dimensional, relativistic, electromagnetic PIC code.[11] An annular relativistic ($\gamma = 2$) electron beam with inner radius $r_i = 10 c/\omega_p$ and outer radius $r_0 = 20 c/\omega_p$ is injected into a plasma-filled conducting cylinder with a radius $r_c = 30c/\omega_p$ and length $L = 100 c/\omega_p$. The beam density n_b is 1 % of the plasma density n_p. There is also an axial magnetic field imposed that gives an electron cyclotron frequency $\omega_c = 0.1 \omega_p$. The cell size is 0.5 c/ω_p on each side and about 10^4 particles are used. The time step is $0.2 \omega_p^{-1}$. The graphs in Fig. 1 show the axial electric field located at the radial center of the beam as a function of axial

118

Return-Current Heating and Implosion of Cylindrical CO2-Laser-Driven Targets

A. Hauer and R. J. Mason

Los Alamos National Laboratory, University of California, Los Alamos, New Mexico 87545

The Helios laser system has been used to deliver 2.3 kJ to the capped end of 0.75-mm-long, 130-μm-diam hollow rods of 5-μm wall thickness. Soft-x-ray pinhole pictures demonstrate the cylindrical implosion of these targets. The measured 130-eV core temperatures from the filtered pictures and the 7×10^6-cm/s collapse velocity from optical streak photographs are consistent with heating by a 0.8×10^6-A return current, representing the recycling of 15% of the hot-electron emission.

At intensities which exceed 10^{15} W/cm^2 most of the energy absorbed from CO2 lasers goes directly into a relatively small number of highly energetic (>200 keV) suprathermal electrons.[1] This energy must be transferred to a much larger number of localized thermal electrons to accomplish laser fusion. Since direct classical coupling of the suprathermals to the background plasma has proven inefficient, we have initiated an effort to use the self-generated fields in specialized targets to improve the energy transfer. Charge imbalance develops as suprathermals leave a laser spot. The resultant E fields can draw a return current, if an appropriate path is provided. Benjamin et al.[2] have demonstrated the existence of these currents, and their ability to heat a target support stalk. This Letter reports the first experimental results from targets designed to use the return currents to heat and implode a thin-walled hollow cylinder—to produce a micro Z pinch.

A schematic of the "augmented return current" (ARC) targets used in the experiments is given in Fig. 1. Four tightly focused CO2-laser beams from the Los Alamos Helios laser system impinge on the capped end of a long hollow, low-Z cylinder, coated with a thin layer of metal (gold or aluminum). The cylinder is mounted at the center of a large high-Z disk. Suprathermals generated at the focus will drift toward the disk in the plasma surrounding the cylinder. A thermal return current is drawn back along its walls. Resistivity of the walls results in Joule heating of the thermals. The B field from the resultant current loop can implode and further heat the cylinder.

Experiments were performed on targets with a variety of diameters and lengths. The smallest cylinders were matched to the minimal laser spot diameter. Their length was set at roughly 5 diameters to maximize the aspect ratio for current-related effects, under the constraint of minimum mass—for maximum temperature gain from energy deposition. The minimum wall thickness was set by limits on structural integrity. The metal layer was added to provide a brighter signature in x-ray pinhole pictures. The earlier experiments[2] recorded currents from electrons escaping to the walls of the target chamber. The ARC targets were designed to augment this current through the axial alignment of the cylinder and beams, with a cylinder much thicker than the earlier 10-μm stalks, and with the addition of the collector disk for possible suprathermal entrainment. The presence of thermoelectric, $\nabla n \times \nabla T$ B fields has been recognized for some time.[3-6] The cylindrical return currents and any pinch effect should serve to enhance these fields. Suprathermal drift down the cylinder[7] is consistent with a B field, directed as in Fig. 1, and with an outwardly directed E field for containment of the electron cloud. The axial E-field component, drawing the return current against resistivity, introduces a "tilt" in the $E \times B$ drift, which should aid capture of the suprathermals by the cylinder wall. Alternatively, the B field around the cylinder should help to shield its interior from suprathermal preheat.[6] The return-current effects discussed here will be reduced to the extent that deposited energy is lost to fast-ion blowoff. However, cylindrical geometry may serve to reduce fast-ion losses, as compared to those from foils,[6] since the area
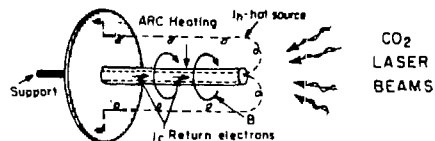

FIG. 1. Sketch of the ARC target design.

459

Eigenfunction analysis of the beam–plasma instability with finite radial dimensions

Michael E. Jones

Applied Theoretical Physics Division. Los Alamos National Laboratory. Los Alamos. New Mexico 87545

A linear eigenfunction analysis of the beam–plasma instability for an annular beam interacting with a plasma filling the space between the conductors of a coaxial transmission line is presented. The beam and plasma electrons are modeled by relativistic cold fluids and the dispersion relation is three-dimensional and fully electromagnetic. Particular attention is given to the radial eigenfunction structure and extensive numerical examples are presented. The behavior of the dispersion relation with various parameters is interpreted in terms of the infinite homogeneous theory. Simple analytical approximations for the dispersion relation for annular beams are given. Also, particle-in-cell simulation results are compared with the predictions of the linear analysis.

I. INTRODUCTION

It has been proposed that intense annular relativistic electron beams be used to efficiently heat plasmas in the density range of 10^{17}–10^{20} cm^{-3}. The resulting hot annular plasma has a variety of applications including utility as an inertial confinement fusion driver.[1] Recent experiments designed to test the feasibility of heating annular regions of dense plasma have used beams with a radius of 1 cm and a thickness of 0.2–0.3 mm at an energy of 3 MV (Ref. 2). For these very thin beams it might be expected that the usual assumptions of an infinite homogeneous beam–plasma system are inapplicable. The purpose of the present work is to analyze the effect of finite radial dimensions on the linear stability of this beam–plasma system.

This work represents a generalization of previous analyses with finite radial dimensions to the case of an annular relativistic beam interacting with a plasma which fills the annular region between the conductors of a coaxial transmission line as illustrated in Fig. 1. The dispersion relation presented here is three-dimensional, fully electromagnetic, and is obtained by assuming a relativistic cold-fluid approximation. Although the emphasis is on annular beams, the dispersion relation for solid beams is contained as a subset of the more general analysis. Extensive numerical results are presented. Particular emphasis is given to the relationship of the dispersion relation for an annular beam to that for the infinite homogeneous system.

The beam–plasma instability is one of the most thoroughly studied microinstabilities in plasma physics. For a summary of the analyses of nonrelativistic beams, including the effects of finite radial dimensions, the reader is referred to the review article by Briggs.[3] A review of the work with finite radial dimensions for relativistic beams and electromagnetic waves is given by Aronov, Bogdankevich, and Rukhadze.[4] Perhaps the earliest analysis of a finite relativistic beam was by Frieman *et al.*[5] who studied the case of a solid beam in an infinite plasma. Recent refinements have included the effects of finite external magnetic fields and beam temperature.[6-10]

The radial eigenfunctions are examined in detail in the present analysis. It is found that the unstable waves are evanescent outside the beam annulus. This behavior results in an effective quantization of the wave vector perpendicular to the beam direction, $k_\perp$. The quantization is determined by the beam thickness. The stable waves are found to be radially oscillatory everywhere and possess an effective $k_\perp$ quantization determined by the dimensions of the conductors. Annular beams are found to possess two unstable surface waves. These waves always have lower growth rates than the bulk modes. One of these surfaces modes is found to be analogous to the $k_\perp = 0$ wave of the infinite homogeneous theory.

To a good approximation it is found that the unstable waves for thin annular beams correspond to the waves in the infinite homogeneous theory with $k_\perp$ replaced by $k_\perp = (k, + \frac{1}{2})\pi/\tau$, where τ is the beam thickness and k, is an integer, and as mentioned earlier, there is a mode for $k_\perp = 0$. The growth rate of the most unstable mode is given by Eq. (14).

Finally, the usefulness of the eigenfunction analysis is tested via particle-in-cell simulation. The results indicate that while the eigenfunctions probably do not describe the entire response of the system, many of the features of the present analysis are observed in the simulations.
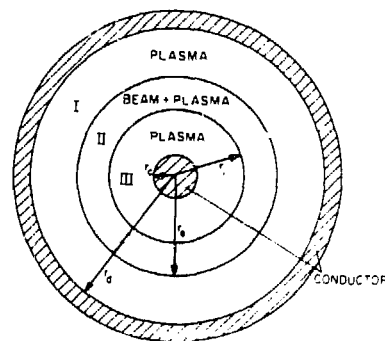

FIG 1 Most general geometrical configuration considered in the analysis

Shear-driven instabilities of annular relativistic electron beams in vacuum

Michael A. Mostrom and Michael E. Jones

Intense Particle Beam Theory Group, Los Alamos National Laboratory, Los Alamos, New Mexico 87545

The study of instabilities driven by azimuthal shear (diocotron) and axial shear is extended to annular relativistic beams. The analysis is done nonrelativistically in the beam frame where the instability is assumed to be electrostatic, and the dispersion relation is then transformed back to the laboratory frame where magnetic perturbations are non-negligible. This requires keeping finite axial wavenumber k_z in the analysis. The axial and azimuthal shears are related through the self-consistent equilibrium, assuming emission from an equipotential cathode. Axial shear destabilizes the diocotron modes at higher azimuthal wavenumbers l. It also produces a set of modes including $l = 1$ modes, that are unstable as the result of wave–particle interactions. The annular configuration introduces an important second pole in the differential equation.

I. INTRODUCTION

The diocotron and v_z-shear-driven instabilities in non-relativistic annular electron beams are generally considered to be well understood, but there are some important omissions. Levy's work on the diocotron instability included significant cylindrical effects[1] but ignored the radial shear in the axial velocity v_z and considered only the case $k = 0$ (i.e., no z variation) which corresponds to the maximum growth rate. Rome and Briggs included v_z shear with all k (with finite v_z shear, the growth rate is not maximized at $k = 0$) but considered only a cylindrical solid beam which eliminates the diocotron instability.[2] Antonsen and Ott investigated simultaneously the diocotron and v_z-shear instabilities for all k but limited themselves to planar slab beams.[3] In an earlier paper Jones and Mostrom studied the diocotron instability for all k in annular beams but treated v_z shear only to the extent of obtaining conditions for its neglect.[4] The first step in the present paper is to generalize the nonrelativistic theory by including both the diocotron and v_z-shear instablities for all k in annular beams.

The main application of these theories has been microwave generation in crossed field magnetrons. In recent areas of experimental and theoretical interest, intense annular relativistic electron beams are employed. These include free electron lasers.[5] multigapped accelerators,[6] and the anomalous intense driver fusion concept.[7] Because the nonlinear state of the diocotron and v_z-shear instabilities can disrupt the beam by causing filamentation,[8,9] it is important to understand these instabilities in the relativistic regime including cylindrical effects.

There have been several recent attempts at such a relativistic cylindrical theory, but again all suffer from various degrees of omission of important effects. Kapetanakos, Hammer, Striffler, and Davidson found an $\omega = 0$ spatial growth in an annular beam.[4] But, they incorrectly assumed that the instability is electrostatic in the lab frame and also ignored v_z shear. Uhm and Siambis[10] and also Chen and Palmadesso[11] investigated the diocotron instability in annular beams but limited themselves to $k = 0$ in the lab frame and ignored v_z shear. Both v_z shear and relativisitc effects

shift the maximum growth rate away from $k = 0$. In the previously mentioned paper, Jones and Mostrom obtained the diocotron dispersion relation for all k in the lab frame by a transformation from the beam frame, but found that neglect of v_z shear limited their results to small azimuthal mode number l (Ref. 4). In none of the above relativistic theories was the v_z-shear-driven instability studied which can destabilize the $l = 1$ mode. In the present analysis we generalize the previous relativistic cylindrical analysis of Jones and Mostrom by including v_z-shear effects. It can also be thought of as a relativistic cylindrical generalization of the nonrelativistic planar finite v_z-shear analysis by Antonsen and Ott.

The dispersion relation analytically obtained here is studied numerically and compared with previous analysis where appropriate. For the diocotron instability, the primary effect of finite v_z shear on the growth rate is to maintain and enhance the instability for much larger l than otherwise would be possible. This is accomplished through frequency shifts of the component waves in the resonant wave–wave interaction. For the v_z-shear instability, an annular beam introduces into the differential equation for the perturbed electrostatic potential an important second pole that is not present for a constant density cylindrical solid[2] or planar slab[3] beam. The present analysis treats this pole to only second order but serves to identify this problem and ascertain its importance. For large l, this second pole becomes important even for the diocotron instability.

II. EQUILIBRIUM MODEL

The electron beam is assumed to be initially in an azimuthally symmetric equilibrium inside a conducting drift tube of radius d as illustrated in Fig. 1. A large externally applied axial magnetic field is required for equilibrium. The azimuthal equilibrium velocity $v_{\theta 0}(r)$ of the electrons is an $E \times B$ rotational drift induced by the applied magnetic field B_z and the radial electric self-field $E_r(r)$ of the unneutralized beam. Space charge effects radially shear the electron axial velocity $v_{z0}(r)$. The beam frame referred to throughout this paper is defined such that $v_{z0} = 0$ at $r = a$, the inner beam radius. Using the radial force balance equation, conservation

121

Field saturation for arbitrary temperature in resonance absorption

B. Bezzerides and S. J. Gitomer

University of California, Los Alamos National Laboratory, Los Alamos, New Mexico 87545

A nonlinear theory of a driven, inhomogeneous, one-dimensional plasma of arbitrary temperature is presented. The model is solved numerically and analytically and detailed expressions are given for the saturated electric field excited at critical density. The results of the calculation are valid for arbitrary temperature and connect in a continuous manner the limits of cold wavebreaking and linear convective saturation. Comparison of the results of the calculation with particle simulations is made and good agreement is obtained.

I. INTRODUCTION

Since the classic work of Ginzberg,[1] the study of resonance absorption in a warm plasma has advanced by the use of particle simulation techniques.[2-4] Whereas the Ginzberg work achieves a saturated electric field level solely through the convective stabilization of the field due to finite background temperature, the simulations show the importance of hot-electron production for stabilization at sufficiently high values of the external field. Thus for strong driving, one may anticipate the diminished importance of the background temperature for establishing the final electric field level. Wavebreaking in cold-plasma models[5] has provided useful scaling laws when the background temperature can be completely ignored. Although the precise connection between wavebreaking in a fluid model and hot-electron production is not fully understood, it is argued that the onset of wavebreaking in the fluid theory signals the creation of hot electrons. The time of onset of wavebreaking is then used to estimate the saturated field level of the excited electric field.

To assess the relative importance of background temperature upon the level of the saturated electric field in resonance absorption, Kruer[6] combined results from the cold wavebreaking model[5] and a homogeneous undriven waterbag model.[7] This calculation provided a prediction of the effect of plasma temperature on wavebreaking amplitudes. However, the results are essentially limited to relatively low temperatures, since in some sense the approach used relies on a perturbation in temperature about the cold-plasma case. One may also question the consistency of Kruer's calculation; however, the predictions are in reasonable agreement with the results of particle simulations at least for relatively low temperatures.

In this paper we present a consistent fluid model of a driven, inhomogeneous, warm plasma. We show how one may obtain the saturated value of the electric field excited at critical density. Of course, in such a model, the effect of hot-electron production is not included. Nevertheless, here we find, through comparison with particle simulations, that accurate saturated field levels are obtained from numerical solution of the fluid model and by an approximate analytic theory. In Sec. II, we outline the model, providing an approximate solution in Sec. III, and we present the numerical results and comparisons in Sec. IV, ending with some concluding comments.

II. LAGRANGIAN FLUID MODEL

Consider a one-dimensional plasma of mobile electrons and fixed ions. The equations of continuity and momentum along with Poisson's equation provide a complete fluid description, given the pressure P:

$$\frac{\partial n}{\partial t} + \frac{\partial}{\partial x}(n\,v) = 0, \tag{1a}$$

$$\frac{\partial v}{\partial t} + v\,\frac{\partial v}{\partial x} = -\frac{e}{m_e}(E + E_0) - \frac{1}{m_e n}\frac{\partial P}{\partial x}, \tag{1b}$$

$$\frac{\partial E}{\partial x} = 4\pi e[n_0(x) - n(x,t)], \tag{1c}$$

where n and v are the fluid density and velocity, e and m_e are the electron charge and mass, E and E_0 are the self-consistent and driving electric fields, respectively, and n_0 is the fixed ion density. If the gradient of the heat flux is assumed to be zero, then it is a simple matter to truncate the fluid equations to obtain the pressure in terms of the density. Such an assumption ignores the presence of hot-electron production, a condition consistent with the early stage of time evolution of the plasma fluid prior to the onset of wavebreaking. We find[3,4]

$$P/n^3 = \text{const}. \tag{1d}$$

For this one-dimensional set of equations it is convenient to introduce the Lagrangian transformation $x = x_0 + \delta(x_0, \tau)$ and $t = \tau$, where $\delta(x_0,\tau) = \int \bar{v}(x_0, \tau')\,d\tau'$, with $\bar{v}(x_0, \tau) = v(x, t)$. Using the above transformation we obtain the following equation of motion for δ:

$$\frac{\partial^2 \delta}{\partial \tau^2} + v\,\frac{\partial \delta}{\partial \tau} + \int_{x_0}^{x_0 + \delta} \omega_p^2(x_0')\,dx_0'$$
$$= -\frac{eE_D}{m_e}\sin \omega\tau - \frac{1}{m_e n_0}\frac{\partial \tilde{P}}{\partial x_0}, \tag{2}$$

where v includes dissipation due to linearized Landau damping and a spatially dependent *ad hoc* damping introduced to avoid boundary anomalies in the numerical solution. The third term in Eq. (2) accounts for the plasma-restoring force for the general ion density profile; however, in what follows

122

Magnetohydrodynamics in Laser Fusion:
Fluid Modeling of Energy Transport in Laser Targets

J. U. BRACKBILL AND S. R. GOLDMAN
Los Alamos National Laboratory

Abstract

Fluid models for two-dimensional, electron energy transport are examined It is shown that enhanced lateral transport due to particle drifts in self-generated magnetic fields occurs when certain transport terms are flux-limited by artificially enhancing collisions. With flux limiting, fluid models reproduce the essential features of numerical simulations of transport in CO_2 laser target experiments

Introduction

New results (cf. [1]–[3]) suggest that magnetic fields play a central role in energy transport in laser target experiments. In recent numerical simulations of collisionless plasmas (cf. [1]) using the VENUS code (cf. [4]) and laser experiments at 10.6-μm wavelength (cf. [3]), it is observed that lateral energy transport is convective rather than diffusive. The convection is associated with the formation of a magnetized sheath on the target surface.

Although magnetic fields have been observed before (cf. [5], [6]) and modeled theoretically (cf. [7], [8], [10]), their role in electron energy transport was thought to be a passive one. Simply by their presence at the periphery of a laser spot, they were believed to block electron energy transport across the target surface (cf. [9]).

The new transport model is different from the old in two respects. First, a thermal magnetic wave (cf. [10]) rapidly propagates the magnetic field away from the source across the target surface. Thus, the magnetic field covers the target surface instead of being localized to the periphery of the laser spot as previously believed. Second, the hot electrons generated by the absorption of laser energy drift in the magnetic field and convect energy away from the source. As a result, hot electrons uniformly fill a magnetized sheath which covers a large area of the target surface. These electrons form a reservoir of energy which is eventually transformed to ion motion without ever penetrating to the interior of the target.

On physical grounds the new model is plausible, and there is much experimental evidence to support it (cf. [3]). Several features of the simulation results

Magnetic-Field–Induced Surface Transport on Laser-Irradiated Foils

D. W. Forslund and J. U. Brackbill

Los Alamos National Laboratory, Los Alamos, New Mexico 87545

Electrons heated by absorption of laser energy are shown to generate intense magnetic fields which rapidly spread from the edge of the laser spot along the target surface. The fields convectively transport hot electrons and confine a major fraction of the deposited laser energy in the corona. Eventually, this energy is lost to fast-ion blowoff or deposited at large distances from the spot. This model qualitatively explains many experimental observations of thermal-transport inhibition and fast-ion loss.

The generation of magnetic fields when intense laser light is absorbed in a plasma is well known.[1] It has been studied because its inhibition of electron transport would explain the inferred flux limits needed to model energy transport in laser-produced plasmas.[2] Here we report new results from fully self-consistent calculations in collisionless plasmas.[3] These show large self-generated magnetic fields in the corona which convectively transport 30% or more of the absorbed energy laterally and collimate the remainder behind the laser spot. The results appear to qualitatively explain for the first time from first principles a wide variety of experimental data on fast-ion loss and lateral transport at various laser wavelengths.

Coronal magnetic field generation by collisionless processes is modeled in the relatively simple geometry shown in Fig. 1. We consider a plasma foil 500 μm wide in y in a 600-μm-wide system with a sharp initial density gradient in x. The deposition by a 10.6-μm laser at an average absorbed intensity of 5×10^{13} W/cm^2 in a 60-μm spot is modeled by accelerating some electrons from 2.5 to about 20 keV down the density gradient in a

20° half-angle cone with maximum heating at the center. At the boundary behind the high-density material, heat is absorbed by a cool electron thermal bath. The ion to electron mass ratio is 1836. This system is numerically simulated with a two-dimensional, implicit electromagnetic simulation code, VENUS,[4] which solves Maxwell's equations and Newton's laws self-consistently for particle electrons and ions. The behavior with [(d)–(f)] and without [(a)–(c)] self-generated magnetic fields is shown in Fig. 2.

Without magnetic fields, the electrons accelerated outward return from the sheath back towards the foil. In the y-v_x phase space of Fig. 2(a), the

FIG. 1. Diagram showing geometry of model where the shaded box is the laser deposition region. The system is uniform in z and the maximum density is twice critical density for 10.6-μm light.
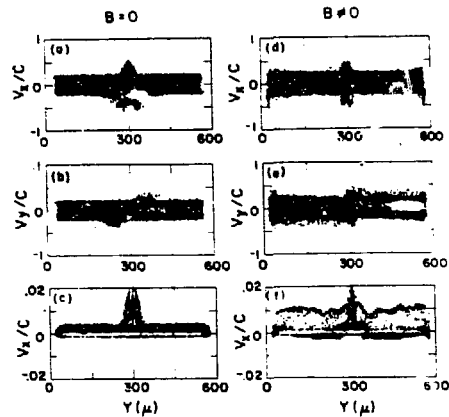
FIG. 2. Results of simulations with a 60-μm spot on a 500-μm-wide foil at 12 psec. (a)–(c) correspond to $B = 0$ and (d)–(f) correspond to $B \neq 0$. (a) and (d) are electron phase space v_x vs y for all x, (b) and (e) are electron phase space v_y vs y for all x, and (c) and (f) are ion phase space v_x vs y for all x. Only electrons with $|v| > 0.17c$ and ions with $|v| > 0.00125c$ are plotted.

An Implicit Method for Electromagnetic Plasma
Simulation in Two Dimensions*

J. U. BRACKBILL AND D. W. FORSLUND

*Applied Theoretical Physics Division, Los Alamos National Laboratory,
Los Alamos, New Mexico 87545*

Received November 13, 1981

A new method for modeling low-frequency plasma phenomena is presented. The method
uses an implicit formulation of the Vlasov–Maxwell equations to relax restrictions on the
time step and mesh spacing so that larger values which correspond to the frequencies and
wavelengths of interest can be used. As a result, the range of length and time scales accessible
to plasma simulation is increased by orders of magnitude. The algorithm, as embodied in a
new code VENUS for electromagnetic plasmas in two dimensions, is described, its stability
and accuracy analyzed through linear and nonlinear analysis, and its properties, including
suppression of the finite grid instability, illustrated through its application to the Weibel
instability.

INTRODUCTION

To extend the reach of nonrelativistic electromagnetic plasma simulation in two
dimensions to longer physical length and time scales, an implicit method has been
developed. The implicit method alters the way the coupled field and particle
equations are advanced in time and eliminates many of the constraints on the time
and space steps imposed by stability conditions.

As is well known, explicit formulations of the Vlasov–Maxwell equations are stable
only for values of the time step Δt and mesh interval Δx that resolve all time and
space scales [1, 2]. In electromagnetic plasma simulation, for example, one is
required to use time steps which resolve light waves and space steps which resolve the
Debye length, even when neither radiation nor charge separation effects are
important. In many cases, the time and length intervals of interest are very large
compared with the values of Δx and Δt that satisfy the stability conditions, and then
many time and space steps are required to integrate over them. This prevents the
application of explicit plasma simulation methods to many problems [3].

271

Plasma Mechanism for Ultraviolet Harmonic Radiation Due to Intense CO₂ Light

B. Bezzerides, R. D. Jones, and D. W. Forslund

University of California, Los Alamos National Laboratory, Los Alamos, New Mexico 87545

(Received 15 June 1981)

A theoretical explanation is presented of some observations from recent CO₂-laser experiments by introducing a novel mechanism for harmonic light emission. The theoretical model provides new insight into the properties of large-amplitude waves in the extremely inhomogeneous environment caused by strong profile modification of the critical-density plasma.

Harmonic generation in laser-irradiated plasmas has been the subject of a number of experimental[1,2] and theoretical papers.[3] These studies have been confined primarily to second-harmonic (SH) emission. The analytic efforts to understand SH have relied on perturbation theory based on the assumption of a weakly nonlinear response by the plasma in which the source current for the SH is due to beats between the first-harmonic field. Higher harmonics up to the eleventh harmonic of CO₂-laser light have been reported by Burnett *et al*.[4] The relative efficiency of the emitted lines in this work was a decreasing function of harmonic number, again a result corresponding to a weakly nonlinear plasma response.

A recent paper reported the observation of CO₂ harmonic light as high as the 29th harmonic,[5] and more recently, as high as the 46th harmonic.[6] The unique feature of these data is the constant relative efficiency of the lines. It is obvious that to understand these data one must introduce a new approach which goes beyond any analysis based on mode coupling and perturbation theory. Furthermore, these data are compelling evidence for nonlinearity heretofore unexplored in the study of laser-plasma interactions. The purpose of this Letter is to understand some of the properties of this nonlinearity.

Before we discuss the nonlinear mechanism for the high-harmonic CO₂ emission, let us consider the absorption of the incident light. It is generally accepted that the dominant absorption mechanism of intense CO₂-laser light in laser-fusion applications is resonant absorption.[7] Resonant absorption in a fixed plasma density profile is a linear mechanism whereby incident light tunnels from the electromagnetic turning point and excites plasma density oscillations at the critical density, n_c, where $\omega = \omega_p$, with ω the incident light frequency and ω_p the local plasma frequency, respectively. Throughout the pulse time of the laser the plasma density is certainly not fixed

and can develop a sharp plasma boundary as a result of the very substantial pressure of the intense laser light ($> 10^{16}$ W/cm²). The importance of this steepened plasma density profile will become apparent in what follows.

To understand the emitted spectrum we start with the radiation field,

$$\bar{B}(\bar{x}, t) = \int \left(\frac{[\dot{\bar{j}}']}{cR} + \frac{[\bar{j}]}{R^2} \right) \times \hat{R}\, dt', \quad (1)$$

where the square brackets denote retarded time, the current $\bar{j} = -en\bar{v}$, with n and $\bar{v}$ the electron fluid density and velocity, respectively, and $\bar{R} = \bar{x} - \bar{x}'$. Introducing the Lagrangian variables $\bar{x}' = \bar{x}_0' + \bar{\delta}(\bar{x}_0', \tau')$, $\tau' = t'$, where $\bar{\delta} = \int^\tau d\tau' \, \bar{v}(\bar{x}_0, \tau')$ with $n_e d^3x' = n_0 d^3x_0'$, we find for the far field,

$$\bar{B}(\bar{x}, t) = -\frac{e}{c^2} \left(\int d^3x_0' \, n_0 \frac{\hat{R} \times \partial \bar{v}/\partial \tau}{R} (\bar{x}_0', \tau) \right), \quad (2)$$

where n_0 is the ion density, assumed fixed, and now $\bar{R} = \bar{x} - \bar{x}_0'$. We have neglected relativistic corrections, and used $\omega \delta/c \ll 1$, which requires $v_0/c \ll 1$, as we will see, where $v_0 = eE_0/m\omega$ with E_0 the incident field intensity. This form for $\bar{B}$ is useful since it shows that only the fluid acceleration, albeit in Lagrangian coordinates, is needed to calculate $\bar{B}$. The justification for the use of Lagrange-transformed variables for all time, even though hot electrons are produced at high incident intensity, follows from the observation that fluid-element crossing does not occur if the full electron pressure is included in the electron Euler equation.[8] Except for the integral over the radiating material Eq. (2) is identical to the single-particle result and leads to the well-known Larmor formula for the total power radiated.

The acceleration is given by

$$\frac{\partial \bar{v}}{\partial t} + \frac{1}{2} \nabla v^2 = -\frac{e}{m} \bar{E} - \frac{\nabla \cdot \bar{P}_e}{mn_e}, \quad (3)$$

where we have used the relation $\nabla \times \bar{v} = e\bar{B}/mc$, and $\bar{P}_e$ is the electron-pressure tensor. We now

202   © 1982 The American Physical Society

**REPRINTS IN
SPACE PHYSICS
SINCE 1982**

Collective Capture of Released Lithium Ions in the Solar Wind

D. WINSKE,[1] C. S. WU,[2] Y. Y. LI,[2,3] AND G. C. ZHOU[2,4]

The capture of newly ionized lithium ions in the solar wind by means of electromagnetic instabilities is investigated through linear analysis and computer simulation. Three instabilities, driven by a lithium velocity ring perpendicular to and drifting along the magnetic field, are considered. The capture time of the lithium by the solar wind is roughly 10 linear growth times, regardless of whether resonant or nonresonant modes dominate initially. Possible implications of the results for the Active Magnetosphere Particle Tracer Explorer (AMPTE) mission are discussed.

1 INTRODUCTION

One of the principal tasks of the Active Magnetospheric Particle Tracer Explorer (AMPTE) mission will be the release of lithium atoms in the solar wind in front of the earth's bow shock and the subsequent monitoring of them as they pass into the magnetosphere. A description of the mission, its overall goals, and the spacecraft instrumentation is given by *Krimigis et al.* [1982]. A key issue is where to release the lithium to achieve the most efficient transmission into the magnetosphere. The most promising strategy is to release the lithium close to the quasiperpendicular portion of the bow shock so that its gyromotion will quickly carry it into the downstream region, as has been shown by following single particle trajectories [*Brinca*, 1984; *Decker et al.*, 1983, this issue; *Haerendel and Papamastorakis*, 1983]. Because the solar wind conditions are sometimes highly dynamic and unpredictable, it is also important to know what happens if the lithium ions do not gyrate rapidly through the shock, either because the bow shock recedes away from the release point or the orientation of the interplanetary magnetic field changes to be more nearly aligned with the solar wind. In this case, motion along the magnetic field is also important, and how rapidly the lithium ions are "captured" by the solar wind, that is, brought up to a velocity equal to that of the solar wind in the direction parallel to the magnetic field, becomes an issue.

Here we examine this question, in particular with regard to the role of collective effects in the capture process. The basic picture we propose is that after ionization the newborn lithium ions form a ring in velocity space perpendicular to the magnetic field (in the solar wind frame), while drifting relative to the solar wind along the magnetic field. Such a ring beam velocity distribution is unstable to various electrostatic and electromagnetic instabilities. The situation is similar to that discussed by *Wu and Davidson* [1972]. *Wu et al.* [1973], *Hartle and Wu* [1973], and *Wu and Hartle* [1974], who considered the problem of the capture of newly created He⁺ ions of planetary origin. In these articles the authors hypothesized that the newborn ions can excite a variety of wave modes, and consequently, the instabilities and ensuing turbulence can

result in the collective capture of the He⁺ ions. Interest in this problem has been revived by the AMPTE project. The purpose of this brief report is to summarize recent results, which demonstrate by means of linear stability analysis and computer simulation that low-frequency electromagnetic instabilities due to the newborn lithium ions may play an important role in the capture process.

While there are many parameters to be considered, we concentrate here on only one, the density of the lithium cloud, which is highly uncertain. The density may be comparable to that of the solar wind if ionization occurs very rapidly, say ionization by the gas-plasma interaction process [*Alfvén*, 1954], or much smaller than that of the solar wind if photoionization by solar ultraviolet radiation prevails. In the analysis we take the lithium density as small but arbitrary and examine the results over a wide range of density ratios (10^{-5} to 10^{-1}). It is conceivable that even larger lithium concentrations could be possible, but in that case we would expect that large local density variations would develop, invalidating the theory we present.

The plan of the paper is as follows. In section 2 we describe the model in detail and summarize the results of the linear analysis for the three instabilities considered. Results of computer simulations used to investigate the nonlinear behavior of the instabilities are then presented, first for an idealized (infinite, homogeneous) situation and then for more realistic cases in which the finite extent of the lithium cloud, its expansion in time, and interaction with upstream turbulence are considered. Because of the length restrictions of this brief report, we limit the discussion to a summary of the major points; the details will be presented later in a full length article. In section 3 we summarize the results and discuss possible consequences for the AMPTE mission.

2. RESULTS

2.1. Model

The distribution of newly ionized particles in the solar wind has been described by *Wu and Davidson* [1972]. If $\mathbf{n} = \mathbf{B}_0/B_0$ is a unit vector along the interplanetary magnetic field $\mathbf{B}_0$, in the solar wind frame such ions have a parallel velocity $v_{0\parallel} = \mathbf{n} \cdot (\mathbf{V}_{sw} - \mathbf{v}_i)$, where $\mathbf{V}_{sw}$ is the solar velocity and $\mathbf{v}_i$ is the newborn ion velocity. The ions gyrate perpendicular to the magnetic field with a transverse speed $v_{0\perp} = |(\mathbf{V}_{sw} - \mathbf{v}_i) \times \mathbf{n}|$. For simplicity, we take the angle between $\mathbf{V}_{sw}$ and $\mathbf{B}_0$ to be 45° and neglect $\mathbf{v}_i$ so that the lithium ions form a ring with $V_\perp = V_{sw}/\sqrt{2}$, streaming relative to the solar wind with $V_\parallel = V_\perp$. As the angle between $\mathbf{V}_{sw}$ and $\mathbf{B}_0$ changes, the source of free energy, and thus the character of the instability, changes from being more beamlike when $\mathbf{V}_{sw}$ and $\mathbf{B}_0$ are more aligned

[1] Los Alamos National Laboratory, Los Alamos, New Mexico.
[2] Institute for Physical Science and Technology, University of Maryland, College Park, MD 20742.
[3] Permanently at Southwestern Institute of Physics, Leshan, Sichuan, China.
[4] Permanently at Institute of Space Physics, Chinese Academy of Sciences, Beijing, China.

7327

Low-Altitude Image Striations Associated With Bottomside Equatorial Spread F: Observations and Theory

James F. Vickrey

SRI International, Radio Physics Laboratory

Michael C. Kelley and Robert Pfaff

School of Electrical Engineering, Cornell University

S. Robert Goldman

Los Alamos National Laboratory

Ionospheric plasma instabilities are usually discussed in terms of local parameters. However, because electric fields of scale size $\lambda \gtrsim 1$ km map along magnetic field lines, plasma populations far away from a locally unstable region may be affected by the instability process and vice versa. We present observations of electron density variations in the F_1 region of the ionosphere at two locations near the magnetic equator. Oscillations in electron number density that were confined to a narrow wavelength regime were observed in a region of the ionosphere with a very weak vertical density gradient. Since magnetic flux tube interchange instabilities cannot create structure in such an environment we suggest that these are "images" of instabilities occurring elsewhere along the magnetic field line. A simple steady state theory of image formation is developed that is in good agreement with the observations. Moreover, this theory predicts a scale size dependent "effective diffusion" process in the F region that may dominate over classical cross-field diffusion at kilometer scale sizes. Such a scale size dependent diffusion process is required to explain recent scintillation observations of decaying equatorial plumes.

1 Introduction

Ionospheric plasma instabilities are often discussed in terms of local parameters. However, magnetic field lines can link unstable regions to other plasma populations that may affect the evolution of the instability process. An example is the role of a conducting E region in diffusive damping of F region structure and in the suppression of electrostatic instabilities [*Volk and Haerendel*, 1971; *Goldman et al.*, 1976; *Vickrey and Kelley*, 1982].

Another effect most often studied in conjunction with F region barium cloud striations is the generation of image striations in the background medium. As discussed in more detail below, an image forms at altitudes where the ion gas is compressible, namely, the E and lower F_1 regions. To date, the existence of images has not been experimentally verified, although computer simulations have predicted their generation [*Goldman et al.*, 1976; *Lloyd and Haerendel*, 1973].

The data discussed here come from fixed bias Langmuir probes flown on two rockets launched just off the magnetic equator during equatorial spread F conditions. One, a Javalin sounding rocket, was launched by NASA from Natal, Brazil, on November 18, 1973, at 2122 UT [*Kelley et al.*, 1976, 1979; *Costa and Kelley*, 1978]. The second, a Terrier-Malemute designated as PLUMEX I, was launched by the Defense Nuclear Agency from Kwajalein Atoll on July 17, 1979, at 1233 UT [*Szuszczewicz et al.*, 1980; *Rino et al.*, 1981; *Kelley et al.*, 1982]. We will show that the spectrum of density structure observed in the F_1 layer valley (160- to 200-km altitude) off the magnetic equator is consistent with that expected from the image formation process (which depends on scale length and

density) driven by the gravitational Rayleigh-Taylor instability operating on the bottomside F layer at the equator itself.

2. Data Presentation

A plasma density profile from the downleg of the Natal rocket flight is reproduced in Figure 1a with an expanded plot of the F layer valley and E region density profiles in Figure 1b (upleg data is not available in these flights in the low-altitude region due to the timing of sensor deployment). The plasma density profile was extremely structured throughout the flight. Near and just below the F region peak, the turbulence has been interpreted in terms of the nonlinear gravitational Rayleigh-Taylor instability (see earlier references). The low-altitude layered (90–130 km) structure is typical of the equatorial E region and is not produced by the "image" process. Of interest to the present study are the quasi-sinusoidal fluctuations in the F_1 layer valley (170 to 200 km) where the local zero-order vertical plasma density gradient nearly vanishes. Because of the finite dip angle at Natal, these fluctuations project along magnetic field lines to the magnetic equator at heights ranging from 280 to 315 km. Note that this altitude range corresponds to heights where the local equatorial F region is suspected to be unstable to the gravitational Rayleigh-Taylor process. The geometry is illustrated schematically in Figure 2. Of course, we do not have simultaneous F region observations directly at the equator, but it is highly likely that bottomside spread F was occurring there also.

Another example from the PLUMEX I rocket downleg is presented in Figure 3. Again, quasi-sinusoidal oscillations were observed in the F_1 layer valley region at heights that map to the magnetic equator in the altitude range at which the local equatorial spread F fluctuations were detected. The detector used in the present study was not deployed during the upleg of PLUMEX I. However, *Narcisi and Szuszczewicz*

EXTENSION OF THE RECONNECTION THEORY
OF TWO-RIBBON SOLAR FLARES

R. A. KOPP

Inertial Fusion and Plasma Theory Group, Los Alamos National Laboratory,
Los Alamos, NM 87545, U.S.A.

and

G. POLETTO

Osservatorio Astrofisico di Arcetri, Largo Enrico Fermi 5, 50125 Firenze, Italy

Abstract. The magnetic reconnection theory for two-ribbon flares and flare loops hypothesizes that the gradual energy release during the decay phase is a direct result of dissipative relaxation of the open coronal magnetic configuration created by an eruptive prominence/coronal transient precursor. This scenario is here developed quantitatively to the point where a realistic comparison with observational data can be attempted Our major refinements are (i) to use an analytical description of the reconnecting field geometry specifically chosen to characterize the spatial scale of the active region where a flare occurs, and (ii) to take account of the fact that the volume occupied by X-ray-emitting plasma (hot loops) generally increases with time during the flare.

As a test of the modified theory we have undertaken a new representation of the Skylab observations of the large two-ribbon flare of 29 July, 1973. It is hereby found that the simultaneous inclusion of the above two factors yields an excellent agreement between the theoretical prediction and observations of the time variation of flare-plasma energy density; such was not possible within the framework of previous work along these lines. The agreement extends, moreover, to rather early times in the flare history, where the short-comings of earlier studies became especially noticeable. This result constitutes strong evidence to support previous speculations that magnetic reconnection may provide the sole energy source throughout nearly the entire flare lifetime.

1. Introduction

The magnetic reconnection theory for the 'decay phase' of two-ribbon flares, as developed originally by Kopp and Pneuman (1976) and subsequently by Pneuman (1981, 1982), Cargill and Priest (1982), Forbes and Priest (1982, 1983a, b), and others, is generally regarded (Švestka *et al.*, 1980; Pallavicini and Vaiana, 1980) as providing a comprehensive and self-consistent description of the relationships between a wide variety of flare-associated phenomena – filament eruptions, Hα-ribbon brightenings and separations, hot (X-ray) and cool (Hα) flare-loop growth, and nonthermal particle generation and storage. Briefly, the theory hypothesizes that a two-ribbon flare is the visible manifestation of magnetic reconnection in the corona above the flare site, the stressed open-field structure within which this reconnection occurs having been created immediately beforehand by a filament activation/disruption and coronal transient. The excess magnetic energy of the distended field is released (rapidly at first and more gradually as the flare progresses) as reconnection allows a lower energy configuration

Collisionless Dissipation in Quasi-Perpendicular Shocks

D. W. FORSLUND, K. B. QUEST, J. U. BRACKBILL, AND K. LEE

Los Alamos National Laboratory

Microscopic dissipation processes in quasi-perpendicular shocks are studied by two-dimensional plasma simulations in which electrons and ions are treated as particles moving in self-consistent electric and magnetic fields. Cross-field currents induce substantial turbulence at the shock front reducing the reflected ion fraction, increasing the bulk ion temperature behind the shock, doubling the average magnetic ramp thickness, and enhancing the upstream field aligned electron heat flow. The short scale length magnetic fluctuations observed in the bow shock are probably associated with this turbulence

INTRODUCTION

Understanding of the dissipation of energy in collisionless magnetic shocks has been sought for many years. Satellite observations of the earth's bow shock illuminate the structure of collisionless shocks including ion reflection [*Montgomery et al*, 1970; *Paschmann et al*, 1982], magnetic field overshoot [*Heppner et al*, 1967; *Livesey et al*, 1982], thickness of the transition layer [*Russell and Greenstadt*, 1979], electron and ion heating rates [*Bame et al*, 1979], and high-frequency fields [*Greenstadt et al*, 1980; *Rodriguez and Gurnett*, 1975, 1976] in the shock layer itself. Compared with these observations, one-dimensional particle simulations [*Biskamp and Welter*, 1972; *Auer et al*, 1971] typically overestimate the number of reflected ions because cross-field resistivity is absent. One-dimensional hybrid simulations [*Leroy et al*, 1981, 1982] that treat the resistive heating phenomenologically describe the thickness of the foot region and the overshoot region. However, the mechanism for electron heating is unknown and the proper ramp thickness is not obtained in such models. Here, some preliminary results are presented from two-dimensional plasma simulations of quasi-perpendicular shocks that resolve the ion and electron time and space scales. The new results not only reproduce or extend most of the one-dimensional simulation results reported earlier, but also allow one to identify important new electron and ion dissipation processes in the earth's bow shock and to observe upstream field aligned electron heat flow.

SIMULATION RESULTS

The bow shock is modeled in two dimensions by a newly developed implicit particle-in-cell simulation technique [*Brackbill and Forslund*, 1982]. Very high frequency, ω_{pe}, oscillations are eliminated without removing electron inertial and kinetic effects. In the simulation code VENUS [*Brackbill and Forslund*, 1982], two spatial coordinates and three velocities are treated for each species in the self-consistent, three-component electric and magnetic fields. Numerical dissipation in the code is smaller than the dissipation in the shock due to self-consistent collisionless collective effects.

A magnetic piston is used to drive the shock. The piston, a tangential discontinuity which pushes the plasma towards

the left, is generated at the right boundary by a transverse electric field E_z (Figure 1). By analogy with the earth's dayside magnetopause, the piston is a magnetic barrier through which the magnetic field intensity increases and the number density drops to zero. In the frame moving with the piston, a super Alfvénic plasma hits the barrier, launching compressional waves which propagate upstream and steepen to form a shock. The angle between upstream B and v is 78° and allows for some motion of the electrons along the field lines into and out of the shock.

The simulation parameters chosen are for a $\beta_e = 2$ plasma with $\beta_i = 2$ or 0.2 and an Alfvén mach number of the shock of 4.5. The units of length in our figures are upstream c/ω_{pi}, typically of order 100 km; velocity is shown in units of the upstream Alfvén speed, and time is given in terms of the inverse ion gyrofrequency, Ω_i^{-1}. For economy, we have chosen $m_i/m_e = 100$ and $\omega_{pe}/\Omega_e = 20$.

The direction of the ambient field relative to the simulation plane can strongly affect the types of instabilities allowed in the code. This can be used to advantage in studying shocks. For example, in a perpendicular shock propagating in the x direction through an ambient magnetic field in the y direction, the diamagnetic currents are in the z direction and thus out of the plane of simulation. Thus cross field current instabilities are not allowed, but pitch angle scattering instabilities are. However, by rotating the ambient field out of the plane, the currents move into the plane allowing cross-field instabilities to occur. We make use of this difference to illustrate the transition from essentially zero cross-field resistivity to the finite level self-consistently produced by cross-field current instabilities.

In Figure 2 we show phase space plots with B in the simulation $(x - y)$ plane $(B_z = 0)$ and $T_e/T_i = 10$. In this plane cross-field current driven instabilities cannot be excited, so we anticipate a quasi-laminar shock structure with substantial ion reflection. The three components of velocity of ions and electrons are plotted versus the coordinate x at $\Omega_i t = 4.5$ to show the ion reflection and heating of ions and electrons behind the shock.

At the time chosen the shock position is approximately $x = 12c/\omega_{pi}$ and is separated from the piston by a distance of $6-7c/\omega_{pi}$. As will be seen, the separation distance corresponds to several ramp thicknesses, so the processes operating within the ramp may be examined separately from those near the piston. Additionally, the shock separation from the left wall is large enough so that boundary effects may be neglected.

2142

131

Collisionless Dissipation Processes in Quasi-Parallel Shocks

K. B. Quest, D. W. Forslund, J. U. Brackbill, and K. Lee

Los Alamos National Laboratory, Los Alamos, New Mexico 87545

ABSTRACT. The evolution of collisionless, quasi-parallel shocks ($\theta_{Bn} < 45°$, where θ_{Bn} is the angle between the shock normal and the upstream magnetic field) is examined using two dimensional particle simulations. Reflected ions upstream from the shock are observed with average guiding center velocity and gyrational energy which agree well with the prediction of simple specular reflection. Strong ion heating through the shock ramp is apparently caused by large amplitude whistler turbulence. A flux of suprathermal electrons is also observed upstream with increased flux oblique to the magnetic field direction. Much stronger ion heating occurs in the shock than electron heating. The relevance of this work to the earth's bow shock is discussed.

Introduction

Collisionless shocks in the solar wind are generated by flares and by the steepening of high-speed solar wind streams at large heliocentric distances (Greenstadt and Fredricks, 1979), while bow shocks surround every planet. Because of the extensive data from ISEE satellites, detailed comparisons with theory are possible. For example, using particle-in-cell plasma simulations with idealized boundary conditions and geometries, one can obtain "snapshots" of the instantaneous velocity distribution functions and the full magnetic field profile at any desired time. These may be compared with analytic theories and satellite data to test the understanding of the physics of collisionless shocks.

Here we present the results of recent two-dimensional electromagnetic, fully kinetic simulations of quasi-parallel shocks (Similar simulations of quasi-perpendicular shocks are reported in Forslund, et al., 1982). Using an implicit algorithm (Brackbill and Forslund, 1982) we calculate the full electron and ion dynamics on large spatial scales (many ion gyroradii) for long times (many gyroperiods) with ion to mass ratios of O(100). Thus we remove the earlier restrictions of one dimensionality (Biskamp and Welter, 1972) and of a resistive fluid treatment of the electrons (Leroy, et al., 1981).

Removing these restrictions allows us to separate spatially the shock and piston (see below), to examine electron dissipation, and to observe such features as field aligned heat flux and electron trapping. This is particularly important for quasi-parallel shocks, where motion along the field line can result in strong acceleration of the electrons through the shock transition layer. Two dimensionality also allows us to model the turbulence due to the transverse

currents in the shock front. Finally, including electron inertial effects allows us to properly treat whistlers generated in quasi-parallel shocks.

Simulation Model and Parameters

We consider a uniform density plasma in a uniform magnetic field ($B_x,0,B_z$) with Maxwellian ion and electron distributions at T_i and T_e respectively. A magnetic piston is driven into the plasma from the right, launching a shock that runs ahead of the piston.

In our simulations $\theta_{Bn} = 37°$, the Alfvén Mach number is approximately 4, and the upstream electron β is 2. These values approximate observations made during a bow shock crossing by ISEE 1,2 on August 15, 1978, (Gosling et al., 1982). To explore the effect of different ion temperatures, we have held T_e fixed and used $T_e/T_i=1$ and 10. For an upstream electron β of 2, varying T_e/T_i varies the magnetosonic Mach number from about 2.5 (when $T_e/T_i=10$) to 1.8 ($T_e/T_i=1$). The units of length in the figures, c/ω_{pi}, are typically of order 100 km in the solar wind. The velocity is shown in units of the upstream Alfven speed, and time is given in units of the inverse ion gyrofrequency, Ω_i^{-1}. To keep the electron scale lengths reasonably resolved, we have chosen $m_i/m_e = 100$ and $\omega_{pe}/\Omega_e = 20$, where ω_{pe} is the electron plasma frequency. All the results below are at $t=4.5\Omega_i^{-1}$, when the shock and piston are well separated.

Simulation Results.

In Fig. 1 we show phase space plots of the ions versus the shock normal coordinate x for the two
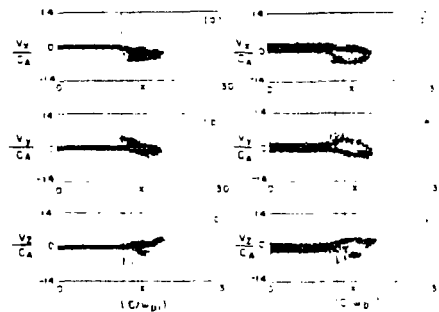
Fig. 1 Phase space plots of ions vs x for simulation with $T_e/T_i=10$ (a-c) and $T_e/T_i=1$ (d-f) at $\Omega_i t=4.5$. Simulation grid is 32 c/ω_{pi} (c/ω_{pi}) by 256 cells in x (30 c/ω_{pi} ... 10000 each of electrons and ions and a time step of $4\omega_{pe}^{-1}$ was used.

REPRINTS IN
DRIVER TECHNOLOGY
AND
FACILITIES
SINCE
1982

Ion Source Development for the Los Alamos Heavy
Ion Fusion Injector, H.L. RUTKOWSKI, S. HUMPHRIES, E.A.
MEYER, H. OONA, R. SHURTER, and L. ENGELHARDT,* Los
Alamos National Laboratory, Los Alamos, NM 87545--The
Heavy Ion Fusion Injector program at Los Alamos is
oriented toward producing a 16-beam, high current,
2 MeV injector which will serve as a source for multi-
ple beam accelerator experiments and as a prototype in-
jector for the High Temperature Experiment (HTE)
accelerator.   The ion source requirements for this
device are quite stringent. We are reporting on char-
acterization experiments performed in a test stand
extractor system, with aluminum spark, pulsed plasma
sources. The pulsed plasma is kept out of the extrac-
tor gap with a double grid plasma switch. Currents are
measured with a gridless Faraday probe. Emittance is
measured with a pepper-pot method. The beam itself is
imaged with a thin film aluminum fluorescer. We also
discuss a multiple beam extractor experiment to study
multiple beam effects at low energy.

Submitted by: _____

H.L. Rutkowski
Los Alamos National Laboratory
P-7, MS E525
Los Alamos, NM 87545
(505) 667-9315

Classification #: A03   Presentation Option: Oral

To Be Presented at CLEO '85, Baltimore, Maryland, May 21-24, 1985

PERFORMANCE OF THE LARGE APERTURE MODULE OF THE AURORA

KRYPTON FLUORIDE LASER SYSTEM

G. W. York, Jr.
S. J. Czuchlewski
L. A. Rosocna
E. T. Salesky

Los Alamos National Laboratory
Group P-16, MS E543
Los Alamos, New Mexico 87545
Telepnone: (505) 667-3714

SUMMARY

Tne Large Aperture Module (LAM) is tne final amplifier of the Los Alamos Aurora krypton fluoride (KrF) laser system.[1] An artist's conception of the device is shown in Fig. 1. It consists of a laser chamber witn a 1-m x 1-m aperture and a 2-m active lengtn wnicn is directly pumped by opposing 1-m x 2-m electron beams (up to 675 kV @ 20 A/cm^2). Eacn electron gun is driven by two 2.7Ω water pulse forming lines (PFL) connected in parallel. Tne PFLs are eacn 10.7 m long, giving a 650-ns pump pulse. Eacn pair of water lines is pulse cnarged by a Marx generator capable of producing up to 1.8 MV. A pair of Helmnolz coils is provided to prevent beam pincning in the diodes and to ensure uniform pumping in the laser gas volume. The laser chamber can be filled witn up to 1.5 atm of an Ar, Kr, F_2 lasing mixture.

To date, tne amplifier nas been operated at up to about 75% of its rated voltage and preliminary experiments nave been performed to evaluate its performance. An unstaole resonator optical cavity was installed as

-2-

To Be Presented at CLEO '85, Baltimore, Maryland, May 21-24, 1985

Gain and Absorption Measurements of KrF Mixtures
With High Kr Concentrations

by

E.T. Salesky

Los Alamos National Laboratory

P.O. Box 1663

Los Alamos, New Mexico 87545

Telephone: (505) 667-5320

and

Wayne D. Kimura

Mathematical Sciences Northwest

2755 Northup Way

Bellevue, Washington 98004

Telephone: (206) 827-0460

ABSTRACT

Small signal gain ($g_o-\alpha$) and out-of-band (261 nm) absorption measurements are made of e-beam pumped KrF laser mixtures (Ar diluent) with 4%-99.6% Kr concentrations. Our computer model agrees with the results.

To Be Presented at CLEO '85, Baltimore, Maryland, May 21-24, 1985

Generation and Amplification of Single 5-ns 248-nm

Krypton Fluoride Pulses

by

S. J. Thomas and M. D. Burrows
P-16, MS E543
Los Alamos National Laboratory
P. O. Box 1663
Los Alamos, New Mexico 87545
Telephone: (505)667-9545

ABSTRACT

A Pockels cell is used to slice a 5-ns pulse from a longer 25-ns krypton fluoride pulse at 248 nm. The 5-ns pulse is then amplified in a discharge-pumped krypton fluoride amplifier with typical single-pass extraction energies of 200 mJ. The amplified 5-ns pulse is then used to drive a fusic. laser amplifier chain.

137

ENERGY EXTRACTION AND GAIN MEASUREMENTS ON THE
LOS ALAMOS LARGE APERTURE KrF LASER

G. W. York, S. J. Czuchlewski, E. T. Salesky, and L. A. Rosocha

Los Alamos National Laboratory
Los Alamos, New Mexico

SUMMARY

The Large Aperture Module (LAM) is designed to be the final amplifier of the Los Alamos Aurora KrF laser system. It is a double-sided direct electron beam pumped KrF amplifier with an aperture of 1 m x 1 m and an active length of 2 m. In initial tests, this device has been recently successfully operated as a KrF oscillator, producing an average flux greater than 0.4 J/cm^2 on an array of calorimeters. This 248-nm laser output was produced over the $1-m^2$ aperture using a positive branch, confocal unstable resonator optics set. This resonator consists of a pair of dielectric coated glass reflectors which form a telescope with a magnification of 2.88, resulting in an output coupling of 88%. The output window for these experiments consists of a mosaic array of 8-in. x 8-in. fused silica windows with a net transmission of approximately 60%, resulting in a delivered optical pulse of ~2.5 kJ. Correcting for window losses, this corresponds to an extracted energy from the pumped volume of >5 kJ in the 400-ns FWHM pulse at an energy efficiency of ~4%.

Small-signal gain measurements have also been performed at similar operating conditions, and the results will be compared to the predictions of the Los Alamos KrF kinetics code. The data are in good agreement with the code predictions. Details of the design of the amplifier will be presented.

THE ANTARES FACILITY FOR INERTIAL FUSION EXPERIMENTS

- STATUS AND PLANS

P. D. Goldstone, G. Allen, H. Jansen,
A. Saxman, S. Singer, and M. Thuot

Los Alamos National Laboratory
Los Alamos, NM 87545

INTRODUCTION

In the last decade several increasingly powerful short pulse CO_2 lasers have been constructed at Los Alamos National Laboratory to investigate the feasibility of CO_2 as an inertial fusion driver. The advantage of CO_2, a gas laser with high rep-rate capability, electrical efficiency as high as 10%, and scalability to large energies, must outweigh important difficulties in target physics due to the copious production of suprathermal electrons if CO_2 is to be considered a viable driver option.

Since 1978, Los Alamos has used the 10-kJ, eight beam Helios laser[1] to perform a variety of experiments aimed at elucidating basic laser-matter interaction mechanisms and beginning to determine the scalability of CO_2-driven targets to high driver energies. Antares, currently under construction, will be the next CO_2 laser used to further the experimental ICF program. Scheduled for operation early in FY-84, the Antares laser is designed to provide 30-40 kJ in a nominal 0.7 ns pulse, utilizing 24 independently pointable beams. Since Helios is generally limited to ~ 5 kJ operation in most target experiments, this will provide a significant increase in the energy available for target experiments, enabling us to study the energy scaling of target interaction phenomena as well as to perform experiments which are energy-limited at Helios.

Laser-initiated vacuum plasma shutters using a dielectric aperture for retropulse isolation

T. W. Sheheen, S. J. Czuchlewski, J. Hyde, and R. L. Ainsworth

University of California, Los Alamos National Laboratory, Los Alamos, New Mexico 87545

It is demonstrated that sintered LiF spatial-filter apertures may be used in a vacuum environment of 10^{-6} Torr as laser-initiated plasma shutters for retropulse isolation in high-energy laser fusion systems. In the experimental data presented, a 1.1-ns duration pulsed CO_2 laser at 10.6-μm wavelength with an energy of 3.0 J is used for plasma initiation. A chopped cw CO_2 laser tuned to 9.6 μm is used as a probe laser in determining the time the plasma blocks transmission of a CO_2 laser beam. Both the 10.6- and the 9.6-μm transmission were measured as a function of pulsed laser fluence on the aperture edge, up to 240 J/cm². Blocking times in excess of 1.0 μs were observed for an aperture diameter of 800 μm, for a Gaussian beam with a diameter of 1.2 mm determined at the $1/e^2$ intensity points.

PACS numbers: 42.60.Kg, 42.80.Bi

I. INTRODUCTION

In all high-energy laser-fusion systems, an important consideration is the protection of the front-end oscillator and optical components from damage by laser pulses that are reflected back into the laser systems from fusion targets. Any apparatus used in isolating the retropulse should be efficient, with a high forward transmission and low backward transmission, have a minimum of complexity for reliable operation, and for some applications function in a vacuum environment. It has previously been shown that an active shutter using an exploding wire device[1] may be used as a plasma source at the aperture of a spatial filter to block target-retroreflected light. Metal irises in air or ambient nitrogen environment also have been shown to produce a laser-initiated plasma[2] sufficient to "clamp" a retropulse transmission to a low level.

In this presentation, we demonstrate that a CO_2 (10.6-μm) laser-initiated plasma may be formed at the aperture of a LiF spatial filter in a vacuum of 10^{-6} Torr, of sufficient density and lifetime to block the retropulse from reentering the laser system. The plasma-initiation process is controlled by the fluence incident on the aperture edge of the spatial filter. Blocking times of the 9.6-μm probe laser are measured as a function of the incident laser fluences. Blocking times were also observed with the 10.6-μm pulse laser focused 2.0 mm off the axis in a radial direction of the cone shaped spatial filter. With a 1.1-ns pulsed 10.6-μm CO_2 laser incident on the LiF aperture, at a fluence level of 63 J/cm² on the edge of the 0.7847-mm-diam aperture, we have found that a plasma is initiated within the 1.1-ns pulse width, producing a small-signal transmission of 65%. Within 40 ns, the plasma reaches a critical density of 10^{19} cm^{-3}, sufficient to block the 9.6-μm probe laser. The plasma persists at or above the critical density for 680 ns; at larger values of edge fluences, blocking times in excess of 1.0 μs are possible. While considerable damage to metal irises in vacuum at high fluence levels has been observed, the sintered LiF spatial filter shows only minimal damage and no distortion of the aperture after more than 200 pulses in 10^{-6} Torr vacuum.

II. EXPERIMENTAL TECHNIQUE

A. Experimental arrangement

The present experiments employ up to a 3.0-J/pulse CO_2 laser at 10.6 μm, with a pulse width of 1.1 ns that is focused on a LiF spatial filter in a vacuum of 10^{-6} Torr with NaCl optical components. A continuous-wave (cw) chopped CO_2 probe laser at 9.6 μm is used to determine the blocking time of the laser-initiated plasma. The beam paths and experimental configuration are shown schematically in Fig. 1. The primary laser beam, with diameter of 3.0 cm, is focused on the spatial filter in the vacuum chamber using a NaCl lens of 60-cm focal length for an f/20 system. The input energy, sampled by using a wedge beam splitter, and the energy transmitted through the spatial filter are measured with pyroelectric joulemeters. Input fluence was varied without changing the beam diameter by inserting calibrated CaF_2 attenuators into the beam. Calibrated CaF_2 attenuators also were inserted into the beam in front of the joulemeters during calibration. The spatial filter is mounted on a lens holder (shown in Fig. 2) that has vertical and horizontal (x, y) micrometer drives that are adjusted from outside the vacuum system. The lens holder and drivers are in turn mounted on an optical rail in the chamber giving x, y, and z fine adjustment capability. Provided with these adjustments, the preliminary spatial filter alignment is obtained using a He-Ne laser beam sent through the optical system, with the spatial filter positioned for maximum transmission. This position is indicated and marked on a video monitor that views the spatial filter with a video camera and telescope. Final alignment of the filter is performed using the pulsed CO_2 laser, attenuated sufficiently to prevent plasma formation or flashing at the spatial filter aperture. The filter then is adjusted for maximum transmission while being viewed using the video system. The video system gives information on the deviation between the CO_2 and the He-Ne beam, as well as providing a monitor for observing any asymmetries during plasma formation. Beam spatial filter alignment was accomplished for

REPRINTS IN
MATERIALS
TECHNOLOGY
SINCE
1982

UNBACKED CYLINDRICAL METAL FOILS OF SUBMICRON THICKNESS*

DAVID V. DUCHANE AND BARRY L. BARTHELL

Los Alamos National Laboratory, Los Alamos, NM 87545 (U.S.A.)

Implosion experiments often utilize cylindrical thin metal foils. Previously these foils have been made either from flat sheets, with a seam where the edges joined, or in the form of a composite polymer/metal laminate, in which the plastic film acts as a supporting substrate.

A method has been developed to produce unbacked cylindrical metal foils of submicron thicknesses. This process utilizes a temporary substrate consisting of a water-soluble polymer film as a base for the electron beam deposition of the metal layer. After formation of the metal foil, the polymer is removed by immersion of the assembly in water. Unbacked metal foil cylinders as thin as 0.17 μm with extremely smooth wrinkle-free surfaces have been produced by this technique.

1. BACKGROUND

Cylindrical thin metal foils are of interest to a number of researchers conducting pulsed power experiments[1]. The earliest work in this area was carried out using commercially available flat foils. These were simply wrapped around a pair of support rings to produce a foil cylinder[2]. The seam at the point where the edges of the foil were joined was highly undesirable from the standpoint of implosion symmetry. It presented a region of essentially zero mass if a butt joint was formed, or an area with twice the mass per unit area of the main body of the foil when an overlap joint was utilized.

To overcome the problems associated with this joint, a technique for producing seamless foils was developed by Kindel *et al.*[3] In their process they utilized a cylindrical polymer substrate made according to the method of Grader *et al.*[4] The product was not a pure metal foil, but a composite consisting of a polymer film substrate with a continuous and uniform metal overlay. While this seamless polymer/metal laminate was an improvement over the previous wrapped foils, it presented a number of problems in fabrication and use. The polymer film was formed from a noxious organic solvent by a dip-casting process. Because the

---

Scattering of light by laser fusion targets with small defects

David E. Cooper, Dau-Sing Wang, and Milton Kerker

The extended boundary condition method was used to determine the effect imperfections in small glass and metal shells have on scattered light at 10.6 μm. The results indicate that imperfections cause a shift in the locations of the minima in the differential scattering curve, a change in the extinction efficiency, and the presence of depolarized components for off-axis orientation of the object. Among these, the presence of and changes in the depolarized component are most sensitive to imperfections. We compute the depolarized scatter from shells with types I, II, and III defects and discuss the potential of light scattering as a characterization tool for laser fusion targets

I. Introduction

Light scattering has long been known to be an extremely sensitive probe of the structure of small particles.[1,2] This fact suggests that it might be possible to use light scattering to measure specific types of defects on the surfaces of small shells used in the construction of laser fusion targets. Typical shells are fabricated out of either glass, plastic, or a high-Z metal such as gold.[3] For a shell to be useful as a target in laser fusion studies, certain well-defined types of defects must be kept below a minimum value. The defects of primary interest, referred to as types I, II, and III,[4] are illustrated in Fig. 1. A type I defect occurs when both inside and outside surfaces of the shell are spherical but not concentric. If either surface is ellipsoidal, we have a type II defect, and a local defect, such as a bump or dimple, is labeled type III.

The characterization requirements on a simple glass or metal shell used in a laser fusion target are quite severe and are illustrated in Fig. 2. Specifically, types I and II defects must be below 1%, whereas a type III defect must be held to below 0.1%. Techniques currently used to characterize shells with such sensitivities include optical interferometry, x-ray microradiography, and scanning electron microscopy.[5] While such techniques are quite sensitive, they are rather time-consuming and do not lend themselves to examination of the large numbers of targets that will eventually be required for a power generating station. Light scattering offers to be both a sensitive and fast technique of defect detection as well as being considerably easier to implement than the techniques now in use. It is, therefore, of interest to determine what effect a defect has on the light scattered by a glass or metal shell.

This paper presents the results of computer studies to determine the effect of types I, II, and III defects on the light scattered by small spherical shells. Although computations were actually carried out in both the optical (0.5 μm) and IR (10.6 μm) regions for both glass and metal shells, only the latter will be presented here, since, for the same size parameters, there were only minor differences. The size parameters studied ranged from 5 to 30. The computer code used in these studies relies on the extended boundary condition method (EBCM) and will be briefly discussed in Sec. II. The complexity of these calculations is substantial, requiring as much as 30 min of computation time on a Cray-1 computer at the largest size parameters studied. Section III presents the results of the calculations, and Sec. IV discusses the feasibility of using light scattering to detect defects of interest on small shells, presents a novel detection scheme, and discusses some difficulties that yet need to be overcome.

II. Theory

The scattering calculations use the EBCM, which was first developed by Waterman[6,7] originally for conducting objects, and was then applied to multilayered objects.[8-10]

In this approach, we utilize the spherical harmonic expansions for the incident fields, the scattered fields, and the fields inside the object in conjunction with boundary conditions at the surfaces between adjacent layers to obtain a system of linear equations. The unknown expansion coefficients of the scattered fields are

David E. Cooper is with University of California, Los Alamos National Laboratory, P.O. Box 1663, Los Alamos, New Mexico 87545; D. S. Wang is with McDonnell Douglas Research Laboratory, St. Louis, Missouri 53166; and M. Kerker is with Clarkson College of Technology, Potsdam, New York 13676.

TYPE I   TYPE II   TYPE III
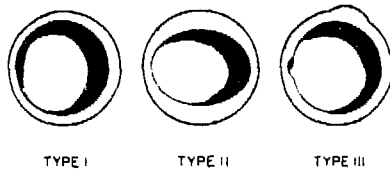
Fig. 1. Defect types of primary interest in glass or metal shells.

● SPHERICITY

$\frac{D_{max} - D_{min}}{D_{avg}}$ ≤ 1% (0.3% DESIRED)

● WALL THICKNESS UNIFORMITY

$\frac{t_{max} - t_{min}}{t_{avg}}$ ≤ 1% (0.3% DESIRED)

● SURFACE SMOOTHNESS
(DEFECT DIAM ≪ t_{avg})

$\frac{\Delta t}{t}$ ≤ 1%

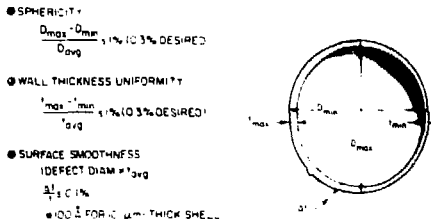● 100 Å FOR 1 μm THICK SHELL

Fig. 2. Characterization requirements on shells used in laser fusion targets.
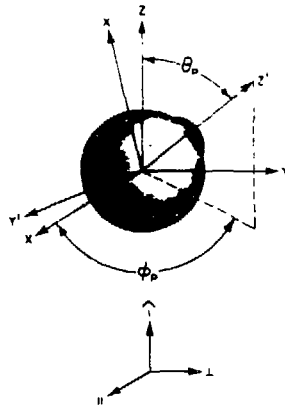
Fig. 3. Geometry used in the scattering calculations.

obtained in terms of the known expansion coefficients of the incident fields by directly solving these linear equations. Details of the development can be found elsewhere.[11]

In this paper we are interested in determining the scattering by a slightly nonspherical glass or metal shell. Since a shell with either a type I, II, or III defect is a body of revolution, we may apply the technique of using two sets of coordinates in the scattering calculations to take advantage of the fact that the EBCM is particularly efficient for axisymmetric objects. As depicted in Fig. 3, for a shell with a type III defect (modeled as a hemispherical bump in this paper), the two sets of coordinates used are the BODY frame ($x'y'z'$) and the LAB

frame (xyz). The two sets of coordinates are related by angles θ_p and ϕ_p. In the BODY frame the z' axis is oriented along the defect symmetry axis. In the LAB frame (xyz), the x-z plane is defined as the scattering plane, and the z axis is parallel to the direction of incidence. The components of the incident and scattered fields which are parallel to the x-z plane are defined as the horizontally polarized components, and those components perpendicular to the x-z plane are defined as the vertically polarized components. The major portion of the scattering calculation is performed in the BODY frame, and the solutions are then transformed into the LAB frame. Using the relations between the two coordinate systems, the scattering calculations can be carried out for any specified orientation of the object and hence location of the defect with respect to the incident wave.

The formulation of the EBCM begins with a set of integral equations which relate the fields in different regions:

$$\left.\begin{array}{c}\mathbf{E}^3(\mathbf{r}) \\ 0\end{array}\right\} = \mathbf{E}^i(\mathbf{r}) + \mathbf{E}^s(\mathbf{r}) = \mathbf{E}^i(\mathbf{r})$$
$$+ \nabla \times \int_{s_2} [\hat{n}_2 \times \mathbf{E}^3(k_3\mathbf{r}')] \cdot \bar{G}(k_3R)ds'$$
$$- \nabla \times \nabla \times \int_{s_2} \frac{1}{j\omega\epsilon_3}(\hat{n}_3 \times \mathbf{H}^3(k_3\mathbf{r}')$$
$$\cdot \bar{G}(k_3R)ds'; \begin{cases} \text{outside } S_2, \\ \text{inside } S_2. \end{cases} \quad (1)$$

$$\left.\begin{array}{c}\mathbf{E}^2(\mathbf{r}) \\ 0\end{array}\right\} = \nabla \times \int_{s_2} [-\hat{n}_2 \times \mathbf{E}^3(k_2\mathbf{r}') \cdot \bar{G}(k_2R)ds'$$
$$- \nabla \times \nabla \times \int_{s_2} \frac{1}{j\omega\epsilon_2} [-\hat{n}_2 \times \mathbf{H}^3(k_2\mathbf{r}')] \cdot \bar{G}(k_2R)ds'$$
$$+ \nabla \times \int_{s_1} [\hat{n}_1 \times \mathbf{E}^3(k_2\mathbf{r}')] \cdot \bar{G}(k_2R)ds'$$
$$- \nabla \times \nabla \times \int_{s_1} \frac{1}{j\omega\epsilon_1} [\hat{n}_1 \times \mathbf{H}^3(k_2\mathbf{r}')]$$
$$\cdot \bar{G}(k_2R)ds'; \begin{cases} \text{between } S_1 \text{ and } S_2, \\ \text{outside } S_2 \text{ and inside } S_1, \end{cases} \quad (2)$$

where S_2 is the outer surface of the shell, and S_1 is the inner surface, k_3, k_2, ϵ_3, and ϵ_2 are the wave numbers and the dielectric constants in the surrounding medium and in the shell, respectively. $\bar{G}(\mathbf{k}R)$ is the Green's dyadic for unbounded space, and $R = |\mathbf{r} - \mathbf{r}'|$. $\mathbf{E}^i$ is the incident electric field. $\mathbf{E}^s$ is the scattered electric field, $\mathbf{E}^3$ and $\mathbf{H}^3$ are the total fields outside the object, and $\mathbf{E}^2$ and $\mathbf{H}^2$ are the fields in the shell. Additional relations between the fields are obtained by applying the boundary conditions at the surfaces S_1 and S_2, which require the tangential components of the fields to be continuous, i.e.,

$$\left.\begin{array}{c}\hat{n}_2 \times \mathbf{E}^3 = \hat{n}_2 \times \mathbf{E}^2 \\ \hat{n}_2 \times \mathbf{H}^3 = \hat{n}_2 \times \mathbf{H}^2\end{array}\right\} \text{ on } S_2, \quad (3)$$

$$\left.\begin{array}{c}\hat{n}_1 \times \mathbf{E}^2 = \hat{n}_1 \times \mathbf{E}^1 \\ \hat{n}_1 \times \mathbf{H}^2 = \hat{n}_1 \times \mathbf{H}^1\end{array}\right\} \text{ on } S_1, \quad (4)$$

The electric field of an incident plane wave can be expanded as

Vacuum deposition of high quality metal films on porous substrates

Barry L. Barthell and David V. Duchane

Los Alamos National Laboratory Los Alamos, New Mexico 87545

A composite mandrel has been developed consisting of a core of low density polymethylpentene foam overcoated with a thin layer of film-forming polymer. The surface tension and viscosity of the coating solution are important parameters in obtaining a polymer film which forms a continuous, smooth skin over the core without penetrating into the foam matrix. Water soluble film formers with surface tensions in the range of 45 dyn/cm and minimum viscosities of a few hundred centipoises have been found most satisfactory for coating polymethylpentene foam. By means of this technique, continuous polymer films with thicknesses of 10–20 μm have been formed on the surface of machined polymethylpentene foam blanks. Aluminum has been vacuum deposited onto these composite mandrels to produce metal films which appear smooth and generally defect free even at 10 000 times magnification.

PACS numbers: 81.15.Ef

I. INTRODUCTION

The substrate plays a key role in the fabrication of thin metal films by vacuum deposition, since any defects or irregularities in the surface of the substrate tend to be reproduced in the film.[1] Further, if a freestanding film is to be produced, the substrate must be removed after deposition of the film material. This can readily be accomplished with parting agents when films are formed as flat sheets of moderate size, but when they are to be made with closed shapes such as cylinders or spheres, removal of the mandrel is much more difficult. In these cases mandrels are generally removed by leaching processes which may be very time consuming. Mechanical agitation is often employed in the leaching process, but this poses a risk to the integrity of the thin film. In addition, the leaching fluid itself must be carefully chosen. Metal mandrels require lechants which may be corrosive, difficult to handle, and prone to attack the thin film itself if parameters such as temperature and pH are not carefully controlled. Polymeric mandrel materials, while soluble in organic liquids which pose no danger to the deposited metal film, are usually slow to dissolve and often swell noticeably prior to becoming completely fluid. Such swelling can destroy the deposited shell.

The ultimate goal of the work reported herein is the development of a composite mandrel consisting of a core of low density, open cell, polymeric foam, overcoated with a thin layer of a smooth polymer film. Such a mandrel would have a microscopically smooth surface, an extremely high surface-to-mass ratio, and an effective void volume approaching 95%. These qualities would largely obviate many of the problems associated with the fabrication of metal-walled fusion targets. The smooth surface would permit the deposition of metallic films of good strength and uniformity. Leaching would be facilitated by the high surface-to-mass ratio, or could possibly be eliminated enitrely by simply filling the voids with fuel and leaving the foam core as a permanent structural support.

Coating of polymer foams has been practiced in the plastics industry for a number of years, but microscopically smooth finishes have not generally been among the goals of coating processes.[2] Such surface smoothness as has been achieved often involves the use of fillers and relatively thick coatings.[3]

It has been the primary object of this work to develop coating materials which will form continuous thin films on the surface of a low density, open cell foam without penetrating significantly into the body of the foam structure. As will be shown below, the surface tension and viscosity of the coating solution are important factors in the success of this technique.

II. EXPERIMENTAL

The polymer foam used in this work was obtained by a process recently developed at the Los Alamos National Laboratory.[4] It consists of polymethylpentene, and is originally produced as a filled material. For these experiments, the filled foam was first machined into hollow cylinders 23 mm long and 13 mm in diameter. The filler was then leached out to yield a mandrel core of low density (about 0.05 g/cm³), open cell, pure hydrocarbon material. At this stage of the process, the surface of the foam was macroscopically smooth but microscopically rough and porous with an average cell size of about 25 μm.

In each trial the coating solution was applied to the surface of the foam by lowering the core into the coating liquid on a rod extended through its center until it was totally immersed, and then withdrawing it at a constant rate of about 15 mm/min. The excess coating fluid was allowed to drain from the surface while the sample was suspended vertically.

The samples were dried in a laminar air flow hood to minimize dust contamination. After drying, each sample was inspected visually and by scanning electron microscopy (SEM). Aluminum was vapor deposited onto samples of foam coated with the most promising formulations, and the aluminized surfaces again examined by SEM.

The coating solutions were prepared by dissolving polymers known to be good film formers in water or methanol. The materials and concentrations were chosen to give solu-

145

Automated computer analysis of x-ray radiographs greatly facilitates measurement of coating thickness variations in laser fusion targets

D. M. Stupin, K. R. Moore, G. D. Thomas, and R. L. Whitman

Los Alamos National Laboratory, University of California, Los Alamos, New Mexico 87545

We have built an automated system to analyze x-ray radiographs of laser fusion targets which greatly facilitates the detection of coating thickness variations. Many laser fusion targets require opaque coatings 1 to 20 μm thick which have been deposited on small glass balloons 100 to 500 μm in diameter. These coatings must be uniformly thick to 1% for the targets to perform optimally. Our system is designed to detect variations as small as 100 Å in 1-μm-thick coatings by converting the optical density variations of contact x-ray radiographs into coating thickness variations. Radiographic images are recorded in HRP emulsions and magnified by an optical microscope, imaged onto television camera, digitized and processed on a Data General S/230 computer with a code by Whitman. After an initial set-up by the operator, as many as 200 targets will be automatically characterized.

PACS numbers: 68.55. + b, 67.70. + n, 52.50.Jm

INTRODUCTION

We have built an automated system to analyze x-ray radiographs of laser fusion targets at the Los Alamos National Laboratory, which greatly facilitates the detection of coating thickness variations in these targets. The Microradiographic Analysis System (MIRAS—from the Spanish *look*) is sensitive to 1% variations in coating thickness for nonconcentricities and 2% variations for elliptical defects, and, therefore, meets the requirements imposed by target designers for these two types of defects. We have proven the accuracy and sensitivity of this system by direct comparison with data taken with a flatbed microdensitometer and optical interference measurements. The on-line processing features of MIRAS give fast turn-around time for the analysis of the targets and the automated features of the system mean that the operator is not required to devote his attention full-time to the analyses.

Laser fusion targets are typically hollow glass microballoons 100 to 500 μm in diameter, coated with 1- to 20-μm-thick layers of various plastics and metals. While the glass microballoons are transparent, it is usually not practical to measure the coating uniformity or the coating thickness with optical techniques, because the coatings are usually opaque. However, the uniformity of the microballoon wall and the subsequent coatings must be stringently controlled to guarantee the performance of the targets. X-ray radiography has been shown to be effective in detecting target defects in opaque and transparent coatings,[1-9] and we are developing the most sensitive methods to find these defects with x rays.

Coating thickness variations are detected by measuring x-ray transmission through the targets as shown in Fig. 1. X-rays incident from the top of the figure pass through the asymmetric microballoon and expose the film underneath the microballoon. However, the intensity of the x rays is attenuated exponentially by the amount of the material they pass through. Hence, the x-ray flux to the center of the balloon is not attenuated as much as the flux near the left or
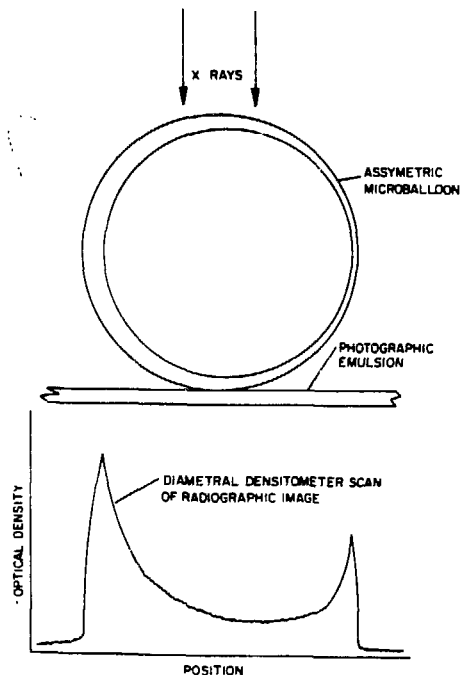
FIG. 1. Coating thickness variations are detected by measuring x-ray transmission through the targets. The images are recorded in photographic emulsions and the optical densities of the emulsions are a measure of the transmitted x-ray flux. Therefore, coating thickness variations are detected as variations in the optical density. In this example, an asymmetric microballoon gives an unsymmetric optical density plot.

FIG. 2. Miras uses a television camera to digitize radiographic images. Contact microradiographs are placed on the computer-controlled *x-y* stage and viewed through the microscope by a television camera. The video images are digitized and stored in computer memory where an analysis program calculates the sizes of defects and prints the results.

right edge. When the optical density of the radiographic image is plotted along the image diameter, as shown at the bottom of the figure, one typically gets cupshaped plots. Furthermore, because of the asymmetry of the microballoon, the cup rim is higher on the left-hand side of the plot that it is on the right-hand side. This asymmetry in the optical density plot can be detected by a computer and quantified.

APPARATUS

MIRAS uses a television camera to digitize the radiographic image of a target as shown in Fig. 2. First, a contact microradiographic image is made in photographic emulsion with an x-ray source. Then this image is placed in MIRAS on the computer-controlled *x-y* stage and viewed in the microscope by a television camera. The video signal is digitized,

FIG. 3. Three types of defects are found in microballoons. Type-I defects are nonconcentricities between the inner and outer surfaces. Type-II is an elliptical inner or outer surface, or both. Type-III are warts or dimples in either surface, or cracks or voids in the coating or density variations in the coating.

this digital data is stored in the computer, and the computer searches the digital data for defects and prints the results of the search. Up to 200 images in a single radiographic array will be analyzed automatically without further assistance after the operator has indicated the location of the images and assigned identification numbers. The computer prints the identification, microballoon diameter, thickness of the coating, nonconcentricity (Type-I defect), ellipticity (Type-II defect), and volumes of the warts and pits (Type-III defect) for each image. A more detailed description of this process is in the Appendix.

PERFORMANCE

MIRAS meets the requirements of inertial confinement fusion target designers for sensitivity to Type-I and Type-II defects. We have arbitrarily divided the types of defects typically found in microballoons and coatings into three types which are shown in Fig. 3. The Type-I defect is a nonconcentricity between the outer and inner surface, a Type-II is an elliptical inner or outer surface, or both, and Type-III is a small local defect such as a wart or a dimple, on either surface, or a density variation in the coating. Target designers have estimated that Type-I or Type-II defects smaller than 1% in $\Delta t / t$ will not degrade target performance, where t is the average coating thickness and Δt is the variation about the average. Defects of Type-III must be smaller than 0.1% in $\Delta t / t$ if they cover an area of t^2. Whitman[3,4] has shown that the analysis code in MIRAS is sensitive to 1% Type-I defects and 2% Type-II.

The accuracy of MIRAS is proven by comparison with flatbed densitometer data and optical interference measurements. In Fig. 4 are shown the measured nonconcentricities in percent $\Delta t / t$ for ten microballoons which were analyzed with data taken with both a flatbed densitometer and with

147

Summary Abstract: A technique for calculating DT content in glass microballoons from x-ray counts

B. S. Jorgensen

University of California. Los Alamos National Laboratory. P. O. Box 1663. Los Alamos, New Mexico 87545

The x-ray counting method[1] is very useful for determining DT content of glass microballoons (GMBs). A quantitative measurement is complicated, however, by the pressure- and diameter-dependent self-absorption of the beta particles in the gas and by wall composition and thickness effects on x-ray generation.[2,3] We have experimentally studied the effects of wall thickness, diameter, and fill pressure on x-ray count rate as measured by a NaI detector and, in addition, the attenuation caused by a plastic coating on the microballoon. At this time, the effects of glass composition were not investigated. A 5% Na, 12% Ca, 2% K, 0.03%B, and 81% Si composition was used in all cases. The results were combined in an equation which calculates the fill pressure directly from the x-ray count rate by an iterative process.

The effects of varying the wall thickness, diameter, and fill pressure were studied by holding two of the parameters constant and varying the third. Several GMBs were filled by permeation with 50/50 DT for each case. The x-ray attenuation caused by a plastic coating (parylene) was found by measuring x-ray count rates of individual microballoons before and after coating. The data were plotted as shown in Figs. 1 (a) through (d), and expressions were found for the effects of each variable on the count rate by entering the data on a curve-fitting program on a programmable calculator. In each case, a nonlinear, least-squares fit of the data gave a minimum confidence of 0.93.

The effects on the x-ray count rate of the wall thickness, diameter, and fill pressure may be expressed by

$$C/V = K_w e^{-0.09W}, \quad \text{for } D = D_r, \text{ and } P = P_r. \tag{1}$$

$$C/V = K_D(1.22 - 9 \times 10^{-4}D), \quad \text{for } W = W_r. \tag{2}$$

for $W = W_r$, and $P = P_r$.

$$C/(VP) = K_P P^{-0.14}, \quad \text{for } W = W_r, \text{ and } D = D_r. \tag{3}$$

where C is the counts per second, V is the volume of the microballoon in cubic microns, W is the wall thickness in microns, D is the diameter in microns, P is the pressure in standard atmospheres, K is a calibration constant, and the subscript r refers to a reference microballoon.

Combining Eqs. 1, 2, and 3, and solving for P yields

$$P = \frac{e^{0.09W}P^{0.14}C}{K(1.22 - 9 \times 10^{-4}D)V}, \tag{4}$$

where K is the appropriate combination of K_w, K_D, K_P.

The equation may be used to calculate the fill pressure of plastic-coated microballoons by including a factor for the x-ray attenuation due to the plastic. The attenuation factor is the count rate of a coated microballoon (C_T) divided by the count rate of the microballoon before it was coated (C). As shown in Fig. 1(d),

$$C_T/C = e^{-0.00397T} \text{ or } C = C_T e^{0.00397T}$$

This relationship is valid for coatings from 0- to at least 100-μm-thick (the upper limit of our measurements). Therefore, the fill pressure of a plastic-coated microballoon may be calculated by

$$P = \frac{e^{0.09W}P^{0.14}e^{0.00397T}C_T}{K(1.22 - 9 \times 10^{-4}D)V}. \tag{5}$$

The calibration constant can now be found for a specific x-ray counter and GMB type by measuring the x-ray count rate of a DT-filled GMB and then measuring the fill pressure directly by some destructive technique such as mass spectroscopy. Unknown fill pressures can then be calculated using the above equation in an iterative process on a programmable calculator. An estimated P, which does not need to be a close approximation to the actual P, is inserted in the equation and only a few iterations are required to arrive at the fill pressure.

The actual effects derived from first principles are much more complicated,[2] but the above correlations hold at least for glass microballoons with wall thicknesses varying from 1.5 to 5.5 μm, diameters from 150 to 600 μm, and pressures from 10 to 100 atm. The fill pressures calculated using this equation have been compared to the equilibrium fill pressure for numerous recently filled targets. We have found better that 10% agreement. Also, multiple calibrations were made via destructive measurements and we again found better than 10% agreement in the range of pressures and sizes mentioned.

We have found this method to be quick and easy for assaying the fuel content of glass microballoons to be used for laser fusion targets. With the increasing use of plastic coatings on targets, the factor for x-ray attenuation due to the plastic is extremely useful since the fill pressure can be calculated from the x-ray count rate of the finished target. The effects of varying the glass composition still need to be studied, since other glass types are frequently used for targets

148
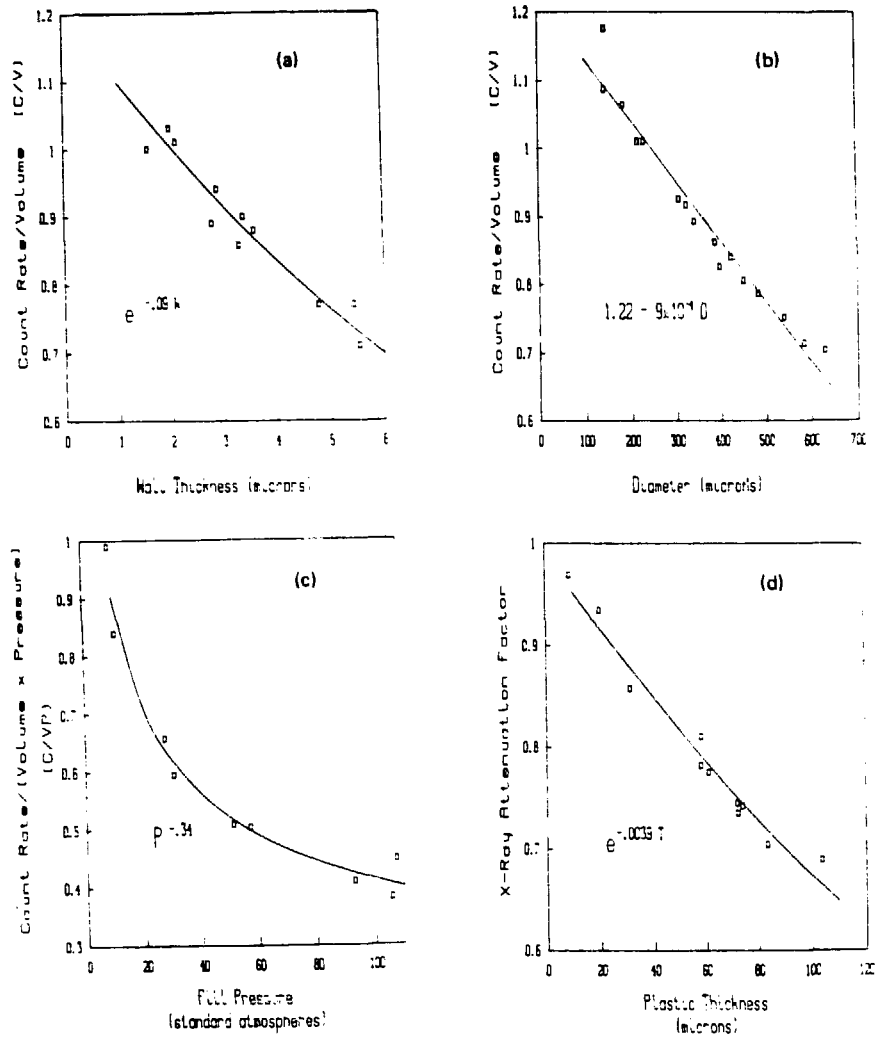
FIG. 1. (a) Effect of wall thickness on x-ray count rate. (b) Effect of diameter on x-ray count rate. (c) Effect of fill pressure on x-ray count rate. (d) Attenuation of x-rays due to plastic coating.

[1] R. J. Fries and E. H. Farnum, Nucl. Instr. Methods 126, 285 (1975).
[2] M. M. Mueller, 1975 Annual Division of Plasma Physics Meeting of the American Physical Society, St. Petersburg, Florida (1975), Los Alamos Report LA-UR-75-2002.
[3] 1980 Annual Technical Report, KMS-Fusion, Inc., Ann Arbor, Michigan, Sec. 1.3.3.

Fabrication of thin-wall, freestanding inertial confinement fusion targets by chemical vapor deposition

D. W. Carroll and W. J. McCreary

Los Alamos National Laboratory, Los Alamos, New Mexico 87545

To meet the requirements for plasma physics experiments in the inertial confinement fusion (ICF) program, chemical vapor deposition (CVD) in fluid beds was used to fabricate freestanding tungsten spheres and cylinders with wall thicknesses less than 5.0 μm. Molybdenum and molybdenum alloy (TZM) mandrels of the desired geometry were suspended in a carrier bed of dense microspheres contained in an induction-heated fluid-bed reactor. The mandrels were free to float randomly through the bed, and using the reaction $WF_6 + 3H_2 \xrightarrow{723\,K} W + 6HF$, very fine-grained tungsten was deposited onto the surface at a rate and in a grain size determined by temperature, gas flow rate, system pressure, and duration of the reaction. After coating, a portion of each mandrel was exposed by hole drilling or grinding. The mandrel was then removed by acid leaching, leaving a freestanding tungsten shape. Experimental procedures, mandrel preparation, and results obtained are discussed.

PACS numbers 81 15 Gh. 52.50 Jm

I. INTRODUCTION

The use of metal foils as inertial confinement fusion (ICF) targets has recently gained importance in physics experiments applicable to thermonuclear ignition.[1,2] The current requirements for these foils dictate that they must be a specific size and geometry, freestanding, defect-free, less than 5.0-μm uniform wall thickness, and be capable of withstanding manipulation during the fixturing process. To produce foils satisfying these specifications, a fluid-bed technique in combination with chemical vapor deposition (CVD) was utilized.[3,4] Molybdenum or molybdenum alloy (TZM) mandrels machined to the desired size and shape were placed in a bed of dense spherical particles. Hydrogen was passed into the bed to begin fluidization. This action provided support for the mandrels and caused them to move through the bed in a random manner. After the fluid bed was stabilized at temperature, tungsten hexafluoride (WF$_6$) was admitted. Using the reaction $WF_6 + 3H_2 \xrightarrow{723\,K} W + 6HF$, strong, smooth tungsten coatings exhibiting fine grain structure were deposited on the mandrel. Subsequent mandrel removal by acid leaching yielded thin-walled (typically 1.5 to 3.0 μm), freestanding hollow tungsten cylinders and spheres. This paper will describe the apparatus required and the specialized techniques developed to produce such unique tungsten foils.

II. EXPERIMENTAL

Hollow cylindrical mandrels were machined and polished from molybdenum tubing using conventional techniques. Molybdenum was chosen because of its close coefficient of thermal expansion match with tungsten and because it would selectively acid leach without affecting the tungsten coating. Approximately 0.5 mm was added to the length of cylinders as allowance for polishing back to the mandrel prior to leaching. Although cylindrical mandrels of various sizes were tungsten coated, the coating process described applies specifically to mandrels 10.0-mm diam $\times$ 13.6-mm long.

After ultrasonic cleaning, a single molybdenum cylinder was placed in a bed fluidized by hydrogen. A typical fluid bed was contained within a graphite coater and consisted of 8 cm^3 of $\sim$350-μm-diam spherical uranium carbide coated with tungsten. Average bed density was 12 g/cm^3. One unique aspect of this process is that by varying bed composi-
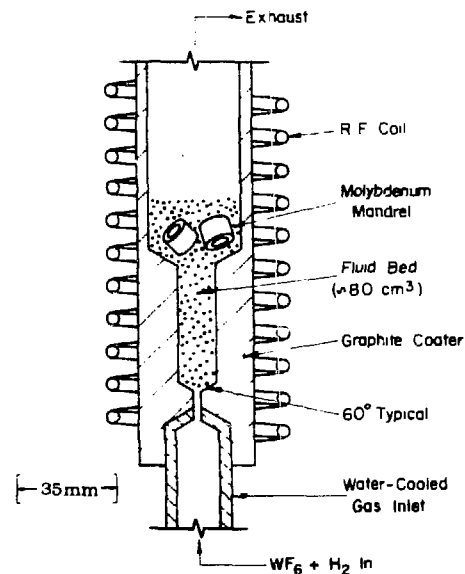

FIG 1 CVD coating apparatus, cross section through coater

150

Preparation of multishell ICF target plastic foam cushion materials by thermally induced phase inversion processes

A. T. Young, D. K. Moreno, and R. G. Marsters

University of California, Los Alamos National Laboratory, PO Box 1663, Los Alamos, NM 87545

Homogeneous, low-density plastic foams for ICF targets have been prepared by thermally induced phase inversion processes. Uniform, open cell foams have been obtained by the rapid freezing of water solutions of modified cellulose polymers with densities in the range of 50–7 mg/cm³ and respective average cell sizes of 2 to 40 μm. In addition, low-density, microcellular foams have been prepared from the hydrocarbon polymer poly(4-methyl-l-pentene) via a similar phase inversion process using homogeneous solutions in organic solvents. These foams have densities from 20 to 50 mg/cm³ and average cell sizes of 20 μm.

PACS numbers: 82.70.Rr, 81.20.Sh

I. INTRODUCTION

Several laboratories have recently been involved in the development of multishell fusion targets for laser interaction experiments.[1,2] Initial designs consist of a DT-fuel-filled, gold-coated, hollow glass microsphere centered in the interior of an outer pusher-ablative shell (Fig. 1). Nonconcentricity between the inner and outer shells must be 2% or less. Between the two shells is a low-Z cushion layer, which, depending on the particular design, requires densities from 0.01 to 1 g/cm³ or more. This cushion layer can be a gas, a small-cell plastic foam, or a full-density plastic.

Multishell fusion targets have been fabricated using a gas cushion layer with a thin plastic film supporting the inner shell.[1] Considerable effort has been expended to fabricate low-Z, low-density, microcellular foams for this cushion layer.[2,3] In the study by Rinde and Stone[3] a cellulose acetate foam was prepared by extrusion of an acetone solution of the

polymer into a "phase inversion" environment. This process is similar to the methods for making asymmetric, reverse-osmosis membranes for water desalination.[4] Rinde and Stone were able to produce cellulose acetate foam strands with densities about 50 mg/cm³ and cell sizes of 1 to 2 μm.

Coudeville *et al.*,[2] have reported coating of stalk-mounted glass microspheres with a dextran foam with a density of 50 mg/cm³ and average cell sizes of 1 to 2 μm. Their process involved the rapid cooling of a water–dioxane solution of the dextran polymer to a temperature well below the freezing point of the solvent mixture. The solvent mixture was then removed via sublimation under vacuum (i.e., freeze-drying) to give the polymer foam structure.

In a parallel study at this laboratory, plastic foams have been made from a water solution of the ammonium salt of carboxymethylcellulose (Figs. 2 and 3) via this process over a range of densities from 50 mg/cm³ with 2-μm cells to 16 mg/cm³ with 10-μm cells. In addition, foams with a density

POLARIS PRIME

INNER PUSHER,
GOLD, 12 μm THICK

MANDREL, GLASS
MICROBALLOON, 1 μm THICK

FUEL, DT ICE,
~10 μm THICK

ABSORBER/ABLATOR,
PLASTIC, 75 μm THICK

OUTER PUSHER/SHIELD,
GOLD, 75 μm THICK

CUSHION, GAS OR
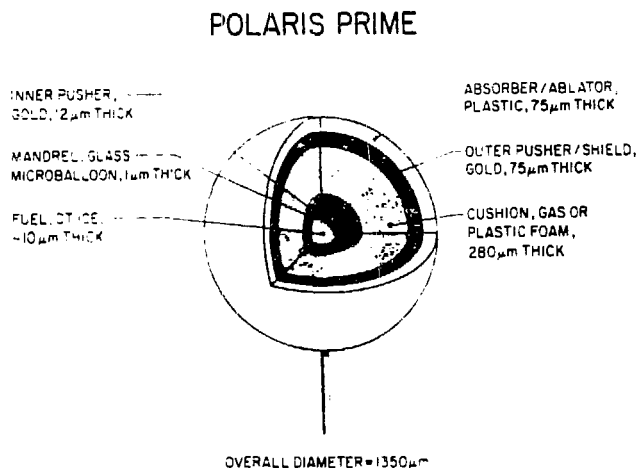PLASTIC FOAM,
280 μm THICK

OVERALL DIAMETER = 1350 μm

FIG. 1. Cutaway view of a typical multishell ICF target

151
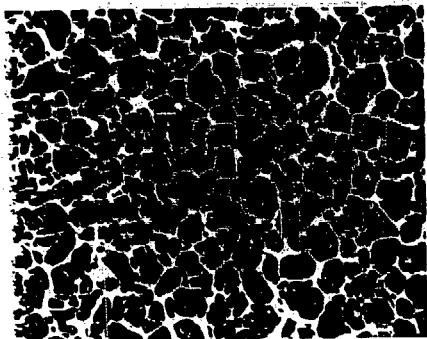
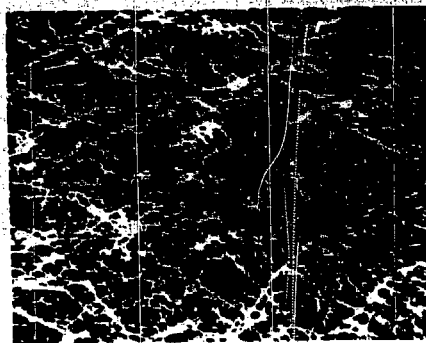FIG. 2. Carboxymethylcellulose foam; density = 50 mg/cm³; average cell size = 2 μm.

FIG. 4. Methylcellulose foam; density = 7 mg/cm³; average mean free path distance between ribs = 40 μm.

of 7 mg/cm³ (Fig. 4) were prepared from a water solution of methylcellulose.

I. THERMALLY INDUCED PHASE INVERSION PROCESSES

The process employed by Coudeville and in our laboratory falls into the general category of thermally induced phase inversion processes. In these phase inversion processes, a homogeneous polymer solution is cooled in order to force separation of the solvent from the polymer to form a continuous polymer matrix in which is dispersed discrete cells of solvent. Removal of the solvent droplets from the matrix generally results in an open cell plastic foam structure where the voids are replicas of the solvent droplets. In a thermally induced process the solvent is selected from a class of solvents which are good solvents at one temperature and poor solvents at a lower temperature. Controlled cooling of a polymer dissolved in this solvent can yield a polymer foam.

During the cooling step, the temperature region at which solvent-polymer phase separation occurs may be defined as
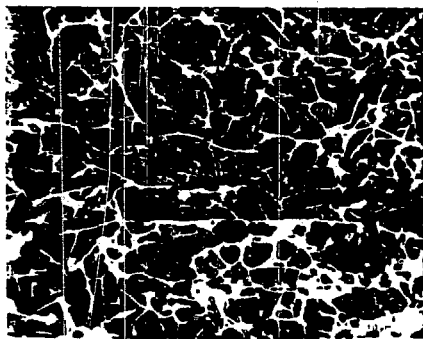

FIG. 3 Carboxymethylcellulose foam; density = 16 mg/cm³, average mean free path distance between ribs = 10 μm

critical miscibility zone. For polymers having a broad molecular weight range, the zone may occur over a temperature range rather than at a single temperature.

III. EXPERIMENTAL

Since dextran and the chemically modified celluloses contain appreciable oxygen (an undesirable constituent in some target designs), we have studied thermally induced phase inversion foam generation with solutions of polymers containing only carbon and hydrogen (CH). We have been able to develop CH polymer foams with densities in the range of 50 mg/cm³ and cell sizes from 10 to 30 μm. In addition, we have developed a process whereby these delicate foams can be readily fabricated into desirable configurations via conventional micromachining techniques.

Poly(4-methyl-1-pentene), which is manufactured by Mitsui Petrochemical Co. in Japan under the trade name "TPX," is a linear CH polymer having a density of 0.83 g/cm³. The polymer is relatively insoluble in most common organic solvents, and only recently have solvents been published for TPX.[6]

We have found that homogeneous TPX solutions can be obtained with particular solvents by extended heating at elevated temperatures. Such solutions are then cooled at a rate and to a temperature such that nonequilibrium liquid–liquid phase separation is initiated. As the solutions are cooled, it is necessary that no mixing or any other form of agitation be

TABLE I. Solvents used in preparing TPX forms

Solvent	Physical state at room temperature	Boiling point or melting point
Diphenylmethane	Liquid	264 °C
Phenyl ether	Liquid	259 °C
Cyclohexylbenzene	Liquid	239 °C
1-Phenyloctane	Liquid	261 °C
Bibenzyl	Solid	49.6 °C
Hexamethylbenzene	Solid	162 °C

**REPRINTS IN
ICF SYSTEM STUDIES
SINCE
1982**

.

IMPROVEMENT OF THE TWO-TEMPERATURE RADIATIVE TRANSPORT MODEL

THOMAS J. McCARVILLE *TRW Energy Development Group*
One Space Park, R1/2128, Redondo Beach, California 90278

GREGORY A. MOSES and GERALD L. KULCINSKI
University of Wisconsin-Madison, Department of Nuclear Engineering
1500 Johnson Drive, Madison, Wisconsin 53706

IHOR O. BOHACHEVSKY *Los Alamos National Laboratory*
Los Alamos, New Mexico 87545

The frequency dependence of a thermal radiation field complicates the computation of radiative energy transport in optically thin media because the spectrum may be uncoupled from local thermodynamic conditions. A model for combining the effect of the frequency dependence into a radiation temperature chosen to represent the temperature of both local and nonlocal emitting regions is described. The derived equations are much easier to solve than the frequency-dependent equations and can be applied to a broad class of problems. The equations are used to investigate the response of a gas in an inertial confinement fusion (ICF) reaction chamber to target explosions. The response is compared for ambient densities of 1.77×10^{18} and 1.77×10^{17} atom/cm³. The error in using the brightness temperature instead of a color temperature to evaluate the opacities is illustrated. An analytic analysis shows the cooling wave observed from energy releases $>10^{18}$ erg will not occur in an ICF cavity. This is confirmed by the numerical calculations.

I. INTRODUCTION

There are a variety of models for computing thermal radiation transport. The model that best applies to a particular application depends on the opacity of the transport medium. For example, if the mean-free-paths of emitted photons are much smaller than the distance over which the temperature changes significantly, then the radiation field is isotropic and the frequency spectrum is determined by the local temperature. Under these circumstances, the dependence on angle and frequency can be integrated out of the radiation transport equation. However, in many applications the medium is optically thin to emitted radiation, and the angle and frequency variables must be retained.

This paper describes a method of integrating the frequency variable out of the transport equation when the medium contains optically thin regions. The integration leaves a parameter called the radiation temperature to represent the frequency spectrum, where the radiation temperature is chosen to reflect local and nonlocal emitting regions. The model is referred to as a two-temperature model because both the local and radiation temperature appear in the equations. The equations are identical in form to those set forth by Moses and Peterson,[1] but the derivation presented here suggests a method of evaluating the radiation temperature that avoids problems associated with the previous two-temperature model. The model derived here is particularly well suited to a medium composed of alternately transparent and opaque layers, but is an economical first estimate for any application where net energy transport is of primary interest, and a detailed description of the frequency spectrum is not needed.

The two-temperature equations are derived in Sec. II. Thermal conduction and motion of the medium are ignored in that section because neither influences the derivation. The equations are used in Sec. III to analytically study the phenomena following the explosion of an inertial confinement fusion (ICF) target in a gas. The trends revealed

5

154

PROPAGATION OF IONS THROUGH CONDUCTING FLUIDS WITH IMBEDDED MAGNETIC FIELDS

ICF CHAMBER
ENGINEERING

IHOR O. BOHACHEVSKY, JOHN C. GOLDSTEIN, and
DONALD O. DICKMAN *Los Alamos National Laboratory*
Analysis and Assessment Division, P.O. Box 1663
Los Alamos, New Mexico 87545

Studies of applications of inertial confinement fusion motivated the development of a plasma model composed of

1. perfectly conducting fluid

2. relatively energetic ions not in thermal equilibrium with the fluid

3. an electromagnetic field.

The fluid is modeled as a continuum, but the trajectories of the ions are determined from integration of the equations of motion for a statistically representative sample of simulation particles because the ion ranges in the fluid are comparable to characteristic dimensions of containment vessels. The model constituents interact electrodynamically, collisionally, and through ionization and recombination processes. The model of the collisional interaction is based on the stopping power of the fluid; it leads to technical difficulties because of the widely different characteristic lengths associated with collisional interactions and with macroscopic fluid phenomena. These difficulties are resolved with a specially constructed elementary one-dimensional model of the collisional interaction. The finite difference equations describing the evolution of the complete ion-plasma system are integrated numerically for an isotropic ion source located on the cylinder axis. The solutions indicate different ion behaviors for low- and high-fluid densities. The ions expand as a diffuse cloud through low-density fluids, but aggregate into perpendicular-to-the-magnetic-field sheets in high-density fluids; the discovery of these strikingly different behaviors constitutes the main contribution of this work.

I. INTRODUCTION

In the inertial confinement fusion (ICF) process, the reaction occurs sufficiently fast (in $<10^{-9}$ s) to resemble a small explosion (called a microexplosion) that produces relatively high-energy (1- to 100-keV) ions. Investigations of the expansion of these ions and their interaction with an externally generated magnetic field imbedded in a residual background fluid led to the study of a plasma model composed of

1. an ionized fluid

2. relatively energetic ions not in thermodynamic equilibrium with the surrounding fluid

3. an electromagnetic field.

The assumptions implicit in this model are:

1. The background medium is collision-dominated, behaves as an ideal gas with a constant ratio of specific heats, and is ionized to a degree at which its electrical resistivity may be neglected.

2. The discrete ions do not directly interact with each other and are not in thermodynamic equilibrium with the surrounding fluid in which their ranges are comparable to the characteristic dimensions of interest.

3. The interaction force between the ions and the surrounding fluid is always tangent to the ion trajectory, i.e., scattering is neglected.

4. An adequate number of sufficiently mobile electrons are available to ensure local charge neutrality and to short out any electrostatic field.

5. The electric and magnetic fields are always and everywhere perpendicular.

6. High-frequency phenomena are ignored, i.e., the displacement current is neglected.

155

CYCLIC TEMPERATURE AND THERMAL STRESS FLUCTUATIONS IN FUSION REACTORS
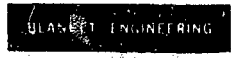
IHOR O. BOHACHEVSKY *Los Alamos National Laboratory*
P.O. Box 1663, Los Alamos, New Mexico 87545

RONALD N. KOSTOFF* *U.S. Department of Energy*
Office of Energy Research, Washington, D.C. 20545

Cyclic thermal loads and stresses in two critical components of fusion reactors, including fusion-fission hybrids, are modeled and calculated The two critical components are the solid wall adjacent to the fusion plasma ("first wall") and the fissile fuel elements in the high-power density region of the blanket. These two components exemplify two limiting cases of thermal loading: The first-wall loads are generated by predominantly shallow energy deposition that may be approximated with a flux across the surface and the fuel elements loads are generated by volumetric heating.

Two approaches are used to solve the heat conduction equation and to calculate the resulting stresses in terms of system parameters. The first is expansion into Fourier series and determination of periodic solutions: the second is analysis and superposition of single-pulse responses weighted with appropriate time delay and decay factors. Approximate closed-form expression for temperature excursions and thermal stresses are derived: these expressions may be evaluated conveniently and rapidly for comparison of different systems. The results provide a quantitative basis for trade-off studies and comparative assessments of different fusion reactor systems.

I. INTRODUCTION AND SUMMARY

A number of potential applications of fusion reactors have been identified and investigated: several

---

*The views expressed in this paper are those of the author and do not necessarily represent the views of the Department of Energy.

that appear technically and economically feasible are production of electricity, process heat, synthetic fuels, and fissile fuels. Realization of these applications requires solution of many outstanding and challenging scientific and engineering problems. One of the outstanding problems for most fusion systems is the modeling and analysis of cyclic thermal stresses with a view toward reducing their effects on availability, reliability, and component lifetime.

From the mechanical engineering point of view, one fundamental difference between the fusion and fission reactors (including advanced fuel breeders) is the type of operation: Fission reactors operate in a steady state while fusion reactors, in general, are expected to operate cyclically. The cycle time or period may range from tens of minutes to small fractions of a second and the fraction of the cycle during which fusion energy is released may range from nearly unity to 10^{-6} or less. Consequently, the characteristics of cyclic thermal and mechanical loads in fusion reactors will span a wide range of parameter values.

In this paper we model and analyze cyclic thermal loads and stresses in the complete potential range of operating conditions. We examine two critical components of fusion reactors (including fusion-fission hybrids): namely, the solid wall adjacent to the fusion plasma ("first wall") and the fuel elements located in the high-power density region of the blanket. These two components exemplify two limiting cases of thermal loading: The first-wall loads are generated by predominantly shallow energy deposition that may be approximated with a flux across the surface and the fuel element loads are generated by predominantly volume energy deposition or volumetric heating. For these two types of loading, we derive approximate closed-form expressions for temperature increases and thermal stresses that may be evaluated conveniently and rapidly for comparison of different systems.

(LA-UR-82-484)
Publication

Consistency of Neutron Cross-Section Data, S_N Calculations, and Measured Tritium Production for a 14-MeV Neutron-Driven Sphere of Natural Lithium Deuteride

William A. Reupke* and D. W. Muir

*Los Alamos National Laboratory, P.O. Box 1663
Los Alamos, New Mexico 87545*

and

J. Narl Davidson

*Georgia Institute of Technology School of Nuclear Engineering
Atlanta, Georgia 30332*

We present algorithms, describe a computer program, and give a computational procedure for the statistical consistency analysis of neutron cross-section data, S_N calculations, and measured tritium production in 14-MeV neutron-driven integral assemblies. Algorithms presented include a reduced matrix manipulation technique suitable for many-group, 14-MeV neutron transport calculations. The computer program incorporates these algorithms and is expanded and improved to facilitate analysis of such integral experiments. Details of the computational procedure are given for a natural lithium deuteride experiment performed at the Los Alamos National Laboratory. Results are explained in terms of calculated cross-section sensitivities and uncertainty estimates. They include a downward adjustment of the ^{6}Li(n,xt) 14-MeV cross section from 328 ± 22 to 284 ± 24 mb, which is supported by the trend of recent differential and integral measurements. It is concluded that with appropriate refinements, the techniques of consistency analysis can be usefully applied to the analysis of 14-MeV neutron-driven tritium production integral experiments.

INTRODUCTION

To increase the accuracy of the neutronics analysis of fission reactors, physicists and engineers have employed a variety of techniques, including the adjustment of multigroup differential data to improve consistency with integral data. Of the various adjustment strategies, a generalized least-squares procedure that adjusts the combined differential and integral data can significantly improve the accuracy of neu-

tronics calculations compared to calculations employing only differential data. This investigation analyzes a 14-MeV neutron-driven integral experiment, using a refined methodology and a combined sensitivity analysis and consistency analysis code, to extend the domain of adjustment from the energy range of fission reactors to the energy range of deuterium-tritium fusion reactors.

In the higher energy regime of the fusion reactor, several problems in the application of consistency analysis can be expected. Because of the higher energies involved, a larger number of cross-section energy groups are used. Moreover, the higher energy

416

Power plant design for inertial confinement fusion: Implications for pellets *

T. G. Frank and J. H. Pendergrass

Los Alamos National Laboratory, Los Alamos, New Mexico 87545

O. L. Cook

Sandia National Laboratory, Albuquerque, New Mexico 87185

J. H. Pitts

Lawrence Livermore National Laboratory, Livermore, California 94550

Potential commercial applications of inertial fusion include the production of electricity and fissile and chemical fuels. In all these applications, a significant amount of high-temperature heat will be produced and converted to electricity. Most of the implications for fusion pellets are common to all applications; the emphasis in this discussion is on central station electric power plants. The requirements and constraints on fusion pellets for power plant applications include: survivability in hostile reaction chamber environments, the ability to withstand large acceleration forces encountered in high-velocity injection, sufficiently large energy releases for economic power production, and high-rate automated manufacture at costs which are not a large fraction of the value of the fusion energy released.

PACS numbers: 28.50.Re, 52.50.Jm

I. INTRODUCTION

Potential commercial applications of inertial fusion include the production of electricity and fissile and chemical fuels. In all these applications, a significant amount of high-temperature heat will be produced and converted to electricity. Because most of the implications for fusion pellets are common to all applications, the emphasis in this discussion is on central station electric power plants.

In an inertial fusion electric power plant, fusion pellets containing deuterium and tritium (DT) will be injected into one or more reaction chambers at rates of 1–10/s at high velocity where they are intercepted, in flight, by laser or particle beam driver pulses. The fusion fueld is compressed and heated to conditions necessary for fusion reactions to take place. Energy is released from the pellet as x rays, high-energy neutrons, and energetic pellet debris. The x rays and pellet debris ions deposit their energy very near surfaces of incidence, whereas neutron energy deposition occurs volumetrically in relatively thick blanket regions surrounding the reaction chambers. Special provisions are required to accommodate the x-ray and pellet-debris energy deposition without severe damage to the interior surfaces of reaction chambers of reasonable size. Pellet energy releases are converted to sensible heat in reactor structures and coolants and are transported by a flowing coolant to appropriate power conversion equipment.

The requirements and constraints on fusion pellets for power plant applications include: survivability in hostile reaction chamber environments, the ability to withstand large acceleration forces encountered in high-velocity injection, sufficiently large energy releases for economic power production, and high-rate automated manufacture at costs

which are not a large fraction of the value of the fusion energy released. These requirements and their dependence on the several possible combinations of generic reactor-driver combinations are discussed in this paper.

II. PELLET CONCEPTS

The basic concept for producing energy from fusion pellets is illustrated in Fig. 1. Driver energy is delivered to a fusion pellet by intense, short-pulse laser or particle beams. An outer layer of the pellet is heated very rapidly causing it to expand with high velocity. The fusion fuel is compressed and heated, due to the recoil impulse of the expanding material, to high density (1000 to 10 000 times liquid density) and temperature, with ignition occurring at 3–5 keV. The thermonuclear burn spreads rapidly through the compressed fuel releasing many times the driver input energy.

At the present time, research is being conducted to establish the technical feasibility of the basic process through single-shot physics and pellet experiments using high-energy lasers and light-ion-beam accelerators. Comprehensive reviews of the experimental programs are given in Refs. 1 and 2. Studies of conceptual designs of inertial fusion power plants are based on theoretical fusion pellet designs capable of fusion gains (fusion energy output divided by driver energy input to the pellet) ranging from approximately 50 to several hundred with driver pulse energies in the 2–10 MJ range. Although pellet designs appropriate for power plant application have not yet been demonstrated, work to date does permit projections to be made on design and quality control requirements.[3] Figure 2 shows the general features of several generic designs of fusion pellets. In addition to the designs shown, pellets having multiple fuel regions are being

**PATENTS
SINCE
1982**

United States Patent [19]

Duchane et al.

[11] Patent Number: 4,481,999

[45] Date of Patent: Nov. 13, 1984

[54] METHOD OF FORMING A THIN UNBACKED METAL FOIL

[75] Inventors: David V. Duchane, Los Alamos; Barry L. Barthell, Tesuque, both of N. Mex.

[73] Assignee: The United States of America as represented by the United States Department of Energy, Washington, D.C.

[21] Appl. No.: 351,378

[22] Filed: Feb. 23, 1982

[51] Int. Cl.³ B22C 7/02; B22C 9/24; B22D 23/00; B22D 29/00

[52] U.S. Cl. 164/6; 164/36; 164/44; 164/45; 164/46; 164/131; 164/138

[58] Field of Search 164/6, 14, 15, 23, 33, 164/44, 45, 46, 47, 72, 74, 131, 132, 138, 36

[56]   References Cited

U.S. PATENT DOCUMENTS

1,447,683	3/1923	Morris	164/178
1,889,905	12/1932	Saeger	164/14
3,181,209	5/1965	Smith, Jr.	164/95 X
3,195,199	7/1965	Ochs	164/46
4,128,121	12/1978	Sigsbee	164/46

FOREIGN PATENT DOCUMENTS

1465908	3/1977	United Kingdom	164/131
697244	11/1979	U.S.S.R.	164/45

OTHER PUBLICATIONS

Kindel, F. W. et al., "Thin Foil Fabrication," in Review of Scientific Instruments, vol. 50, No. 12, Dec. 1979, pp 1550–1552.
Springer, R. W. et al., "Structure and Mechanical Properties of Al/Al₂O₃ Vacuum Deposited Laminates," in Thin Solid Films, vol. 54, 1978, pp. 197–205.

Primary Examiner—Kuang Y. Lin
Assistant Examiner—J. Reed Batten, Jr
Attorney, Agent, or Firm—William A. Eklund; Paul D. Gaetjens; Michael F. Esposito

[57]   ABSTRACT

In a method of forming a thin (<2 μm) unbacked metal foil having a desired curviplanar shape, a soluble polymeric film, preferably comprising polyvinyl alcohol, is formed on a supporting structure having a shape that defines the desired shape of the foil product. A layer of metal foil is deposited onto one side of the soluble film, preferably by vacuum vapor deposition. The metallized film is then immersed in a suitable solvent to dissolve the film and thereby leave the metal foil as an unbacked metal foil element mounted on the supporting structure. Aluminum foils less than 0.2 μm (2,000 Å) thick and having an areal density of less than 54 μg/cm² have been obtained.

2 Claims, 3 Drawing Figures
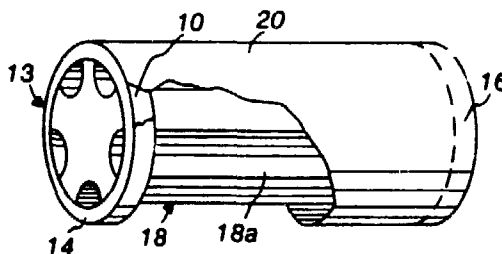
United States Patent [19]

Duchane et al.

[11] **4,448,622**

[45] **May 15, 1984**

[54] **COMPOSITE POLYMERIC FILM AND METHOD FOR ITS USE IN INSTALLING A VERY THIN POLYMERIC FILM IN A DEVICE**

[75] Inventors: **David V. Duchane**, Los Alamos; **Barry L. Barthell**, Tesuque, both of N. Mex.

[73] Assignee: **The United States of America as represented by the United States Department of Energy**, Washington, D.C.

[56] **References Cited**

U.S. PATENT DOCUMENTS

3,484,409	12/1969	Ashikaga et al.	.... 525/61
3,505,264	4/1970	Thoese et al.	
3,859,125	1/1975	Miller et al.	.... 428/116
4,119,604	10/1978	Wysong	.... 428/220
4,372,311	2/1983	Potts	.... 428/507
4,379,805	4/1983	Downing et al.	.... 525/61

[57] **ABSTRACT**

A composite polymeric film and a method for its use in forming and installing a very thin (< 10 μm) polymeric film are disclosed. The composite film consists of a thin film layer and a backing layer. The backing layer is soluble in a solvent in which the thin film layer is not soluble. In accordance with the method, the composite film is installed in a device in the same position in which it is sought to finally emplace the thin film. The backing layer is then selectively dissolved in the solvent to leave the insoluble thin film layer as an unbacked film. The method permits a very thin film to be successfully installed in devices where the fragility of the film would preclude handling and installation by conventional methods.

14 Claims, No Drawings

United States Patent [19]

Liepins

[11] 4,390,567

[45] Jun. 28, 1983

[54] METHOD OF FORMING GRADED POLYMERIC COATINGS OR FILMS

[75] Inventor: Raimond Liepins, Los Alamos, N. Mex.

[73] Assignee: The United States of America as represented by the United States Department of Energy, Washington, D.C.

[21] Appl. No.: 242,807

[22] Filed: Mar. 11, 1981

[51] Int. Cl.³ B05D 7/24; C23C 11/00
[52] U.S. Cl. 427/214; 376/151; 376/152; 376/916; 427/6; 427/215; 427/217; 427/221; 427/222; 427/250; 427/252; 427/255.6; 427/255.7
[58] Field of Search 376/151, 152, 916; 427/250, 252, 38, 39, 6, 40, 41, 213, 214, 215, 217, 220, 221, 222, 255.6, 255.7

[56] References Cited

U.S. PATENT DOCUMENTS

2,984,575	5/1961	Fitch	106/1
3,163,665	12/1964	Fitch	260/430
3,914,472	10/1975	Nakanishi et al.	427/250
3,920,483	11/1975	Johnson, Jr. et al.	427/38 X
3,994,822	11/1976	De Pacci et al.	427/6 X
4,123,308	10/1978	Nowlin et al.	427/41
4,224,261	9/1980	Halpern	376/152 X
4,290,847	9/1981	Johnson et al.	427/6 X

Primary Examiner—Norman Morgenstern
Assistant Examiner—Thurman K. Page

[57] ABSTRACT

Very smooth polymeric coatings or films graded in atomic number and density can readily be formed by first preparing the coating or film from the desired monomeric material and then contacting it with a fluid containing a metal or a mixture of metals for a time sufficient for such metal or metals to sorb and diffuse into the coating or film. Metal resinate solutions are particularly advantageous for this purpose. A metallic coating can in turn be produced on the metal-loaded film or coating by exposing it to a low pressure plasma of air, oxygen, or nitrous oxide. The process permits a metallic coating to be formed on a heat sensitive substrate without the use of elevated temperatures.

14 Claims, No Drawings

United States Patent [19]

Duchane

[11] **4,376,751**

[45] **Mar. 15, 1983**

[54] **PRODUCTION OF SUPER-SMOOTH ARTICLES**

[75] Inventor: **David V. Duchane, Los Alamos. N. Mex**

[73] Assignee: **The United States of America as represented by the Department of Energy, Washington. D.C.**

[21] Appl. No.: **268,423**

[22] Filed: **May 29, 1981**

[51] Int. Cl.³ B29C 25/00
[52] U.S. Cl. 264/341; 428/409
[58] Field of Search 264/341, 428/409

[56] **References Cited**

U S PATENT DOCUMENTS

2,209,940	7/1940	Smith	264/341
2,572,719	10/1951	Ginell et al	264/331
3,625,755	12/1971	Potrafke	117/160
3,684,553	8/1972	Van Dyk	264/341
4,133,912	1/1979	Stuart	264/341
4,302,418	11/1981	Cullis	264/341

OTHER PUBLICATIONS

Chemical Abstracts, vol 82. 1975. pp. 43–44. No 98967m
Chemical Abstracts. vol. 83, 1975, p 83, No. 115655y
Chemical Abstracts, vol. 90. 1979, p 53, No 90 169698c
Chemical Abstracts, vol. 84, 1976, p. 50, No 84: 606589.
Daniels et al. Physical Chemistry, 2nd Edition. Wiley and Sons, New York, 1963. p. 354.
Modern Plastics Encyclopedia, pp. 533-536. Gross Editor—in—Chief (McGraw—Hill, NY 1974-1975).

Primary Examiner—James H. Derrington
Attorney. Agent. or Firm—Elizabeth O. Slade; Paul D Gaetjens; Richard G. Besha

[57] **ABSTRACT**

Super-smooth rounded or formed articles made of thermoplastic materials including various poly(methyl methacrylate) or acrylonitrile-butadiene-styrene copolymers are produced by immersing the articles into a bath. the composition of which is slowly changed with time. The starting composition of the bath is made up of at least one solvent for the polymer and a diluent made up of at least one nonsolvent for the polymer and optional materials which are soluble in the bath. The resulting extremely smooth articles are useful as mandrels for laser fusion and should be useful for a wide variety of other purposes, for example lenses

12 Claims, 6 Drawing Figures

163

United States Patent [19]

McCreary et al.

[11] **4,265,982**

[45] **May 5, 1981**

[54] **COATED WOVEN MATERIALS AND METHOD OF PREPARATION**

[75] Inventors: William J. McCreary; David W. Carroll, both of Los Alamos, N. Mex.

[73] Assignee: The United States of America as represented by the United States Department of Energy, Washington, D.C.

[21] Appl. No.: 47,445

[22] Filed: Jun. 11, 1979

[51] Int. Cl.³ B05D 1/22; B32B 7/08
[52] U.S. Cl. 428/608; 427/243; 427/244; 427/245; 427/247; 428/263
[58] Field of Search 427/213, 243, 244, 245, 427/247, 249, 251; 428/263, 608

[56] **References Cited**

U.S. PATENT DOCUMENTS

3,178,308	4/1965	Oxley et al.	427/213
3,202,537	8/1965	Norman et al.	427/213 X
3,264,073	8/1966	Schmitt	29/182
3,343,979	9/1967	Hamm	427/213 X
3,594,215	7/1971	Wakefield	427/213 X
3,796,589	3/1974	Ciraolo et al.	427/213 X
4,071,304	1/1978	Chauvin et al	427/213 X
4,080,927	3/1978	Brown	427/213 X
4,169,911	10/1979	Yoshida et al.	428/258 X
4,180,428	12/1979	Rile et al.	427/249 X

OTHER PUBLICATIONS

Powell et al., "The Formation of Metallic Coatings by Vapor Phase Techniques", *Metal Finishing,* vol. 50, No. 4, Apr. 1952, pp. 64–69.

Primary Examiner—James R. Hoffman
Attorney, Agent, or Firm—Elizabeth O. Slade; Paul D. Gaetjens; Richard G. Besha

[57] **ABSTRACT**

Coating of woven materials so that not only the outer surfaces are coated has been a problem. Now, a solution to that problem is the following: Woven materials are coated with materials, for example with metals or with pyrolytic carbon, which materials are deposited in Chemical Vapor Deposition (CVD) reactions using a fluidized bed so that the porosity of the woven material is retained and so that the tiny filaments which make up the strands which are woven (including inner as well as outer filaments) are substantially uniformly coated.

22 Claims, 11 Drawing Figures